Spring 3-28-2019

Investigation of the Coupled Nuclear, Thermal-Hydraulic, and Thermomechanical Response of a Natural Circulation Research Reactor Under Severe Reactivity-Initiated Accident Transients

Darren G. Talley
University of New Mexico

Darren Glenn Talley

Candidate

Mechanical Engineering

Department

This dissertation is approved, and it is acceptable in quality and form for publication:

Approved by the Dissertation Committee:

Prof. Yu-Lin Shen, Chairperson

Prof. C. Randall Truman

Prof. Sang Lee

Prof. Christopher Perfetti

Investigation of the Coupled Nuclear, Thermal-Hydraulic, and Thermomechanical Response of a Natural Circulation Research Reactor Under Severe Reactivity-Initiated Accident Transients

by

Darren Glenn Talley

B.S.M.E., Mechanical Engineering, University of Arkansas, 1988

M.S.E., Nuclear Engineering, University of Michigan, 1989

DISSERTATION

Submitted in Partial Fulfillment of the

Requirements for the Degree of

Doctor of Philosophy

Engineering

The University of New Mexico

Albuquerque, New Mexico

May 2019

Dedication

For my wonderful wife Angela. I love you.

Acknowledgments

I would like to thank my advisor, Dr. Yu-Lin Shen, for his continual encouragement and guidance along this journey. It was his initial encouragement a few years ago which helped me see that this goal was attainable. To the members of my dissertation committee, Dr. Randy Truman, Dr. Sang Lee, and Dr. Chris Perfetti, thank you for your time and knowledge.

I would like to thank my managers over the years at Sandia National Laboratories, James Bryson, Michael Greutman, and Jason Petti, who have encouraged and supported this pursuit of graduate education. I am also grateful for the Tuition Assistance Program at Sandia National Laboratories for making this possible.

Several of my colleagues at Sandia have spent many hours exercising the Razorback code and reviewing drafts of code documentation. Aaron Miller, Ed Parma, Salvador Rodriguez, Rachel Chang – thank you for the comments and the discussions. Thank you to the operations staff at Sandia's Annular Core Research Reactor for their skill in running this fine machine. To all my colleagues at Sandia's Technical Area V, past and present, I am grateful to be a part of this fine organization.

Without the support of my family, I would not be where I am today. Mom and Dad: thank you for all that you have done for me. Angela: never has there been, nor will there ever be a more awesome wife than you. Thank you so much for your love, patience, and encouragement. Daniel and Sydney, Hannah and Matt, and Laurel: I'm so proud of you, and I love you all. Noah and Mia: Grandpa's going to have even more time to play with you now.

Sandia National Laboratories is a multi-mission laboratory managed and operated by National Technology and Engineering Solutions of Sandia Corporation, LLC., a wholly owned subsidiary of Honeywell International, Inc., for the U.S. Department of Energy's National Nuclear Security Administration under contract DE-NA-0003525.

Investigation of the Coupled Nuclear, Thermal-Hydraulic, and Thermomechanical Response of a Natural Circulation Research Reactor Under Severe Reactivity-Initiated Accident Transients

by

Darren Glenn Talley

B.S.M.E., Mechanical Engineering, University of Arkansas, 1988
M.S.E., Nuclear Engineering, University of Michigan, 1989

Ph.D., Engineering, University of New Mexico, 2019

Abstract

Research reactors play an important role in higher education, scientific research, and medical radioisotope production around the world. It is thus important to ensure the safety of facility workers and the public. This work presents a new reactor transient analysis code, referred to as Razorback, which computes the coupled reactor kinetics, fuel element heat transfer, fuel element thermal expansion and thermal stress, and thermal-hydraulic response of a natural circulation research reactor. The code was developed for the evaluation of large rapid reactivity addition in research reactors, with an initial focus on the Annular Core Research Reactor (ACRR) at Sandia National Laboratories. Razorback has been validated using ACRR pulse operations, and the simulation results are shown to agree very well with measured reactor data. Razorback is also used to examine the response of a natural circulation research reactor (i.e., the ACRR) to large rapid reactivity additions. The reactor kinetic response, the thermal-hydraulic response of the fuel and coolant, and the thermomechanical response of the fuel element materials are each examined separately. Safety analysis and operational implications are discussed.

Contents

Abstract v

List of Figures viii

List of Tables xiv

1. Introduction 1
   - 1.1. Research Motivation 3
   - 1.2. Overview of the Annular Core Research Reactor 3
   - 1.3. Approach 6

2. Review of Related Literature 7
   - 2.1. Introduction 7
   - 2.2. Safety Analysis for Research Reactors 7
   - 2.3. Analytical Methods for Reactivity Initiated Accidents 8
   - 2.4. Computer Code Use for Research Reactor Transient Analyses 12
   - 2.5. Conclusions 14

3. Theory and Design of the Razorback Reactor Transient Analysis Code 17
   - 3.1. Introduction 17
   - 3.1. Code Overview 18
   - 3.3. Reactor Kinetics Model 19
     - 3.3.1. Point-Reactor Kinetics Equations 19
     - 3.3.1. Reactor Power Peaking Factors 21
     - 3.3.2. System Reactivity 23
     - 3.3.3. Reactivity Feedback 24
     - 3.3.4. Weighting of Reactivity Feedback 28
   - 3.4. Fuel Element Heat Transfer Model 31
   - 3.5. Fuel Element Thermal Expansion Model 34
   - 3.6. Coolant Channel Model 37
     - 3.6.1. Coolant Channel Governing Equations 37
     - 3.6.2. Coolant Channel Heat Transfer Coefficients 37
     - 3.6.3. Coolant Equation of State 41
     - 3.6.4. Coolant Channel Two-Phase Flow Equations 42
   - 3.7. Conclusions 53

4. Verification and Validation of the Transient Analysis Code 55
   - 4.1. Introduction 55
   - 4.2. Point-Reactor Kinetics Verification 55
     - 4.2.1. Step Reactivity Addition Without Feedback 55
     - 4.2.2. Ramp Reactivity Addition Without Feedback 58
     - 4.2.3. Sinusoidal Reactivity Addition Without Feedback 59
     - 4.2.4. Step Reactivity Addition With Feedback Case 61
   - 4.3. Heat Transfer Verification 64
   - 4.4. Thermal Expansion Verification 66
   - 4.5. Thermal Stress Verification 70

4.6. Validation for ACRR Operations....74
4.6.1. Pulse Operations....76
4.6.2. Slow Transient Operations....87
4.6.3. Steady-State Operations....89
4.7. Conclusions....91
5. Large Rapid Reactivity Addition Events: Reactor Kinetics Response....93
5.1. Introduction....93
5.2. Overview of the Reactor Power Response for the ACRR....94
5.3. Reactor Power Pulse Characteristics....97
5.4. Relative Reactivity Feedback Mechanism Contributions....107
5.5. Impact of Reactivity Addition Rate....109
5.6. Impact of Initial Reactor Power Level....112
5.7. Discussion of Safety Analysis Implications....116
5.8. Conclusions....119
6. Large Rapid Reactivity Addition Events: Thermal-Hydraulic Response....120
6.1. Introduction....120
6.2. Overview of the Thermal-Hydraulic Response for the ACRR....121
6.3. Thermal-Hydraulic Response to Various Large Rapid Reactivity Additions....139
6.3.1. Fuel Response....139
6.3.2. Coolant Response....141
6.4. Impact of a Post-Pulse Rod Drop....148
6.5. Discussion of Safety Analysis Implications....152
6.6. Conclusions....155
7. Large Rapid Reactivity Addition Events: Thermomechanical Response....157
7.1. Introduction....157
7.2. Overview of the Thermomechanical Response for the ACRR....159
7.2.1. Thermal Expansion Response....164
7.2.2. Thermal Expansion Stress Response....166
7.3. Thermomechanical Response to Various Large Rapid Reactivity Additions....173
7.4. Impact of Reactivity Addition Time....176
7.5. Impact of Fission Energy Deposition Profile in Fuel....180
7.6. Discussion of Safety Analysis Implications....183
7.7. Conclusions....190
8. Conclusions....191
9. Future Work....194
References....195

List of Figures

Figure 1. Photograph of the ACRR in its reactor pool tank. 4

Figure 2. Schematic drawing of the ACRR fuel pellets within a fuel element. 5

Figure 3. Reactor power trace for a large rapid reactivity addition (pulse) operation. 6

Figure 4. ACRR axial peaking factor profile for a fuel element. 22

Figure 5. ACRR radial peaking factor profile for the fuel within a fuel element. 22

Figure 6. Void-Static Quality relationship for various "boiling constraint factors". 51

Figure 7. Razorback simulation of a sinusoidal reactivity addition [34]. 60

Figure 8. Fuel element materials and geometry for heat transfer verification [34]. 64

Figure 9. Simple heat transfer problem results compared to analytical solution [34]. .. 65

Figure 10. Magnitude of the relative error for the heat transfer verification [34]. 65

Figure 11. Radial temperature profile of ACRR inner fuel pellet used for thermal expansion verification [34]. 67

Figure 12. Radial temperature profile of ACRR cladding used for thermal expansion verification [34]. 67

Figure 13. Inner ACRR fuel pellet radial displacement for the thermal expansion verification problem [34]. 68

Figure 14. Relative error of the radial displacement (inner pellet) for the thermal expansion verification problem [34]. 68

Figure 15. Cladding radial displacement for the thermal expansion verification problem [34]. 69

Figure 16. Relative error of the radial displacement (cladding) for the thermal expansion verification problem [34]. 69

Figure 17. Inner ACRR fuel pellet radial stress for the thermal stress verification problem [34]. 71

Figure 18. Inner ACRR fuel pellet azimuthal stress for the thermal stress verification problem [34]. 71

Figure 19. Error in the radial and azimuthal stress for the thermal stress verification problem [34]. 72

Figure 20. ACRR fuel element cladding radial stress for the thermal stress verification problem [34]. 72

Figure 21. ACRR fuel element cladding azimuthal stress for the thermal stress verification problem [34]. 73

Figure 22. Error in the cladding radial and azimuthal stress for the thermal stress verification problem [34]..... 73
Figure 23. ACRR fuel element model geometry used for validation against ACRR operations [32]..... 74
Figure 24. ACRR fuel grid arrangement and flow channel model depiction..... 75
Figure 25. Comparison of a Razorback simulation of a $3 pulse to ACRR data [34]. 76
Figure 26. Comparison of a Razorback simulation of a $3 pulse to ACRR data [34]. 77
Figure 27. Comparison of a Razorback simulation of a $3 pulse to ACRR data [34]. 77
Figure 28. Comparison of Razorback peak measured fuel temperature results with ACRR pulse data [34]. 78
Figure 29. Comparison of Razorback peak power results with ACRR pulse data [34]. 79
Figure 30. Comparison of Razorback pulse energy (yield) results with ACRR pulse data [34]. 80
Figure 31. Depiction of the time related characteristics of a reactor power pulse [34]. 81
Figure 32. Comparison of Razorback pulse width results with ACRR pulse data [34]. 82
Figure 33. Photographs of the flowmeter and its thermocouples used for ACRR measurements [34]. 83
Figure 34. Comparison of Razorback prediction with the measured ACRR fuel temperature for pulse operation 11277 [34]. 84
Figure 35. Comparison of Razorback prediction of the long-term cooldown of the ACRR fuel temperature for pulse operation 11277 [34]. 85
Figure 36. Comparison of Razorback prediction with the measured ACRR coolant outlet temperature for pulse operation 11277 [34]. 86
Figure 37. Control rod bank movement history for ACRR operation 11278 [34]..... 87
Figure 38. Measured and predicted power history for ACRR operation 11278 [34]... 88
Figure 39. Measured and predicted fuel temperatures for ACRR operation 11278 [34]. 88
Figure 40. Measured and predicted coolant channel outlet temperature for ACRR operation 11278 [34]. 89
Figure 41. Measured and predicted fuel temperatures for the ACRR [34]. 90
Figure 42. Reactor power pulse for a $3 rapid reactivity addition to the ACRR..... 94
Figure 43. Reactor power history for a $3 rapid reactivity addition to the ACRR. 95
Figure 44. Energy release for a $3 rapid reactivity addition to the ACRR. 96

Figure 45. Initial maximum fuel temperature history for a $3 rapid reactivity addition to the ACRR. 97
Figure 46. Variation of reactor peak power vs. reactivity addition. 98
Figure 47. Variation of peak system reactivity vs. reactivity addition. 99
Figure 48. Extrapolation of reactor peak power illustrating the effect of the reactivity addition time. 100
Figure 49. Extrapolation of energy yield illustrating the effect of the reactivity addition time. 101
Figure 50. Variation of the characteristic pulse width vs. reactivity addition. 101
Figure 51. Variation of minimum reactor period vs. reactivity addition. 102
Figure 52. Variation of the time to the peak power vs. reactivity addition. 103
Figure 53. Razorback time to peak power compared to Nordheim-Fuchs estimate. . 104
Figure 54. Variation of the initial peak maximum fuel temperature vs. reactivity addition. 105
Figure 55. Timing of the effective completion of the pulse energy deposition. 106
Figure 56. Comparison of the reactivity feedback mechanisms during the pulse. 107
Figure 57. Impact on initial pool water temperature on the Doppler and coolant reactivity feedback during the pulse. 108
Figure 58. Impact of the reactivity addition time on the reactor power response to a $3.50 LRRA. 110
Figure 59. Closeup view of the impact of the reactivity addition time on the reactor power response to a $3.50 LRRA. 110
Figure 60. Peak system reactivity for a $3.50 pulse of various reactivity addition times. 111
Figure 61. Initial peak fuel temperature for a $3.50 pulse of various reactivity addition times. 112
Figure 62. Reactor power pulse for a $3.50 reactivity addition with varying initial reactor power. 113
Figure 63. Closeup view of reactor power pulses with varying initial reactor power. 113
Figure 64. Peak reactor power achieved for a $3.50 pulse for various initial powers. 114
Figure 65. Initial peak fuel temperature achieved for a $3.50 pulse for various initial powers. 115
Figure 66. Initial maximum fuel temperature history for a $3 rapid reactivity addition. 122
Figure 67. Maximum fuel temperature history for a $3 rapid reactivity addition. 122

Figure 68. Initial equilibrium between cladding heat transfer rate and coolant energy removal rate. 123
Figure 69. Final equilibrium between energy deposition rate, cladding heat transfer rate, and coolant energy removal rate. 124
Figure 70. Comparison of initial pulse fuel temperature profile with the equilibrium profile. 125
Figure 71. Initial axial coolant temperature profile following the pulse heating. 126
Figure 72. Initial coolant mass flowrate response to the pulse heating. 127
Figure 73. Initial axial coolant pressure profile following the pulse heating. 128
Figure 74. Coolant pressure history vs. axial location due to initial pulse heating. ... 129
Figure 75. Time variation of the coolant axial pressure profile during the pulse heating. 129
Figure 76. Time variation of the coolant mass flux profile during the pulse heating. 130
Figure 77. Early evolution of the coolant mass flux at various axial locations. 131
Figure 78. Evolution of the coolant channel temperature profile after the pulse. 132
Figure 79. Evolution of the coolant channel temperature profile when boiling occurs. 133
Figure 80. Upper and lower axial extent of the boiling region after the pulse. 133
Figure 81. Evolution of the boiling void fraction at various axial locations. 134
Figure 82. Evolution of the coolant mass flux during boiling at various axial locations. 135
Figure 83. Evolution of the coolant temperature profile through and post-boiling. .. 136
Figure 84. Early evolution of the cladding surface temperature. 137
Figure 85. Long-term evolution of the cladding surface temperature. 138
Figure 86. Variation of the initial peak maximum fuel temperature vs. reactivity addition. 139
Figure 87. Extrapolation of the initial peak maximum fuel temperature illustrating the effect of the reactivity addition time. 140
Figure 88. Post-pulse temperature rise following the initial pulse heating. 141
Figure 89. Variation of the initial peak maximum coolant temperature vs. reactivity addition. 142
Figure 90. Variation of the peak maximum coolant channel pressure vs. reactivity addition. 143
Figure 91. Variation of the peak maximum cladding surface temperature vs. reactivity addition. 144

Figure 92. Variation of the peak maximum element heat flux vs. reactivity addition. 144
Figure 93. Variation of the time before bulk boiling occurs vs. reactivity addition. . 145
Figure 94. Variation of the axial location at which bulk boiling first occurs vs. reactivity addition. 146
Figure 95. Variation of the axial extent of the bulk boiling region vs. reactivity addition. 147
Figure 96. Variation of the time duration of a bulk boiling region vs. reactivity addition. 147
Figure 97. Impact of a post-pulse rod drop on post-pulse temperature rise. 149
Figure 98. Impact of a post-pulse rod drop on the peak maximum heat flux. 150
Figure 99. Impact of a post-pulse rod drop on maximum bulk boiling length..... 151
Figure 100. Impact of a post-pulse rod drop on the time duration of bulk boiling..... 151
Figure 101. Radial fission energy deposition profile (peak-to-average) within the ACRR fuel pellets. 158
Figure 102. Initial reactor power history for a $3.00 LRRA. 159
Figure 103. Reactor power history for a $3.00 LRRA. 160
Figure 104. Initial maximum fuel temperature history for a $3.00 LRRA. 161
Figure 105. Maximum fuel temperature history for a $3.00 LRRA. 161
Figure 106. Initial inner and outer fuel pellet temperature profiles for a $3.00 LRRA. 162
Figure 107. Equilibrium inner and outer fuel pellet temperature profiles for a $3.00 LRRA. 163
Figure 108. Initial radial displacement time histories for a $3.00 LRRA. 164
Figure 109. Initial gaps size time histories for a $3.00 LRRA. 165
Figure 110. Radial displacement time histories for a $3.00 LRRA. 166
Figure 111. Initial maximum tensile stress time history in the outer fuel pellet for a $3.00 LRRA. 167
Figure 112. Maximum tensile stress time history in the outer fuel pellet for a $3.00 LRRA. 168
Figure 113. Radial stress profiles in the inner and outer fuel pellets at the time of the peak tensile stress for a $3.00 LRRA. 169
Figure 114. Circumferential stress profiles in the inner and outer fuel pellets at the time of the peak tensile stress for a $3.00 LRRA. 170
Figure 115. Equilibrium radial stress profiles in the inner and outer fuel pellets for a $3.00 LRRA. 171

Figure 116. Equilibrium circumferential stress profiles in the inner and outer fuel pellets for a $3.00 LRRA. 171
Figure 117. Maximum tensile stress time history in the cladding for a $3.00 LRRA. 172
Figure 118. Minimum gap sizes in the fuel element for various reactivity additions. 173
Figure 119. Peak tensile stress in the fuel for various reactivity additions. 174
Figure 120. Time of the peak tensile stress in the fuel for various reactivity additions. 175
Figure 121. Impact of reactivity addition time on the evolution of the gap size for a $3.00 LRRA. 177
Figure 122. Maximum tensile stress in the fuel as a function of reactivity addition time for a $3.00 LRRA. 178
Figure 123. Outer fuel pellet radial stress as a function of reactivity addition time for a $3.00 LRRA. 179
Figure 124. Outer fuel pellet circumferential stress as a function of reactivity addition time for a $3.00 LRRA. 179
Figure 125. Fuel radial energy deposition profiles used in impact study. 180
Figure 126. Maximum tensile stress in the fuel as a function of radial energy deposition profile for a $3.00 LRRA. 181
Figure 127. Outer fuel pellet radial stress as a function of radial energy deposition profile for a $3.00 LRRA. 182
Figure 128. Outer fuel pellet circumferential stress as a function of radial energy deposition profile for a $3.00 LRRA..... 182
Figure 129. Razorback fuel pellet geometry vs. the actual ACRR fuel pellet design. 185
Figure 130. LRRA maximum tensile stress history for different fuel ring geometries. 186
Figure 131. LRRA radial stress results for different fuel ring geometries. 187
Figure 132. LRRA circumferential stress results for different fuel ring geometries. .. 187
Figure 133. Post-LRRA equilibrium radial stress results for different fuel ring geometries. 188
Figure 134. Post-LRRA equilibrium circumferential stress results for different fuel ring geometries. 189

List of Tables

Table 1. Delayed neutron group parameters for the step reactivity addition benchmark cases. 56
Table 2. Point-Reactor kinetics benchmark results for $0.5 step addition [34]. 57
Table 3. Point-Reactor kinetics benchmark results for $1.0 step addition [34]. 57
Table 4. Delayed neutron group parameters for the ramp reactivity addition benchmark cases. 58
Table 5. Point-Reactor kinetics benchmark results for $0.1/s ramp addition [34]. 59
Table 6. Point-reactor kinetics benchmark results for a sinusoidal reactivity addition without reactivity feedback [34]. 61
Table 7. Delayed neutron group parameters for the step reactivity addition with feedback benchmark cases. 62
Table 8. Point-reactor kinetics benchmark results for a $2.0 step reactivity addition with reactivity feedback [34]. 63
Table 9. Material properties used to verify Razorback thermal expansion results. 66
Table 10. Radial dimensions for ACRR fuel element materials. 75

Nomenclature

Variables/Symbols

C_i	Delayed neutron precursor "concentration"
c_p	Specific heat capacity
E	Young's modulus
F_R	Fuel element peaking factor relative to an "average" fuel element
F_r	Intra-fuel element radial peaking factor
F_z	Intra-fuel element axial peaking factor
G	Mass flux
h	Specific enthalpy or heat transfer coefficient (depending upon context)
k	Thermal conductivity or neutron multiplication factor (depending upon context)
P	Reactor power
p	Pressure
q''	Heat flux
r	Radius
T	Temperature
z	Axial elevation

Greek Variables/Symbols

α	Reactivity feedback coefficient, vapor void fraction, or linear thermal expansion coefficient (depending upon context)
β_i	Delayed neutron group fraction for group "i"
β_{eff}	Delayed neutron group fraction (sum of all groups)
$\delta(z)$	Dirac delta function
ε_r	Radial strain
ε_θ	Azimuthal strain
λ_i	Delayed neutron group decay constant for group "i"
Λ	Neutron generation time
ρ	Reactivity or density (depending upon context)
σ_r	Radial stress
σ_θ	Azimuthal stress
σ	Stefan-Boltzmann constant (5.35×10^{-12} W/m^2/K^4)

Abbreviations/Acronyms

ACRR	Annular Core Research Reactor
DOE	Department of Energy
IAEA	International Atomic Energy Agency
LRRA	Large Rapid Reactivity Addition
NNSA	National Nuclear Security Administration
RIA	Reactivity-Initiated Accident
SNL	Sandia National Laboratories

1. Introduction

Research reactors play an important role in higher education, scientific research, and medical radioisotope production in the United States and around the world. The International Atomic Energy Agency (IAEA) has identified ~250 research reactors worldwide [1] based on a March 2013 database. An IAEA report [1] lists multiple applications for research reactors including teaching, training, neutron activation analysis, isotope production, neutron radiography, neutron scattering, reactor physics experiments, and nuclear data measurements. Since research reactors play many vital roles for researchers around the worlds, it is of paramount importance to ensure that workers, the public, and the environment are protected from the radiological hazards associated with the operation of these reactors.

Evaluation of the safety of research reactors generally does not require the degree of rigor associated with the safety analysis of commercial power reactors. The amount of radioactive material available for release in an accident situation involving a research reactor can be orders of magnitude smaller than that for a commercial power reactor. Yet, it remains necessary to demonstrate that a research reactor can withstand postulated accidents with no fuel of fuel cladding damage, and/or minimal radiation dose consequences to workers and the public. In the United States (US), most research reactors (e.g., university research reactors) are regulated by the US Nuclear Regulatory Commission (NRC), while some are regulated by the Department of Energy (DOE) or its National Nuclear Security Administration (NNSA).

The NRC regulates research reactors under Class 104 licenses issued in accordance with 10 CFR 50 [2], and has developed NUREG-1537 [3] to provide guidance for Safety Analysis Reports for its research reactor community. Under NUREG-1537, the licensee is expected to submit analyses of postulated abnormal and accident scenarios, demonstrating that the facility design and safety features prevent unacceptable consequences to the public and the environment. Under United States (US) Department of Energy (DOE) regulations, it is also necessary to assess the potential radiation dose consequences of postulated accident scenarios under the assumption that no preventive or mitigative actions are taken. The purpose of this "unmitigated" analysis is to provide perspective on the importance of the preventive or mitigative function performed by a safety-related system, structure, or component.

Reactivity-initiated accidents (RIAs), are accidents involving the unplanned or uncontrolled addition of "reactivity." Reactivity is normally added when a reactor operator moves neutron absorbing control rods out of a reactor core. Positive reactivity additions increase reactor power, while negative reactivity additions decrease reactor power. However, when too much reactivity is added, or reactivity is added too fast, or both, rapid power increases can result in undesirably high fuel or fuel cladding temperatures which may exceed material melting points. This would be particularly true for the analysis of an unmitigated RIA event, where no action is taken to shut down the reactor. An analysis of a mitigated RIA event (e.g., where a reactor protection system initiates a reactor shutdown when the rapid power rise is detected) would be used to establish the functional requirements for a reactor protection system that would preclude fuel and/or fuel cladding damage.

1.1. Research Motivation

Because of the significantly lower radioactive material inventory for research reactors, simple analytical approaches are often used to conservatively estimate the worst-case fuel and cladding temperatures achieved in postulated RIAs. As such, the accident phenomena considered may be very simplified, such as only evaluating the enthalpy (or temperature) rise of the fuel.

This goal of this research work is to investigate the nuclear, thermal-hydraulic, and thermomechanical response of a natural circulation research reactor to severe RIAs. An in-depth investigation of the detailed thermal and mechanical response of the research reactor fuel element components and their associated coolant channel will enhance understanding and insight into the various phenomena occurring during a large rapid reactivity addition (LRRA). To accomplish this goal, a particular research reactor will serve as the test specimen.

Many existing research reactors perform rapid reactivity additions to produce reactor power pulses, such as General Atomics' TRIGA reactors. However, the Annular Core Research Reactor (ACRR) at Sandia National Laboratories (SNL) performs normal pulse operations in the range of the LRRAs we wish to investigate.

1.2. Overview of the Annular Core Research Reactor

The ACRR is utilized to provide neutron and gamma ray radiation environments for radiation effects testing. Shown in Figure 1, the ACRR core is located in a pool ~3 m in diameter and ~10 m deep. The circulation of the coolant water is driven by means of natural circulation as the reactor heats the water within the core. The core consists of 236

fuel elements (of which 2 are fuel followed neutron absorbing safety rods and 6 are fuel followed neutron absorbing control rods). The elements of the core are arranged in a ~4 cm pitch hexagonal grid.

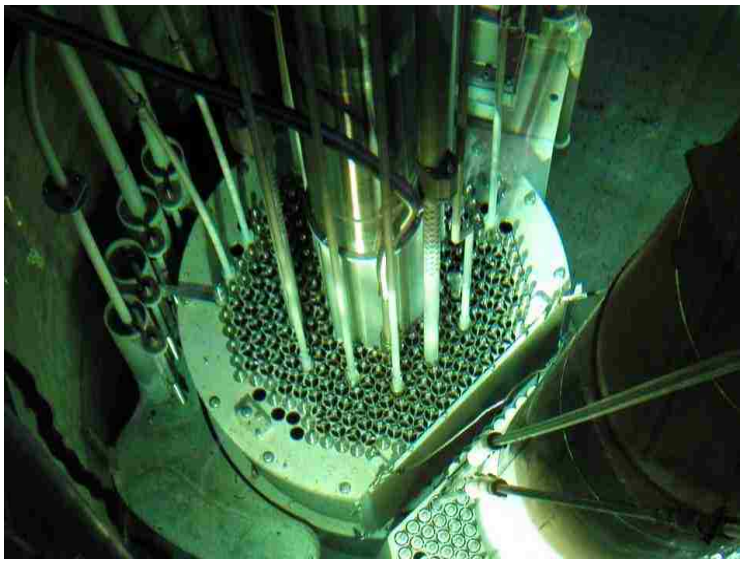

Figure 1. Photograph of the ACRR in its reactor pool tank.

The ACRR fuel, shown in Figure 2, consists of a dispersion of uranium oxide within a beryllium oxide matrix (BeO-UO_2) cold-pressed and sintered into dual concentric annuli. The inner and outer annuli are cut into 180° arcs. These fuel pellets are stacked within niobium cans to a total fuel height of ~0.5 m. The fueled cans are sealed within stainless steel tubes ~3.7 cm in outer diameter. The fuel element is sealed and backfilled with ~2 atm of helium, which occupies the various gap spaces between fuel annuli, the niobium can, and the stainless steel cladding.

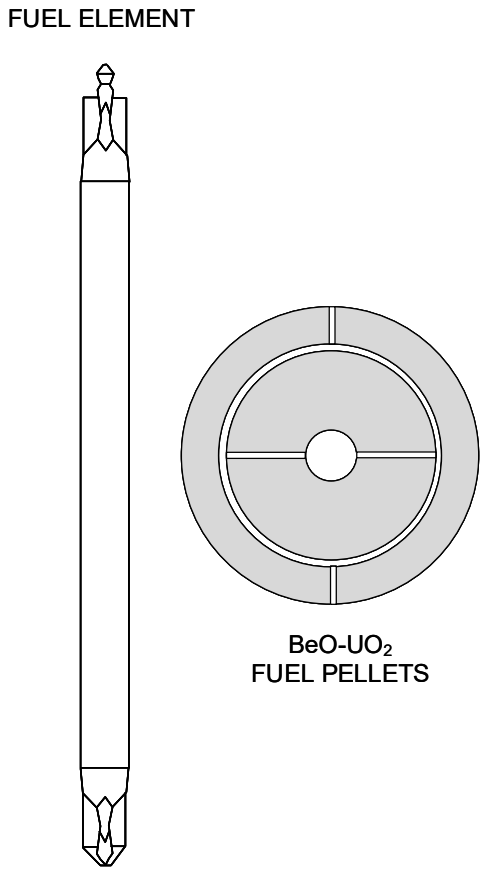

Figure 2. Schematic drawing of the ACRR fuel pellets within a fuel element.

The ACRR has three independent reactivity control mechanisms: a safety rod bank, a control rod bank, and a transient rod bank. The ACRR can be operated in a "steady-state" mode in which relatively slow changes in reactor power level up to ~2.5 MW are made via operator movement of the control rod bank out of or into the core. Rapid ejection of the transient rod bank allows the ACRR to be operated in a "pulse" mode in which Gaussian shaped reactor power pulses result with peak powers of up to ~30,000 MW with pulse widths of ~7 ms (Figure 3). The ACRR was designed to perform such LRRA pulse operations as part of its mission, and data from such operations provides a means to validate predictions of computer codes developed to simulate the operation of research reactors.

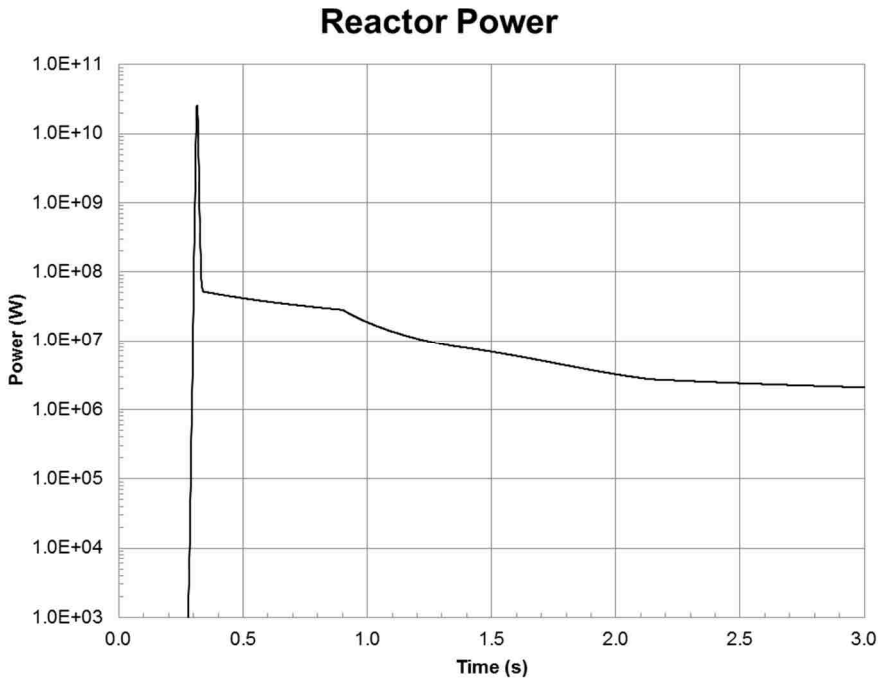

Figure 3. Reactor power trace for a large rapid reactivity addition (pulse) operation.

1.3. Approach

To facilitate the investigation of the response of a natural circulation research reactor such as the ACRR to severe RIAs, a reactor transient analysis code (named Razorback) has been developed which is focused upon a natural circulation research reactor. The Razorback code addresses the kinetic behavior of the reactor, and the thermal-hydraulic and thermomechanical behavior of the reactor's fuel, cladding, and coolant. The code was verified and validated against the LRRA pulse operations performed by the ACRR. The code was then utilized to investigate the response of the ACRR to a spectrum of LRRAs. The responses were evaluated to identify important considerations associated with the safety analysis of RIAs.

2. Review of Related Literature

2.1. Introduction

A review of the existing literature was conducted to identify research related to the safety analysis of research reactors. Three primary areas were considered: (1) safety analysis for research reactors, (2) analysis methods for reactivity-initiated accidents (RIAs), and (3) computer codes used in research reactor safety analyses. The literature search revealed research reactor safety analysis works from the international research reactor community, as well as some from the United States. These international works were related to either the research reactor installation with which the authors were associated, or to the generic International Atomic Energy Agency (IAEA) 10 MW material test reactor (MTR) benchmark.

2.2. Safety Analysis for Research Reactors

In the United States, most research reactors (e.g., university research reactors) are regulated by the Nuclear Regulatory Commission (NRC), while some are regulated by the Department of Energy (DOE) or its National Nuclear Security Administration (NNSA). The goal of each regulator is to ensure the protection of the public and workers from radiological dose consequences resulting from the unplanned release of radioactive material from the reactor facilities.

The NRC has issued NUREG-1537 [3] which contains guidance for its research reactor licensees, describing the format and content expected in the safety analysis report for a research reactor. Within NUREG-1537, a variety of potential accident initiating

events and scenarios are described for consideration by the research reactor licensee to determine applicability to their reactor facility. Accident events listed include: (1) insertion of excess reactivity, (2) loss of coolant, (3) loss of coolant flow, (4) fuel handling accidents, (5) experiment malfunctions, etc. The reactivity-initiated accidents (RIAs), with which this dissertation is primarily concerned, would fall within the "insertion of excess reactivity" category.

Research reactor safety analyses works in the reviewed literature focus mostly upon evaluating RIAs, loss of coolant flow, and loss of coolant events. Hamidouche, et al., [4] present an overview of research reactor accident analysis, in which it is noted that the generic IAEA 10 MW MTR type reactor benchmark includes problems which primarily address RIAs and loss of flow transients. Bousbia-Salah and Hamidouche [5] document one such evaluation of the IAEA 10 MW benchmark for RIAs and loss of flow transients. Bokhari, et al., [6] examine of the response of the Pakistan Research Reactor-1 (PARR-1) to RIAs resulting from a variety of postulated initiating events (a continuous control rod withdrawal, dropping a fuel element into the core, flooding a beam tube with water, and the removal of an in-pile experiment during operation). Kazeminejad [7], and Khater, et al., [8] are additional examples of the examination of the response of a research reactor to RIAs.

2.3. Analytical Methods for Reactivity Initiated Accidents

A useful theoretical model for the nuclear response of a reactor to large rapid reactivity additions (LRRAs) is the point reactor kinetics equations [9]. The term *kinetics* refers to the rate of change of reactor power level. The term *point reactor* refers to the fact that the spatial variation of the power within the reactor, when assumed to be time-

independent, may be factored out of the neutron transport equations. Thus, in terms of its time behavior, the reactor may be considered as a "point" reactor. The model accounts for the prompt neutrons which arise immediately from a nuclear fission event in the reactor fuel, and for the delayed neutrons. The various delayed neutron-producing fission products may be treated as groups of "precursors" for which an effective radioactive decay constant characterizes the neutron production rates for a group.

The point-reactor kinetics equations are given by

$$\frac{dP}{dt} = \frac{\rho - \beta}{\Lambda} P + \sum_{i=1}^{N} \lambda_i C_i \tag{2-1}$$

$$\frac{dC_i}{dt} = -\lambda_i C_i + \frac{\beta_i}{\Lambda} P, \quad i = 1, \ldots N \tag{2-2}$$

where P is the reactor power, ρ is the system reactivity, β is the delayed neutron fraction, Λ is the neutron generation time, λ_i is the decay constant for delayed neutron precursor group "i," C_i is the delayed neutron precursor concentration for group "i," and N is the number of delayed neutron precursor groups. We note that the reactivity may be expressed in "units" of dollars ($), where one dollar corresponds to a reactivity value numerically equal to the delayed neutron fraction β. It is also noted that in this formulation, the delayed neutron precursor "concentration" C_i is a compound variable (the product of the precursor concentration, the reactor volume, the macroscopic fission cross section, and the energy released per fission) having dimensions of energy per unit time.

The response of a research reactor to a LRRA is sometimes assessed using the point reactor kinetics equation model, but assuming the contribution of delayed neutrons to be

negligible. The LRRA is assumed to be a "step" addition (i.e., occurring essentially instantaneously), and the reactivity feedback is assumed to be proportional to the energy release of the reactor (i.e., the time-integrated power). The resulting solutions are commonly referred to as the Nordheim-Fuchs equations. Bell and Glasstone [10] present a derivation of the Nordheim-Fuchs equations (although the equations are described by the name Fuchs-Hansen). The results allow one to estimate the peak power (P_{peak}) and energy release (E_{pulse}) of the power pulse using the approximations below.

$$P_{peak} \approx \frac{(\rho - \beta)^2}{2\Lambda\gamma} \tag{2-3}$$

$$E_{pulse} \approx \frac{2(\rho - \beta)}{\gamma} \tag{2-4}$$

In Eqs. 2-3 and 2-4, ρ is the reactivity addition, β is the delayed neutron fraction, Λ is the neutron generation time, and γ is the energy reactivity feedback coefficient.

Of the Nordheim-Fuchs results, the energy release (Eq. 2-4) is perhaps the most useful for safety analyses. The energy release is equivalent to the enthalpy change. Since this approach treats the reactor as a "point," the enthalpy change must be scaled with appropriate power peaking factors to obtain the highest enthalpy change within the core. From which one may estimate the maximum temperature achieved in the fuel during a LRRA excursion. The maximum fuel temperature may then be compared to known fuel damage points (e.g., melting point) or experimentally determined failure thresholds.

The Nordheim-Fuchs equations may be modified somewhat by formulating the energy reactivity feedback in terms of a temperature-dependent fuel heat capacity. The resulting equations, presented by West et al. [11], may be expressed as

$$P_{peak} = P_0 + C_0 \frac{(\rho - \beta)^2}{2\Lambda\gamma} + C_1 \frac{(\rho - \beta)^3}{6\Lambda\gamma^2} \tag{2-5}$$

$$T_{max} \approx T_0 + \frac{2(\rho - \beta)}{C\gamma} \left[-\frac{3}{8}(\sigma - 1) \pm \frac{3}{8}\sqrt{(\sigma - 1)^2 + \frac{16}{3}\sigma} \right] \tag{2-6}$$

In Eqs. 2-5 and 2-6, P_0 is the initial power, C_0 and C_1 are the zeroth and first order coefficients in a linearly temperature-dependent model of the fuel heat capacity, and T_0 is the initial fuel temperature. The parameter σ is given by

$$\sigma = \frac{\gamma C_0}{(\rho - \beta) C_1} \tag{2-7}$$

and the '+' sign is taken in Eq. 2-6 when the parameter $\sigma > 1$. The safety analysis reports for the Kansas State University TRIGA reactor [12] and the University of Texas TRIGA reactor [13] utilize this modified version of the Nordheim-Fuchs equations in their analyses of LRRA event. As noted above, the maximum fuel temperature in the core is determined by applying appropriate power peaking factors.

One important limitation of this analytical approach is that the results assume a "step" reactivity addition (i.e., LRRA occurs essentially instantaneously, or at least before any appreciable reactivity feedback is developed). Such an idealization leads to over-estimating the peak power and peak fuel temperature for real-world LRRAs where the addition is not rapid enough that the step assumption fails. Over-estimation is generally a virtue in safety analysis, but could lead to unnecessary performance limitations where LRRAs are a desired feature of operation.

Lastly, this analytical approach also provides no means to assess the thermal-hydraulic response of the coolant in the reactor. The timing at which adequate natural circulation coolant flow is developed in the coolant channel to accommodate the cladding surface heat flux resulting from the rapidly heated fuel is important to assessing the potential for post-pulse cladding damage.

For these and other reasons, computer codes are utilized in the analysis of a LRRA. Utilization of a computer to solve the point reactor kinetics equations, and associated thermal-hydraulic equations, allows the analyst to introduce more realism into the LRRA safety analysis problem.

2.4. Computer Code Use for Research Reactor Transient Analyses

The specific computer codes used for analyzing transients in research reactors form a broad set, and this discussion is not intended to provide an exhaustive listing. In general, there are a few codes utilized by many researchers because of community-wide acceptance and familiarity (e.g., RELAP5, PARET). It is also the case that many researchers have opted to develop their own codes.

RELAP5 has a long history in the modeling of commercial power reactors and their response to small-break loss of coolant accidents [14], and its versatility and verification and validation are extensive. RELAP5 was, however, designed to address commercial power reactors. As such, RELAP5 is focused more toward the thermal-hydraulic response of the entire high-pressure forced-flow nuclear steam supply system. This is much different than the relatively low-pressure, low-flow and/or natural circulation environment of a research reactor.

PARET [15] was originally intended for research reactors with plate-type fuel and cylindrical fuel pins. It has been used to evaluate research reactors which participated in the Reduced Enrichment for Research and Test Reactors program. The code does assume the coolant to be incompressible, and utilizes an axially averaged mass flux as opposed to a mass flux which may vary with axial channel location.

Hamidouche [4] and other investigators [8] [16] have recognized the need for simpler codes geared toward the typical research reactor environment and focused on the reactor fuel element performance. The results of such efforts in the international research reactor community have been documented in recent years [4] [5] [6] [7] [8] [17] [18] [19]. Selected examples are noted below.

Kazeminejad [20] examines the impact of reactivity addition events for a pool-type natural circulation reactor with the intent of defining reactivity addition limits. The subject reactor is the generic 10 MW IAEA MTR. A coupled kinetic-thermal-hydraulic code was developed specifically for this application. No protective action (scram) was assumed, and thus the reactor power excursion was terminated by reactivity feedback. However, the reactivity additions evaluated were \$0.50 and \$0.73. These values are much less than the LRRA scenarios we wish to examine in this dissertation. In this work, Kazeminejad also asserts that the study of natural circulation in research reactors has been mostly related to decay heat removal rather than response of a natural circulation research reactor to a reactivity addition event.

Bokhari [6] considers various reactivity addition events using the PARET code. The events are relatively modest in terms of reactivity addition ranging from a \$0.13 start-up rod withdrawal to a \$1.23 drop of a fuel element into the core when the reactor is critical.

All events consider the impact of a reactor power level trip with a setpoint of 11.5 MW. Peak reactor power levels reached in the transients range from just above 11.5 MW for the smaller reactivity additions to ~40 MW for the largest reactivity addition. Peak fuel and cladding temperatures are only in the range of 100°C-130°C. Again, these values are much less than the LRRA scenarios we wish to examine in this dissertation.

Jordan, et al., [21] analyze a reactivity addition accident for the University of Florida research reactor. The PARET/ANL code is used to study reactivity additions up to 1480 pcm (~$2.1 assuming a delayed neutron fraction of 0.007) added over 0.5 s. No protective action is assumed to occur. A peak power of 116 MW is reached. The fuel temperature rises from an initial 60°C to 191°C which, after accounting for 70% uncertainty, implies a ~280°C maximum fuel temperature. It is stated that larger reactivity additions are not considered because of limitations in PARET in predicting departure from nucleate boiling conditions.

Khater, et al., [8] consider a larger reactivity addition of $4, with and without a reactor scram. This magnitude of reactivity addition is in the range of interest for LRRAs we wish to address in this dissertation. However, the $4 is added at a relatively slow rate over 4 s. The analysis of the no-scram event is carried to the point of high fuel temperatures and potential cladding melt. However, no results are presented showing the evolution of the coolant flow rate, which is one of the phenomena of interest in this dissertation.

2.5. Conclusions

In the literature reviewed, the evaluation of reactivity initiated accidents (RIAs) is seen to be an important consideration in research reactor safety analysis. Many recent works from the international research reactor community have addressed these transients.

However, the literature reviewed does not appear to address the LRRAs of interest in this dissertation. In these analyses, a reactor scram is often assumed to act, limiting the severity of the events being analyzed. In addition, these scrams are effective primarily because the magnitude of the reactivity addition is small, and/or the rate at which the reactivity is added is slow.

It was also noted that many investigators have developed their own transient analysis codes to apply to their research reactor investigations. There does not appear to be a code described in these works which couples the reactor kinetics, thermal-hydraulics, and thermomechanical behavior of the fuel/cladding of a research reactor in the modeling of reactor transient events. Bousbia-Salah and Hamidouche [18] do include the effect of thermal expansion of the cladding in their reactivity feedback models. However, the thermal expansion is based on a correlation to cladding temperature rather than a direct computation of the thermal expansion by their reactor transient analysis code. None of the works reviewed addresses the thermomechanical stress response of the research reactor fuel or cladding to RIAs.

Many of the works reviewed do not address the RIA event without a scram. This is not necessarily a shortcoming, given that the typical goal of such analyses is to demonstrate the effectiveness of the reactor trip system in limiting the impact of the event on the fuel and cladding. One benefit of evaluating the event without a scram is that the results would provide perspective on the risk potential and thus the importance of the action of the scram. Some of the works reviewed do explore RIA events with and without a reactor trip. However, when no scram events are considered, the reactivity added is typically small or the addition rate is relatively slow. As such, the ability of the codes

developed for the works discussed above to address a large and rapid reactivity pulse operation has not been demonstrated. LRRAs, such as those conducted at the ACRR, can add up to $3 of reactivity in less than 100 ms.

Based upon this review, a code designed to evaluate low-pressure, low-flow natural circulation research reactor transients would be beneficial. The ability to couple the kinetics response of the reactor, the thermal-hydraulic response of the fuel-coolant system, and the thermomechanical response of the fuel element materials would add considerably to the benefit of the code. Such a code could be validated to measured data from the large rapid reactivity events which are part of the ACRR's normal operation. This would provide confidence in the code's predictive capabilities for analyzing RIAs.

3. Theory and Design of the Razorback Reactor Transient Analysis Code

3.1. Introduction

During a large rapid reactivity addition (LRRA) event, such as a pulse operation (or pulse accident) in a research reactor, the reactor power will increase rapidly, resulting in a rapid temperature rise within the fuel. The increasing temperature will result in thermal expansion of the fuel element components, which will induce thermal stresses. At first, there is little time for significant heat transfer to occur, and the fission energy deposition during this time is essentially adiabatic. Eventually, significant heat transfer within the fuel, and away from the fuel to the coolant channel, will begin to occur. As heat is transferred out of the fuel element and into the coolant channel, the decrease in density of the coolant as its temperature rises will lead to an increase in coolant flowrate. The increasing fuel temperature and decreasing coolant density impact the reactivity of the reactor core in a negative fashion, causing a decrease in core reactivity which begins to offset the reactivity addition. Eventually, this negative reactivity feedback will be sufficiently large in magnitude that it will drive the reactor power down, terminating the reactor power pulse.

As can be seen, there are many different physical phenomena which must be modeled to predict the response of the fuel element and coolant to a LRRA event. This chapter describes the theory and design of a reactor transient analysis computer code, called Razorback, which was developed for this purpose.

3.1. Code Overview

Razorback is a research reactor transient analysis computer code designed to determine the response of a pool-type natural circulation research reactor, such as Sandia National Laboratories' (SNL) Annular Core Research Reactor (ACRR), to reactivity additions. Razorback was designed with the ACRR in mind, but is expected to be useful in application to other research reactors.

Razorback computations are based upon user-provided data related to fuel element geometry and materials, nuclear reactor kinetics parameters and reactivity feedback coefficients, coolant channel geometry, and reactor pool parameters. The nuclear reactor kinetic parameters are utilized to determine the change in reactor power due to the reactivity addition. Reactor power changes drive energy deposition within the fuel element model, which is then transferred within the fuel element components and into the adjacent coolant. Temperature changes within the fuel element induce thermal expansion displacements. Changes in the rate of heat transfer into the coolant result in coolant temperature and flowrate changes. These changes induce reactivity feedback to be coupled with the subsequent reactivity element movements. The overall result is a time history of reactor power, fuel element component temperatures and displacements, coolant channel temperatures and flowrate, etc., in response to the reactivity addition induced reactor transient.

Razorback performs a coupled numerical solution of the point reactor kinetics equations, the energy conservation equation for fuel element heat transfer, the equation of motion for fuel element material thermal expansion, and the mass, momentum, and energy

conservation equations for the water cooling of the fuel elements. The solution is currently formulated in cylindrical coordinates and focused on a single fuel element/coolant channel.

3.3. Reactor Kinetics Model

A nuclear reactor is driven by the fission process by which neutrons "split" nuclei such as ^{235}U. The fission process is most effective with low energy neutrons (~0.2 eV) referred to as thermal neutrons. However, the neutrons "born" from the fission of ^{235}U nuclear, which sustain the fission chain reaction in the core, have average energies of ~2 MeV. Thus, the neutrons need to be slowed down, or moderated. As it turns out, water is both a good neutron moderator as well as a good reactor coolant.

When the nuclei fission, the kinetic energy of the by-product nuclei (called fission products) is deposited in the fuel, thus providing the useful heat source of the nuclear reactor. These fission products are also unstable (i.e., radioactive), and make the fuel highly radioactive. However, certain fission products decay by emitting a neutron, which is beneficial to the fission chain reaction process. These are called delayed neutrons, because the half-life of the radioactive decay process from which they arise varies from ~0.2 s to ~55 s (vs. the neutrons born "promptly" at the time of fission).

3.3.1. Point-Reactor Kinetics Equations

A useful theoretical model for the nuclear response of a reactor to reactivity changes is the point reactor kinetics equations [9]. The term *kinetics* refers to the rate of change of reactor power level. The term *point reactor* refers to the fact that the spatial variation of the power within the reactor, when assumed to be time-independent, may be factored out of the neutron transport equations. Thus, in terms of its time behavior, the reactor may be

considered as a "point" reactor. The model accounts for the prompt neutrons which arise immediately from a nuclear fission event in the reactor fuel, and for the delayed neutrons. The various delayed neutron-producing fission products may be treated as groups of "precursors" for which an effective radioactive decay constant characterizes the neutron production rates for a group.

The point-reactor kinetics equations are given by

$$\frac{dP}{dt} = \frac{\rho - \beta}{\Lambda} P + \sum_{i=1}^{N} \lambda_i C_i \tag{3-1}$$

$$\frac{dC_i}{dt} = -\lambda_i C_i + \frac{\beta_i}{\Lambda} P, \quad i = 1, \ldots N \tag{3-2}$$

where P is the reactor power, ρ is the system reactivity, β is the delayed neutron fraction, Λ is the neutron generation time, λ_i is the decay constant for delayed neutron precursor group "i," C_i is the delayed neutron precursor concentration for group "i," and N is the number of delayed neutron precursor groups. It is noted that in this formulation, the delayed neutron precursor "concentration" C_i is a compound variable (the product of the precursor concentration, the reactor volume, the macroscopic fission cross section, and the energy released per fission) having dimensions of energy per unit time. In the code, the solution of the point reactor kinetics equations is implemented using a Runge-Kutta scheme found in Ronen [22].

3.3.1. Reactor Power Peaking Factors

In order to construct a spatial power distribution based upon the reactor power computed via the point reactor kinetics model, a set of power peaking factors is used. The code performs its simulations based on a single fuel element within the reactor core itself. The simulation may be based on any fuel element in the reactor core by providing a core radial peaking factor (F_R) describing the ratio of the energy deposition in that fuel element to the energy deposition in an "average" fuel element in the core.

Within a fuel element itself, there are two additional power peaking factors utilized in the code's simulations: the axial element peaking factor (F_z) and the fuel material radial peaking factor (F_r). The axial element peaking factor is represented in the code using a 6th order polynomial

$$F_z(z) = \sum_{i=0}^{6} a_i \cdot \left(\frac{z}{H_f}\right)^i \tag{3-3}$$

where a_i are the polynomial coefficients (supplied by the user) and H_f is the height of the fuel material. Figure 4 shows an example of an axial element peaking factor profile for the ACRR.

The radial fuel material peaking factor is represented in the code as an exponential function

$$F_r(r) = Ae^{Br} + C \tag{3-4}$$

where A, B, and C are constants supplied by the user. These peaking factors may be determined for a given reactor core using a neutron transport code such as MCNP [23]. Figure 5 shows an example of a radial fuel material peaking factor profile for the ACRR.

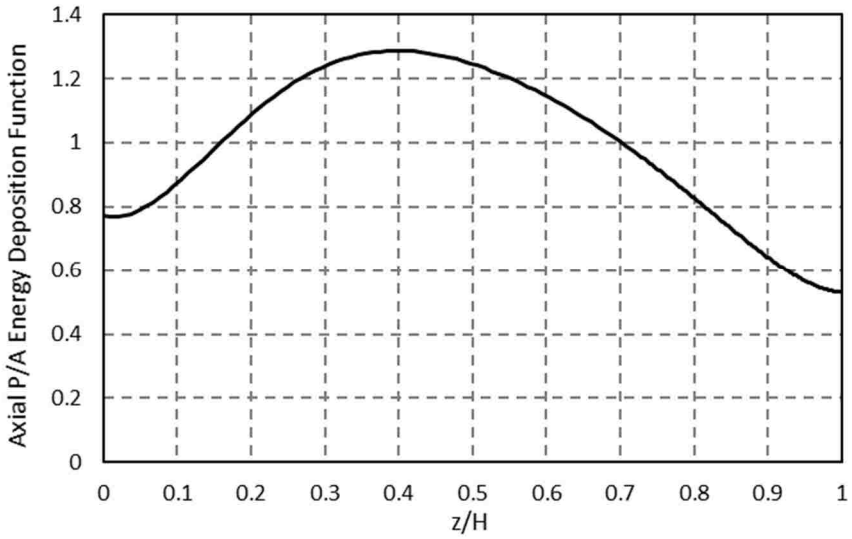

Figure 4. ACRR axial peaking factor profile for a fuel element.

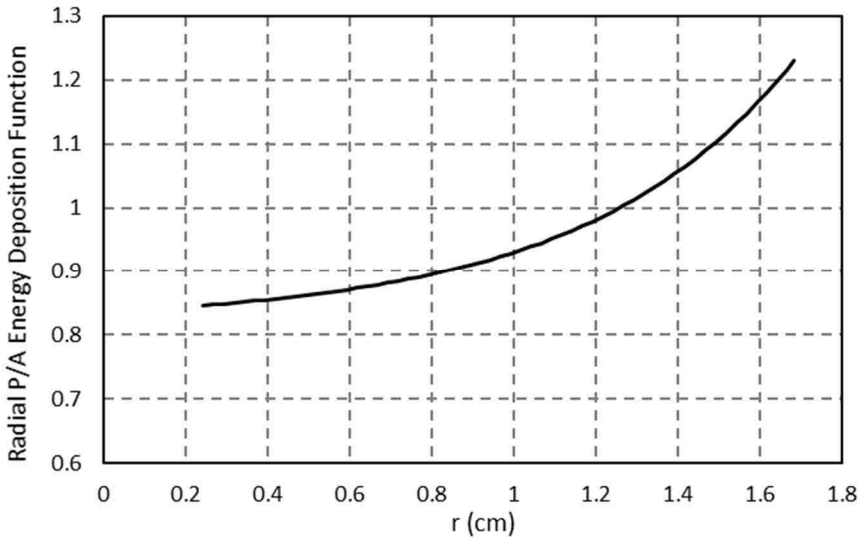

Figure 5. ACRR radial peaking factor profile for the fuel within a fuel element.

3.3.2. System Reactivity

The state of a nuclear reactor can be divided into three sub-states: (1) subcritical, (2) critical, and (3) supercritical. These are often associated with the value of a multiplication factor *k* which expresses the ratio of neutron production to neutron loss. When k<1, loss exceeds production, the reactor is subcritical and the reactor power level tends to decay. When k=1, production equals loss, the reactor is critical and the reactor power level remains constant. When k>1, production exceeds loss, the reactor is supercritical and the reactor power level increases.

A related parameter often used to characterize the state of the reactor is the system reactivity ρ given by

$$\rho = \frac{k-1}{k} \tag{3-5}$$

A negative, zero, or positive value of the reactivity corresponds to the subcritical, critical, and supercritical states discussed above. Changes in reactivity may be induced by movement of neutron absorbing rods associated with the reactor's control system, and changes in coolant temperature and density, fuel temperature, and fuel element component dimensions. The movement of neutron absorbing rods can be referred to as intentional reactivity additions (positive or negative), while the other changes are typically referred to as reactivity feedback (positive or negative).

System reactivity is a dimensionless quantity, but is often expressed in terms of "dollars." The reactivity in dollars is defined as the reactivity divided by the delayed neutron fraction β. For rapid reactivity additions greater than $1, the reactor power increases at an exponential rate determined by the neutron generation time (which is ~24

μs for the ACRR) and the magnitude of the reactivity addition. When such reactivity additions are large enough, the action of control systems (either manual or automatic) is not fast enough to effectively control the power level.

3.3.3. Reactivity Feedback

The system reactivity in Eq. 3-5 is the sum of the reactivity added by control systems (e.g., movement of neutron absorber rods out of or into the reactor core) and the reactivity feedback due to changing conditions in the core. The reactivity feedback effects typically accounted for when analyzing reactor power response are due to fuel temperature changes (referred to as Doppler reactivity feedback), and coolant density feedback (sometimes referred to as coolant void reactivity feedback). Pulse reactors such as the ACRR rely heavily upon the Doppler feedback. This feedback is immediate and negative, and is the primary mechanism by which a large rapid reactivity addition power excursion is turned into a high peak power, short time width, "pulse." The model in Razorback addresses the Doppler and coolant void feedback mechanisms, but also considers reactivity feedback related to the thermal expansion of the fuel material, the thermal expansion of the cladding material, and the neutron energy spectrum changes due to changes in the coolant temperature.

The change in system reactivity may be treated as the sum of intentional control system reactivity additions and the various reactivity feedback mechanisms of the reactor. In differential form, we have

$$d\rho = \frac{\partial \rho}{\partial z}_{cs} dz + \sum_{i=1}^{I} \frac{\partial \rho}{\partial X_i} dX_i \tag{3-6}$$

where $(\partial\rho/\partial z)_{cs}$ would be the differential reactivity addition for changes in control system rod position (z), and $\partial\rho/\partial X_i$ would be the reactivity feedback coefficients for changes in various component parameters (X_i = fuel temperature, coolant density, cladding outer radius, etc.). Thus, models are needed to compute the changes in various reactor component parameters resulting from changes in reactor power induced by changes in control system reactivity additions.

The Doppler effect reactivity feedback coefficient (α_D) in due to changes in the fuel temperature (T_f), and is defined as

$$\alpha_D = \left(\frac{\partial \rho}{\partial T_f}\right) \tag{3-7}$$

This coefficient has been shown [9] to vary inversely as the square root of the absolute temperature of the fuel. This reactivity coefficient is implemented within the code as

$$\alpha_D = c_1 + \frac{c_2}{\sqrt{T_f}} \tag{3-8}$$

where c_1 and c_2 are user inputs, and T_f is the absolute fuel temperature (in K).

The reactivity feedback associated with the thermal expansion of a fuel pellet is assumed to be a function of the pellet outer and inner radii (R_o and R_i), and the density of the fuel (ρ_f). While it is recognized that these parameters are not completely independent of one another, but are related via the equation of motion, the elastic properties of the material and the temperature distribution within the fuel, these parameters are treated as independent for the purposes of computing reactivity feedback coefficients. The reactivity feedback coefficients associated with the fuel outer and inner radii and density (α_{FE_Ro}, α_{FE_Ri}, and $\alpha_{FE\_\rho f}$) are given by the three partial derivatives

$$\alpha_{FE\_Ro} = \left(\frac{\partial \rho}{\partial R_o}\right)_{R_i,\rho_f} \tag{3-9a}$$

$$\alpha_{FE\_Ri} = \left(\frac{\partial \rho}{\partial R_i}\right)_{R_o,\rho_f} \tag{3-9b}$$

$$\alpha_{FE\_\rho f} = \left(\frac{\partial \rho}{\partial \rho_f}\right)_{R_o,R_i} \tag{3-9c}$$

These reactivity coefficients are provided to the code by user input. Each coefficient is implemented within the code as a constant.

The reactivity feedback associated with the thermal expansion of the fuel element cladding is assumed to be a function of the cladding outer and inner radii (R_{oc} and R_{ic}), and the density of the cladding (ρ_{clad}). For the ACRR, this reactivity feedback is primarily due to the change of the local flow area in a fuel element coolant channel as the outer radius of the clad (R_{oc}) changes. As the radius expands, the local flow area decreases, which impacts the local fuel-to-moderator ratio. With the ACRR being an undermoderated core, an increase in fuel-to-moderator ratio has a negative reactivity. The cladding expansion reactivity feedback coefficients associated with the cladding outer and inner radii and density (α_{CE_Ro}, α_{CE_Ri}, and $\alpha_{CE\_\rho c}$) are given by the three partial derivatives

$$\alpha_{CE\_Ro} = \left(\frac{\partial \rho}{\partial R_{oc}}\right)_{R_{ic},\rho_{clad}} \tag{3-10a}$$

$$\alpha_{CE\_Ri} = \left(\frac{\partial \rho}{\partial R_{ic}}\right)_{R_{oc},\rho_{clad}} \tag{3-10b}$$

$$\alpha_{CE\_\rho c} = \left(\frac{\partial \rho}{\partial \rho_{clad}}\right)_{R_{oc},R_{ic}} \tag{3-10c}$$

These reactivity coefficients are provided to the code by user input. Each coefficient is implemented within the code as a constant.

The reactivity feedback coefficient associated with coolant/moderator is considered to be a function of the density of the coolant (ρ_c) and the temperature of the coolant (T_c). It is important to note here that the density of the coolant is obviously related to the coolant temperature. However, in this context, the coolant temperature parameter characterizes the energy spectrum of the neutrons within the coolant. Understood in this manner, these parameters are treated as independent for the purposes of computing reactivity feedback coefficients.

The reactivity feedback coefficients associated with the coolant ($\alpha_{M\_\rho c}$ and α_{M_Tc}) are given by

$$\alpha_{M\_\rho c} = \left(\frac{\partial \rho}{\partial \rho_c}\right)_{T_c} \tag{3-11a}$$

$$\alpha_{M\_Tc} = \left(\frac{\partial \rho}{\partial T_c}\right)_{\rho_c} \tag{3-11b}$$

These reactivity coefficients are provided to the code by user input. Each coefficient is implemented within the code as a constant.

For a given time step, the code will compute the total reactivity feedback from each of the components above (Doppler, fuel expansion, cladding expansion, and moderator). Each contribution is then summed together to provide a total reactivity feedback for use in the point kinetics equation.

3.3.4. Weighting of Reactivity Feedback

The Razorback code was developed to evaluate the response of a reactor core consisting of multiple fuel elements (e.g., 236 with the ACRR) to reactivity additions such as from the movement of neutron absorbing control rods, by modeling a single reactor fuel element. Since only a single fuel element is modeled, the code must incorporate a scheme to weight the contributions of the reactivity feedback at each location within the fuel element and coolant channel models to the total reactivity feedback of the reactor.

Reactivity feedback coefficients provided as inputs to the code are assumed to be determined from neutronic analysis of the reactor core's response to a global average change in a given parameter. In other words, the Doppler feedback coefficient is assumed to have been determined by the results of neutronic analyses in which all of the fuel material in the core is at a given temperature. Thus, the Doppler feedback coefficient is expected to yield the system reactivity change for a change in core-average fuel temperature. It is likewise assumed that all other reactivity feedback coefficients provide system reactivity changes for changes in other core-average parameters. Therefore, the reactivity feedback contributions must be appropriately weighted over the dimensions of the fuel element and coolant channel, and for the peaking factor of the element being evaluated.

The weighting scheme employed in the code is described here using the Doppler feedback contribution as an example. First it is noted that the fuel temperature changes are applicable to the element being analyzed, with a core peaking factor of F_R. The total Doppler feedback contribution $\Delta\rho_D$ is determined by integrating over the fuel material volume in the element, using a weighting function w(r,z).

$$\Delta\rho_D = \frac{1}{V_F}\int_0^{H_f} dz \int_{R_i}^{R_o} dr\, r \left[\int_{T_f(r,z,t_1)}^{T_f(r,z,t_2)} dT_f\, \alpha_D(T_f)\cdot w(r,z)\right] \qquad (3\text{-}12)$$

Here, $T_f(r,z,t_1)$ and $T_f(r,z,t_2)$ are the local fuel temperature at the beginning of the time step (t_1) and the end of the time step (t_2), and V_F is the volume of the fuel.

The weighting function is determined by considering two factors: (1) an importance function based on first-order perturbation theory as applied to neutron transport theory, and (2) a scaling factor to translate the local temperature change to a core-average temperature change. From first-order perturbation theory, one can propose that the importance function is approximated by the neutron flux distribution [9]. For the purposes of this code, the neutron flux distribution within a fuel element is assumed to be represented by the axial ($F_z(z)$) and fuel pin radial ($F_r(r)$) peaking distributions given by the product $F_z(z)^n \cdot F_r(r)^n$, where n would be a user-selected exponent. With this consideration, our weighting function would be in the form

$$w(r,z) = C \cdot F_z^{\,n}(z) F_r^{\,n}(r) \qquad (3\text{-}13)$$

using a multiplicative constant C to allow for adjustments of this model to actual reactor performance data.

The scaling factor for the relation between the change in the local temperature $T(r,z)$ of a fuel element (relative to a reference temperature $T_o(r,z)$) and a change in the temperature $\bar{T}(r,z)$ of a core-average element is determined first by noting

$$T(r,z) - T_o(r,z) = F_R[\bar{T}(r,z) - \bar{T}_o(r,z)] \tag{3-14}$$

where F_R is the overall core power peaking factor of the fuel element under consideration. For a differential change in time we have

$$d\bar{T}(r,z) = \frac{1}{F_R} dT(r,z) \tag{3-15}$$

Since the Doppler coefficient is assumed to have been determined from changes in core-average fuel temperature we have

$$\bar{\alpha}_D(\bar{T}_f) = \left(\frac{d\rho}{d\bar{T}_f}\right) \tag{3-16}$$

Therefore, to translate this to a local temperature change we apply the relation in Eq. 3-15 to obtain

$$\alpha_D(T_f) = \left(\frac{d\rho}{d\bar{T}_f}\right) \cdot \frac{d\bar{T}}{dT} \tag{3-17}$$

By substituting Eqs. 3-15, 3-16, and 3-17 into Eq. 3-12, the total Doppler feedback is this given by

$$\Delta\rho_D = \frac{C}{V_F F_R} \int_0^{H_f} dz \int_{R_i}^{R_o} dr\, r \left[\int_{T_f(r,z,t_1)}^{T_f(r,z,t_2)} dT_f\, \bar{\alpha}_D(T_f) F_z^{\,n}(z) F_r^{\,n}(r) \right] \tag{3-18}$$

and by inspection, we see that the weighting function is given by the product of the importance function and the reciprocal of the peaking factor product, or

$$w(r,z) = \frac{C}{F_R} \cdot {F_z}^n(z){F_r}^n(r) \tag{3-19}$$

The implicit assumption above, which relates the local temperature change to an average temperature change using the peaking factors F_R, F_r, and F_z, is that the energy deposition is rapid so that the fuel heats essentially adiabatically. Thus, the assumption is best suited for a rapid reactivity addition. This weighting scheme, however, is also applied within the code for slower transients in which the adiabatic assumption is not applicable. However, the assumption is still reasonable for application of the core radial (F_R) and element axial (F_z) peaking factors, and the impact of applying the fuel material radial peaking factor (F_r) is assumed to be minimal.

The other fuel element reactivity feedback mechanisms (i.e., fuel and cladding expansion), are treated in the same way (i.e., Eq. 3-18). The coolant channel reactivity feedback is treated in a similar manner, but only the core radial (F_R) and element axial (F_z) peaking factors are used. This assumes that the axial distribution of the neutron-gamma energy deposition in the coolant channel is the same as the axial distribution of the fission energy deposition in the fuel element.

3.4. Fuel Element Heat Transfer Model

The temperature state of the reactor fuel element components (e.g., fuel and cladding) is determined from an energy balance equation for the fuel element given by

$$\rho_m c_p \frac{\partial T}{\partial t} = -\frac{1}{r}\frac{\partial}{\partial r}(rq'') + q''' \tag{3-20}$$

where ρ_m is the material density, c_p is the constant pressure specific heat capacity, T is the temperature, q" is the radial heat flux, and q"' is the internal volumetric heating of the material. Axial heat transfer is treated as negligible, so only a radial heat flux is included in this formulation. However, axial temperature variation (and axially-dependent volumetric heating) will be accounted for by solving Eq. 3-20 numerically for multiple axial "slices" of the fuel element.

When the energy equation is applied to fuel material, the internal volumetric heating is the nuclear fission event energy release. This fission energy release is directly related to the reactor power level (P_{Rx}). The volumetric heating within the fuel in a given fuel element is determined by

$$q'''_{fuel}(r,z) = \frac{P_{Rx} \cdot f_{fuel} \cdot \rho_{fuel}}{N_{elements} \cdot m_{fuel}} F_R \cdot F_z(z) \cdot F_r(r) \qquad (3\text{-}21)$$

where ρ_{fuel} is the density of the fuel, $N_{elements}$ is the number of fuel elements in the reactor, m_{fuel} is the mass of the fuel in an element, and f_{fuel} is the fraction of the reactor power which is deposited in the fuel material of an element. F_R, $F_Z(z)$, and $F_r(r)$ are the core radial, axial, and radial fuel peaking factors, respectively, discussed in Sect. 3.3.1.

When the energy equation is applied to non-fuel material in a fuel element (e.g., the cladding), the internal volumetric heating is due to neutron/gamma heating in that material. This heating is also directly related to the reactor power level (P_{Rx}). In these cases, the volumetric heating is determined by

$$q'''_{material} = \frac{P_{Rx} \cdot f_{material} \cdot \rho_{material}}{N_{elements} \cdot m_{material}} F_R \cdot F_z(z) \quad (3\text{-}22)$$

where $\rho_{material}$ is the density of the material, $m_{material}$ is the mass of the material in an element, and $f_{material}$ is the fraction of the reactor power which is deposited in the material in an element. The core radial peaking factor (F_R) and the axial element peaking factor ($F_z(z)$) are applied, but the energy deposition is assumed to be uniform across the radial width of non-fuel materials.

The radial heat flux (q") through the fuel element materials is given by Fourier's law of heat conduction where the heat flux is proportional to the negative of the local temperature gradient with the local thermal conductivity being the proportionality constant.

$$q''_{cond} = -k\frac{dT}{dr} \quad (3\text{-}23)$$

For the gap regions (assumed to be filled with a gas) in the fuel element, the total radial heat flux (q") is the sum of the conduction component above (q''_{cond}) and a radiation heat flux (q''_{rad}) component. Between the two radiating surfaces (labeled as 1 and 2) of a gap, the radiation heat flux is given by

$$q''_{rad} = \frac{\sigma(T_{s1}^4 - T_{s2}^4)}{\frac{1}{\varepsilon_1} + \frac{1-\varepsilon_2}{\varepsilon_2}\left(\frac{r_{s1}}{r_{s2}}\right)} \quad (3\text{-}24)$$

where σ is the Stefan-Boltzmann constant, T_{s1} and T_{s2} are the temperatures of the two radiating surfaces, ε_1 and ε_2 are the emissivities of the two radiating surfaces, and r_{s1} and r_{s2} are the radii of the two radiating surfaces. If desired, this radiation heat transfer

mechanism across a gap can be set to zero (i.e., turned off) in the code execution by a user input.

A symmetry boundary condition at the inner radius of the fuel element is employed, which is equivalent to an adiabatic boundary condition. Specifically, at the inner radius, the local heat flux is set equal to zero, viz.,

$$q''(r = R_{inner}, z) = -k\left(\frac{dT}{dr}\right)_{r=R_i} = 0 \tag{3-25}$$

The boundary condition at the outer surface of the cladding of the fuel element is a convection heat flux due to the coolant in the coolant channel, using Newton's law of heating/cooling

$$q''(r = R_{outer}, z) = h(z)[T_s(z) - T_b(z)] \tag{3-26}$$

where h(z) is the local heat transfer coefficient, $T_s(z)$ is the local surface temperature of the fuel element cladding, and $T_b(z)$ is the local bulk temperature of the coolant.

3.5. Fuel Element Thermal Expansion Model

The thermal expansion of the components of the fuel element is determined from the equation of motion solved for the displacement arising from temperature changes within the components. The resultant stress field in the components is derived from the displacements. The equation of motion for the fuel element components is given by

$$\rho_m \frac{\partial^2 u}{\partial t^2} = \frac{\partial \sigma_r}{\partial r} + c\frac{\sigma_r - \sigma_\theta}{r} \tag{3-27}$$

where ρ_m is the material density, σ_r is the radial stress, σ_θ is the azimuthal stress, u is the radial displacement, and c is a geometry factor (1 for cylindrical geometry or 0 for rectangular geometry).

The radial and azimuthal stress may be expressed in terms of the radial strain (ε_r), the azimuthal strain (ε_θ), and the strain associated with the local temperature change with respect to a reference temperature T_o. Thus, we have

$$\sigma_r = E'\varepsilon_r + \nu' E'\varepsilon_\theta - E'\int_{T_o}^{T} \alpha' \mathrm{d}T \tag{3-28a}$$

and

$$\sigma_\theta = E'\varepsilon_\theta + \nu' E'\varepsilon_r - E'\int_{T_o}^{T} \alpha' \mathrm{d}T \tag{3-28b}$$

In these definitions (Eqs. 3-28a and 3-28b), we are using a primed notation for the effective Young's modulus (E′), the effective Poisson's ratio (ν′), and the effective linear thermal expansion coefficient (α′). This allows for the definitions to be used for both plane stress and plane strain conditions. Razorback currently utilizes the plane stress condition, and thus, these parameters are given by

$$E' = \frac{E}{1-\nu^2} \tag{3-29a}$$

$$\nu' = \nu \tag{3-29b}$$

and

$$\alpha' = \alpha(1+\nu) \tag{3-29c}$$

The radial and azimuthal strain may be expressed as

$$\varepsilon_r = \frac{\partial u}{\partial r} \tag{3-30a}$$

and

$$\varepsilon_\theta = c\frac{u}{r} \tag{3-30b}$$

Note here that the definition of the azimuthal strain assumes azimuthal symmetry so that the derivative of the azimuthal displacement with respect to θ is zero. With these definitions, the form of the equation of motion that Razorback is designed to solve is given by

$$\frac{\rho_m}{E'}\frac{\partial^2 u}{\partial t^2} = \frac{\partial}{\partial r}\left(\frac{\partial u}{\partial r}\right) + \frac{c}{r}\frac{\partial u}{\partial r} - c\frac{u}{r^2} - \alpha'\frac{\partial T}{\partial r} \tag{3-31}$$

3.6. Coolant Channel Model

3.6.1. Coolant Channel Governing Equations

The temperature and density state of the coolant can be determined from the mass, momentum, and energy balance equations for the fuel element coolant channel given by

$$\frac{\partial \rho_c}{\partial t} = -\frac{\partial G}{\partial z} \tag{3-32}$$

$$\frac{\partial G}{\partial t} = -\frac{\partial p}{\partial z} - \rho g - \frac{\partial}{\partial z}\left(\frac{G^2}{\rho_c}\right) - \frac{f}{D_h}\frac{G|G|}{2\rho_c} - \sum_i K_i \frac{G|G|}{2\rho_c}\delta(z - z_i) \tag{3-33}$$

$$\begin{aligned}\frac{\partial}{\partial t}(\rho_c h) = & -\frac{\partial}{\partial z}(Gh) + q'' \frac{\pi d_{rod}}{A_{flow}} + q''' + \frac{\partial p}{\partial t} \\ & + \frac{G}{\rho_c}\left[\frac{\partial p}{\partial z} + \frac{f}{D_h}\frac{G|G|}{2\rho_c} + \sum_i K_i \frac{G|G|}{2\rho_c}\delta(z - z_i)\right]\end{aligned} \tag{3-34}$$

where ρ_c is the coolant density, G is the mass flux (or momentum density), p is the pressure, g is the gravitational acceleration, *f* is the Darcy-Weisbach friction factor, D_h is the flow channel hydraulic diameter, K_i is the minor loss coefficients at location z_i, h is the enthalpy, q" is the heat flux at the fuel rod surface, d_{rod} is the fuel element diameter, A_{flow} is the flow area, and q"' is the internal volumetric heating of the fluid.

3.6.2. Coolant Channel Heat Transfer Coefficients

The design must also address the heat transfer interface between the fuel element cladding and the coolant flowing in the channel. As noted in Section 4.1.2, this is accomplished by means of a heat transfer coefficient (h). Using Newton's Law of Heating/Cooling, the heat transfer coefficient is given by

$$h = \frac{q''}{T_s - T_b} \tag{3-35}$$

This heat transfer coefficient is often correlated as a part of a dimensionless parameter known as the Nusselt number (Nu), which is given by

$$Nu = \frac{hD_h}{k} \tag{3-36}$$

where D_h is the coolant channel hydraulic diameter, and k is the coolant thermal conductivity.

For single phase coolant flow, the Nusselt number correlation form will vary depending upon the heat transfer regime. In a natural circulation system (i.e., no pumps), when cladding surface heat flux is very low, convective flow currents occur at the cladding surface driven by buoyancy forces on the heated coolant at the cladding surface. However, in the channel further away from the cladding surface, the coolant is nearly quiescent. The heat transfer regime is natural convection, and Nu is given by

$$Nu = CRa^n \tag{3-37}$$

where C is a correlation coefficient, n is a correlation exponent, and Ra is the Rayleigh number. The Rayleigh number is given by

$$Ra = \frac{{\rho_c}^2 g\beta(T_w - T_b){D_h}^3}{\mu^2} \tag{3-38}$$

where ρ_c is the coolant density, g is the acceleration of gravity, β is the coolant volumetric expansion coefficient, T_w is the cladding wall temperature, T_b is the bulk coolant temperature, and μ is the coolant absolute viscosity.

As the cladding surface heat flux is increased, the coolant further away from the cladding surface is no longer quiescent. The coolant at the cladding surface and in the full channel is now flowing, driven by the buoyancy forces due to the coolant external to the flow channel (i.e., natural circulation flow). The heat transfer regime is that of forced convection, although driven by the natural circulation pressure difference of the upper and lower ends of the flow channel. For this regime, the Nusselt number is obtained from a correlation such as the Dittus-Boelter or Colburn correlations [24]. In a general form, Nu is given by

$$Nu = CRe^m Pr^n \tag{3-39}$$

where C is a correlation coefficient, Re is the Reynolds number, m is a correlation exponent for Re, Pr is the Prandtl number, and n is a correlation exponent for Pr. The Reynolds and Prandtl numbers are given by

$$Re = \frac{GD}{\mu} \tag{3-40}$$

and

$$Pr = \frac{\mu c_p}{k} \tag{3-41}$$

where c_p is the coolant specific heat capacity. The correlation coefficient C, and the correlation exponents m and n, will differ, in general, for laminar ($Re \lesssim 2000$) and turbulent ($Re \gtrsim 2000$) flow conditions.

As the cladding surface heat flux increases further, the coolant near the cladding surface can begin to boil, before the bulk of the coolant reaches its saturation temperature. The heat flux of incipient boiling (q_{ib}'') is determined in Razorback using the Bergles-Rohsenow [25] relation (adjusted for SI units)

$$q''_{ib} = 1082p^{1.156}[1.8(T_s - T_{sat})]^{2.1598/p^{0.0234}} \tag{3-42}$$

where p is the coolant pressure (bar), T_s is the cladding surface temperature (°C), and T_{sat} is the local coolant saturation temperature (°C).

In this heat transfer regime, the code is designed to determine the corresponding cladding surface temperature from the Jens-Lottes correlation [26], and then determine the heat transfer coefficient. The Jens-Lottes correlation (adjusted for SI units) is given by

$$\frac{q''_{JL}}{10^6} = \frac{\exp(\frac{4p}{62})}{25^4}(T_s - T_{sat})^4 \tag{3-43}$$

The cladding surface temperature is thus

$$T_s = T_{sat} + 25\exp\left(-\frac{p}{62}\right)\left(\frac{q''_{JL}}{10^6}\right)^{1/4} \tag{3-44}$$

For heat transfer in this regime, the subcooled boiling heat flux (q''_{scb}), is treated as a superposition of the single-phase heat flux (q''_{sp}) characterized by Eqs. 3-35-3-41 and the heat flux characterized by the Jens-Lottes correlation (q''_{JL}). In Razorback, the superposition is formed using the relation

$$q''_{scb} = \sqrt{{q''_{sp}}^2 + \left(q''_{JL} - q''_{ib}\right)^2} \tag{3-45}$$

The heat transfer coefficient is then found from

$$h = \frac{q''_{scb}}{T_s - T_b} \tag{3-46}$$

where T_b bulk temperature of the coolant.

For the case of saturated flow boiling (i.e., the bulk coolant is now saturated), the heat transfer regime is assumed to continue to be this same subcooled boiling regime. The difference in the application of the correlation equations is that the Reynolds number used to compute the single-phase convection term is modified to be

$$Re = \frac{G(1-x)D}{\mu} \tag{3-47}$$

where x is the quality of the coolant.

3.6.3. Coolant Equation of State

An equation of state is needed to address the time derivative of the density in the mass continuity equation. Since the mass continuity equation will be combined with the momentum equation to solve for the pressure distribution in the flow channel, it is desirable to use the equation of state to relate the density, the pressure (p), and the enthalpy (h) of the coolant. Thus, the equation of state is first taken to be in the form of

$$\rho_c = \rho_c(p, h) \tag{3-48}$$

Cast in differential form we have

$$d\rho_c = \left(\frac{\partial \rho_c}{\partial P}\right)_h dp + \left(\frac{\partial \rho_c}{\partial h}\right)_P dh \tag{3-49}$$

The partial derivatives here can be expressed in terms of thermodynamic properties for evaluation using Maxwell relations such as those found in Sears [27]. Specifically,

$$\left(\frac{\partial \rho_c}{\partial P}\right)_h = \frac{c_p}{c_v}\frac{1}{c^2} + \frac{\beta}{c_p}(1-\beta T) \tag{3-50}$$

and

$$\left(\frac{\partial \rho_c}{\partial h}\right)_P = -\frac{\rho_c \beta}{c_p} \tag{3-51}$$

where c_p is the specific heat capacity at constant pressure, c_v is the specific heat capacity at constant volume, c is the speed of sound, and β is the volumetric thermal expansion coefficient.

3.6.4. Coolant Channel Two-Phase Flow Equations

There are several modeling options available to address flow conditions when both liquid and vapor coexist. The simplest modeling approach is to assume that the liquid and vapor exist in a homogenous mixture at mechanical and thermodynamic equilibrium (i.e., the pressure and temperatures of each phase are equal), typically referred to as the homogenous equilibrium model (HEM). Perhaps the most complicated modeling approach is to assume that the liquid and vapor coexist as two distinct flows, where neither mechanical nor thermodynamic equilibrium conditions prevail, referred to as the two-fluids model (TFM). For this approach, it is necessary to develop constitutive relations for relating the pressures and temperatures of the liquid and vapor components, as well as to address heat and momentum transfer at the interfaces between the two components. Intermediate type modeling approaches, such as assuming either mechanical and/or thermodynamic equilibrium, may be used to simplify the models. Finally, a widely employed intermediate type approach is referred to as the drift flux model (DFM). With the drift flux model [28] [29], a relative velocity difference is allowed for the liquid and gas components of the two-phase flow mixture, using appropriate constitutive relations [30] for the relative velocity. Lahey [29] provides a good description of the various relations associated with the DFM.

To begin, we define the void fraction (α) as the ratio of the flow cross-sectional area occupied by vapor (A_g) to the total flow cross-sectional area occupied by the vapor and liquid (A_g and A_f).

$$\alpha = \frac{A_g}{A_g + A_f} \tag{3-52}$$

Next, we define the mixture density ($\overline{\rho}$) as

$$\overline{\rho} = \alpha\rho_g + (1-\alpha)\rho_f \tag{3-53}$$

Note that we assume that the densities of the liquid and vapor are the saturation densities (ρ_f and ρ_g, respectively), which are functions of pressure only. Thus, we are assuming thermodynamic and mechanical equilibrium in the mixture.

To proceed further, we will now identify two-phase mixture definitions for the quantities which are used in the mass, momentum, and energy conservation equations (Eqs. 3-32, 3-33, and 3-34. The mixture mass flux (G) is given by

$$G = \rho_g u_g \alpha + \rho_f u_f (1-\alpha) \tag{3-54}$$

where u_f and u_g are the velocities of the liquid and gas phases, respectively, which are generally not equal. The momentum flux term (G^2/ρ) is given by

$$\frac{G^2}{\rho} = \alpha\rho_g {u_g}^2 + (1-\alpha)\rho_f {u_f}^2 \tag{3-55}$$

The mixture enthalpy density (ρh) is given by

$$\rho h = \alpha\rho_g h_g + (1-\alpha)\rho_f h_f \tag{3-56}$$

where h_f and h_g are the enthalpies of the liquid and gas phases, respectively. And, lastly, the enthalpy flux term (Gh) is given by

$$Gh = \alpha\rho_g u_g h_g + (1-\alpha)\rho_f u_f h_f \tag{3-57}$$

As mentioned above, u_f and u_g are in general not equal. In an upward flow, vapor bubbles will tend to rise faster than the liquid flow speed because of the different buoyancy forces due to the differences in their densities. Thus, the relative velocity of the vapor phase with respect to the liquid phase will be positive. The various approaches to modeling two-phase flow use different methods to address this difference in the velocity of the vapor and liquid phases.

For the drift flux model approach, which will be used in Razorback, an effective drift (u'_{gj}) velocity is defined as

$$u'_{gj} = (C_o - 1)j + u_{gj} \tag{3-58}$$

where C_o is a factor representing the distribution of vapor across the cross-sectional area of the channel, and j is the total volumetric flux of both phases in the channel. We will take C_o to be 1, which essentially ignores the variation of α across the radial dimension of the flow channel. Therefore,

$$u'_{gj} = u_{gj} \tag{3-59}$$

Lahey [29] sets the drift velocity equal to the asymptotic bubble rise velocity, and recommends the following relation

$$u_{gj} = 2.9\left[\frac{(\rho_f - \rho_g)\sigma g}{\rho_f^2}\right]^{\frac{1}{4}} \tag{3-60}$$

where σ is the surface tension of the liquid phase.

The liquid and vapor phase velocities (u_f and u_g) can be expressed as functions of the mass flux and effective drift velocity as follows:

$$u_g = \frac{G}{\overline{\rho}} + \frac{\rho_f}{\overline{\rho}} u'_{gj} \tag{3-61}$$

and

$$u_f = \frac{G}{\overline{\rho}} - \frac{\alpha}{1-\alpha}\frac{\rho_g}{\overline{\rho}} u'_{gj} \tag{3-62}$$

Since we utilize the mass flux G in our formulations, we will not make any changes to the mass conservation equation, other than to have the density becomes the mixture density. Thus, the two-phase mass conservation equation becomes

$$\frac{\partial \overline{\rho}}{\partial t} = -\frac{\partial G}{\partial z} \tag{3-63}$$

However, will we need to revise the momentum flux term (G^2/ρ) by substituting Eqs. 3-61 and 3-62 into Eq. 3-55 as shown

$$\frac{G^2}{\rho} = \alpha\rho_g u_g \left(\frac{G}{\overline{\rho}} + \frac{\rho_f}{\overline{\rho}} u'_{gj}\right) + (1-\alpha)\rho_f u_f \left(\frac{G}{\overline{\rho}} - \frac{\alpha}{1-\alpha}\frac{\rho_g}{\overline{\rho}} u'_{gj}\right) \tag{3-64}$$

which yields the result

$$\frac{G^2}{\rho} = \frac{G^2}{\overline{\rho}} + \frac{\rho_g \rho_f}{\overline{\rho}} \frac{\alpha}{1-\alpha} \left(u'_{gj}\right)^2 \tag{3-65}$$

Therefore, for two-phase flow, the momentum flux gradient term becomes

$$\frac{\partial}{\partial z}\left(\frac{G^2}{\rho}\right) = \frac{\partial}{\partial z}\left(\frac{G^2}{\overline{\rho}}\right) + \frac{\partial}{\partial z}\left[\frac{\rho_g \rho_f}{\overline{\rho}} \frac{\alpha}{1-\alpha} \left(u'_{gj}\right)^2\right] \tag{3-66}$$

with the result that the net effect is to replace ρ with the mixture density $\overline{\rho}$, and to introduce a gradient term involving the drift velocity u'_{gj}. The two-phase momentum equation is now

$$\frac{\partial G}{\partial t} = -\frac{\partial p}{\partial z} - \overline{\rho} g - \frac{\partial}{\partial z}\left(\frac{G^2}{\overline{\rho}}\right) - \frac{\partial}{\partial z}\left[\frac{\rho_g \rho_f}{\overline{\rho}} \frac{\alpha}{1-\alpha}\left(u'_{gj}\right)^2\right] \ldots$$

$$-\frac{f}{D_h}\frac{G|G|}{2\overline{\rho}} - \sum_i K_i \frac{G|G|}{2\overline{\rho}}\delta(z - z_i) \quad (3\text{-}67)$$

Turning to the energy conservation equation, we first consider the term ρh. Equation 3-56 may be recast as

$$\rho h = \overline{\rho}\left[\frac{\alpha\rho_g}{\overline{\rho}} h_g + \frac{(1-\alpha)\rho_f}{\overline{\rho}} h_f\right] \quad (3\text{-}68)$$

The quantity in brackets may be treated as a mixture enthalpy h, where

$$\overline{h} = \frac{\alpha\rho_g h_g}{\overline{\rho}} + \frac{(1-\alpha)\rho_f h_f}{\overline{\rho}} \quad (3\text{-}69)$$

Thus, we find that ρh may be written as

$$\rho h = \overline{\rho} \cdot \overline{h} \quad (3\text{-}70)$$

Before moving on, we will define a mass quality x_s as

$$x_s = \frac{\alpha\rho_g}{\overline{\rho}} \quad (3\text{-}71)$$

This mass quality is the ratio of the vapor mass to the total liquid and vapor mass in a given volume. This mass quality does not address the relative motion of the two phases, so we refer to it as the static quality, because it would represent the vapor-to-total mass ratio for an instant in time.

Utilizing Eq. 3-71, and recognizing that

$$\frac{(1-\alpha)\rho_f}{\overline{\rho}} = 1 - x_s \quad (3\text{-}72)$$

we may recast the mixture enthalpy in terms of the static quality as

$$\overline{h} = x_s h_g + (1 - x_s) h_f \tag{3-73}$$

Introducing this definition into Eq. 3-68, we find

$$\rho h = \overline{\rho}\left[x_s h_g + (1 - x_s) h_f\right] = \overline{\rho} \cdot \overline{h} \tag{3-74}$$

Lastly, we consider the enthalpy flux for a two-phase mixture by substituting Eqs. 3-61 and 3-62 into Eq. 3-57 as shown

$$Gh = \alpha \rho_g \left(\frac{G}{\overline{\rho}} + \frac{\rho_f}{\overline{\rho}} u'_{gj}\right) h_g + (1 - \alpha) \rho_f \left(\frac{G}{\overline{\rho}} - \frac{\alpha}{1 - \alpha} \frac{\rho_g}{\overline{\rho}} u'_{gj}\right) h_f \tag{3-75}$$

to find

$$Gh = G \cdot \overline{h} + \alpha \frac{\rho_g \rho_f}{\overline{\rho}}\, u'_{gj} h_{fg} \tag{3-76}$$

where $h_{fg} = h_g - h_f$, the latent heat of vaporization.

Therefore, for two-phase flow, the enthalpy flux gradient term becomes

$$\frac{\partial}{\partial z}(Gh) = \frac{\partial}{\partial z}\left(G \cdot \overline{h}\right) + \frac{\partial}{\partial z}\left[\alpha \frac{\rho_g \rho_f}{\overline{\rho}}\, u'_{gj} h_{fg}\right] \tag{3-77}$$

with the result that the net effect is to replace h with the mixture enthalpy $\overline{h}$, and to introduce a gradient term involving the drift velocity u'_{gj}. The two-phase energy equation is now

$$\frac{\partial}{\partial t}\left(\overline{\rho} \cdot \overline{h}\right) = -\frac{\partial}{\partial z}\left(G \cdot \overline{h}\right) - \frac{\partial}{\partial z}\left[\alpha \frac{\rho_g \rho_f}{\overline{\rho}}\, u'_{gj} h_{fg}\right] + q'' \frac{P_h}{A_{flow}} \ldots$$

$$+ q''' + \frac{\partial p}{\partial t} + \frac{G}{\overline{\rho}}\left[\frac{\partial p}{\partial z} + \frac{f}{D_h} \frac{G|G|}{2\overline{\rho}} + \sum_i K_i \frac{G|G|}{2\overline{\rho}} \delta(z - z_i)\right] \tag{3-78}$$

which may be simplified to

$$\overline{\rho}\frac{\partial \overline{h}}{\partial t} = -G\frac{\partial \overline{h}}{\partial z} - \frac{\partial}{\partial z}\left[\alpha\frac{\rho_g\rho_f}{\overline{\rho}}\,u'_{gj}h_{fg}\right] + q''\frac{P_h}{A_{flow}} + q''' + \frac{\partial p}{\partial t} \ldots$$

$$+\frac{G}{\overline{\rho}}\left[\frac{\partial p}{\partial z} + \frac{f}{D_h}\frac{G|G|}{2\overline{\rho}} + \sum_i K_i\frac{G|G|}{2\overline{\rho}}\delta(z-z_i)\right] \quad (3\text{-}79)$$

Now that we have recast the mass, momentum, and energy conservation equations to forms which accommodate two-phase flow, we must consider how to determine the void fraction α. To do so, we first examine the definition of the flow quality (x_f) as the ratio of the vapor *flowrate* to the total *flowrate* (liquid and vapor), viz.,

$$x_f = \frac{\rho_g u_g A_g}{\rho_g u_g A_g + \rho_f u_f A_f} \quad (3\text{-}80)$$

or, using Eq. 3-52,

$$x_f = \frac{\alpha\rho_g u_g}{\alpha\rho_g u_g + (1-\alpha)\rho_f u_f} \quad (3\text{-}81)$$

This relation may be rearranged to solve for the void fraction and obtain the void-flow quality relation

$$\alpha = \frac{\frac{\rho_f}{\rho_g}\frac{u_f}{u_g}x_f}{1 + x_f\left(\frac{\rho_f}{\rho_g}\frac{u_f}{u_g} - 1\right)} \quad (3\text{-}82)$$

The relation may be simplified a bit by defining a density ratio (γ)

$$\gamma = \frac{\rho_f}{\rho_g} \quad (3\text{-}83)$$

and a slip ratio (S)

$$S = \frac{u_g}{u_f} \quad (3\text{-}84)$$

By doing so, we obtain the following void-flow quality relation

$$\alpha = \frac{\gamma x}{\gamma x + S(1-x)} \tag{3-85}$$

In the drift flux model approach, a different void quality relation is obtained which accounts for the differing vapor and liquid velocities using the drift velocity (u_{gj}), viz.,

$$\alpha = \frac{x}{C_o\left[x + \frac{1}{\gamma}(1-x)\right] + \frac{\rho_g u_{gj}}{G}} \tag{3-86}$$

It may be further shown (see Ref. 11) that the slip ratio under this approach is given by

$$S = C_o + \gamma x \frac{(C_o - 1)}{(1-x)} + \frac{\rho_f u_{gj}}{G(1-x)} \tag{3-87}$$

which, for our assumption of C_o=1, becomes

$$S = 1 + \frac{\rho_f u_{gj}}{G(1-x)} \tag{5.91}$$

However, with the potential for flow reversals (G<0) during rapid reactivity addition transients, the slip ratio (S) could become less than zero (e.g., a downward liquid velocity and an upward vapor velocity). Likewise, the flow quality could also become less than zero. Therefore, in the formulations for Razorback, we will work with the static quality (x_s), which will always remain between 0 and 1.

The void-quality relation, where the static quality is used is given by

$$\alpha = \frac{\gamma x_s}{1 + x_s(\gamma - 1)} \tag{3-88}$$

However, we must now have a means for determining the static quality. For Razorback, we will take the static quality to be

$$x_s = \frac{\overline{h} - h_f}{h_{fg}} \tag{3-89}$$

Early testing of the two-phase model in Razorback revealed a tendency for divergent flow instabilities to occur when transient rapid boiling situations (e.g., due to large pulse reactivity additions) result in flow disturbances caused by the significant vapor expansion expected in a low pressure boiling situation in the channel. These divergent flow instabilities caused code execution to crash.

As a heuristic approach to reduce the divergent tendency of these flow instabilities, a factor (ξ) was introduced to produce a modified saturation liquid-to-vapor density ratio, viz.,

$$\gamma' = \frac{\rho_f}{\rho_g}\frac{1}{\xi} \tag{3-90}$$

The values for ξ are presumed to be equal to or greater than 1, but restricted to $\xi \leq \gamma$, so that the modified density ratio is limited to 1 (e.g., for $\rho_g = \rho_f$ at the critical pressure).

$$\alpha = \frac{\frac{\gamma}{\xi}x_s}{1 + x_s\left(\frac{\gamma}{\xi} - 1\right)} \tag{3-91}$$

The impact of the introduction of this factor ξ, that is referred to in Razorback as a boiling constraint factor (BCF) can be seen in Figure 6. For a value of 1, the void-static quality relation is unaffected. As ξ increases, the "rate" at which the void fraction approaches 1 as a function of static quality decreases. It is in this sense that ξ "constrains" the evaporative expansion of the boiling. Note, however, that for values of ξ up to γ, the void fraction remains between 0 and 1 as the static quality ranges from 0 to 1. Also, note that for $\xi = \gamma$, the model approaches a homogeneous equilibrium model with pressure equal to the critical pressure where the void fraction is equal to the quality.

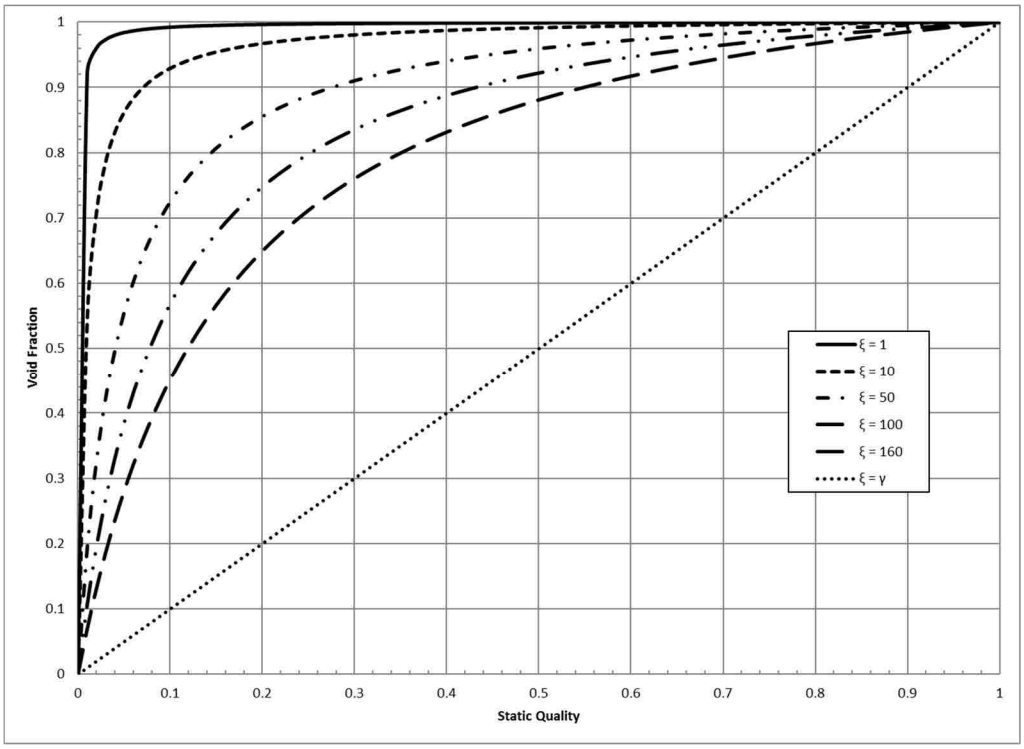

Figure 6. Void-Static Quality relationship for various "boiling constraint factors".

In Razorback, a value for ξ is input by the user. The Razorback User's Manual [31] recommends that ξ be selected, by trial-and-error, as the lowest value for which the transient boiling simulation does not result in crashing the code. Experience has shown that the larger the reactivity addition which leads to a transient boiling situation, the larger the value of ξ is needed to avoid a code crash.

Equations 3-88 and 3-91 are valid for steady-state flow situations, and not necessarily valid for transient conditions. The implementation of Eq. 3-91 in Razorback [32] is a quasi-static approach using

$$\frac{\partial \overline{\rho}}{\partial t} = \left(\rho_g - \rho_f\right)\frac{\partial \alpha}{\partial t} + \alpha\frac{\partial \rho_g}{\partial t} + (1-\alpha)\frac{\partial \rho_f}{\partial t} \qquad (3\text{-}92)$$

where $\frac{\partial \alpha}{\partial t}$ is obtained by taking the partial derivative of Eq. 3-91 with respect to time. An improvement which could remove the need for the heuristic application of the boiling constrain factor ξ would be to use the vapor phase continuity equation

$$\frac{\partial}{\partial t}(\alpha \rho_g) + \frac{\partial}{\partial t}(\alpha \rho_g u_g) = \Gamma_g - \Gamma_c \tag{3-93}$$

where Γ_g is the vapor generation rate at the cladding surface, and Γ_c is the vapor condensation rate (see, for example Talebi, et al. [33]). Of course, this would also introduce the need for constitutive equations for Γ_g and Γ_c.

3.7. Conclusions

A computer code, named Razorback, has been designed and developed. The code computes the coupled reactor kinetics, thermal-hydraulic, and thermomechanical response of a natural circulation research reactor to reactivity inputs. The reactivity inputs can be large rapid reactivity additions (LRRAs) typical of a pulsing research reactor or reactivity-initiated accident (RIA) events often analyzed for research reactors.

The code allows reactivity inputs to be modeled as linear ramp reactivity additions, or as reactivity derived from reactivity rod bank speed commands, coupled with an input differential reactivity worth curve. In the case of the latter, multiple rod bank speed commands may be entered to model a large variety of research reactor transients. A pulse option is also available which computes the reactivity addition based upon a constant acceleration imparted by a pneumatic pulse rod ejection system.

The code models a variety of reactivity feedback mechanisms. These include the fuel temperature Doppler reactivity feedback, fuel expansion reactivity feedback, cladding expansion reactivity feedback, and coolant reactivity feedback due to density and temperature changes.

The fuel element is modeled as an azimuthally-symmetric cylinder (r,z coodinates) with the allowance for multiple radial material zones. Only radial heat transfer (conduction and radiation within the fuel element, and convection to the coolant) is modeled, but the element is modeled with axial nodes with a functional input for an axial position-dependent energy deposition profile. This “quasi-2D” approach allows for the computation of axial position-dependent fuel element component temperatures, and axial position-dependent heat transfer to the coolant.

In addition to heat transfer computations, the code models radial thermal expansion of the fuel element materials. The effect of the quasi-2D approach in the thermal expansion computations is that each axial segment may expand radially with no restriction from the segment above or below (i.e., each axial segment "slides" freely when expanding). The computed thermal expansion results are used to compute radial and circumferential stresses in the fuel element materials. A plane stress assumption is employed in computing the thermal expansion and the thermal stresses.

The coolant in the coolant channel also employs a quasi-2D modeling approach, allowing for an axial position-dependent computation of coolant density, enthalpy, pressure, temperature, and mass flux. The mass, momentum, and energy equations are coupled via a property table-based equation of state. The coolant (currently only water is allowed) is treated as compressible. Two-phase flow (i.e., saturated boiling) is modeled using a drift flux model approach.

Razorback allows for the simulation of a broad range of research reactor transient, including LRRAs. It provides a valuable tool for predicting the performance of a natural circulation research reactor, and investigating the response of the research reactor to normal and abnormal conditions. Verification and validation is discussed in the next chapter.

4. Verification and Validation of the Transient Analysis Code

4.1. Introduction

A reactor transient analysis code called Razorback has been designed and developed for the analysis of large rapid reactivity additions (LRRAs). The code successfully couples the various physical models of the fuel and coolant to predict the nuclear, thermal-hydraulic, and thermomechanical response of the ACRR to LRRAs, called pulse operations. The code has been shown to predict ACRR pulse performance quite well as shown in the Razorback verification and validation report [34]. The following describes a selection of the verification and validation results.

4.2. Point-Reactor Kinetics Verification

The reactor kinetics portion of the code has been verified against a series of numerical benchmarks published by Ganapol [35]. The numerical benchmarks include step reactivity additions with no reactivity feedback, and step reactivity additions with reactivity feedback. The Razorback code's time step controller was utilized when running the benchmark cases.

4.2.1. Step Reactivity Addition Without Feedback

The step reactivity addition benchmark cases [35] were developed using a neutron generation time of $\Lambda = 5 \times 10^{-4}$ s, and the delayed neutron parameters shown in Table 1.

Table 1. Delayed neutron group parameters for the step reactivity addition benchmark cases.

Group	β_i	λ_i (1/s)
1	0.000285	0.0127
2	0.0015975	0.0317
3	0.001410	0.115
4	0.0030525	0.311
5	0.00096	1.40
6	0.000195	3.87
	$\beta = 0.0075$	

Table 2 and Table 3 show the Razorback results for the benchmark cases of a \$0.5 and \$1.0 step reactivity addition. In both benchmark cases, the initial/maximum time step for Razorback was set at 0.0001 s. Subsequent time steps were adjusted by the time step controller built into the code. As may be seen in the tables below, the Razorback results agree quite well with the benchmark results. Additional reduction in the magnitude of the percent differences shown in the tables may be realized by reducing the initial time step in the input file of the run.

Table 2. Point-Reactor kinetics benchmark results for $0.5 step addition [34].

Time (s)	Code Result	Benchmark	% Difference
0.1	1.5332115E+00	1.533112646E+00	0.006448
1.0	2.5115239E+00	2.511494291E+00	0.001179
10.0	1.4215038E+01	1.421502524E+01	0.000090
100.0	8.0060942E+07	8.006143562E+07	-0.000617

Table 3. Point-Reactor kinetics benchmark results for $1.0 step addition [34].

Time (s)	Code Result	Benchmark	% Difference
0.1	2.5158849E+00	2.515766141E+00	0.004721
0.5	1.0362726E+01	1.036253381E+01	0.001855
1.0	3.2183405E+01	3.218354095E+01	-0.000422
10.0	3.2469217E+09	3.246978898E+09	-0.001762
100.0	---*	2.596484646E+89	---*

*Run terminated shortly after 10.0 seconds due to prohibitively long run time.

4.2.2. Ramp Reactivity Addition Without Feedback

The ramp reactivity addition benchmarks were developed using a neutron generation time of $\Lambda = 2 \times 10^{-5}$ s, and the delayed neutron parameters in Table 4 [35].

Table 4. Delayed neutron group parameters for the ramp reactivity addition benchmark cases.

Group	β_i	λ_i (1/s)
1	0.000266	0.0127
2	0.001491	0.0317
3	0.001316	0.115
4	0.002849	0.311
5	0.000896	1.40
6	0.000182	3.87
	$\beta = 0.007$	

Table 5 shows the Razorback results for the benchmark cases of a \$0.1/s ramp reactivity addition. The initial/maximum time step for Razorback was set at 0.0001 s. Subsequent time steps were adjusted by the time step controller built into the code. The Razorback results agree quite well with the benchmark results.

Table 5. Point-Reactor kinetics benchmark results for $0.1/s ramp addition [34].

Time (s)	Code Result	Benchmark	% Difference
0.1	2.5158849E+00	2.515766141E+00	0.004721
0.5	1.0362726E+01	1.036253381E+01	0.001855
1.0	3.2183405E+01	3.218354095E+01	-0.000422
10.0	3.2469217E+09	3.246978898E+09	-0.001762
100.0	---*	2.596484646E+89	---*

*Run terminated shortly after 10.0 seconds due to prohibitively long run time.

4.2.3. Sinusoidal Reactivity Addition Without Feedback

The sinusoidal reactivity addition benchmarks were developed for a one delayed group fast reactor using a neutron generation time of $\Lambda = 10^{-8}$ s, a delayed neutron fraction of $\beta = 0.0079$, and a delayed group decay constant of $\lambda = 0.077$ 1/s [35]. The reactivity addition in the benchmark is given the following with $\rho_o = 0.0053333$ and T = 50 s.

$$\rho(t) = \rho_o \sin\left(\pi \frac{t}{T}\right)$$

Figure 7 shows the Razorback-computed neutron density as a function of time in response to the sinusoidal reactivity addition. Table 6 compares the Razorback code results with the benchmark results for various time points during the run.

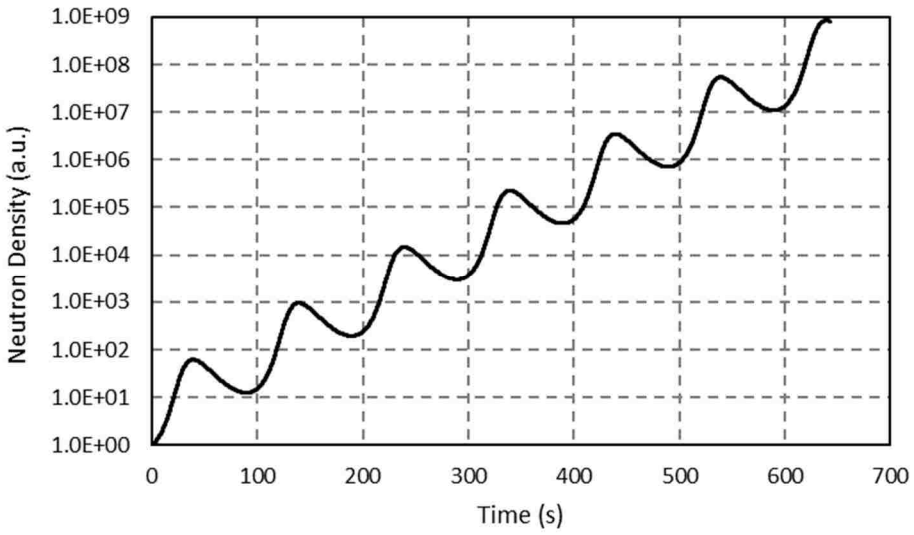

Figure 7. Razorback simulation of a sinusoidal reactivity addition [34].

Table 6. Point-reactor kinetics benchmark results for a sinusoidal reactivity addition without reactivity feedback [34].

Time (s)	Code Result	Benchmark	% Difference
10.0	2.0653843E+00	2.065383519E+00	0.000038
20.0	8.8541395E+00	8.854133921E+00	0.000063
30.0	4.0643559E+01	4.064354222E+00	0.000041
40.0	6.1356093E+01	6.135607517E+01	0.000029
50.0	4.6106298E+01	4.610628770E+01	0.000022
60.0	2.9126355E+01	2.912634840E+01	0.000023
70.0	1.8951775E+01	1.895177042E+01	0.000024
80.0	1.3938296E+01	1.393829211E+01	0.000028
90.0	1.2533538E+01	1.253353406E+01	0.000031
100.0	1.5448172E+01	1.544816514E+01	0.000044

4.2.4. Step Reactivity Addition With Feedback Case

The step reactivity addition with feedback benchmarks [35] were developed using a neutron generation time of $\Lambda = 5 \times 10^{-5}$ s, and the delayed neutron parameters in Table 7. A feedback coefficient (B) of 2.5×10^{-6} 1/s [35] was used in the benchmark based on the following reactivity relationship.

$$\rho(t) = \rho_o(\mathrm{t}) + \mathrm{B}\int_0^t N(t')dt'$$

Table 7. Delayed neutron group parameters for the step reactivity addition with feedback benchmark cases.

Group	β_i	λ_i (1/s)
1	0.00021	0.0124
2	0.00141	0.0305
3	0.00127	0.111
4	0.00255	0.301
5	0.00074	1.13
6	0.00027	3.00
	β = 0.00645	

For use in Razorback, the feedback reactivity must be in terms of dollars. Therefore, the feedback coefficient (B) was divided by the delayed neutron fraction β. The Razorback results are compared with the benchmark data in Table 8.

Table 8. Point-reactor kinetics benchmark results for a $2.0 step reactivity addition with reactivity feedback [34].

Time (s)	Code Result	Benchmark	% Difference
10.0	1.0338084E+02	1.033808535E+02	-0.000013
20.0	3.9138865E+01	3.913886903E+01	-0.000010
30.0	2.2003775E+01	2.200377721E+01	-0.000010
40.0	1.4493671E+01	1.449367193E+01	-0.000006
50.0	1.0318610E+01	1.031861108E+01	-0.000010
60.0	7.6633185E+00	7.663319203E+00	-0.000009
70.0	5.8293948E+00	5.829395378E+00	-0.000010
80.0	4.4994266E+00	4.499427073E+00	-0.000011
90.0	3.5074223E+00	3.507422663E+00	-0.000010
100.0	2.7551266E+00	2.755126886E+00	-0.000010

4.3. Heat Transfer Verification

The heat transfer portion of the code was verified using a simple fuel element heat transfer problem. A simple fuel element model (see Figure 8) with four radial zones was set up. The BeO-UO_2 thermal conductivity was set at 0.160 W/cm-K. The niobium thermal conductivity was set at 0.50 W/cm-K. The stainless steel (SS) thermal conductivity was set at 0.150 W/cm-K. The BeO-UO_2 zone was given a uniform 100 W/cm^3 volumetric heating source. The left-hand boundary of the BeO-UO_2 was treated as adiabatic, while the right-hand boundary of the SS was set at a constant temperature of 120°C.

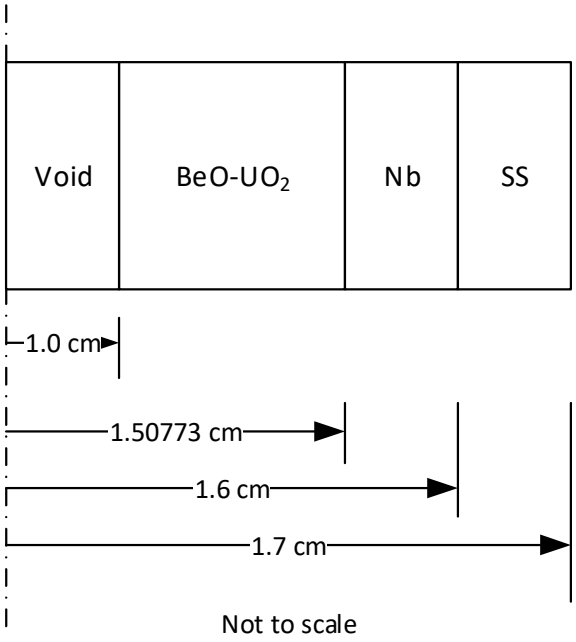

Figure 8. Fuel element materials and geometry for heat transfer verification [34].

A steady-state solution was computed with Razorback. The results, shown in Figure 9, agree very well with the analytical solution. The relative error (shown in Figure 10) is bounded within the range of -0.00002 to 0.00006.

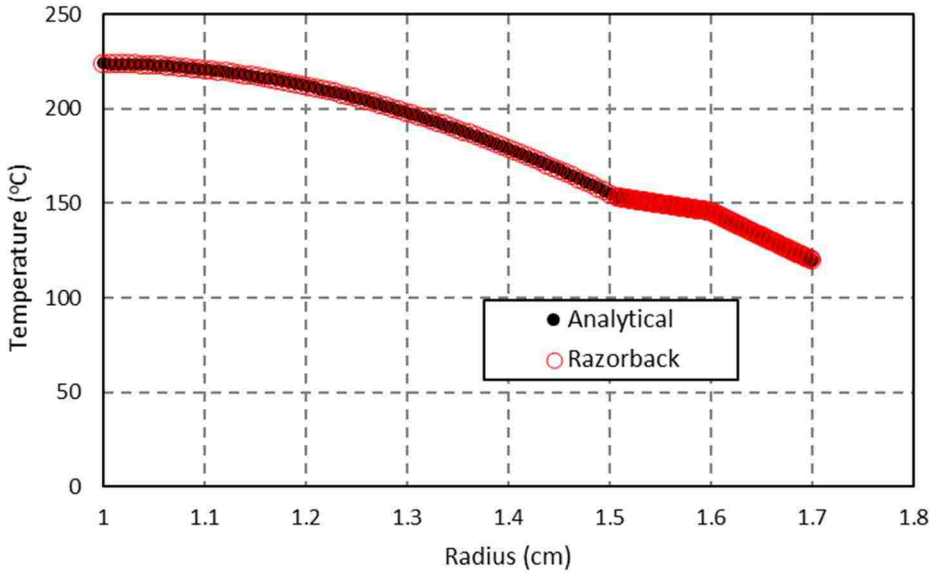

Figure 9. Simple heat transfer problem results compared to analytical solution [34].

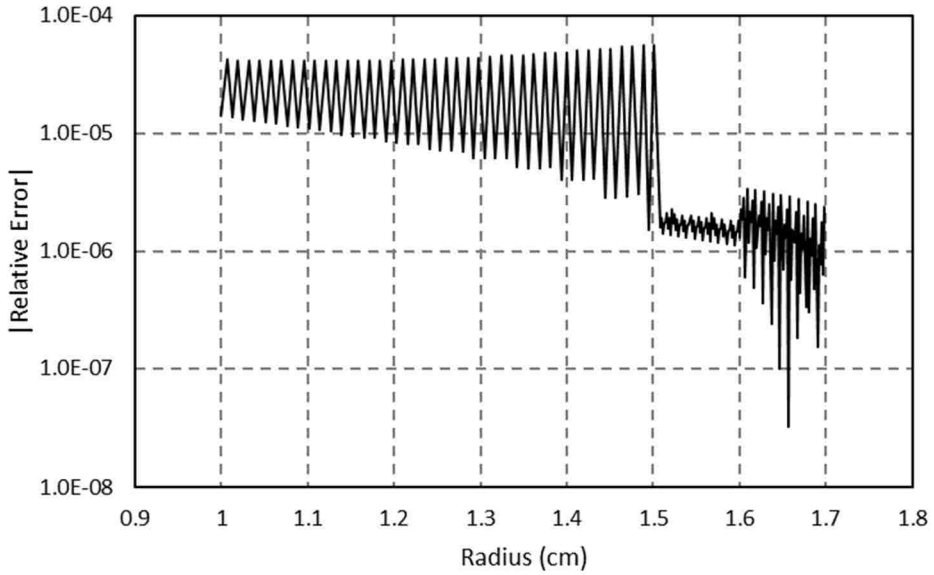

Figure 10. Magnitude of the relative error for the heat transfer verification [34].

4.4. Thermal Expansion Verification

Fuel element thermal expansion was verified against an analytical solution for a circular ring with a known radial temperature distribution under plane stress conditions and a constant thermal expansion coefficient. The analytical solution formulation can be found in Timoshenko [36]. The steady-state temperature distributions across the inner and outer fuel pellets, niobium, and stainless steel cladding of an ACRR fuel element were determined using Razorback, and polynomial fits of the temperature distributions were developed and used to compute the analytical solutions. The results obtained from the thermal expansion routine in Razorback were compared to analytical results. The material properties shown in Table 9 were used.

Table 9. Material properties used to verify Razorback thermal expansion results.

Material	α (1/K)	E (GPa)	ν
BeO-UO_2	8.5×10^{-6}	345	0.26
Niobium	8×10^{-6}	105	0.4
Stainless Steel	17.3×10^{-6}	190	0.3

The radial temperature profiles for the inner fuel pellet and the cladding used in the thermal expansion verification are shown in Figure 11 and Figure 12. The radial displacement results for the inner ACRR fuel pellet and cladding are shown in Figure 13 and Figure 15, respectively, as compared to the analytical solutions. Figure 14 and Figure 16 show the relative errors for each case. In both cases, the radial displacement results agree very well with the analytical solution.

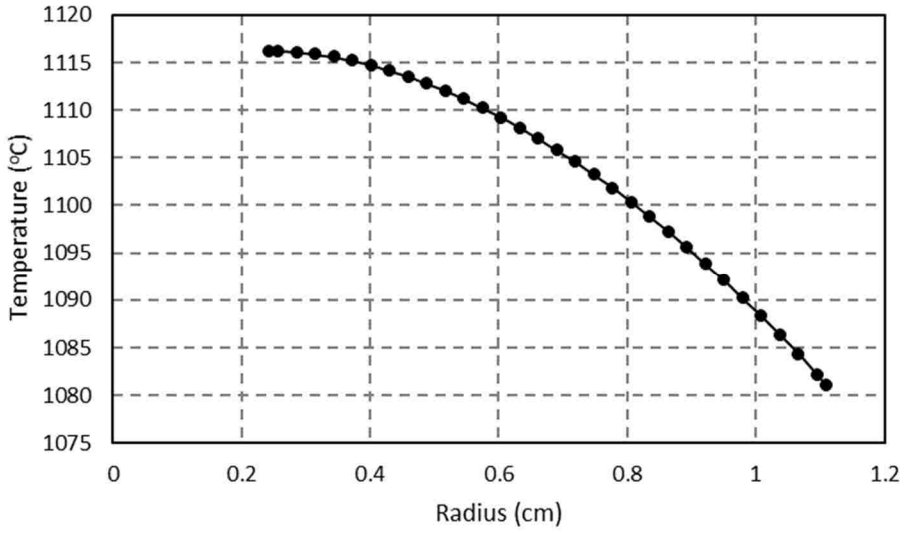

Figure 11. Radial temperature profile of ACRR inner fuel pellet used for thermal expansion verification [34].

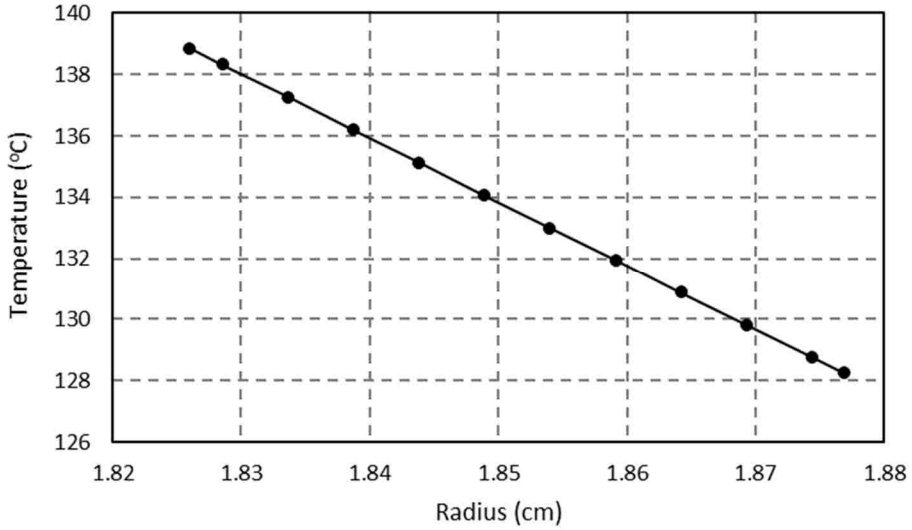

Figure 12. Radial temperature profile of ACRR cladding used for thermal expansion verification [34].

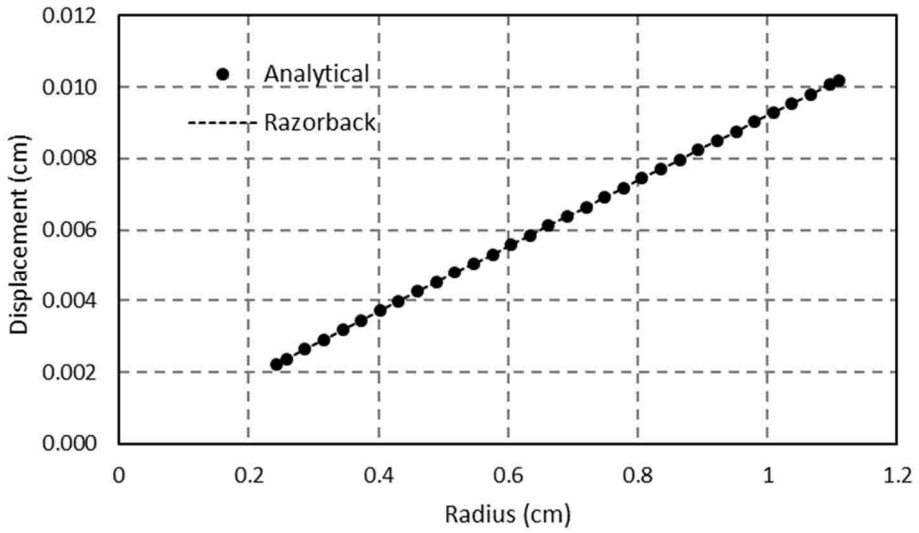

Figure 13. Inner ACRR fuel pellet radial displacement for the thermal expansion verification problem [34].

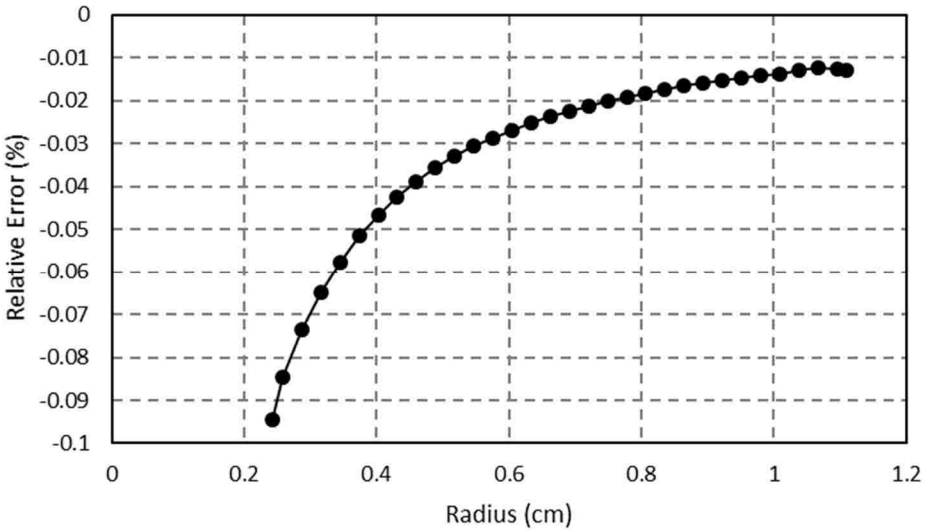

Figure 14. Relative error of the radial displacement (inner pellet) for the thermal expansion verification problem [34].

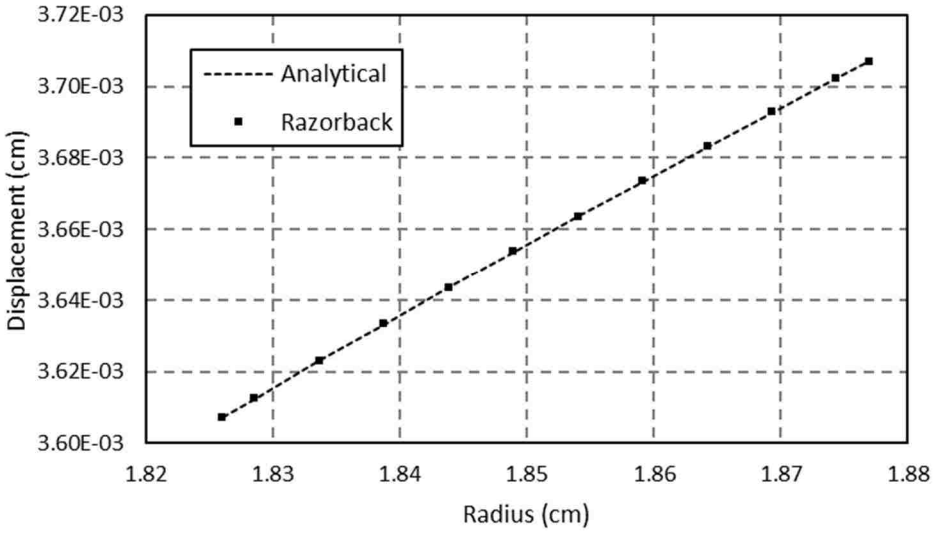

Figure 15. Cladding radial displacement for the thermal expansion verification problem [34].

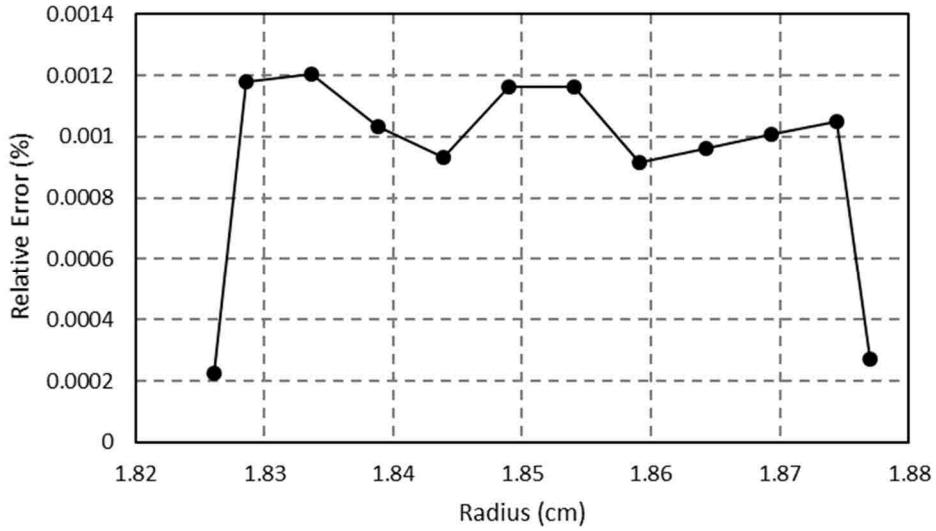

Figure 16. Relative error of the radial displacement (cladding) for the thermal expansion verification problem [34].

4.5. Thermal Stress Verification

The fuel element thermal expansion routine was verified against an analytical solution for a circular ring with a known radial temperature distribution under plane stress conditions and a constant thermal expansion coefficient. The analytical solution formulation can be found in Timoshenko [36]. The material properties shown earlier in Table 9 were used. The steady-state temperature distributions across the inner and outer fuel pellets, niobium, and stainless steel cladding of an ACRR fuel element were determined using Razorback, and polynomial fits of the temperature distributions were developed and used to compute the analytical solutions.

Based on the temperature profile of Figure 11, Figure 17 and Figure 18 compare the results obtained for the radial and azimuthal stress in the inner fuel pellet to the analytical results. Figure 19 shows the error in the results for each case (relative error is not shown because the analytical results include a zero stress). The error of the radial stress computation is smaller in magnitude. The error in both cases is bounded within ±5 MPa, which is reasonable compared to most tensile strengths.

Based on the temperature profile of Figure 12, Figure 20 and Figure 21 compare the results obtained for the radial and azimuthal stress in the fuel element cladding to the analytical results. Figure 22 shows the error in the results for each case (again, relative error is not shown because the analytical results include a zero stress). The error for the fuel element cladding computations is approximately two orders of magnitude smaller, because the cladding is a thin ring compared to the fuel pellets. The error in both cases is bounded within ±0.05 MPa.

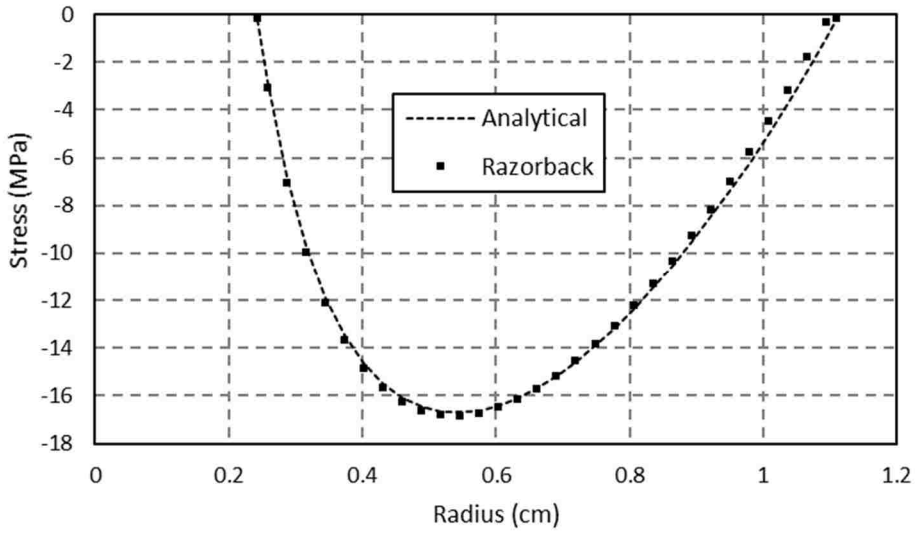

Figure 17. Inner ACRR fuel pellet radial stress for the thermal stress verification problem [34].

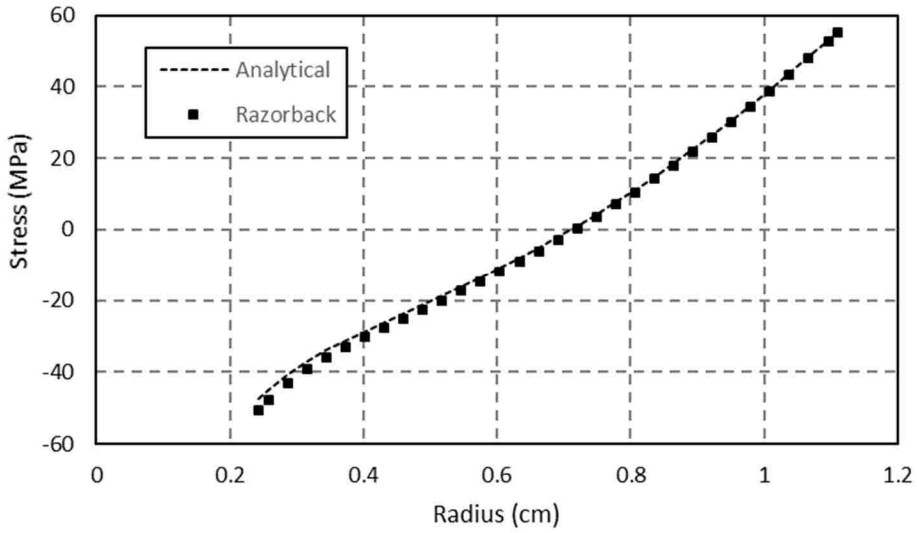

Figure 18. Inner ACRR fuel pellet azimuthal stress for the thermal stress verification problem [34].

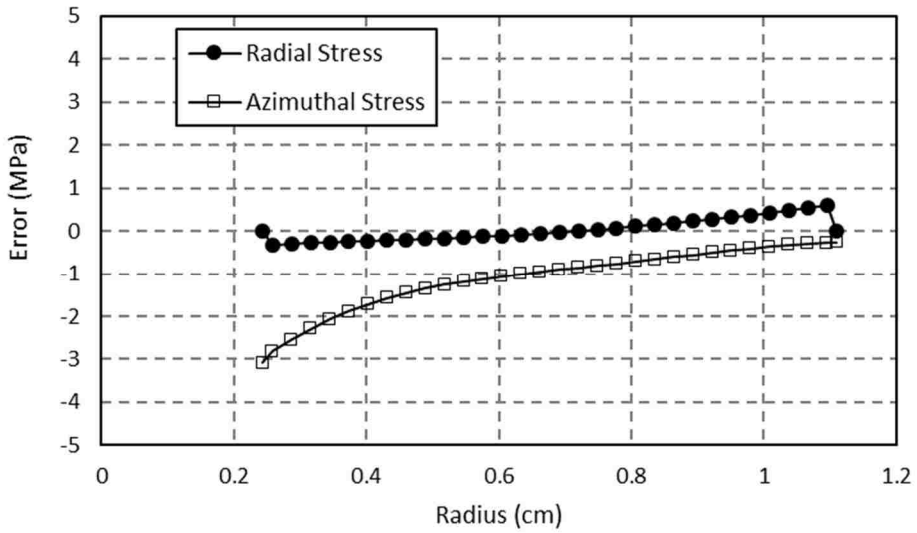

Figure 19. Error in the radial and azimuthal stress for the thermal stress verification problem [34].

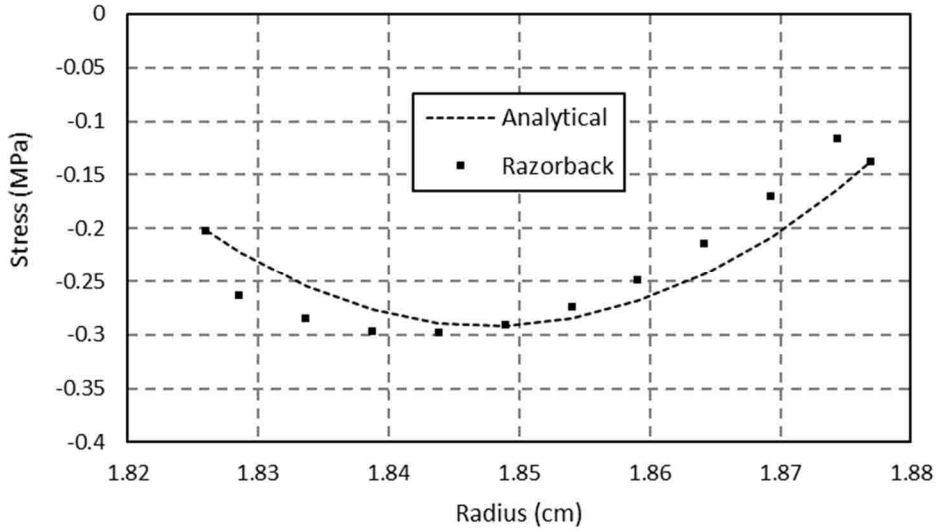

Figure 20. ACRR fuel element cladding radial stress for the thermal stress verification problem [34].

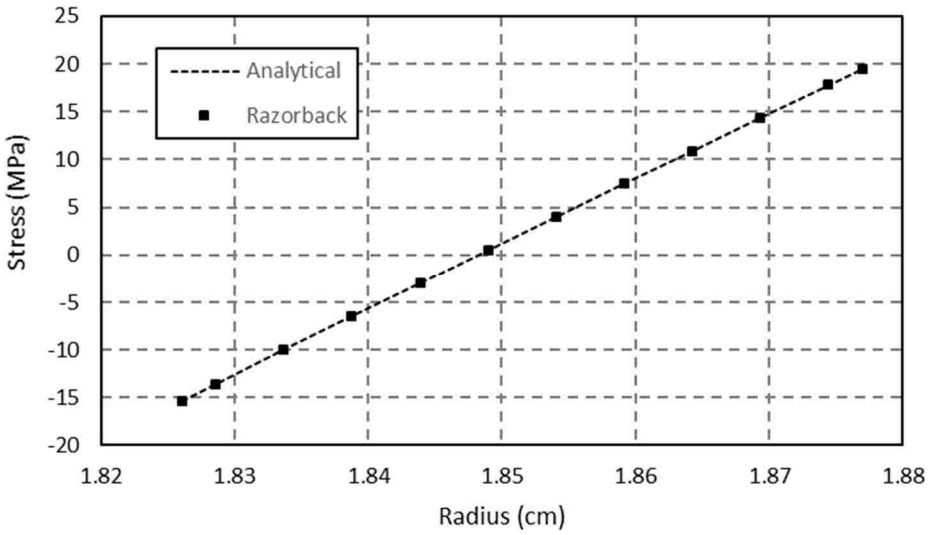

Figure 21. ACRR fuel element cladding azimuthal stress for the thermal stress verification problem [34].

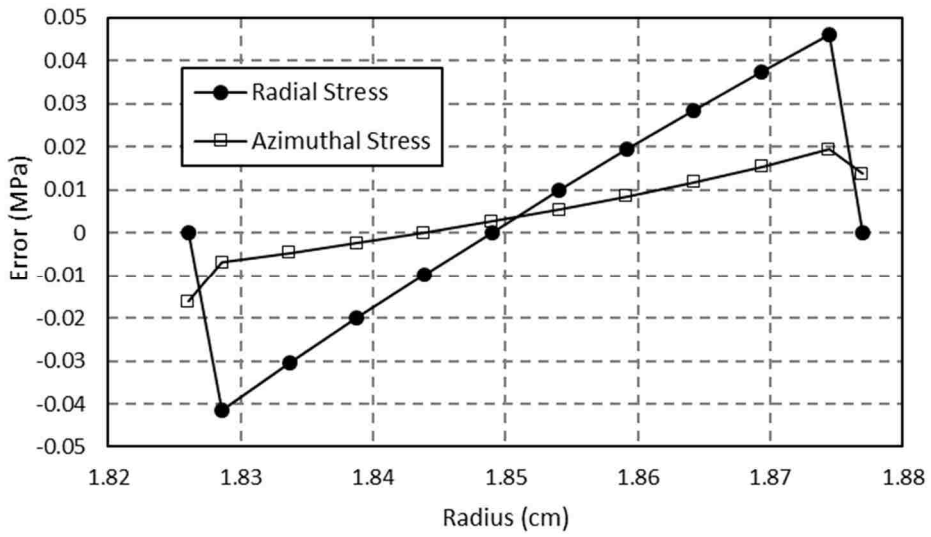

Figure 22. Error in the cladding radial and azimuthal stress for the thermal stress verification problem [34].

4.6. Validation for ACRR Operations

The full functionality of the code was validated using actual ACRR pulse operation data. The ACRR fuel was modeled as shown in Figure 23. The Razorback code cannot model the fuel as slotted annular rings (see Figure 2), so the rings are treated as full rings. Also, the niobium fuel cups have fluting such that at regular angular spacing, the wall has been indented toward the fuel or toward the cladding, in an alternating fashion. For the Razorback model, only a smooth-walled cup can be modeled. The regions between the materials are helium-filled gaps. The fuel element radial dimensions are given in Table 10. The axial height of the fuel is ~0.5 m.

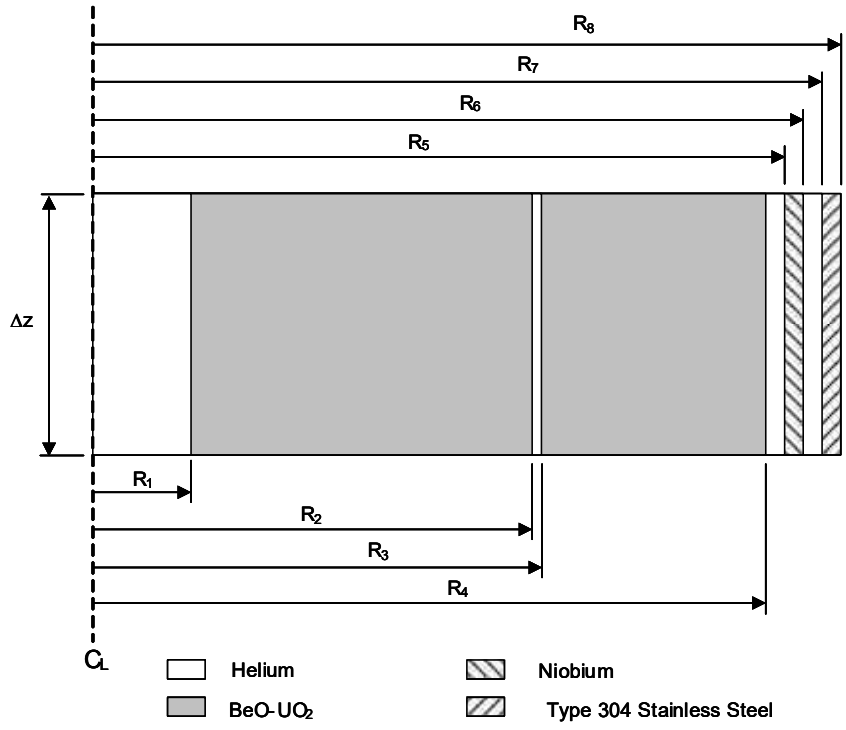

Figure 23. ACRR fuel element model geometry used for validation against ACRR operations [32].

Table 10. Radial dimensions for ACRR fuel element materials.

Material	Inner Radius (cm)	Outer Radius (cm)
BeO-UO_2 Inner Pellet	$R_1 \approx 0.24$	$R_2 \approx 1.1$
BeO-UO_2 Outer Pellet	$R_3 \approx 1.1$	$R_4 \approx 1.7$
Niobium	$R_5 \approx 1.73$	$R_6 \approx 1.77$
Stainless Steel	$R_7 \approx 1.8$	$R_8 \approx 1.87$

The ACRR fuel elements are arranged in a hexagonal grid arrangement, oriented so that the central axis of the fuel element is vertical. The flow channel for a hexagonal core arrangement is "shared" by three fuel elements, as shown in Figure 24. The Razorback model approach treats the channel as associated with the element being modeled (see the right side of Figure 24). The pitch of the grid arrangement is ~4 cm.

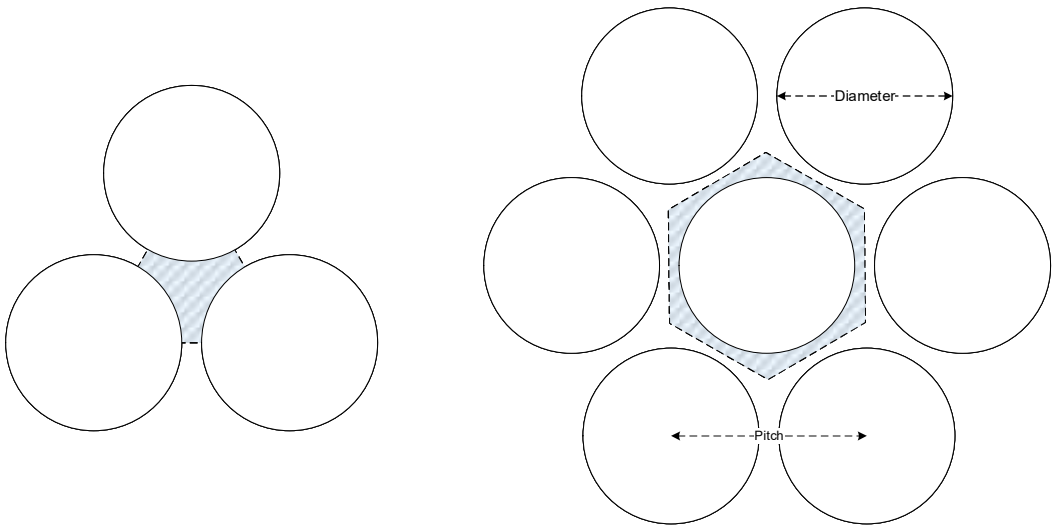

Figure 24. ACRR fuel grid arrangement and flow channel model depiction.

4.6.1. Pulse Operations

Razorback was used to simulate several ACRR pulse operations which were performed as part of annual calibration operations in 2011 and 2016. The computed reactor power history for one of the $3 pulse operations is shown in Figure 25, along with reactor power data from four channels of ACRR instrumentation. The reactor power pulse itself is difficult to discern in this figure, but the Razorback trend follows well with the delayed neutron "shoulder" and "tail." Note that ACRR channels 1 and 2 were detectors intended to capture the pulse and its peak, while channels 4 and 5 were detectors were intended to capture the delayed neutron tail. Figure 26 and Figure 27 show the same pulse, but focus the view upon the delayed neutron shoulder and tail, respectively.

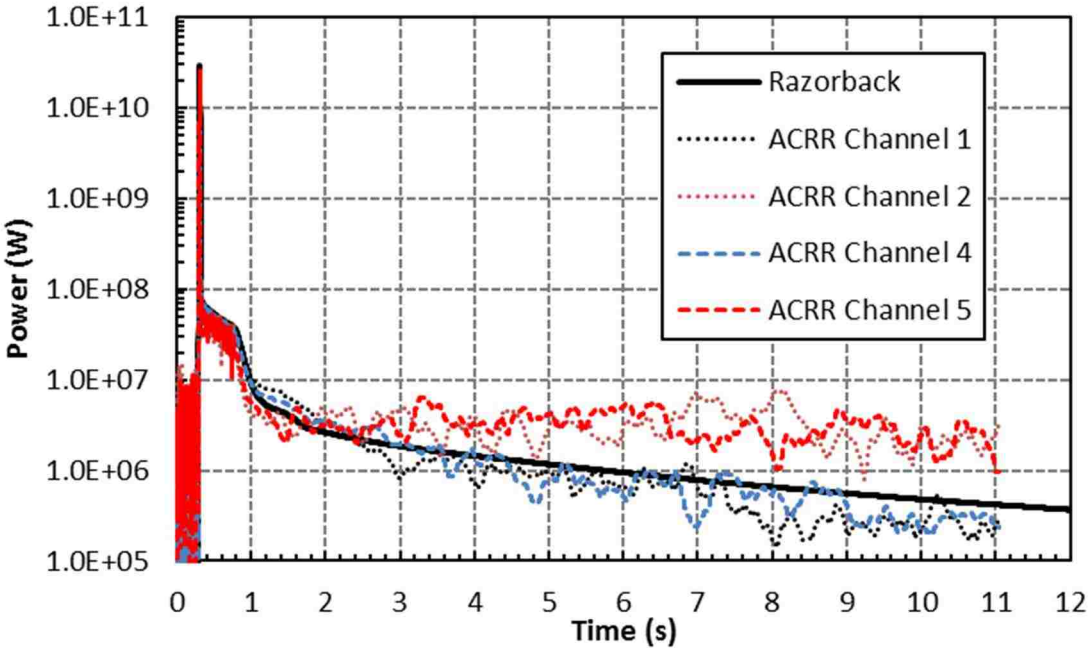

Figure 25. Comparison of a Razorback simulation of a $3 pulse to ACRR data [34].

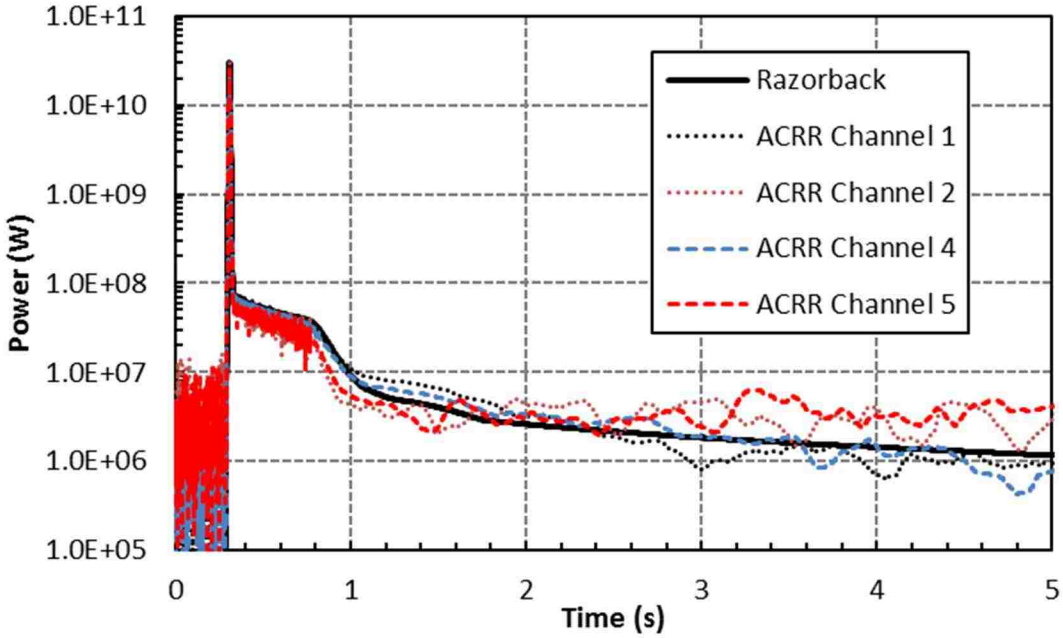

Figure 26. Comparison of a Razorback simulation of a $3 pulse to ACRR data [34].

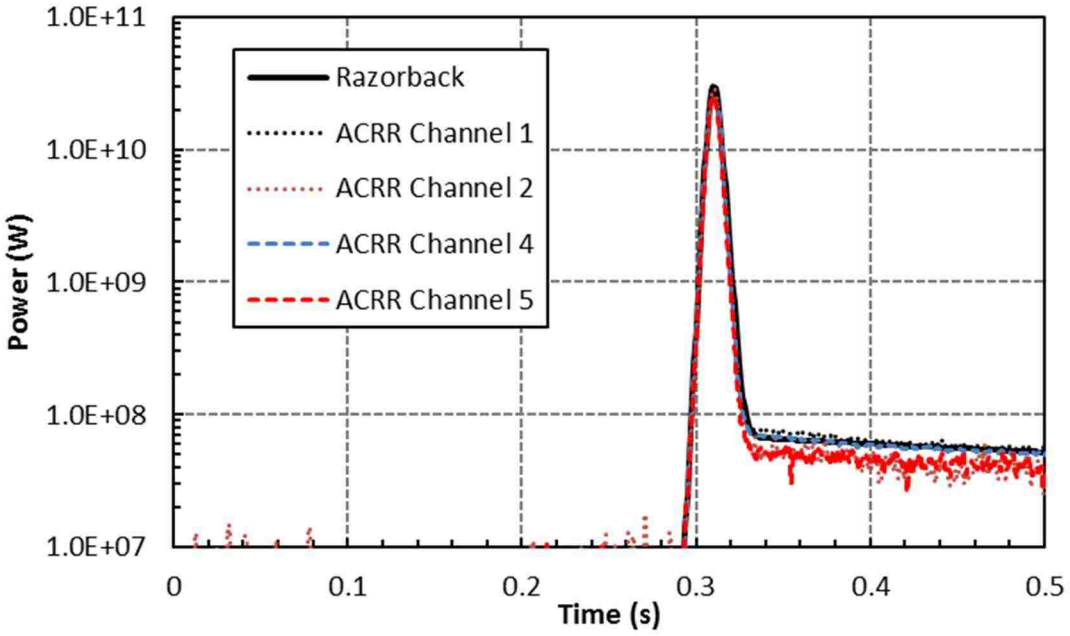

Figure 27. Comparison of a Razorback simulation of a $3 pulse to ACRR data [34].

Figure 28 shows the peak measured temperature recorded for the calibration pulse operations in 2011 and 2016, along with the Razorback simulation results for each. The Razorback results match the data within a range of ~1% to ~10%, with the larger relative discrepancies occurring for the lower reactivity additions.

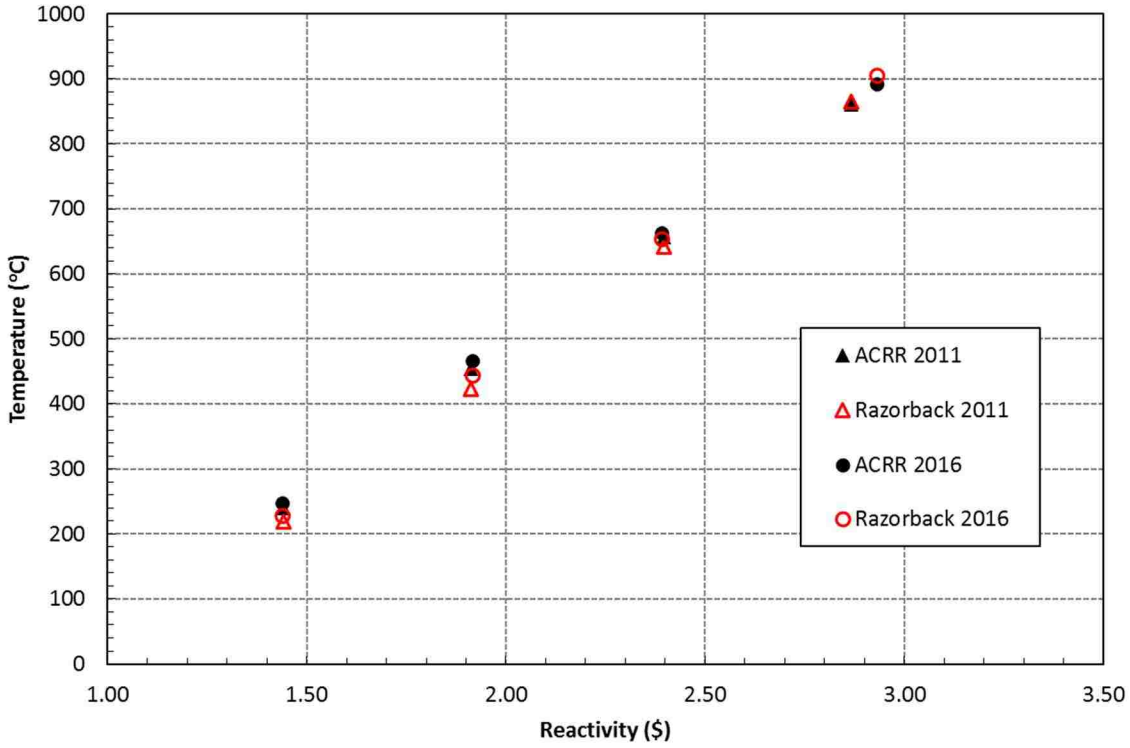

Figure 28. Comparison of Razorback peak measured fuel temperature results with ACRR pulse data [34].

Figure 29 shows the peak measured power recorded for the calibration pulse operations in 2011 and 2016, along with the Razorback simulation results for each. The Razorback results match the data within a range of ~1% to ~20%, with the larger relative discrepancies occurring for the lower reactivity additions.

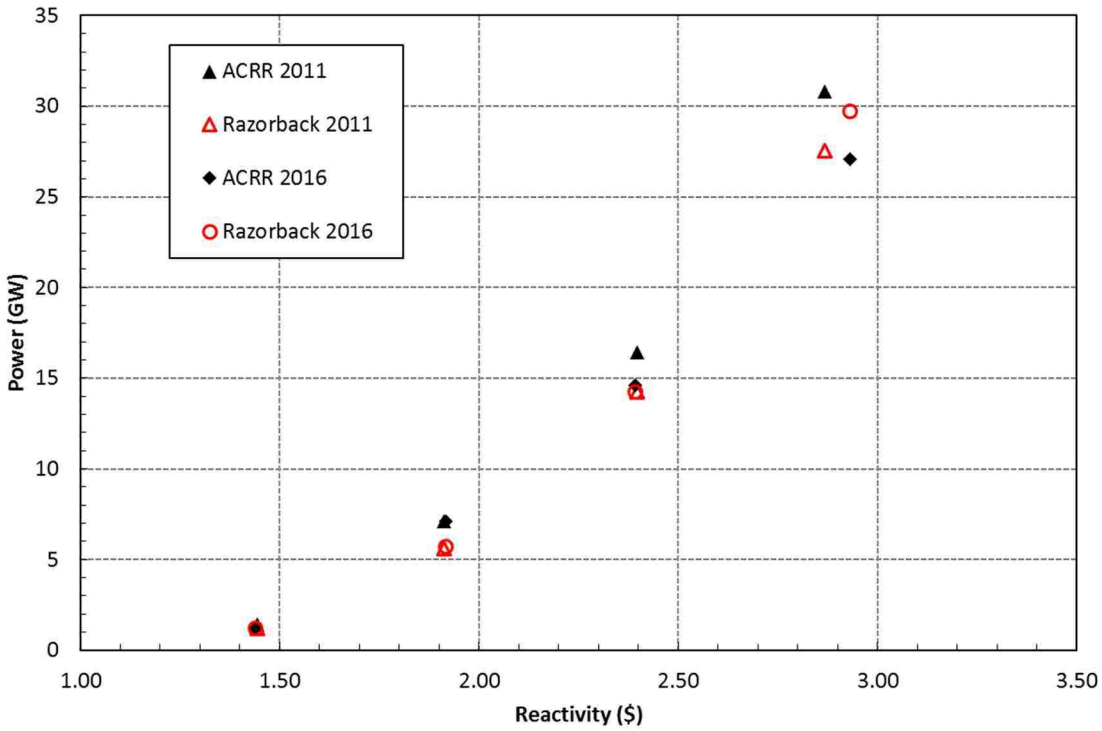

Figure 29. Comparison of Razorback peak power results with ACRR pulse data [34].

Figure 30 shows the pulse energy yield for the calibration pulse operations in 2011 and 2016, along with the Razorback simulation results for each. The pulse energy yield is the integrated power from t = 0 to a time ~3 pulse widths after the time of the power peak. The Razorback results match the data within a range of ~1% to ~15%. There is no apparent trend of magnitude of the relative discrepancies with respect to the reactivity addition. Additional comparisons of the pulse yield characteristics may be made by comparing to the yield at the time of the peak power and the total yield (i.e., after a long time, of 10-20 s). These additional comparisons are found in the Razorback Verification and Validation Report [34].

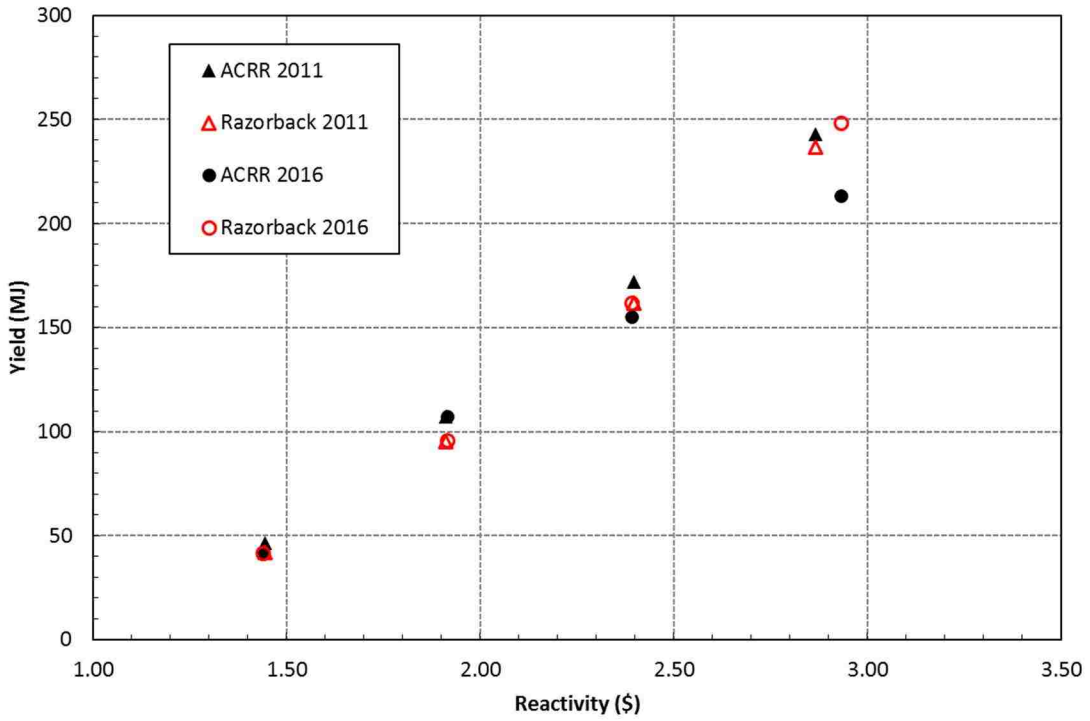

Figure 30. Comparison of Razorback pulse energy (yield) results with ACRR pulse data [34].

The pulse width parameter used to characterize a pulse is referred to as the Full Width at Half-Maximum (FWHM). It is determined by finding the time, before and after the pulse peak, when the power level is equal to one-half of the peak power. The FWHM may be divided into the two timespans on the left and right side of the FWHM. These are referred to as the Leading Edge at Half-Maximum (LEHM) and the Trailing Edge at Half-Maximum (TEHM). If the pulse width were to be fully symmetrical each of these widths would be one-half of the FWHM. An actual pulse has some degree of asymmetry due to the impact of delayed neutrons on the pulse shape. These pulse width parameters are illustrated in Figure 31.

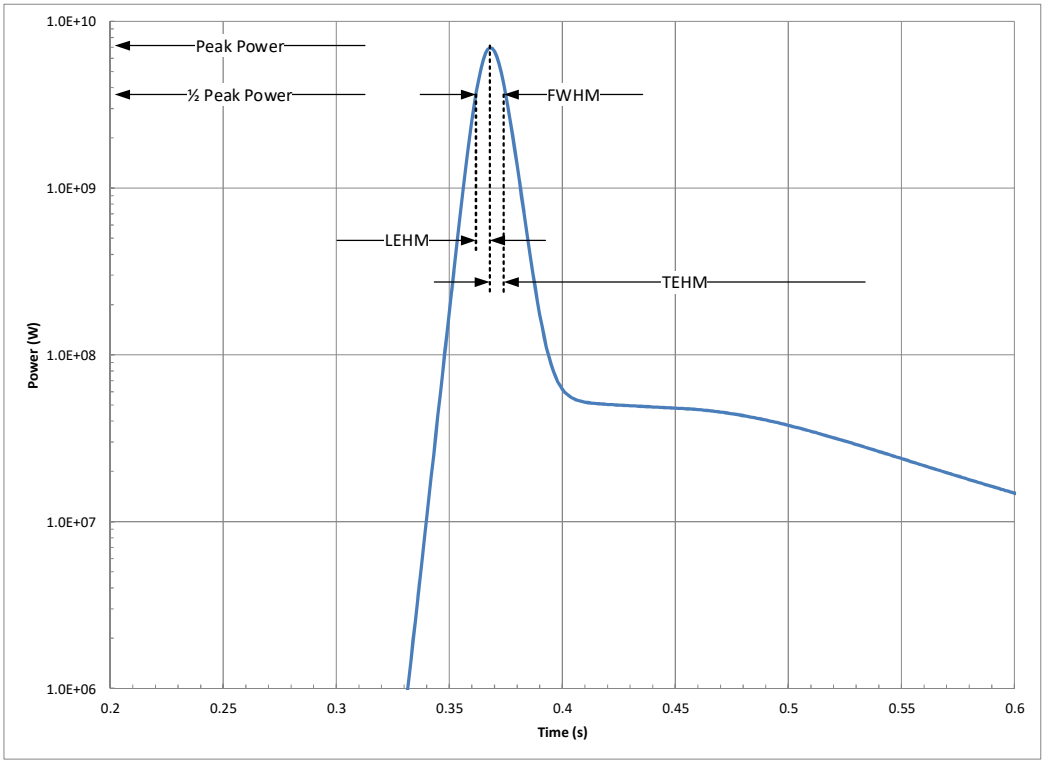

Figure 31. Depiction of the time related characteristics of a reactor power pulse [34].

Figure 32 shows the FWHM parameters as measured for the calibration pulse operations in 2011 and 2016, along with the Razorback simulation results for each. The Razorback results match the data within a range of ~1% to ~10%. There is no apparent trend of magnitude of the discrepancies with respect to the reactivity addition. Additional comparisons of pulse width characteristics (e.g., LEHM and TEHM) may be found in the Razorback Verification and Validation Report [34].

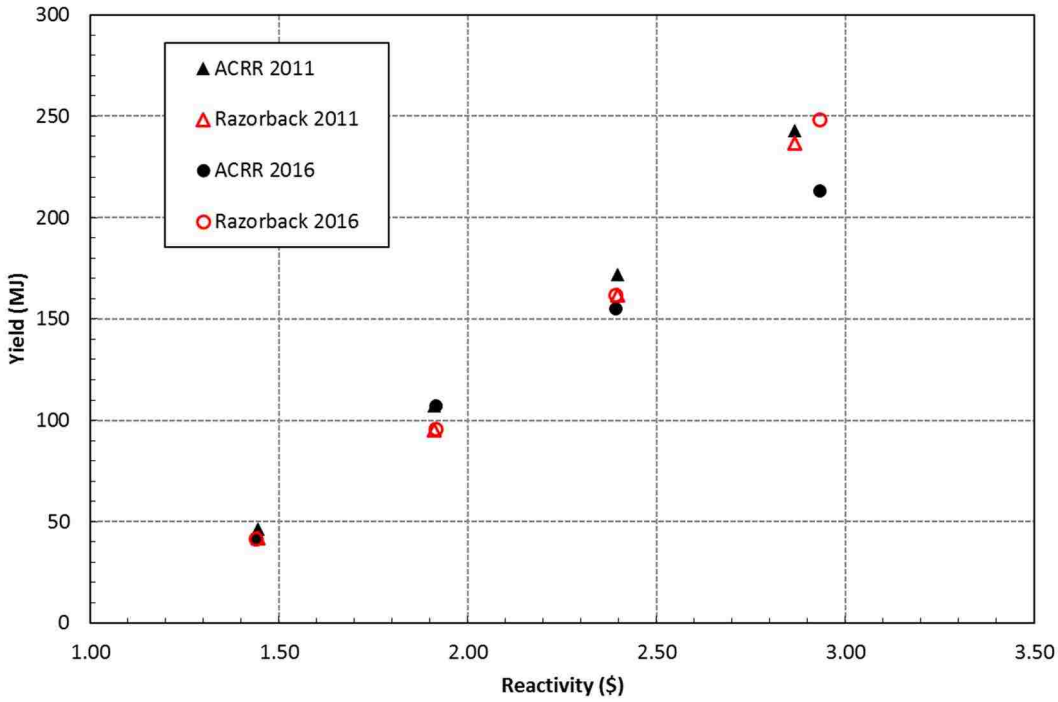

Figure 32. Comparison of Razorback pulse width results with ACRR pulse data [34].

A Razorback simulation of ACRR pulse operation 11277 was performed. Operation 11277 was a "maximum" pulse operation of ~$3 performed on February 2, 2015. The significance of this operation was that in addition to the ACRR Pulse Diagnostic System (which is normally operative during a pulse operation), two additional instruments were deployed: (1) a spare ACRR instrumented element (IE-603) was installed in the core so that a higher sample rate measurement of fuel temperature during the pulse could be obtained, and (2) a flowmeter tube, the entry funnel of which included an internal thermocouple, was placed over the top of a fuel element to obtain measurements of a coolant channel's outlet temperature.

Figure 33 shows the flowmeter/thermocouple fixture. In the upper left photo in Figure 33, the flowmeter can be seen at the center of the fixture between the two end flow

funnels. The flowmeter itself failed during initial testing of the device installed at the core upper grid, presumably due to radiation exposure. The thermocouple, however, remained operable. The flow funnel on the left (which is enlarged somewhat in the upper right photo) is the portion of the fixture which is seated over an ACRR fuel element at the upper grid plate. The bottom photo shows the inside of this flow funnel, and the thermocouple which was used to obtain the channel outlet temperature for a fuel element.

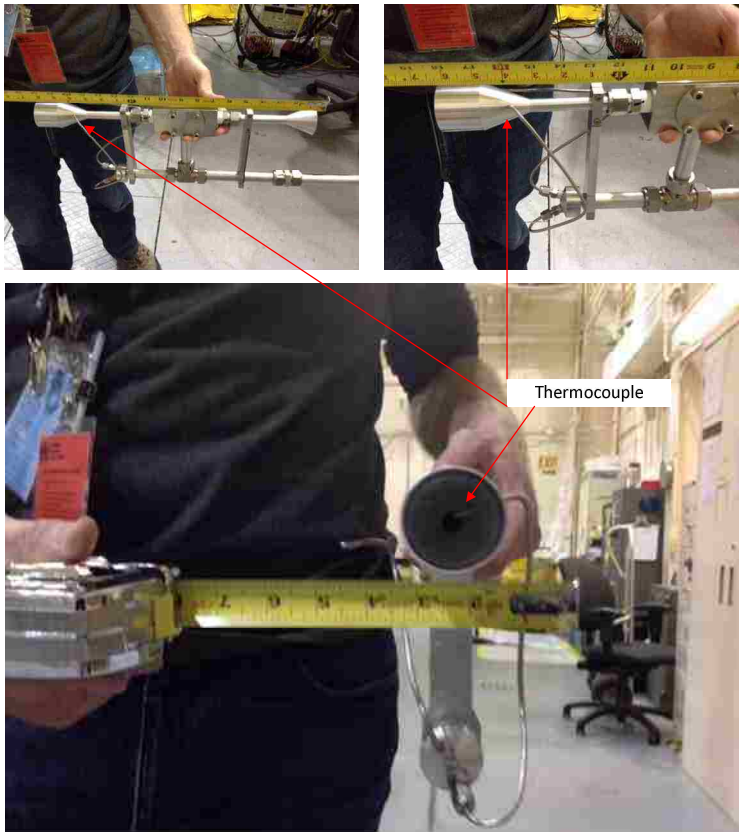

Figure 33. Photographs of the flowmeter and its thermocouples used for ACRR measurements [34].

The signals from IE-603 and the flowmeter thermocouple were recorded using a Yokogawa digital oscilloscope/recorder. In addition to these, data for the ACRR's Plant Protection System (PPS) instrumented fuel elements (IE-602 and IE-603) was obtained

from the ACRR's LogMaster computer. Figure 34 shows the IE-603 fuel temperature trace from Operation 11277, along with the Razorback measured fuel temperature prediction for an element with a peaking factor of 1.44 (i.e., the peaking factor associated with the IE-603 location). Note first the near instantaneous rise in the IE-603 temperature to ~410°C at the beginning of the transient. This initial temperature rise is due to gamma radiation heating of the IE-603 fuel thermocouple itself, which is made of a W/Re alloy. There is then an initial cooling of the thermocouple until the heat transfer from the BeO-UO_2 fuel begins to heat the thermocouple. The subsequent time evolution of the increase in the measured temperature is due to the thermal time constant of the thermocouple.

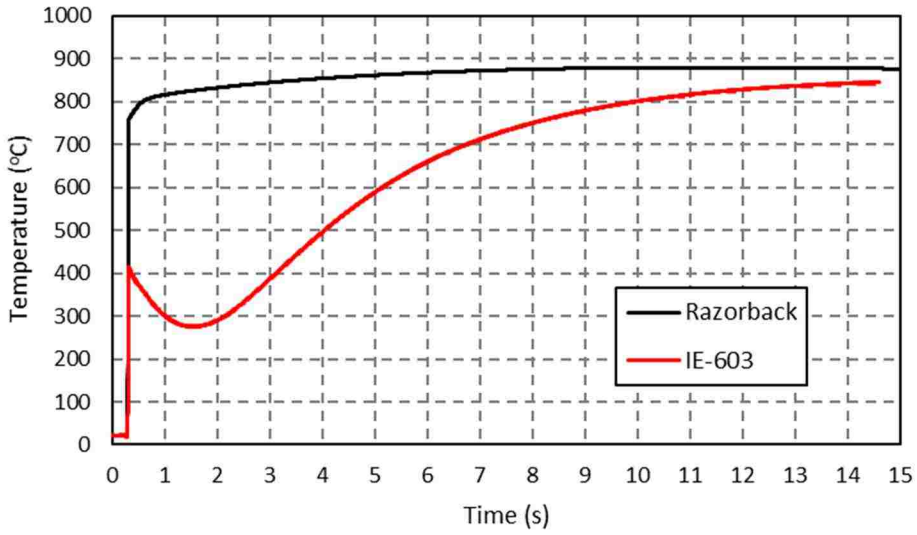

Figure 34. Comparison of Razorback prediction with the measured ACRR fuel temperature for pulse operation 11277 [34].

The Razorback measured temperature trace peaks between 10 and 12 seconds, while the fuel thermocouple has still not attained equilibrium with the surrounding fuel.

This behavior is typical of thermocouples. Eventually, the fuel thermocouple is nearing equilibrium at ~14 s, where the Razorback prediction is ~30-40°C higher.

Figure 35 shows the Razorback prediction of the long-term fuel cooldown for a fuel element to simulate the response of IE-602 for the PPS1 fuel temperature. The PPS1 fuel temperature recorded by the Logmaster computer was sampled at a rate of only ~1 sample per minute. The results show reasonable success early in the transient, and late in the transient. Discrepancies on the order of 70-80°C are seen at intermediate times. The discrepancies may be due to underestimating the clad-to-coolant heat transfer coefficient due to the choice of heat transfer coefficient correlation parameters or due to underestimating the local coolant flow rate.

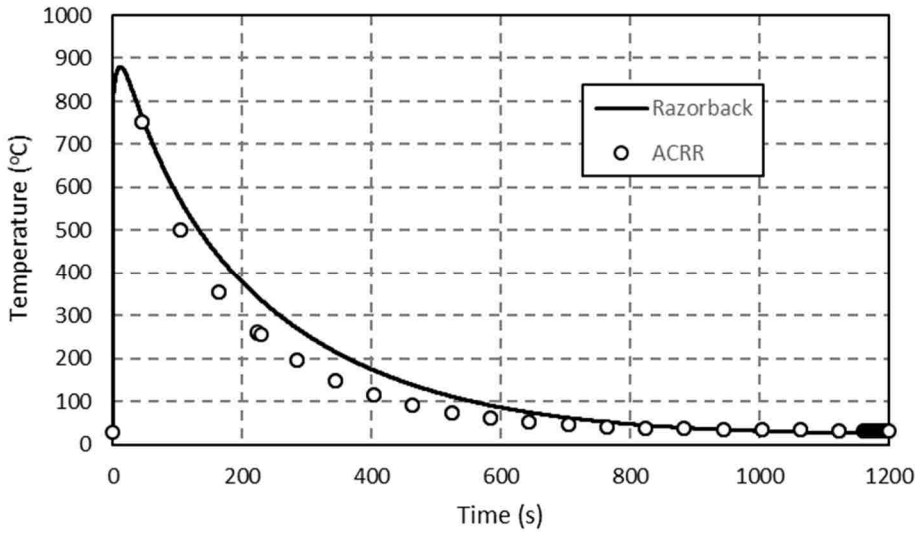

Figure 35. Comparison of Razorback prediction of the long-term cooldown of the ACRR fuel temperature for pulse operation 11277 [34].

Figure 36 shows the flowmeter funnel thermocouple temperature trace from Operation 11277, along with the Razorback coolant channel outlet temperature prediction

for an element at the location of the flowmeter/thermocouple fixture. The simulation includes an increased outlet minor loss coefficient of 4.5 (vs. 1.5 for a typical ACRR coolant channel exit) to account for the effect of the flowmeter placed over the channel outlet. Initially, there is a near instantaneous rise in the temperature to ~33°C, due to gamma radiation heating of the thermocouple itself (a Type K chromel/alumel). There is then an initial cooling of the thermocouple until the heat transfer from the coolant begins to heat the thermocouple. The subsequent time evolution of the increase in the measured temperature is due to the thermal time constant of the thermocouple. Note especially that the Razorback-predicted outlet temperature peaks at about 5.5 seconds, while the thermocouple has still not attained equilibrium with the flowing water. In this case, the result is that the thermocouple "misses" the peak of the outlet temperature history. At about 13-14 seconds, the thermocouple appears to have reached equilibrium with the flowing water, and the Razorback simulation matches well at this point.

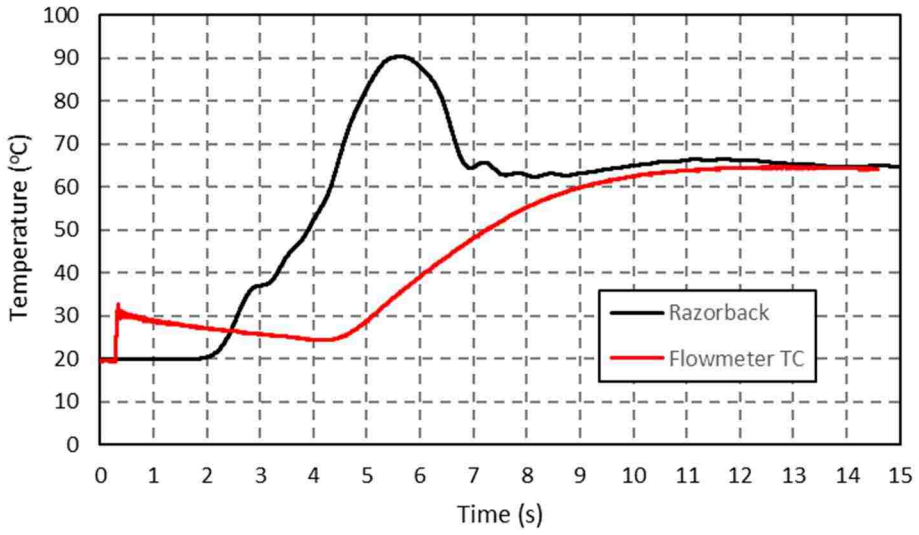

Figure 36. Comparison of Razorback prediction with the measured ACRR coolant outlet temperature for pulse operation 11277 [34].

4.6.2. Slow Transient Operations

Lastly, an extended ACRR operation (Operation #11278) in which the control rod bank was lowered into the core in a series of finite steps was simulated. The control rod bank motion for the operation is shown in Figure 37, along with the Razorback program for control rod bank motion.

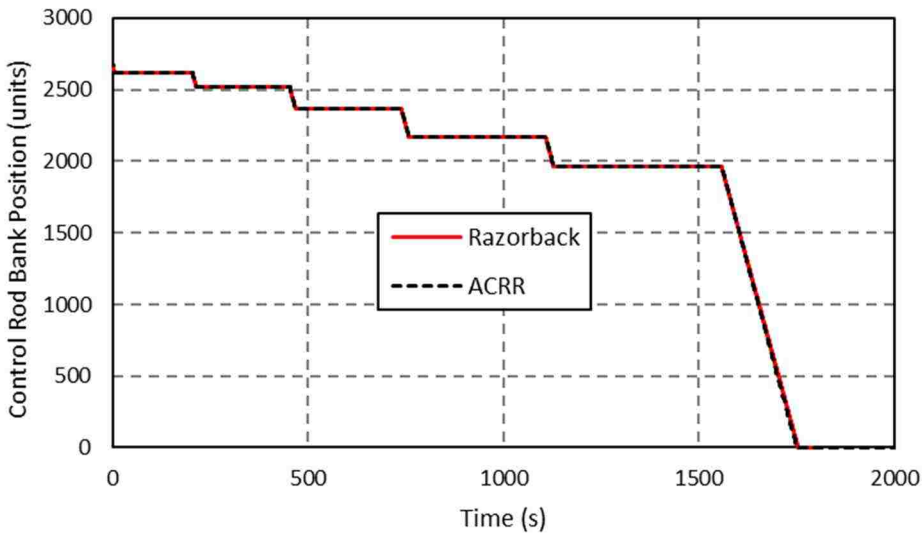

Figure 37. Control rod bank movement history for ACRR operation 11278 [34].

Figure 38 and Figure 39 show the results for the power and "measured" fuel temperature history of the Razorback simulation compared to the ACRR power and temperature history. The initial reactor power level was ~90 %FP, before the control rod bank motion plan was commenced. The power history results match reasonably well, with better agreement at power levels above about 20-30 %Full Power (%FP). A significant discrepancy arises around 10-20%FP.

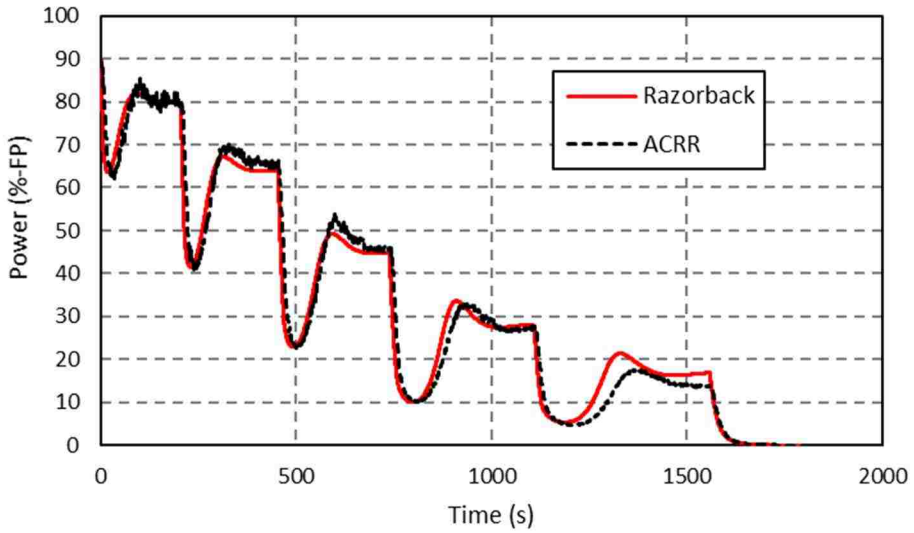

Figure 38. Measured and predicted power history for ACRR operation 11278 [34].

The temperature history matches well in general shape, but there is clearly an offset in the magnitude of the predicted temperature which is on the order of 150-200°C.

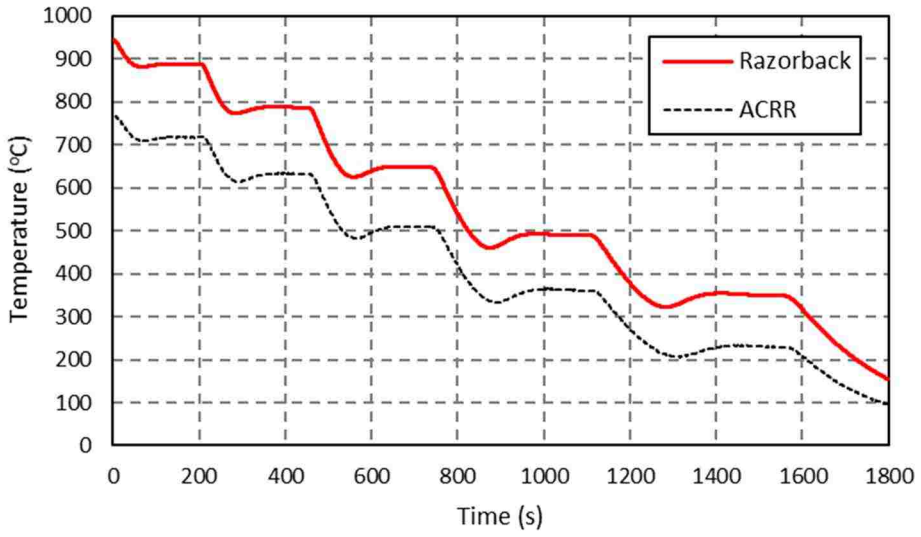

Figure 39. Measured and predicted fuel temperatures for ACRR operation 11278 [34].

Figure 40 shows the results of the Razorback simulation for the coolant channel outlet temperature compared to measured data. Here, Razorback is overpredicting the outlet temperature by 5-7°C over the first 800 s of the operation. The results converge as the reactor power falls below ~30 %FP.

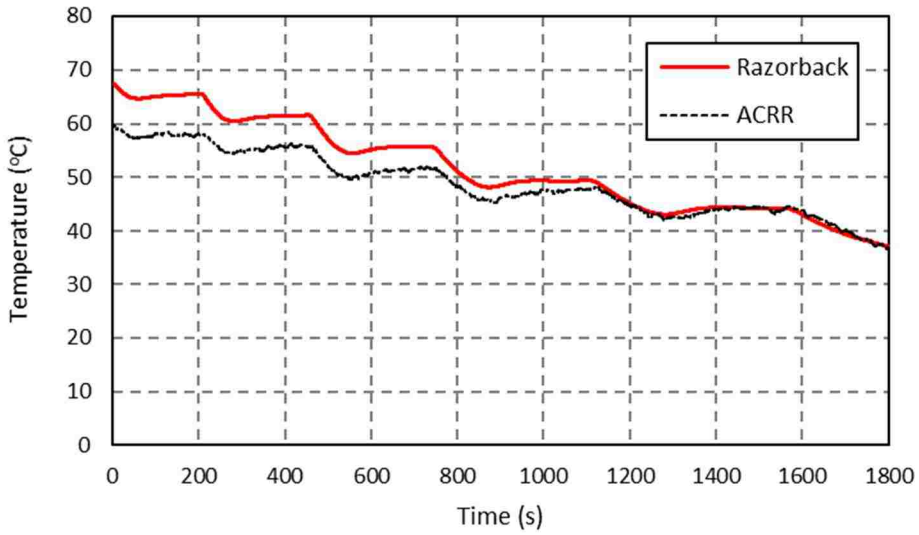

Figure 40. Measured and predicted coolant channel outlet temperature for ACRR operation 11278 [34].

4.6.3. Steady-State Operations

The Razorback code was run in steady-state mode to compute estimates of the measured fuel temperature in the ACRR for various element power levels. Figure 41 shows this and two other temperature vs. power data sets for comparison. The first is "ACRR T vs. P Correlation," which is a correlation of ACRR measured fuel temperatures to power level used by the ACRR staff. The second is a set of temperatures measured at the ACRR for the power plateaus for Operation 11278 (see Figure 39).

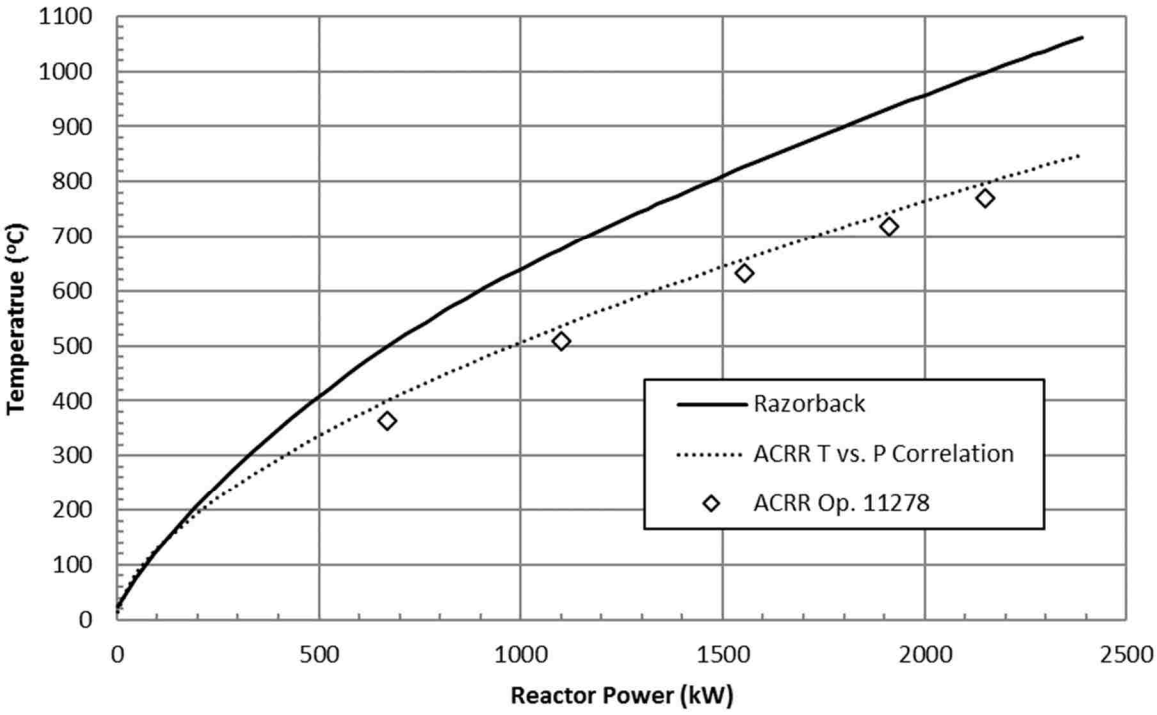

Figure 41. Measured and predicted fuel temperatures for the ACRR [34].

Razorback is clearly overpredicting the ACRR fuel temperature by a significant amount. Differences increase above 200 kW reactor power, increasing monotonically to ~200°C at a reactor power of 2400 kW. Potential causes for this discrepancy are being explored (e.g., over-simplified model of the niobium can geometry features, impact of the thermocouple positioning plate in the instrumented element, and the possibility that the measured reactor power is less than expected).

4.7. Conclusions

The agreement of the code results with analytical solution data is excellent (with relative errors on the order of 0.1%) for the reactor kinetics model (covering a wide variety of reactivity inputs), the model for heat transfer within a fuel element, and the model for thermal expansion of the fuel element materials.

The agreement of code results with analytical solution data for mechanical stress is good (within 1-5 MPa for stresses). Stresses are computed from gradients of the displacement results, and involve numerical differentiation of the discrete numerical displacement results. Numerical differentiation of a small set of discrete data points is problematic. However, the accuracy of the stress computations does not impact the reactor kinetics or thermal-hydraulics evaluations.

The pulse operation simulations agree well with the ACRR's Pulse Diagnostic System (PDS) data. Maximum measured fuel temperatures during a simulated pulse are within 2% for pulses above \$2, and within 5%-10% for pulses below \$2. Predicted peak power is generally low by ~10%-15%, although the predicted peak power for both \$2 pulses used for comparison about 20% low. The reason for this particular discrepancy is unknown. Prediction of peak power is improved when better estimates of the initial reactor power are available. Predicted pulse energy yield is generally within ~±10%-15%. Predicted FWHMs are 1%-12% high. The author is not aware of a documented evaluation of the measurement error associated with the PDS, but an estimate of ±10% for overall accuracy would not be unreasonable.

Simulation of the long-term cooldown of a fuel element after a pulse indicates (Fig. 35) that Razorback may be underestimating the fuel-to-coolant heat transfer rate. The

power stepdown transient operation simulation agrees well with the ACRR reactor power history data. However, there is a clear offset (~30-40%) in the prediction of the ACRR measured fuel temperatures for that power history.

Razorback predictions of ACRR fuel temperature using the code's steady-state mode also appear to be high (~25% for appreciable element power levels). Further work is needed to determine the reason for this offset in predicted fuel temperatures for steady-state and quasi-steady-state operation. Work on a finite element model of the ACRR instrumented fuel element is currently underway to determine is measured fuel temperature prediction may be improved by better detail in the fuel element geometry. The Razorback fuel temperature results are, in general, conservative.

The Version 1.0 release of the Razorback code is considered adequately verified and validated for use in the simulation of ACRR transient and steady-state operation.

5. Large Rapid Reactivity Addition Events: Reactor Kinetics Response

5.1. Introduction

The initiation of a large rapid reactivity addition (LRRA) begins with a rapid change in system reactivity. Reactor power will increase exponentially, driven by prompt fission neutrons, with a very small time constant related to the neutron generation time (which is ~24 ms for the ACRR) divided by the magnitude of the prompt reactivity addition. The rapidly increasing power will result in a nearly adiabatic and rapid temperature rise within the fuel. The negative reactivity feedback due to the increase in fuel temperature (i.e., the Doppler reactivity feedback) will begin to rapidly reduce the system reactivity, causing the power increase to slow. As the system reactivity reaches and falls below a value numerically equal to the delayed neutron fraction β, the reactor power will peak, and begin to rapidly decrease, creating a power "pulse." After the initial power pulse, the reactor power will decay slowly at a relatively high power level (driven by the delayed neutron precursors produced during the pulse).

In many reactors, a LRRA would be an undesirable reactivity-initiated accident (RIA). For the ACRR, such LRRAs are part of normal operation. Thus, by simulating the response of the ACRR using a code such as Razorback, one may investigate the phenomena associated with a LRRA, without damaging the reactor. In this chapter, we will investigate the power pulse characteristics associated with a LRRA.

5.2. Overview of the Reactor Power Response for the ACRR

To evaluate the response of a research reactor to a large rapid reactivity addition, we will first consider a \$3.00 reactivity addition to the ACRR. The reactivity will be introduced as a ramp over a time of 80 ms, i.e., a \$37.5 per second ramp addition terminated after 80 ms. Figure 42 shows the reactor power resulting from the reactivity addition, peaking at 29.7 GW at a time of 81 ms, with a pulse width (at half-maximum power) of 7.4 ms. The period (τ) of the reactor power is given by the inverse of the fractional rate of change of the power, or $\tau = \left(\frac{1}{P}\frac{dP}{dt}\right)^{-1}$. The minimum period for this \$3 LRRA was 2.0 ms, and it occurred at 72.7 ms (i.e., before the full reactivity addition was complete).

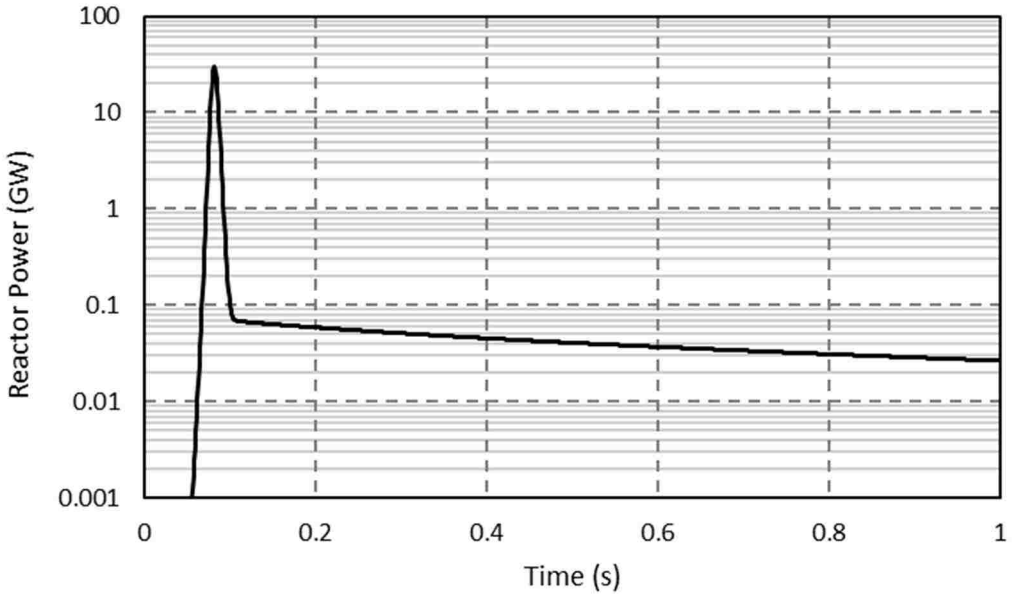

Figure 42. Reactor power pulse for a \$3 rapid reactivity addition to the ACRR.

Subsequent to the power pulse, the reactor power decays over time from an elevated power level (~70 MW) due to the presence of delayed neutron emitting fission products

produced during the power pulse. Figure 43 shows the reactor power as it decays following the pulse, but eventually rises again to an equilibrium power level of 1.34 MW. The rise of the power to an equilibrium level occurs because after the reactivity has been added, no further reactivity control system action is modeled (i.e., no action is taken to shut down the reactor after the reactivity addition). Thus, as the power decays, the fuel will begin to cool off. As the fuel cools, the Doppler fuel temperature reactivity feedback is now positive, so that reactor power may again increase. Ultimately an equilibrium power level, commensurate with the initially added reactivity, is attained.

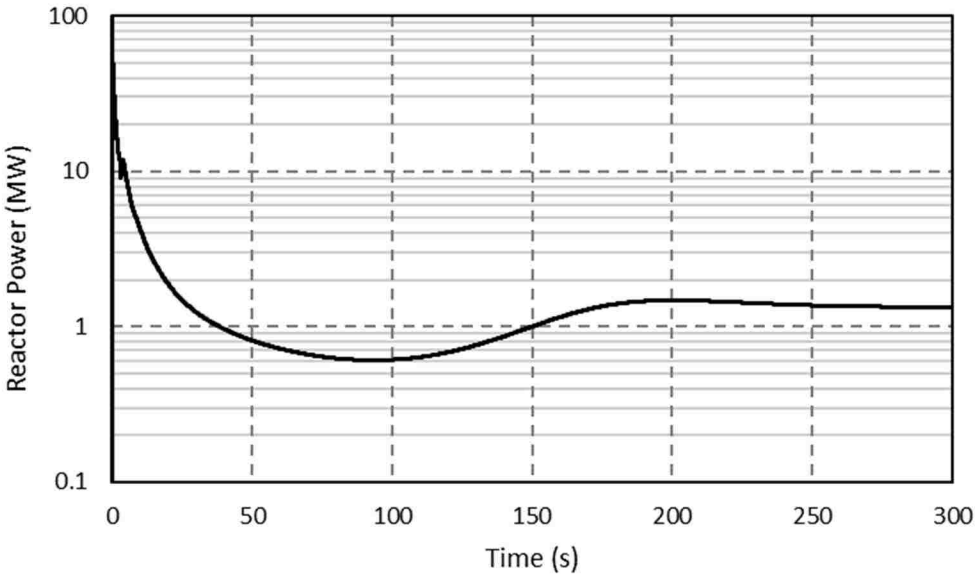

Figure 43. Reactor power history for a $3 rapid reactivity addition to the ACRR.

Figure 44 shows the integrated reactor power for the $3 LRRA, which corresponds to the energy released, or energy yield of the LRRA. First, note that there is an initial rapid energy release (yield) due to the power pulse. This is followed by a monotonic rise in the yield thereafter, since the power reaches an equilibrium level. If action were taken to shut

down the reactor, the yield would eventually reach a maximum value. Thus, any specification of a energy yield for the LRRA will depend upon the time at which the yield is determined.

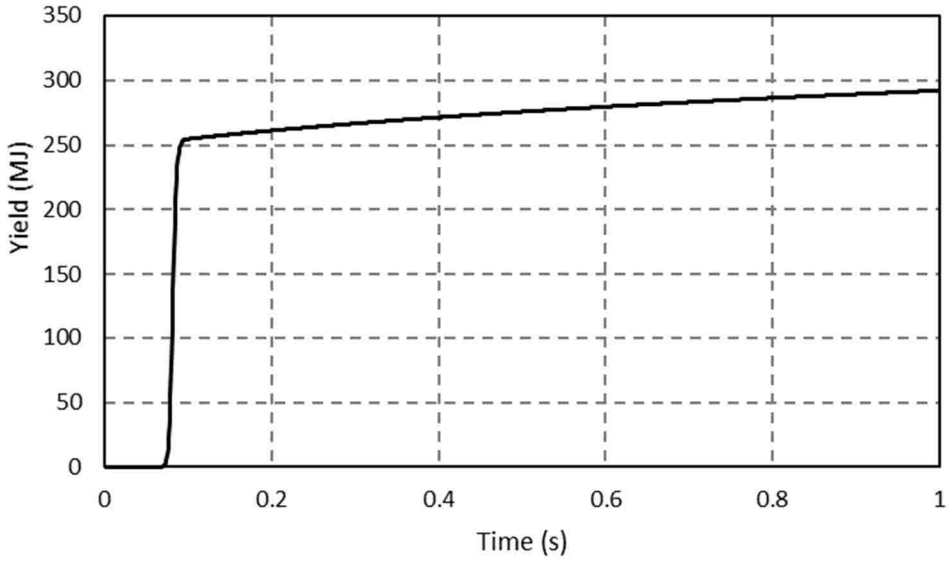

Figure 44. Energy release for a $3 rapid reactivity addition to the ACRR.

At the ACRR, the pulse yield of a pulse operation is defined as the integrated power up to a point in time shortly after the peak of the power pulse, and that time is taken to be three times the pulse width at half of its peak power. This pulse width is referred to as the full width at half-maximum, or FWHM. For the $3 LRRA under consideration here, the pulse yield is 248.5 MJ, and the FWHM is 7.38 ms.

Directly related to the yield of the pulse is the associated temperature rise of the fuel. As noted earlier, the initial temperature response to the pulse is a near adiabatic heating of the fuel. Figure 45 shows this initial fuel temperature rise for the $3 pulse operation. An initial peak value is reached (~1060°C here), followed by a slight decrease

as the power pulse concludes, followed by a slower temperature rise as delayed neutron fission heating becomes dominant.

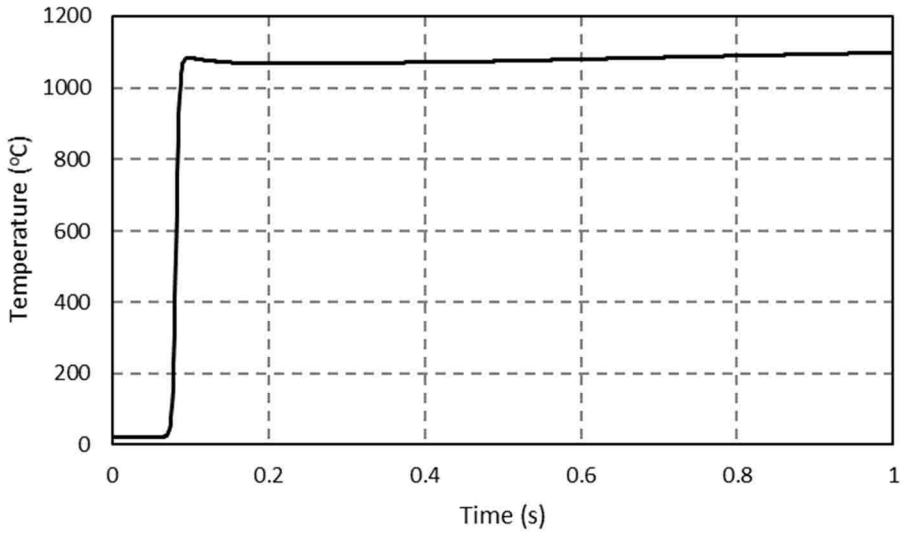

Figure 45. Initial maximum fuel temperature history for a $3 rapid reactivity addition to the ACRR.

5.3. Reactor Power Pulse Characteristics

We will now examine the variation in power pulse characteristics for a range of LRRAs. In each case, the LRRA was modeled as a linear ramp addition over a reactivity addition time of 80 ms. Figure 46 shows the variation in the peak value of the reactor power pulse for each LRRA. It is immediately apparent that there is a discontinuity of slope for reactivity additions of ~$3.

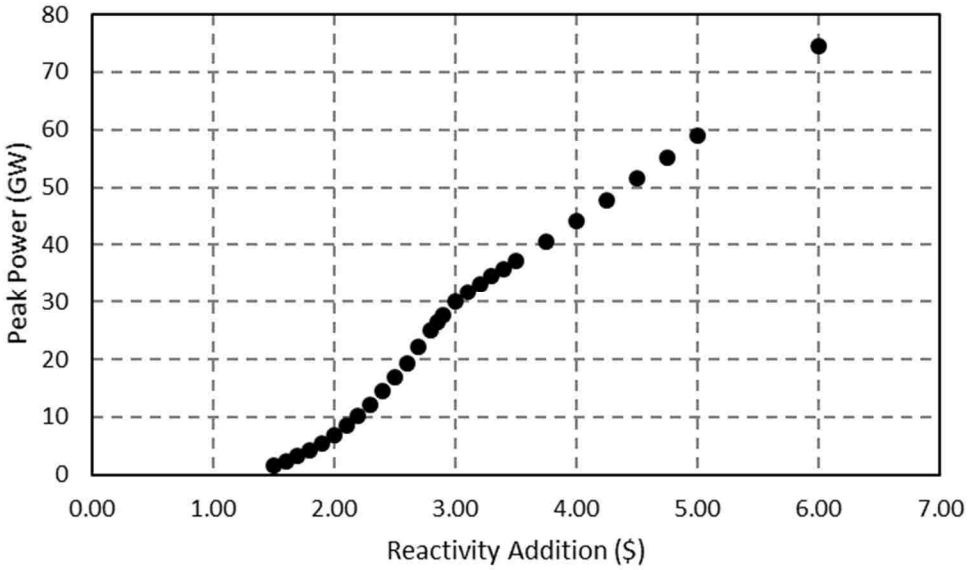

Figure 46. Variation of reactor peak power vs. reactivity addition.

The classical Nordheim-Fuchs model [10] for prompt critical reactivity additions shows that the peak power of the pulse should vary with the square of the reactivity addition. In the Nordheim-Fuchs model, the variation is with the square of the *prompt* reactivity addition, which is the reactivity addition above \$1 (e.g., the prompt reactivity addition for a \$3.50 pulse is \$2.50). The use of the total reactivity addition here, however, amounts to a simple shift on the horizontal axis. The results shown in Figure 46 exhibit this Nordheim-Fuchs type of behavior, for reactivity addition up to ~\$3. As the reactivity addition increases beyond approximately \$3, the peak power appears to have a more linear variation with reactivity addition.

The reason for the change in response behavior for the peak power is that reactivity feedback begins to "overtake" the reactivity addition. In this case, the heating of the fuel produces an appreciable fuel temperature change (and, thus, an appreciable Doppler reactivity feedback) before the full reactivity addition is complete.

To see this, consider Figure 47, which shows the maximum system reactivity attained during the LRRA. Although the total reactivity addition may be \$3, the maximum system reactivity attained is only \$2.65. Thus, the reactivity addition (which we recall occurs over an 80 ms addition time) is simply not rapid enough to be complete before significant reactivity feedback occurs. The data plotted in Figure 47 show that the peak system reactivity fails to attain to the full reactivity addition beginning at ~\$2.50.

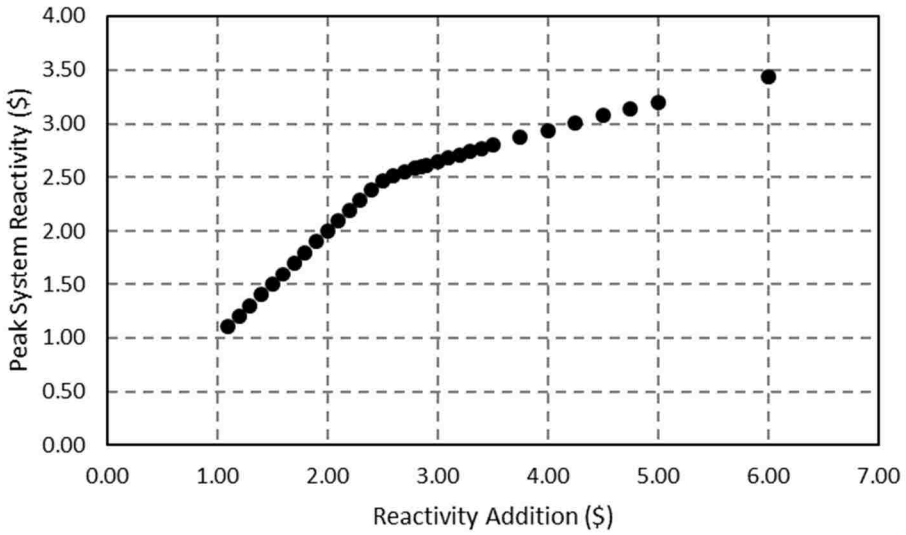

Figure 47. Variation of peak system reactivity vs. reactivity addition.

As a result of this impact on the reactivity addition, we would expect that the pulse characteristics (e.g., peak power, yield, etc.) would be less than predicted by a Fuchs-Nordheim approach. Taking the peak power data plotted in Figure 46, we may develop an extrapolation of the peak power vs. reactivity addition data. A third order polynomial fit of the data up to a \$3 addition was obtained. This resulting polynomial extrapolation is shown in Figure 48, and it represents the predicted peak power for what would effectively be a "step" reactivity addition.

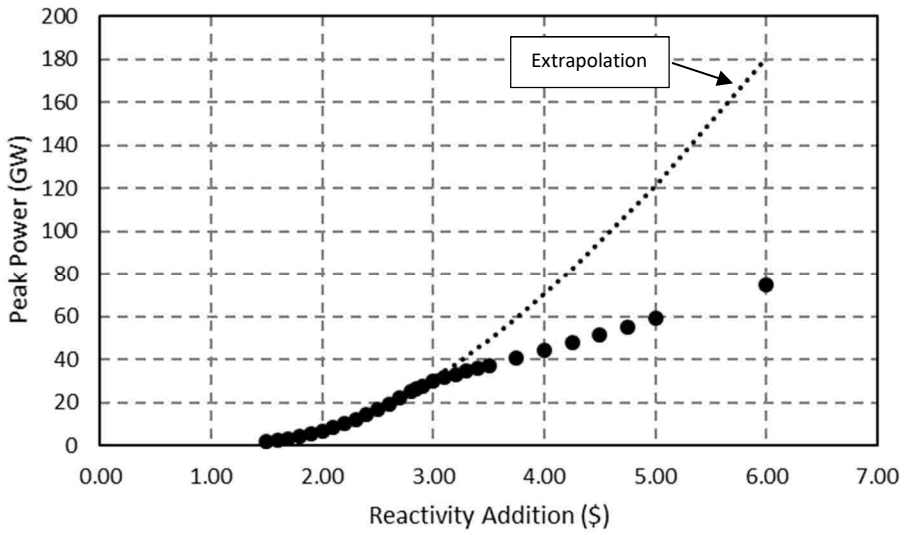

Figure 48. Extrapolation of reactor peak power illustrating the effect of the reactivity addition time.

Figure 49 shows the variation of pulse energy (i.e., integrated power to a time of 3·FWHM past the pulse peak) with reactivity addition. A similar extrapolation process was followed, using a second order polynomial fit. As with the peak power of the pulse, the energy yield of the pulse is significantly impacted beyond a reactivity addition of ~$3.

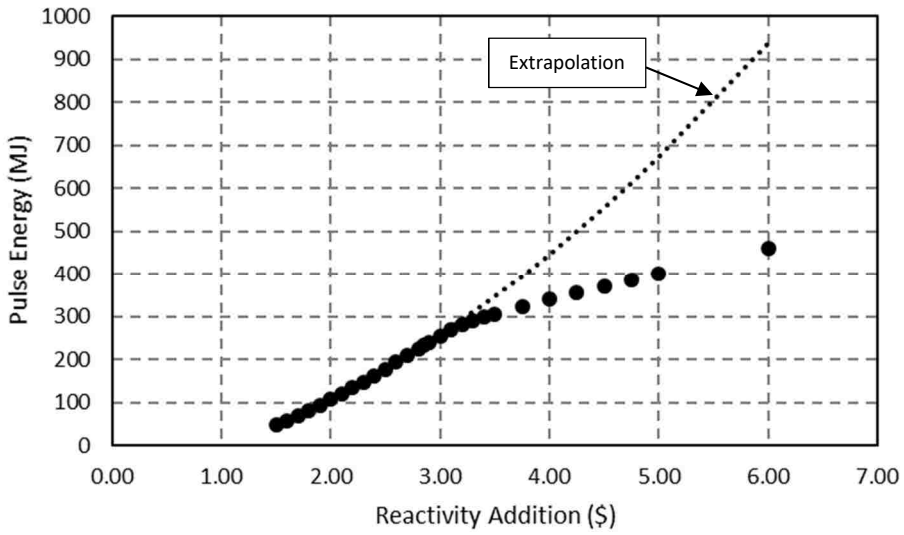

Figure 49. Extrapolation of energy yield illustrating the effect of the reactivity addition time.

Figure 50 shows the variation in the FWHM as a function of the reactivity addition. As with the peak power and energy yield, there is a change in the trend of the FWHM beginning at a reactivity addition of ~$3.

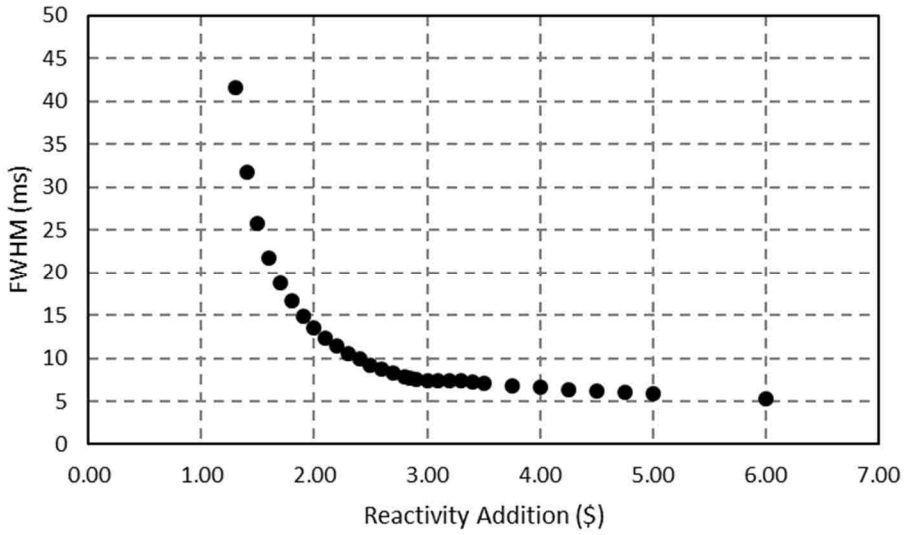

Figure 50. Variation of the characteristic pulse width vs. reactivity addition.

The minimum reactor period is shown in Figure 51, along with the Nordheim-Fuchs model prediction of the minimum period. The discontinuity in slope is evident beginning at a reactivity addition of ~$2.70. The Nordheim-Fuchs model overpredicts the minimum period below ~$1.40, where the development of the pulse is slow enough that delayed neutrons have an impact. The minimum period is underpredicted by the Nordheim-Fuchs model for greater than ~$2.70, where the peak system reactivity attained is less than the reactivity addition.

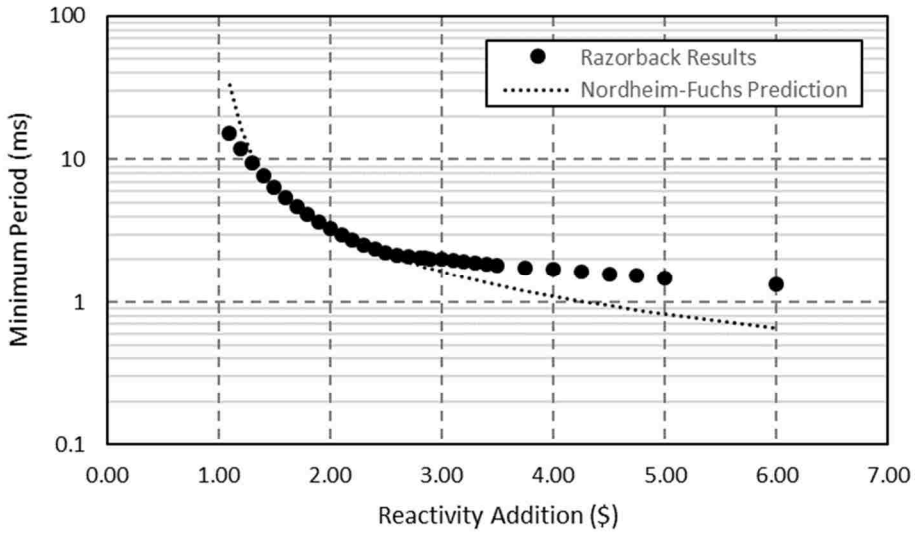

Figure 51. Variation of minimum reactor period vs. reactivity addition.

The time required for the pulse to reach its peak power is shown in Figure 52 as a function of the reactivity addition. It appears that the trend here does not have a visually discernable discontinuity of slope such as can be seen in the previous plots. We see that at ~$3, the time to the peak power falls below the 80 ms reactivity addition time.

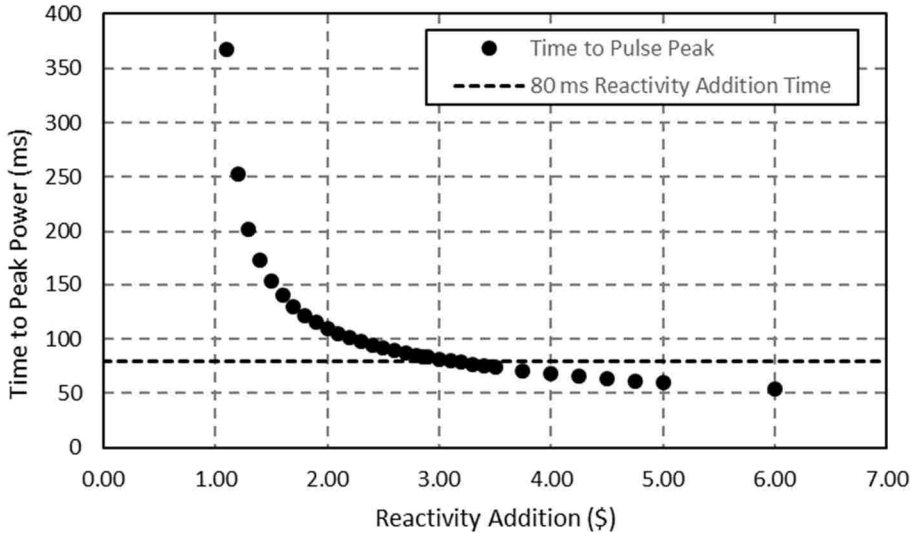

Figure 52. Variation of the time to the peak power vs. reactivity addition.

The time to the peak power may be estimated using the Nordheim-Fuchs model for step reactivity additions. The Nordheim-Fuchs derived relationship [10] for the time to peak power (t_{peak}) may be written as

$$t_{peak} = \Lambda^* \frac{ln\left[\frac{2(\rho_\$ - 1)^2}{\gamma_\$ \Lambda^* P_o}\right]}{(\rho_\$ - 1)} \tag{5-1}$$

where Λ^* is the neutron generation time divided by the delayed neutron fraction, $\rho_\$$ is the reactivity addition in units of \$, $\gamma_\$$ is the energy release reactivity feedback coefficient in \$ per unit energy divided by Λ^*, and P_o is the initial power level. The energy release reactivity feedback coefficient is a core-wide average value, so $\gamma_\$$ in Eq. 5-1 was manually adjusted until the t_{peak} for a \$1.10 reactivity addition matched the result obtained from Razorback. This yielded a $\gamma_\$$ of ~0.073 \$/MJ.

Figure 53 shows the resulting Nordheim-Fuchs prediction of t_{peak} as compared to the Razorback results. The Razorback results are shown as obtained, and also with the 80

ms reactivity addition time subtracted. The adjusted results line up reasonably well with the Nordheim-Fuchs predictions up to ~$1.50. After this, the finite (80 ms) reactivity addition time begins to significantly impact the time required for the pulse to reach its peak power. Note particularly that the adjusted results fall below zero at ~$3.00 (after which, the results are not plotted). In these cases, the peak power is reached before the full reactivity addition has been completed.

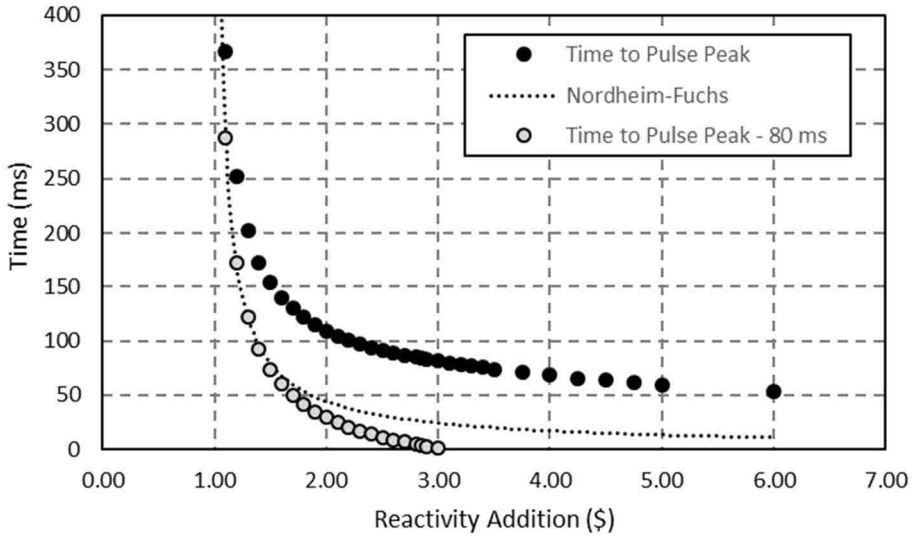

Figure 53. Razorback time to peak power compared to Nordheim-Fuchs estimate.

Finally, we consider the initial peak in the temperature of the fuel in response to the power pulse, shown in Figure 54. As noted earlier, this initial peak is a time period of essentially adiabatic heating. However, below an addition of $1.90, the transient is slow enough that there is no distinguishable initial fuel temperature peak, so only LRRAs ≥$1.90 are shown. The discontinuity in the slope of the data again occurs at ~$3, which is the same behavior which was observed for the pulse energy yield. Thus, the initial peak in fuel temperature would be significantly overestimated if the impact of the reactivity addition rate is not considered.

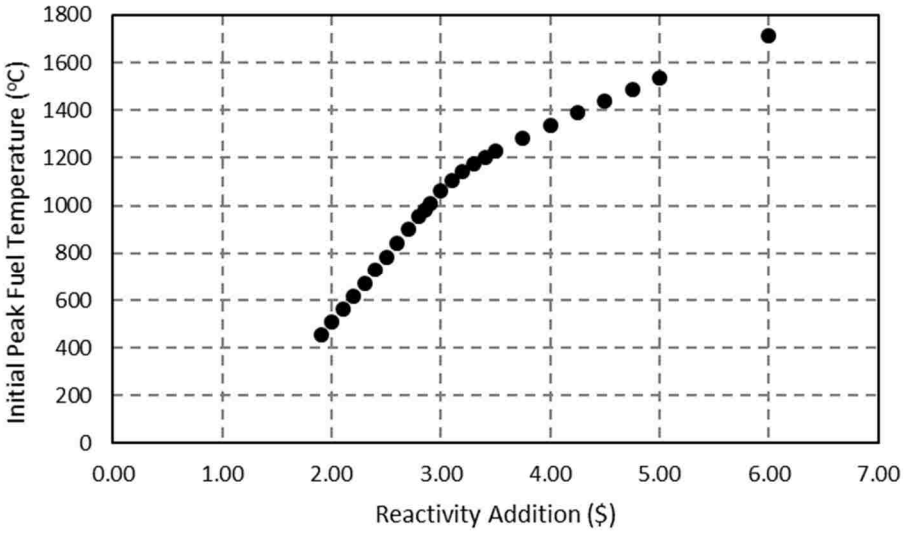

Figure 54. Variation of the initial peak maximum fuel temperature vs. reactivity addition.

It is of interest to consider the time at which the initial peak fuel temperature occurs in relation to the time of the peak power of the pulse. We may characterize this time span by dividing by the FWHM of the pulse, obtaining the number of FWHM between the pulse power peak and the initial fuel temperature peak. Figure 55 presents a plot of the results of this analysis.

The conclusion we may draw from Figure 55 is that the initial adiabatic energy deposition of the pulse is complete between 2 and 3 FWHMs after the peak power. This provides some justification of our use of $t_{peak}+3\cdot FWHM$ as the time point for determining pulse energy yield.

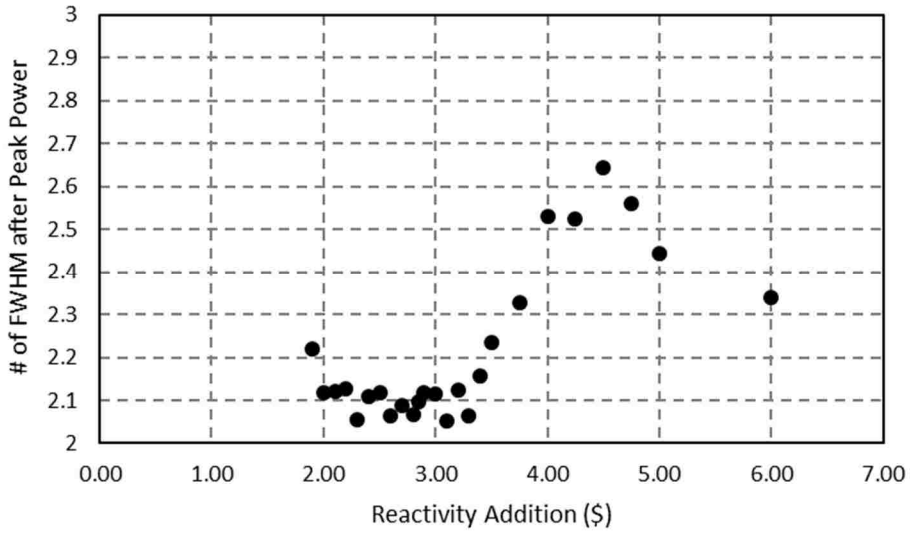

Figure 55. Timing of the effective completion of the pulse energy deposition.

5.4. Relative Reactivity Feedback Mechanism Contributions

After the reactivity addition has been initiated, the reactivity feedback mechanisms of the reactor begin to respond. The primary mechanisms for the ACRR are the fuel temperature (i.e., Doppler) feedback, the fuel expansion feedback, the cladding expansion feedback, and the coolant temperature and density feedback. Figure 56 shows the relative magnitude of these feedback mechanisms for a $3 reactor pulse. The timeframe of Figure 56 is restricted to during and shortly after the reactor power pulse. The longer term post-pulse timeframe will be discussed in a subsequent chapter.

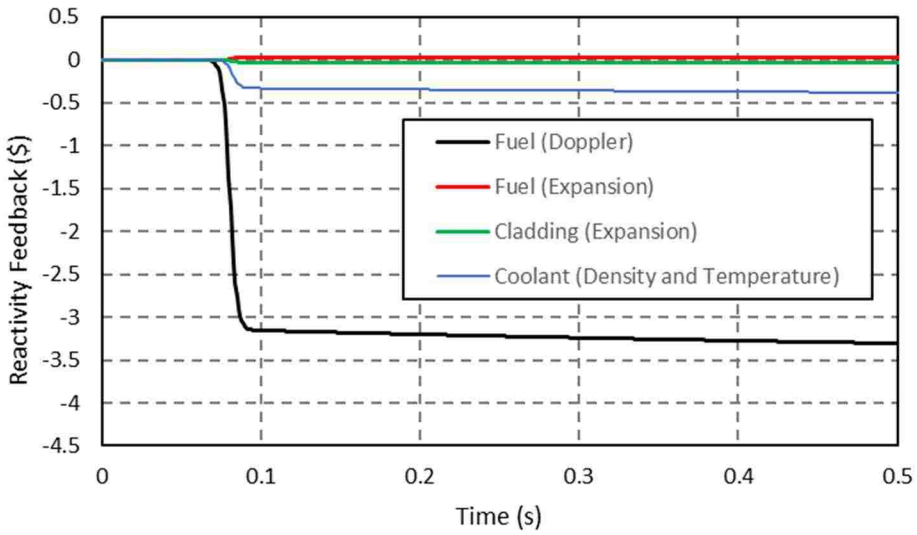

Figure 56. Comparison of the reactivity feedback mechanisms during the pulse.

It is clear from Figure 56 that the Doppler feedback is the dominant reactivity feedback mechanism. Further, it responds essentially instantaneously, while the other mechanisms are slightly delayed. The Doppler feedback is large and negative, and is the primary means of terminating the reactor power pulse. The coolant feedback is the next

most significant in magnitude, and at this stage of the pulse operation the coolant heating is due to direct energy deposition of neutrons and gamma rays interacting with the water. The cladding expansion feedback is also negative, but plays only a small role in the overall reactivity feedback effect. Note, however, that the fuel expansion feedback initially provides a positive feedback, albeit relatively small in magnitude. The initial expansion of the outer fuel radius increases the fuel-to-moderator area ratio within a fuel element cross-sectional "cell," which enhances the probability of a neutron's path intersecting the fuel material.

Figure 57 shows the impact of a different coolant channel inlet temperature on the effect "balance" between the Doppler feedback response and coolant feedback response. Because the coolant is now at higher temperatures along the channel, the reactivity feedback from the coolant density change increases more quickly than it does for a 20°C inlet temperature.

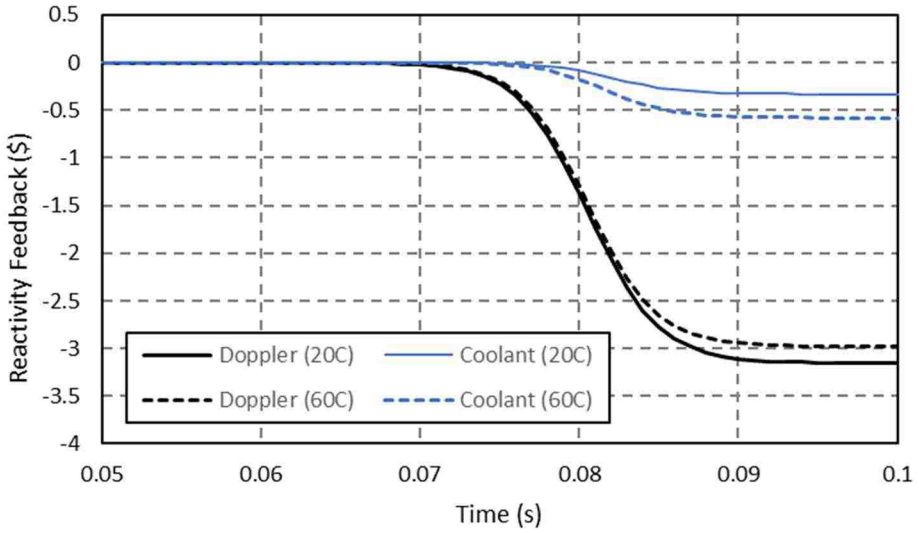

Figure 57. Impact on initial pool water temperature on the Doppler and coolant reactivity feedback during the pulse.

5.5. Impact of Reactivity Addition Rate

The LRRAs examined so far have used a reactivity addition time of 80 ms. Theoretically, the reactivity addition time could be shorter or longer, depending upon the design and characteristics of the system utilized to add the reactivity to the reactor. Thus, we will examine the impact of varying the reactivity addition time.

Figure 58 shows the response to a $3.50 LRRA with the reactivity addition times varying from 80 ms to 160 ms. The peak power of the pulses trends lower as the reactivity addition time increases. A $3.50 LRRA has already been seen to achieve a peak system reactivity of only $2.80 with a reactivity addition time of 80 ms. As the reactivity addition time increases, the peak system reactivity achieved will decrease and the peak reactor power achieved will decrease. The power levels after the pulse are relatively similar, but they do not immediately converge. Ultimately, the power level after the system achieves equilibrium will be the same, because the total reactivity addition for each was the same $3.50.

Figure 59 provides a closer view of the power trace of the pulse near the peak. For reactivity addition rates of 80-120 ms, the power level just after the peak shows a slow, steady decrease. However, for longer reactivity addition times (140-160 ms), there is an increase in the power level after the pulse. This post-pulse increase in power is due to the fact that the reactivity addition is still progressing after the pulse has occurred. Thus, if the reactivity addition time is long enough, a second “mini-peak” in the power will occur.

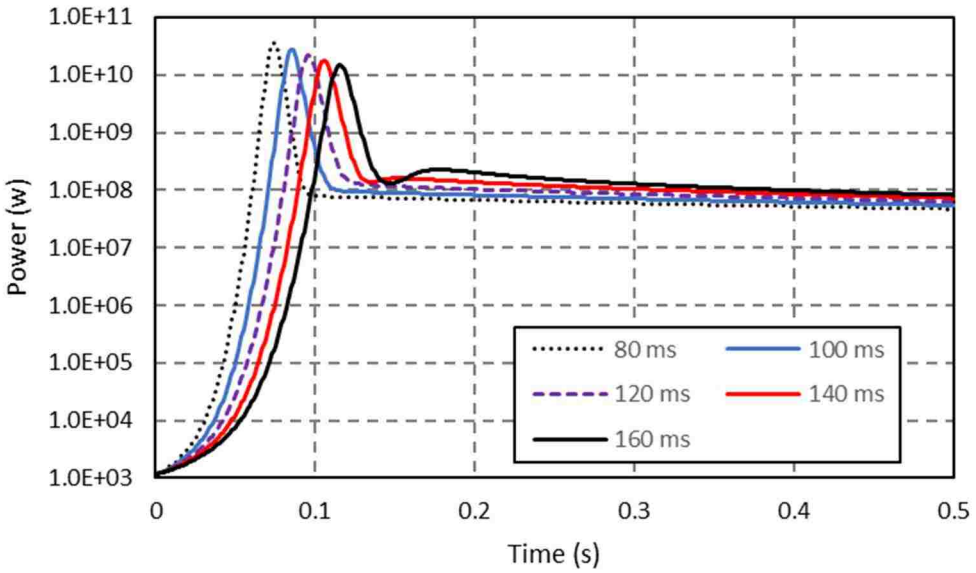

Figure 58. Impact of the reactivity addition time on the reactor power response to a $3.50 LRRA.

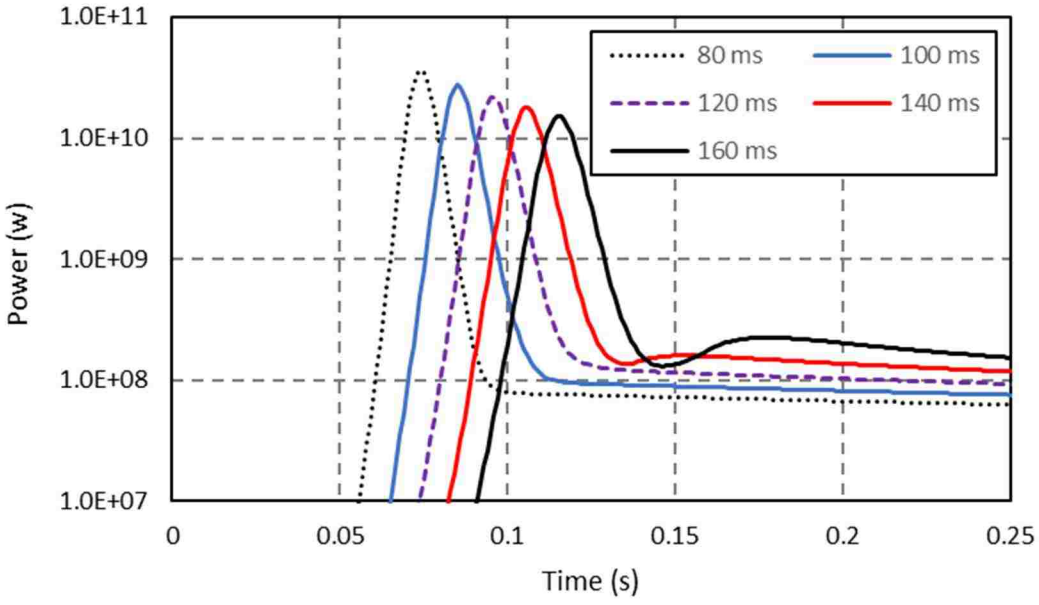

Figure 59. Closeup view of the impact of the reactivity addition time on the reactor power response to a $3.50 LRRA.

Figure 60 presents the peak system reactivity achieved for a $3.50 LRRA as a function of the reactivity addition time. This clearly shows that the decrease of reactivity addition time results in a plateau of peak system reactivity equal to the reactivity of the LRRA. Thus, the system response does approach that of a step reactivity addition. As the reactivity addition time increases beyond 30-40 ms, the peak system reactivity decreases.

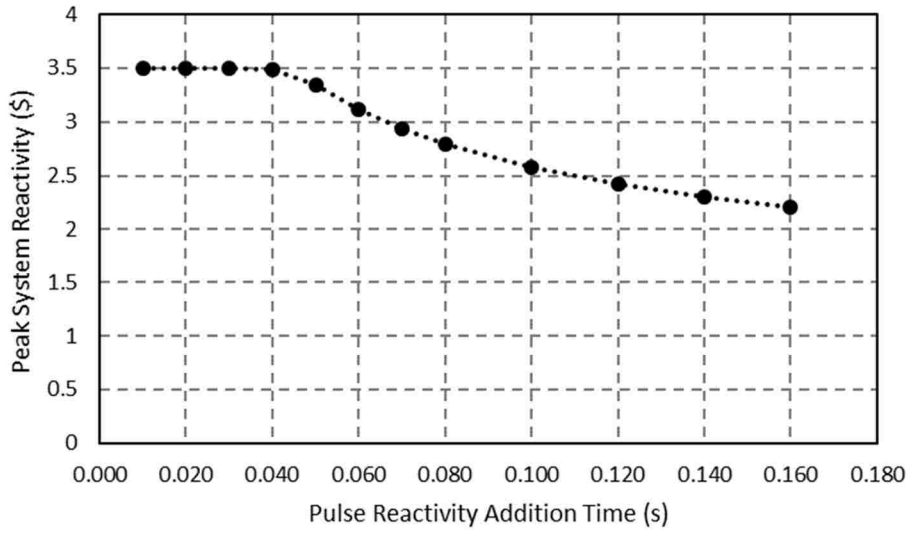

Figure 60. Peak system reactivity for a $3.50 pulse of various reactivity addition times.

Figure 61 presents the initial peak in the maximum fuel temperature achieved for a $3.50 LRRA as a function of the reactivity addition time. Again, we see that the decrease of reactivity addition time results in a plateau of the initial peak maximum fuel temperature achieved. This demonstrates that the initial peak maximum fuel temperature is a function of the reactivity addition only when the reactivity addition time approaches a step reactivity addition.

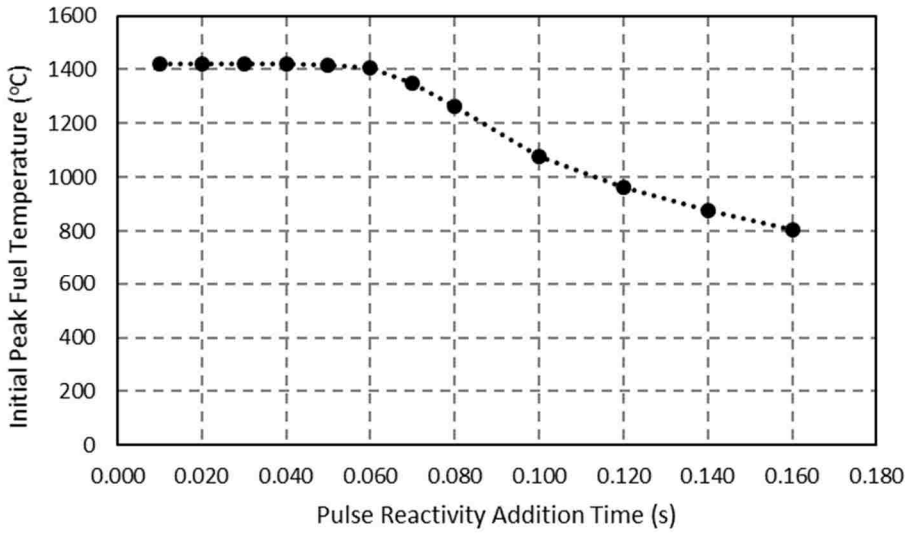

Figure 61. Initial peak fuel temperature for a $3.50 pulse of various reactivity addition times.

It is interesting to note here that as the reactivity addition time increases beyond 40-50 ms, the initial peak maximum fuel temperature decreases. This decrease begins to occur at a larger reactivity addition time than the beginning of the decrease in peak system reactivity seen in Figure 47.

5.6. Impact of Initial Reactor Power Level

When a LRRA does not occur rapidly enough to approximate a step reactivity addition, the initial reactor power level has an impact on certain reactor response parameters. In this discussion, the initial reactor power is presented in units of %FP, corresponding to a percentage of full power, which is 2.39 MW for the ACRR. The initial reactor power level for the LRRAs examined so far has been 0.05 %FP (~1.2 kW).

Figure 62 and Figure 63 show the reactor power pulses resulting from a $3.50 LRRA with initial reactor power levels varying from 5E-2 %FP (0.05 %FP) to 5E-6 %FP (0.000005 %FP). The peak power of the pulse increases as the initial power decreases.

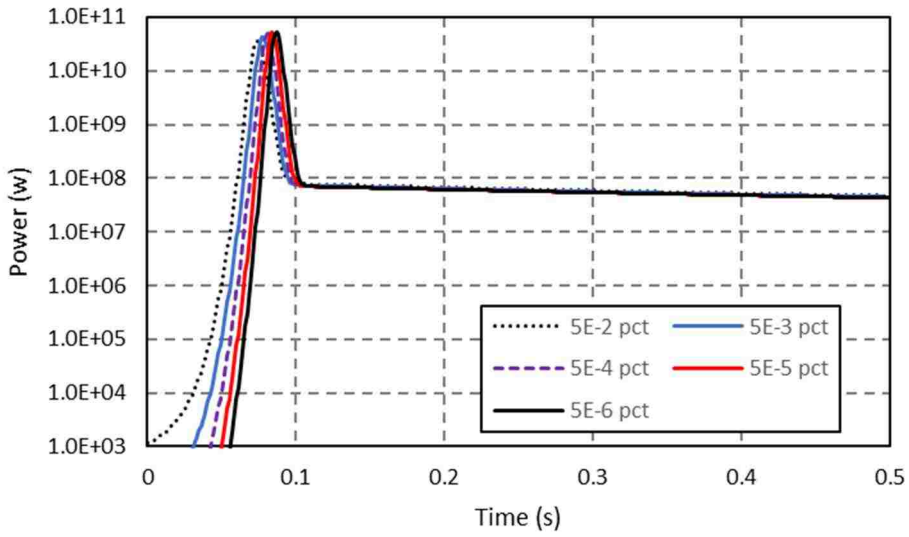

Figure 62. Reactor power pulse for a $3.50 reactivity addition with varying initial reactor power.

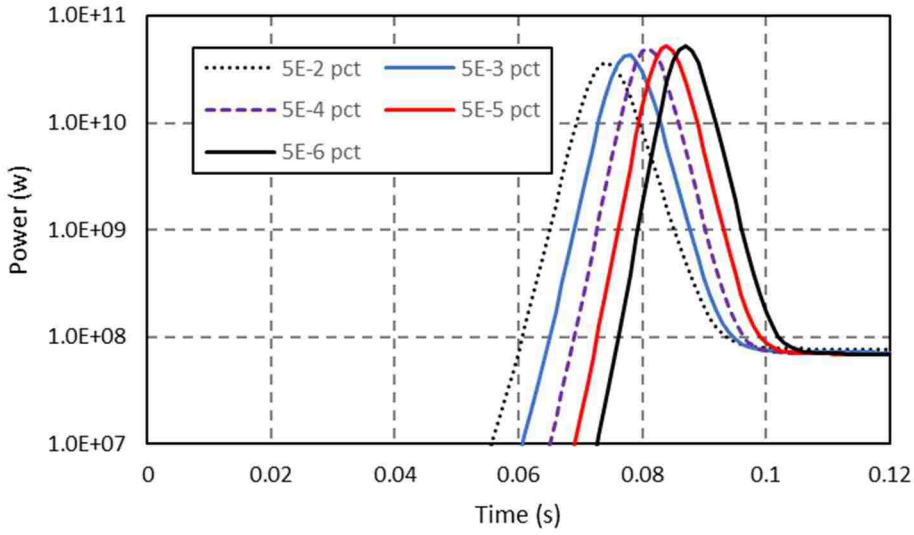

Figure 63. Closeup view of reactor power pulses with varying initial reactor power.

Figure 64 shows the trend of the peak reactor power for the $3.50 LRRA with initial reactor power levels varying from 1.0E-7 %FP (0.0000001 %FP) to 10 %FP. The peak power of the pulse is seen to increase to a plateau as the initial power decreases from 0.05 %FP. Thus, decreasing the initial reactor power of the LRRA is equivalent in effect to decreasing the reactivity addition time.

While the peak power decreases as the initial power increases, we see that at ~5 %FP (~120 kW) the peak power begins to increase again. An initial power of 120 kW is only ~0.0004% of a peak power on the order of 30 GW, which should be negligible from a Nordheim-Fuchs model perspective. However, as the initial power increases, so does the initial fuel temperature, and the magnitude of the Doppler feedback coefficient decreases as fuel temperature increases. The resulting impact is that a higher peak power is needed to produce a higher temperature rise needed to offset the decreasing Doppler feedback.

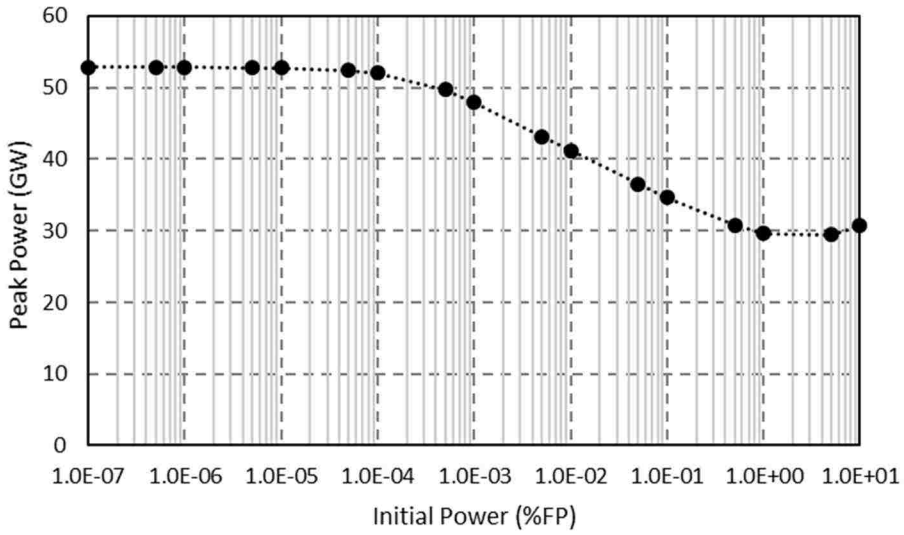

Figure 64. Peak reactor power achieved for a $3.50 pulse for various initial powers.

Figure 65 shows the trend of the initial peak maximum fuel temperature for the \$3.50 LRRA with varying initial reactor power. The initial peak maximum fuel temperature is seen to increase to a plateau as the initial power decreases from 0.05 %FP. While the initial peak maximum fuel temperature decreases as the initial power increases, we see that at ~1 %FP (~24 kW) the initial peak maximum fuel temperature begins to increase again. This is consistent with the previous discussion of the effect on peak power. Note that Fig. # also shows that the relatively steep increase in the initial peak maximum fuel temperature beginning at ~1 %FP is mostly due to the initial temperature of the fuel, since the change in the initial peak maximum fuel temperature does not increase as sharply.

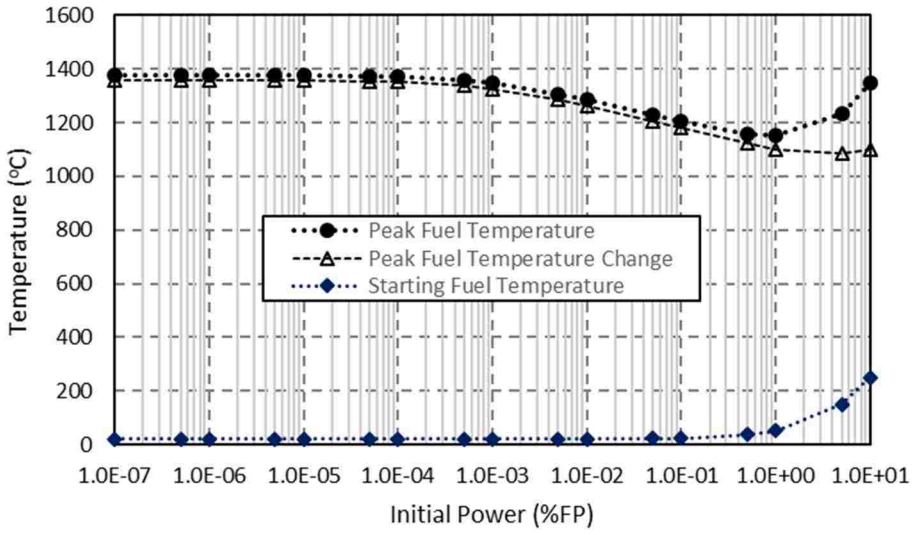

Figure 65. Initial peak fuel temperature achieved for a \$3.50 pulse for various initial powers.

5.7. Discussion of Safety Analysis Implications

The response of a natural circulation cooled research reactor to a large rapid reactivity addition (LRRA) is the production of a reactor power pulse. This of course assumes a strong, rapid, negative reactivity feedback mechanism to turn the reactor power excursion, and thus produce a "pulse." Typically, this mechanism will be the Doppler feedback reactivity associated with the parasitic absorption of neutrons by ^{238}U as its temperature increases. The primary goal of the safety analysis will be to determine reactivity addition limits which ensure that the reactor fuel will be able to "accommodate" the energy released during the reactor power pulse with an acceptable temperature rise.

Determination and enforcement of reactivity addition limits is preferred because the action of reactor scram after a certain monitored parameter (e.g., power, temperature, etc.) is exceeded will most likely be too late. With the ACRR, for example, the pulse width of reactor power pulse can be on the order of a few milliseconds. Thus, the pulse event would be over by the time a high power condition was detected, the scram signal processed, and the scram action initiated. By this time the majority of the energy of the power pulse will have been deposited in the fuel. The only manner by which the fuel may "accommodate" the near adiabatic heating of the power pulse is by its specific heat capacity.

When performing the safety analysis, an analyst would typically desire to assume a sufficiently small pulse reactivity addition time, so that the full reactivity addition occurs before appreciable reactivity feedback comes into play. This would ensure that the calculated peak fuel temperature reaches its maximum potential value, and provides

conservative predicted maximum fuel temperatures for comparison to allowable fuel temperatures.

A Nordheim-Fuchs approach could be used to compute such results, since it is based on an assumed step reactivity addition. However, if the actual reactivity addition system cannot physically achieve such a short addition time, then Figure 49 illustrates how the Nordheim-Fuchs predictions may be overly conservative for larger reactivity additions. A more sophisticated analysis tool (such as the code used in this dissertation) would need to be employed to avoid unnecessarily limiting the reactor's performance because of an over-conservatism in predicted maximum fuel temperature.

For the reasons noted earlier, a reactor scram system is generally considered ineffective for LRRAs. A reactor scram could be used, however, to reduce the total energy yield (i.e., the sum of the pulse energy yield and the delayed neutron tail energy yield) and the peak post-pulse fuel temperature. An added benefit is that a reactor scram would avoid reliance upon operator action to terminate reactor operation after the LRRA.

If a reactor power scram were to be used in this capacity, care must be taken in selecting the setpoint. It would presumably be desirable to set the power scram high enough to accommodate normal operations (e.g., normal pulse operations). However, as seen in Figure 46, the peak power of the pulse does not follow the "expected" behavior for rapid reactivity additions where the time-to-peak approaches the reactivity addition time (above ~$3 for the ACRR examined herein). For a reactor power scram setpoint of 60 GW, for example, no scram actuation would occur for reactivity additions below ~$5, according to Figure 48, even though a Nordheim-Fuchs model approach would suggest that a scram would occur at ~$3.70.

The Nordheim-Fuchs model provides the insight that the peak power is inversely proportional to the neutron generation time. Thus, a change in the neutron generation time (e.g., due to the presence of an experiment and/or experiment fixture in the reactor core) will have an impact on the peak reactor power resulting from an LRRA. This, in turn, would have an impact on the effectiveness of a reactor power scram setpoint.

A similar implication arises with the selection of an energy yield scram setpoint. A reactor power energy yield setpoint of 500 MJ, for example, would not be actuated until sometime after the pulse was over for reactivity additions up to, and beyond \$6 according to Figure 49. One would need to factor in the *total* energy yield to determine at what time *after* the pulse that the total energy yield would reach the 500 MJ setpoint, and determine whether that delay is acceptable.

The use of a reactor period trip might also be considered. The reactor period (the reciprocal of the fractional rate of change of the power) would be monitored, and a scram would be initiated if the period fell below the setpoint. This type of reactor trip would function early in the reactor transient, as the minimum reactor period occurs at the time that the peak system reactivity is achieved. Again, one must take into account the impact of the actual reactivity addition time when selecting a setpoint.

The impact of the initial reactor power level on the response to a LRRA was seen in Figure 65. The initial peak fuel temperature at first decreases as the initial reactor power increases, but eventually begins to increase. This behavior is due to the increase in the initial equilibrium fuel temperature that is associated with an increased initial equilibrium power level. From these considerations, a pulse-from-high-power accident might be better thought of as a pulse-from-high-temperature accident.

5.8. Conclusions

An overview of the reactor power, pulse timing characteristics, and the initial temperature rise response characteristics of a natural circulation research reactor to a large rapid reactivity addition (LRRA) has been presented. The peak power response was seen to follow a Nordheim-Fuchs model trend (i.e., proportional to the square of the prompt reactivity addition) for reactivity additions up to ~$3. After this point, a Nordheim-Fuchs model significantly overpredicts the peak power response. This behavior was determined to be an impact of the finite reactivity addition time (80 ms for the investigations here), which allowed for Doppler fuel temperature reactivity feedback to overtake the reactivity addition.

The maximum fuel temperature was seen to incur an initial peak increase due to the near-adiabatic heating induced by the reactor power pulse. The initial peak fuel temperature, as well as the energy release (i.e., integrated reactor power), were seen to follow a Nordheim-Fuchs model trend. As with the peak power response, there is a point at which the Nordheim-Fuchs model will significantly overpredict the temperature increase and energy yield.

The use of a Nordheim-Fuchs model for safety analysis purposes was seen to be acceptable, given that the predictions will be either reasonable or conservative. However, establishing reactivity controls based on Nordheim-Fuchs analyses could unnecessarily limit reactor performance capabilities. Also, any plans to utilize peak power, energy yield, or reactor period as trip setpoints should consider the impact of a finite reactivity addition time to avoid unnecessarily limiting reactor performance capabilities.

6. Large Rapid Reactivity Addition Events: Thermal-Hydraulic Response

6.1. Introduction

During a large rapid reactivity addition, such as a pulse operation (or accident) in a research reactor, the reactor power will increase rapidly, resulting in a rapid temperature rise within the fuel. Since there is little time for significant heat transfer to occur during the pulse, the energy deposition during this time is essentially adiabatic. After the initial power pulse, the reactor power will decay slowly at a relatively high power level (driven by the delayed neutron precursors produced during the pulse). The fuel temperature continues to increase, while heat transfer within the fuel and outward from the fuel to the coolant is established.

In the fuel element coolant channel, the initial coolant flowrate is very low, since the initial reactor power is very low. During the pulse, energy is directly deposited into the coolant due to neutron and gamma interactions, causing an initial rise in the coolant temperature. Subsequently, heat will be transferred from the fuel element to the coolant, causing a much greater increase in the coolant temperature. The increase in coolant temperature causes a buoyancy force imbalance, which leads to an increase in the flowrate of the channel. Eventually, an equilibrium power level is reached in the reactor, along with an equilibrium coolant flowrate and axial temperature distribution.

6.2. Overview of the Thermal-Hydraulic Response for the ACRR

To evaluate the thermal-hydraulic response of a research reactor to a large rapid reactivity addition (LRRA), we will first consider a $3.00 reactivity addition to the ACRR. This is the same $3.00 pulse considered in Chapter 5, which resulted in a 29.7 GW peak power, peaking at t = 81 ms, with a FWHM pulse width of 7.4 ms. Subsequent to the power pulse, the reactor power decays over time from an elevated power level (~70 MW) due to the presence of delayed neutron emitting fission products produced during the power pulse, and eventually reaches an equilibrium power level of 1.34 MW. Refer to Figure 42 and Figure 43 to see power history plots for the pulse.

For the thermal-hydraulic response, we are interested in the temperature history of the fuel. The initial temperature response to the pulse is a near adiabatic heating of the fuel. This is depicted in Figure 66, which plots the maximum temperature within the fuel element independent of radial or axial location. This maximum fuel temperature reaches an initial peak value of 1060°C. One may estimate the maximum expected adiabatic temperature rise, accounting for core radial, element axial, and element radial power peaking factors, to be ~1155°C. This is slightly higher than the result from the code, indicating that the pulse is not "fast enough," and that some degree of heat transfer does occur before the peak temperature is reached. On the other hand, the result also shows that the pulse produces an initial fuel heating that is very close to adiabatic.

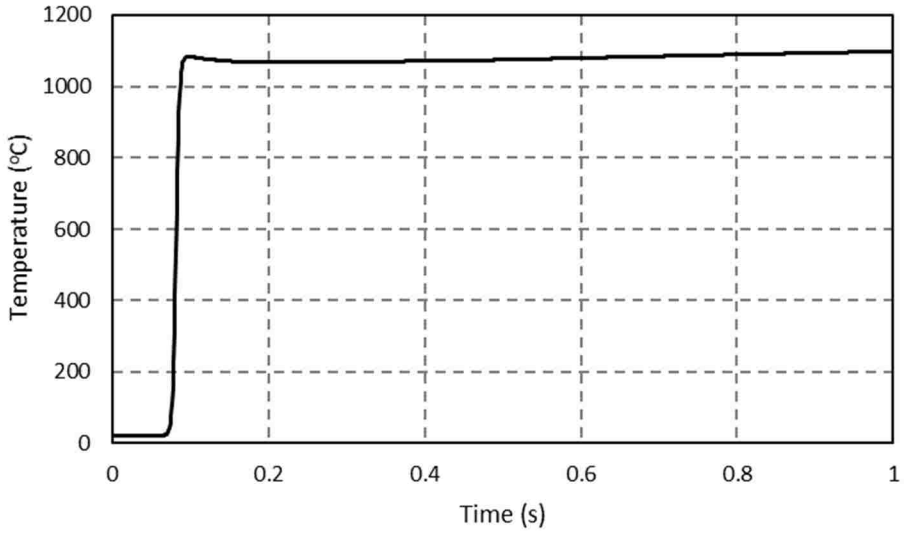

Figure 66. Initial maximum fuel temperature history for a $3 rapid reactivity addition.

After the initial, near-adiabatic, fuel heating, the fuel temperature begins to rise again, but at a slower rate (since the post-pulse reactor power is now primarily due to fissions caused by delayed neutrons). In Figure 67, we see that the maximum fuel temperature rises again to a peak value of 1253°C, at 21.1 s.

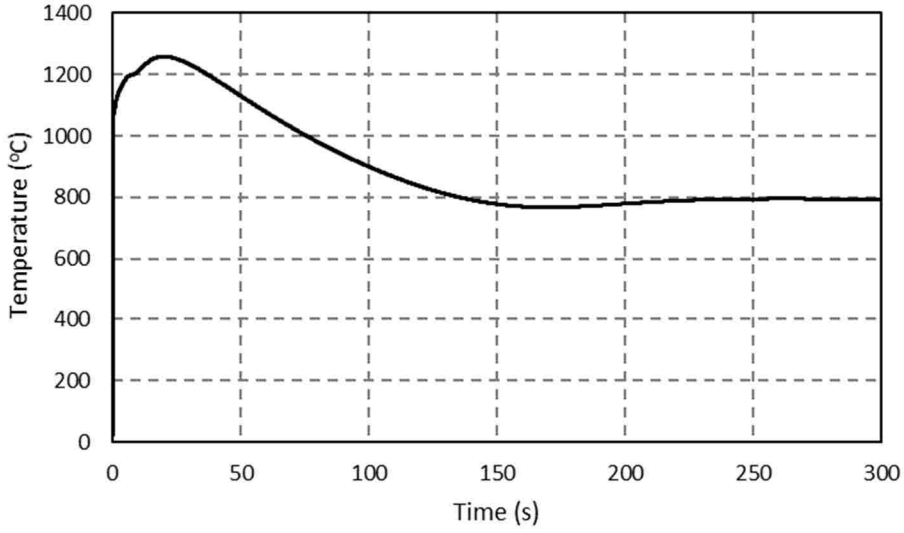

Figure 67. Maximum fuel temperature history for a $3 rapid reactivity addition.

The peak occurs when the natural circulation flow has stabilized in the coolant channel so that the rate at which the coolant flow carries away energy matches the convection heat transfer rate from the fuel element to the coolant. This is shown in Figure 68 below.

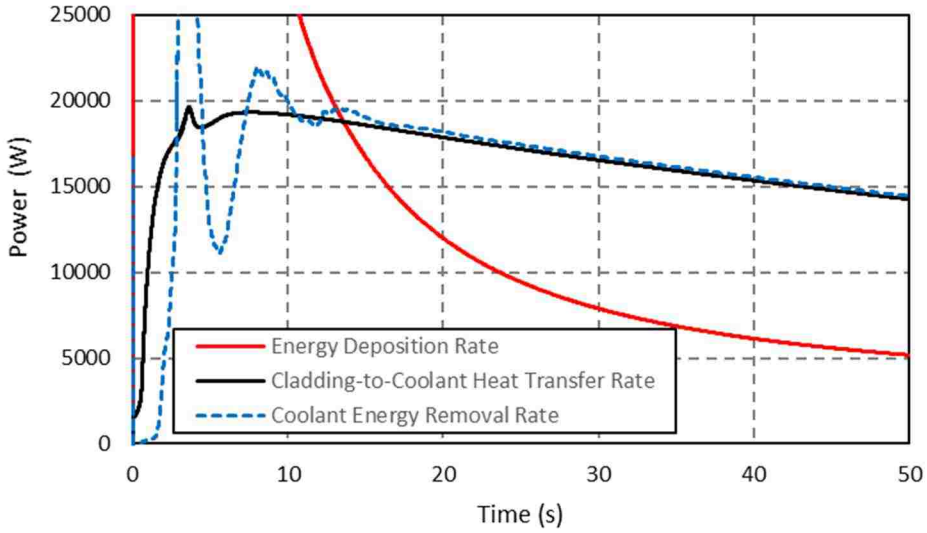

Figure 68. Initial equilibrium between cladding heat transfer rate and coolant energy removal rate.

Following the peak, there a slow decline in temperature (see Figure 67). During this decline, the energy deposition rate into the fuel (fission heating) is less than the heat transfer rate to the coolant. As noted above, the energy removal rate of the coolant has already achieved equilibrium with the heat transfer rate from the element. Eventually, all three energy deposition/transfer rates achieve an equilibrium, as shown in Figure 69 below. This establishes equilibrium fuel temperatures, and the maximum fuel temperature within the fuel at equilibrium is ~800°C (refer back to Figure 67).

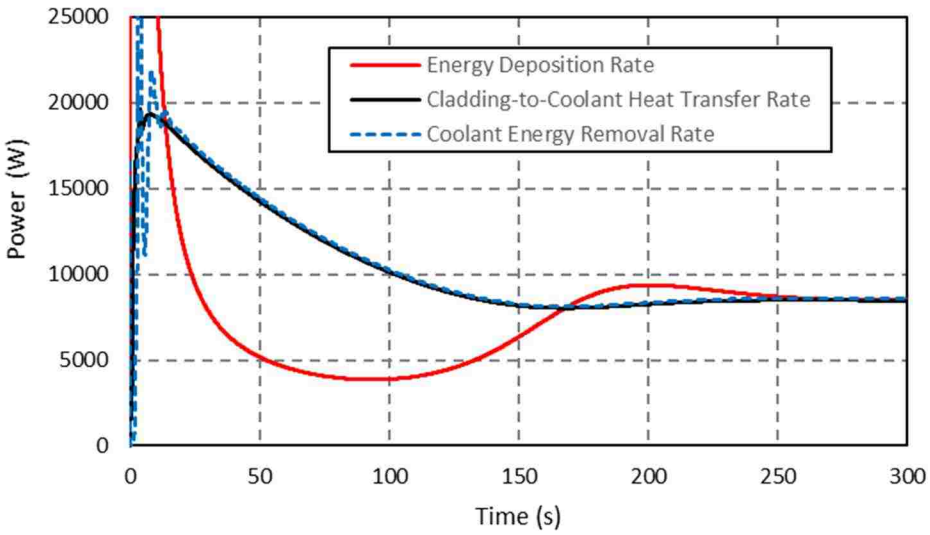

Figure 69. Final equilibrium between energy deposition rate, cladding heat transfer rate, and coolant energy removal rate.

The radial temperature distribution within the fuel during the near-adiabatic initial fuel heating follows the shape of the fission energy deposition distribution, which is an input (determined using the MCNP neutron transport code) to the Razorback code. The fission energy deposition profile is peaked at the outer edge of the outer fuel pellet, decreasing monotonically to a minimum at the inner radius of the inner pellet. Figure 70 shows the fuel temperature distribution across the inner and outer fuel pellet at a time of 0.120 s (~23 ms after the initial peak in fuel temperature occurs), and the general shape of the fission energy deposition profile can be seen. Note, however, the downward slope at the outer edge of the outer fuel pellet, indicating the impact of heat transfer away from the fuel toward the niobium cup. After the system has achieved equilibrium, the temperature distribution across the fuel pellets (also shown in Figure 70) is seen to be the familiar center-peaked radial profile. The relative "flatness" of the profile is due to the relatively high thermal conductivity of the BeO-UO_2 fuel.

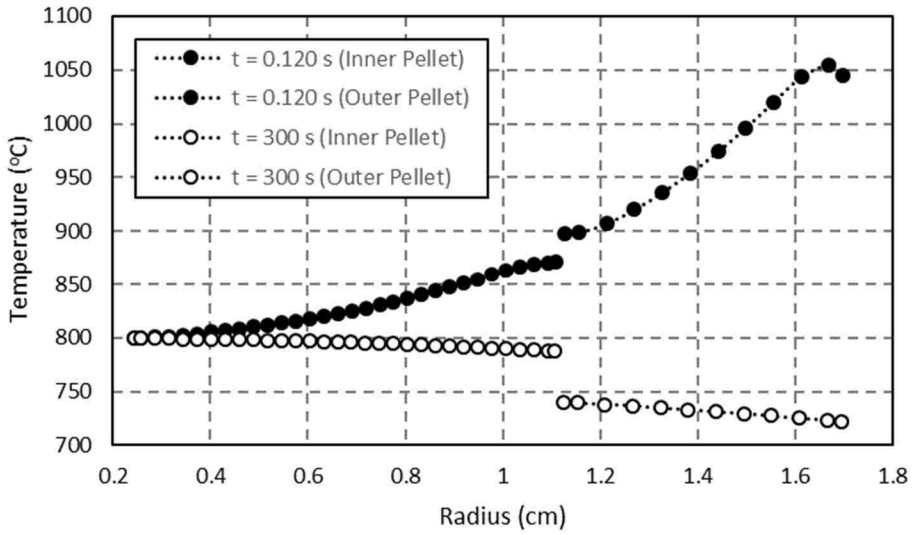

Figure 70. Comparison of initial pulse fuel temperature profile with the equilibrium profile.

For the thermal-hydraulic response, we are also interested in the conditions within the fuel element's coolant channel, such as the temperature, density, and mass flowrate. The temperature and density are especially important because of their contributions to reactivity feedback. As with the fuel, the initial temperature response of the coolant to the pulse is a near adiabatic heating. This is depicted in Figure 71, which plots the coolant temperature distribution along the axial length of the coolant channel at t = 0.1 s (~3 ms after the initial peak of the fuel temperature). Note that the fuel region begins at ~12 cm axial location, and extends to ~64 cm. The Razorback code implements an axial direct energy deposition profile in the coolant to simulate the heating of the coolant by neutron scattering and gamma ray absorption and scattering. The axial energy deposition profile in the coolant is assumed to be the same as that for the fuel. As with the fuel the initial

near-adiabatic heating of the coolant results in a coolant temperature profile which reflects the energy deposition profile. The maximum coolant temperature is ~50°C.

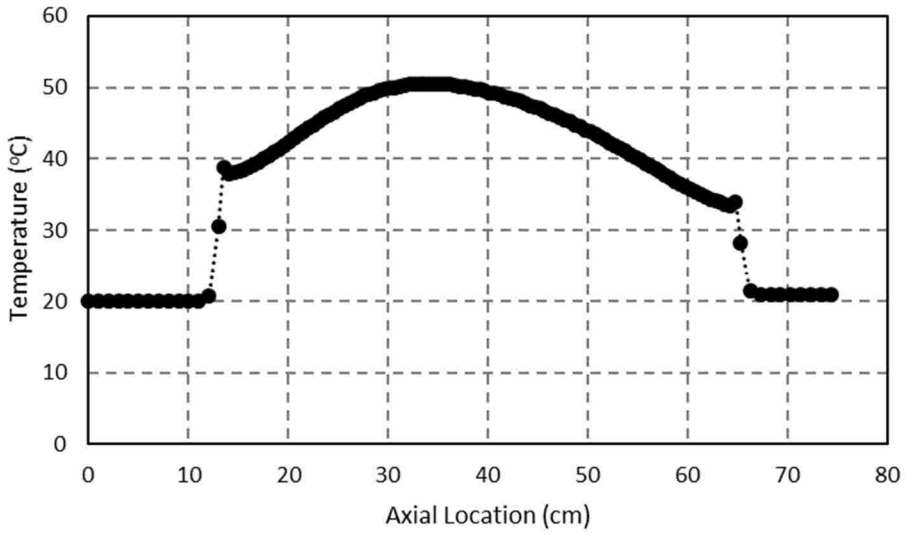

Figure 71. Initial axial coolant temperature profile following the pulse heating.

As the coolant is heated in a near-adiabatic manner, it begins to expand. This expansion occurs in both an upward and downward direction along the axial coolant channel. If we examine the mass flowrate at the inlet and outlet of the coolant channel, shown in Figure 72, we see that a significant increase in the mass flowrate which resembles the shape of the reactor power pulse. Likewise, we see a similar mass flowrate "pulse" at the channel inlet, but in the opposite direction (i.e., out of the channel). While the rapid expansion of the coolant in response to the power pulse produces significant mass flowrates, the duration of the pulse is short (~10 ms FWHM). Thus, little total coolant mass is actually moved out of the channel (upward and downward) during this expansion.

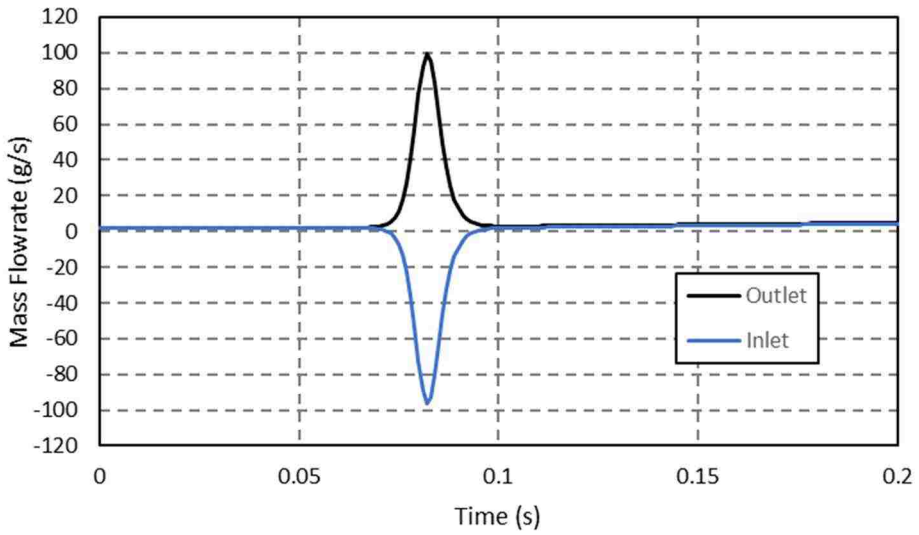

Figure 72. Initial coolant mass flowrate response to the pulse heating.

The expansion of the coolant in the channel implies an increase in the local pressure of the coolant along the channel. In Figure 73, we see the initial pressure distribution in the channel to be a linear distribution. The pressure decreases from ~22 psia at the inlet of the coolant channel to ~21 psia at the top of the coolant channel. This is the expected "ρgH" pressure gradient due to the change in elevation from the bottom of the channel to the top of the channel. The magnitude of the pressure is set by the depth of water above the coolant channel, since the ACRR is an open pool reactor, and the atmospheric pressure at the top of the pool water.

Also shown in Figure 73 is the distribution at t = 0.08 s, which is just before the peak reactor power occurs (0.0814 s). At the axial peak of the t = 0.08 s pressure distribution, the pressure has increased ~1.7 psi.

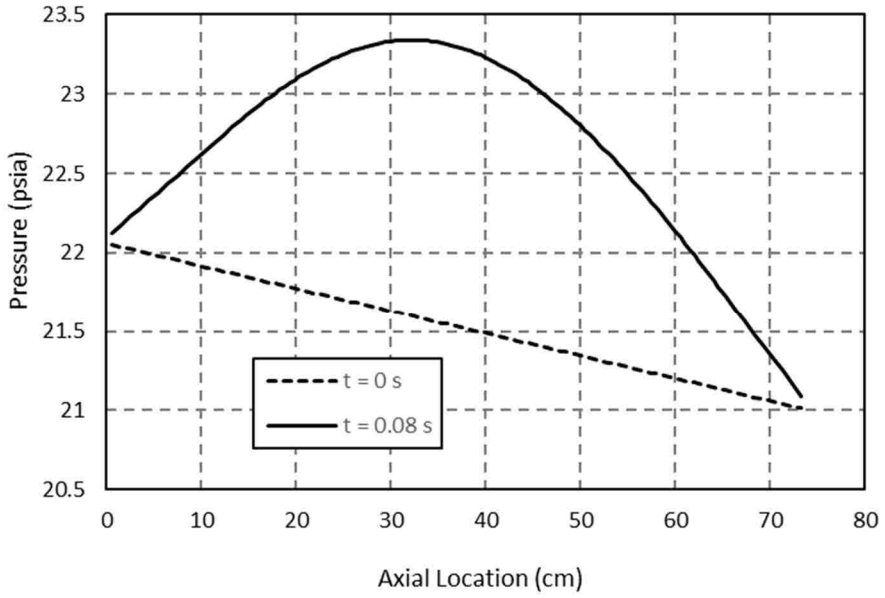

Figure 73. Initial axial coolant pressure profile following the pulse heating.

Viewed from different perspective, Figure 74 shows the time history of the pressure at several axial locations along the channel. The pressure increase is seen to depend upon the axial location in the channel as shown above. However, we also see that there is an associated pressure decrease at each location, occurring shortly after the initial pressure pulse. At the lower end of the channel, the pressure drops below the pressure at the channel inlet. At the other channel locations shown in Figure 74, the pressure drops below that of the channel exit. This reversal in the pressure gradient in the channel, caused by the expansion due to the heating of the coolant, provides the restoring force to halt the coolant expansion. Figure 75 shows the channel pressure distribution at various times before and after the peak of the power pulse. Note that by t = 0.10 s, the pressure distribution has returned to its initial linear form.

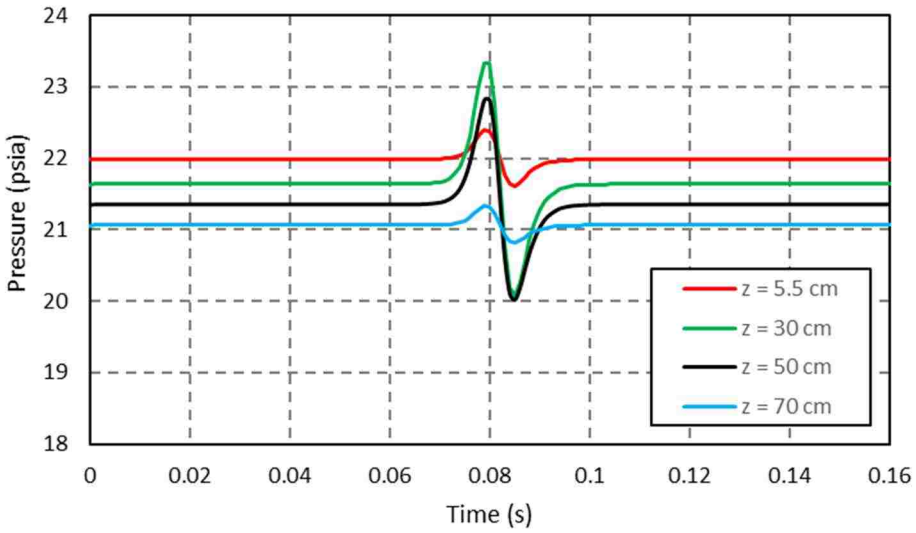

Figure 74. Coolant pressure history vs. axial location due to initial pulse heating.

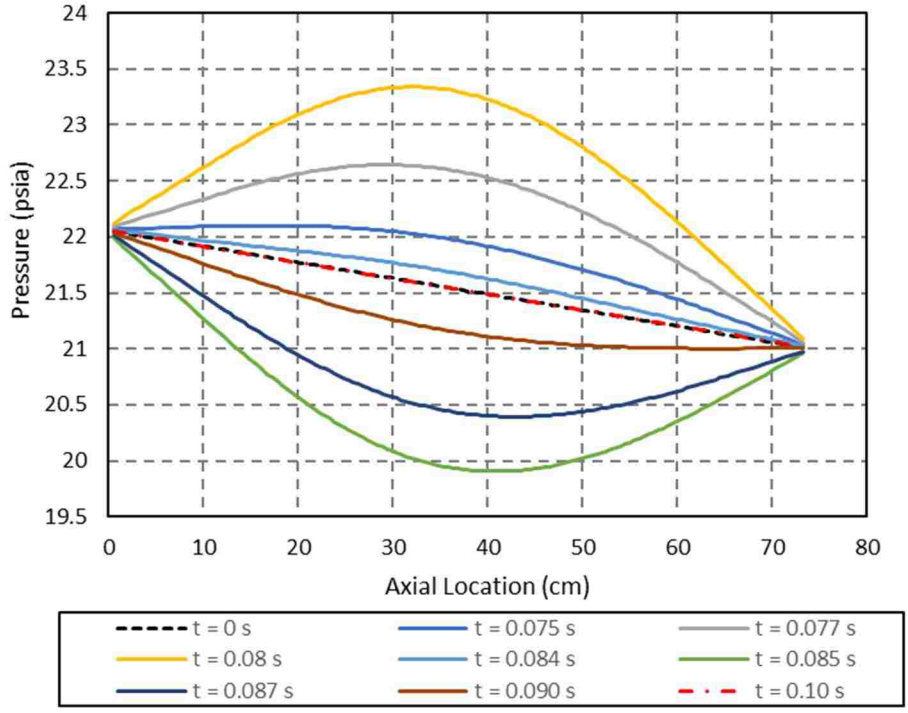

Figure 75. Time variation of the coolant axial pressure profile during the pulse heating.

The mass flux (flowrate per unit area) during the initial heating of the coolant also exhibits an axial distribution in response to the changing pressure distribution shown above. Figure 76 shows the mass flux distribution corresponding to the times in Figure 75. The acceleration of the coolant from approximately the axial center of the channel is evident. Also, just as the pressure distribution returned to essentially its initial state shortly after the time of the power peak, the mass flux returns to its near quiescent initial profile.

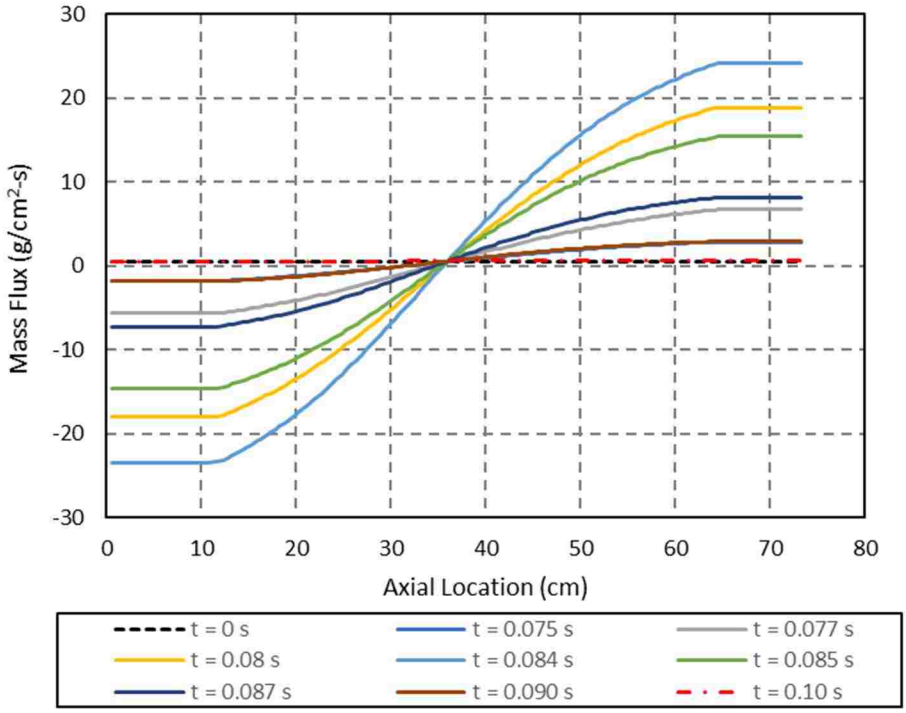

Figure 76. Time variation of the coolant mass flux profile during the pulse heating.

After the initial heating and expansion of the coolant, the new density distribution of the coolant begins to produce a buoyancy force-driven natural circulation flow. As seen in Figure 77, the mass flux increases almost linearly with time at nearly the same rate at all points along the channel. During this time the coolant continues to be heated directly by

neutron/gamma interactions, but the heat transfer from the fuel element cladding will become increasingly more significant with time.

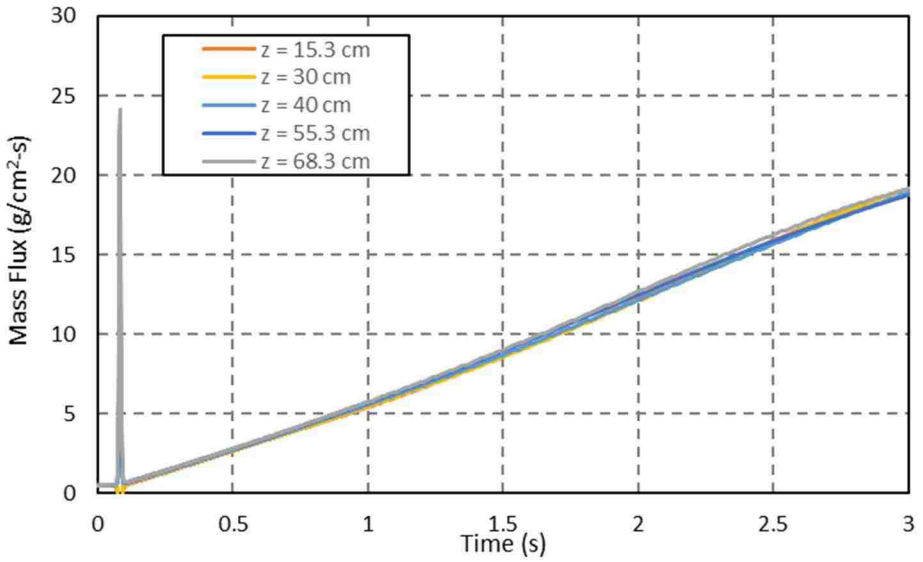

Figure 77. Early evolution of the coolant mass flux at various axial locations.

The increase in heat transfer rate to the coolant from the element cladding affects the coolant channel temperature profile. Figure 78 shows the evolution of the coolant temperature profile with time over the first three seconds of the transient. The shape of the initial temperature profile is somewhat maintained at first, but by t = 2.0 s, the profile has changed significantly with the increase in heat transfer rate and increasing natural circulation flowrate. The peak of the profile moves from the approximate center of the channel upward toward the exit of the channel. Ultimately, we would expect an equilibrium profile of a monotonic increase in temperature along the length of the channel. We note here the "ripples" seen in the lower portion of the channel as the temperature profile evolves. It is unclear, as yet, whether these are the result of numerical anomalies

or the impact of the expansion of the coolant near the center of the channel as the cladding-to-coolant heat transfer rate is introducing more energy into the evolving flow.

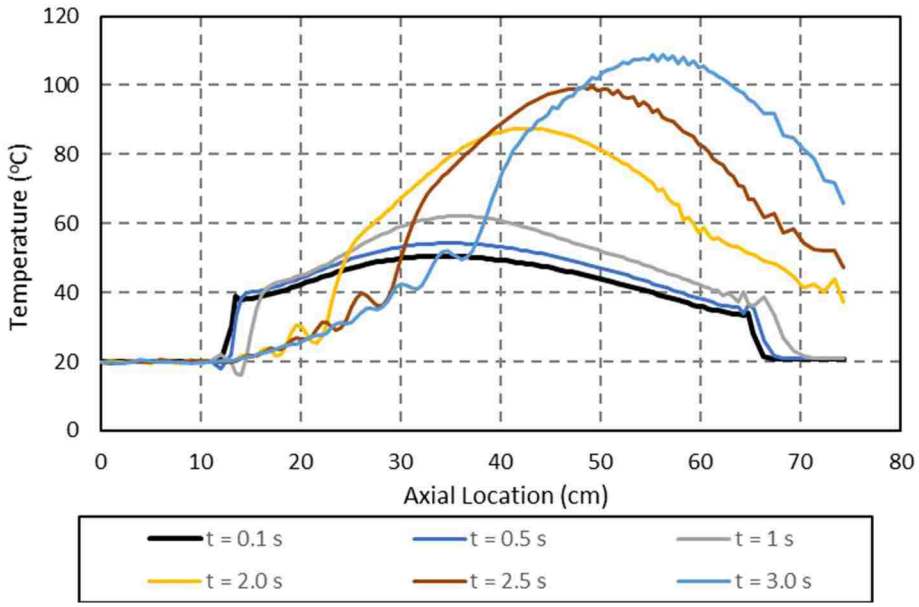

Figure 78. Evolution of the coolant channel temperature profile after the pulse.

The peak coolant temperature has begun to approach the saturation temperature (~110°C for pressures in the core channel) at t = 3.0 s. Figure 79 shows the coolant channel temperature profile over the next 0.5 s, and one can see the flattening of the profile near the end of the channel as the temperature "saturates," which is indicative of bulk boiling of the coolant.

Figure 80 shows the location of the upper and lower extents of the boiling region in the channel. The boiling begins at ~58 cm, and the region begins to extend upward in the channel from there. The lower extent of the boiling region then begins to move upward in the channel until the vapor region eventually exits the channel.

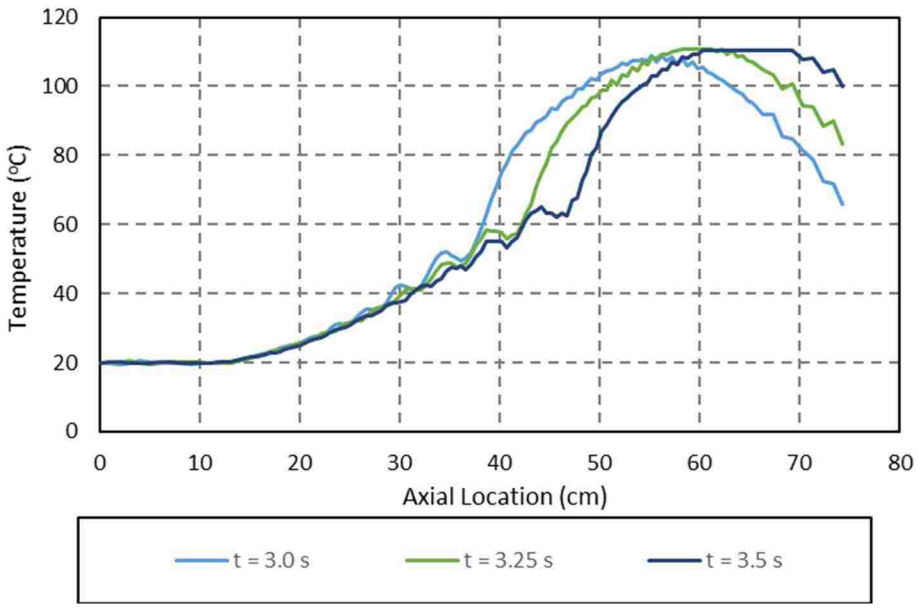

Figure 79. Evolution of the coolant channel temperature profile when boiling occurs.

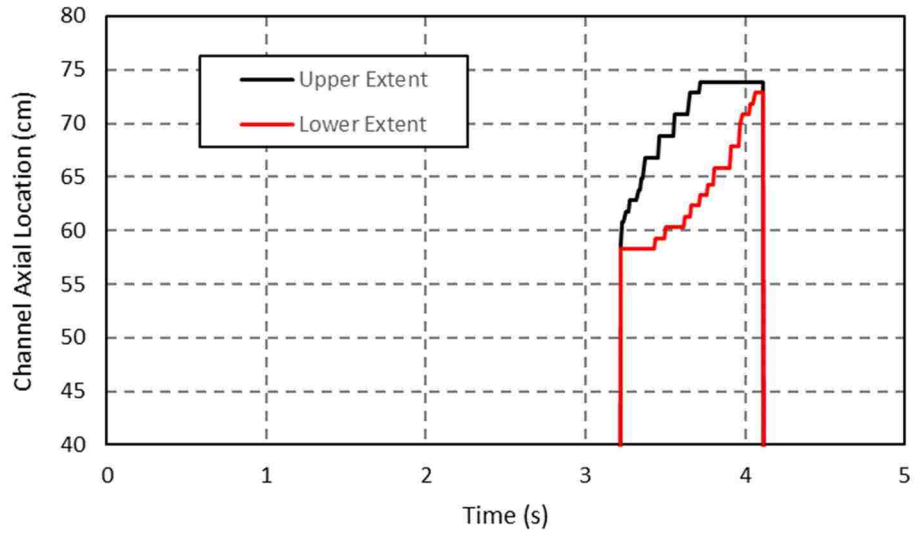

Figure 80. Upper and lower axial extent of the boiling region after the pulse.

If we examine the void fraction results near the end of the channel for this time span, we see in Figure 81 that bulk boiling indeed is occurring. The boiling begins at ~58

cm into the channel, which is ~6 cm below the end of the fuel region of the element. As Figure 81 shows, the void fraction grows as it moves up the channel, but then begins to decrease again before exiting the channel. The time duration of this instance of boiling in the channel is seen to be < 1 s, and no additional boiling instances occur.

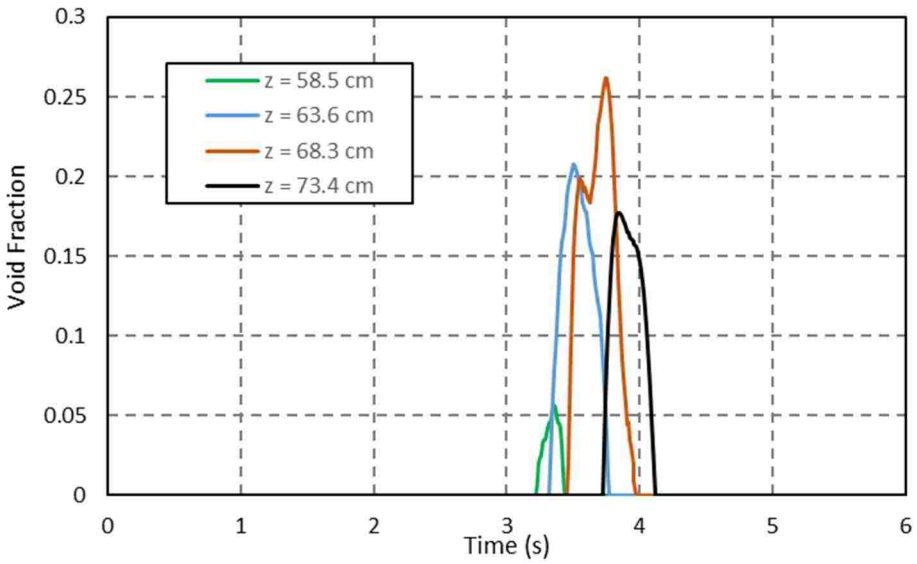

Figure 81. Evolution of the boiling void fraction at various axial locations.

The mass flux in the channel is impacted by the formation of vapor voids near the end of the channel. Figure 82 shows the mass flux at various locations along the channel. The mass flux at each channel location is approximately the same just before the boiling begins. When the vapor begins to form at 3.25 s, the mass flux below the point where boiling begins (~58 cm) is decelerated, while the mass flux above this point accelerates significantly. At 3.5 s, the mass flux at z = 68.3 cm decreases (although clearly fluctuating) because the vapor region carries significantly less mass than the liquid region. The mass flux below the vapor region, however, begins to increase markedly, as the decrease in effective channel density induces a buoyancy mismatch. The increase in flow below the point of boiling both helps to force the void region out of the channel, and provides more

liquid to quench continued void formation. After the vapor has been forced out of the channel, the reduction in effective coolant channel density causes the mass flux to again decrease.

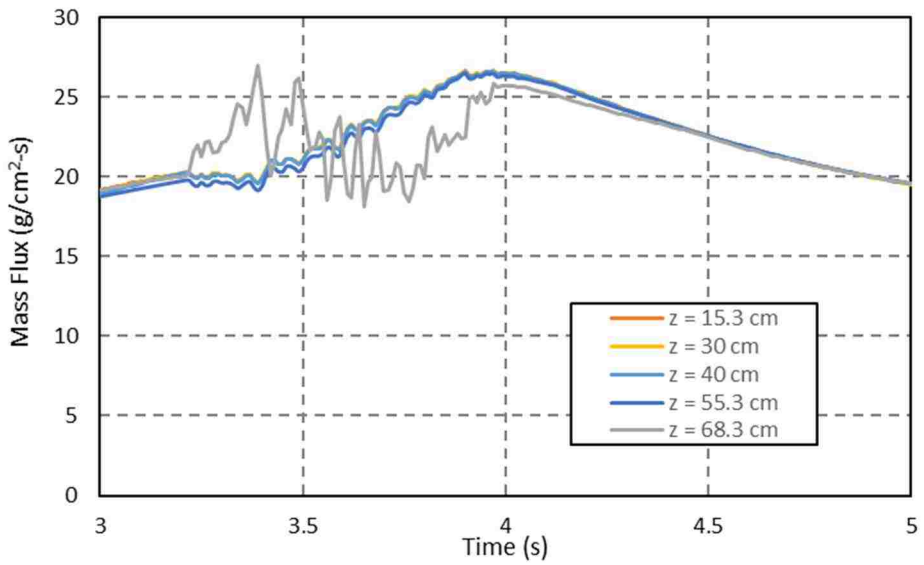

Figure 82. Evolution of the coolant mass flux during boiling at various axial locations.

As noted earlier, this is the only instance of boiling which is predicted to occur during the $3 pulse being examined. The temperature profile in the coolant channel now continues to evolve toward its equilibrium profile. This is shown in Figure 83. At equilibrium, the channel outlet temperature is 58°C, and the mass flowrate in the channel is 53 g/s.

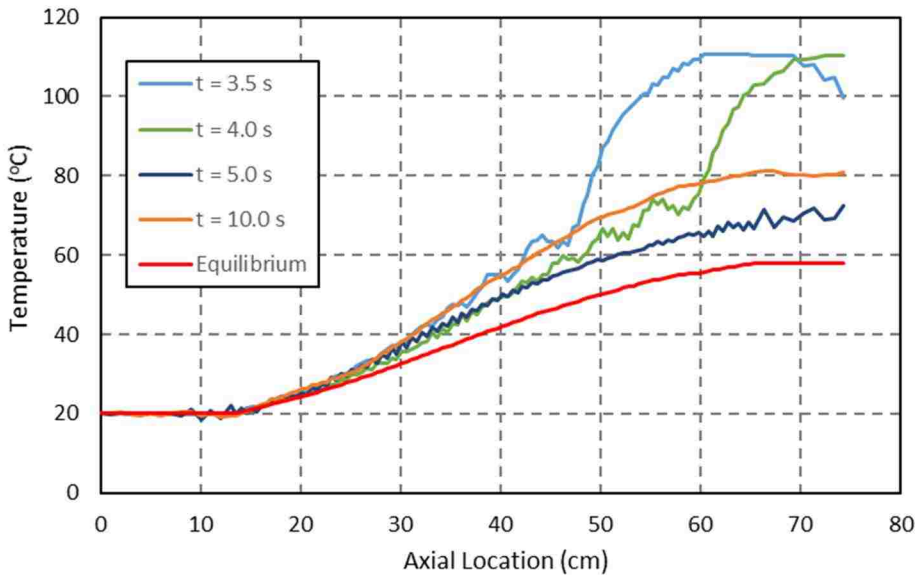

Figure 83. Evolution of the coolant temperature profile through and post-boiling.

Lastly, for the thermal-hydraulic response, we are also interested in the temperature of the fuel element cladding. The cladding is the primary barrier to release of radioactive fission products within the fuel element, and it is thus important to monitor its temperature. As with the fuel and coolant, the initial temperature response of the cladding to the pulse is a near adiabatic heating. The Razorback code implements an axial direct energy deposition profile in the cladding to simulate the heating of the cladding by neutron and gamma ray interactions. The axial energy deposition profile in the cladding is assumed to be the same as that for the fuel. Figure 84 shows the initial near-adiabatic heating of the cladding results in a cladding surface temperature profile which reflects this energy deposition profile at a time of 0.1 s (there is a small energy deposition in the cladding due to neutron/gamma interactions) . The maximum cladding surface temperature at this time is ~95°C. With this surface temperature below the coolant saturation temperature (~110°C), the heat transfer mechanism to the coolant is expected to be single phase

convection. As time progresses, heat transfer from the fuel to the cladding increases the cladding surface temperature above the coolant saturation temperature, and the cladding-to-coolant heat transfer mechanism shifts to subcooled boiling. This is a very efficient heat transfer mechanism, and it tends to maintain the cladding temperature below ~130°C. Prior to t = 3 s, there are some regions of the cladding surface where single phase heat transfer continues, but eventually, nearly the entire cladding surface has transitioned to subcooled boiling.

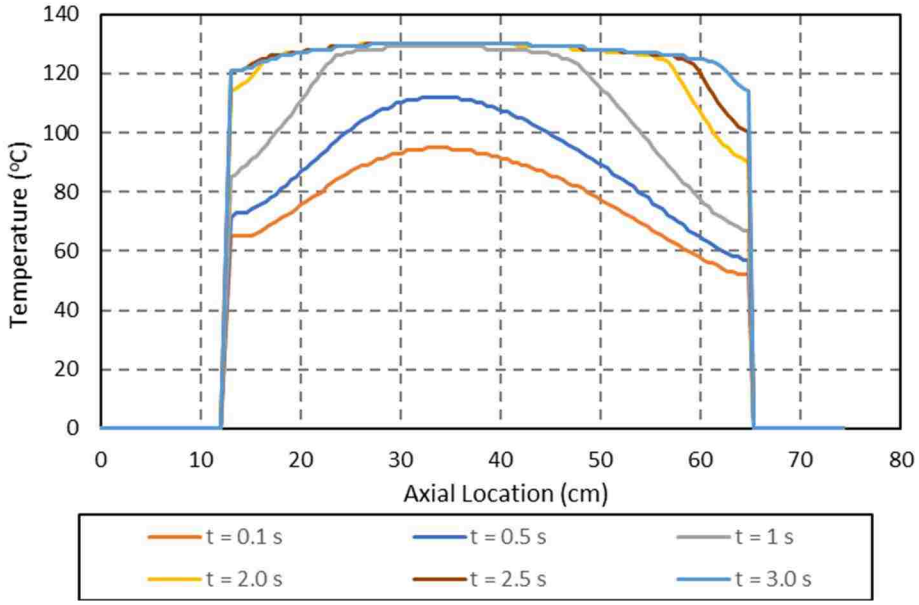

Figure 84. Early evolution of the cladding surface temperature.

Figure 85 shows the cladding surface temperature profile as it evolves over the remainder of the transient up to equilibrium. The subcooled boiling mechanism clearly remains active up to and into equilibrium, although the lower and upper portions of the channel trend back towards single phase convection.

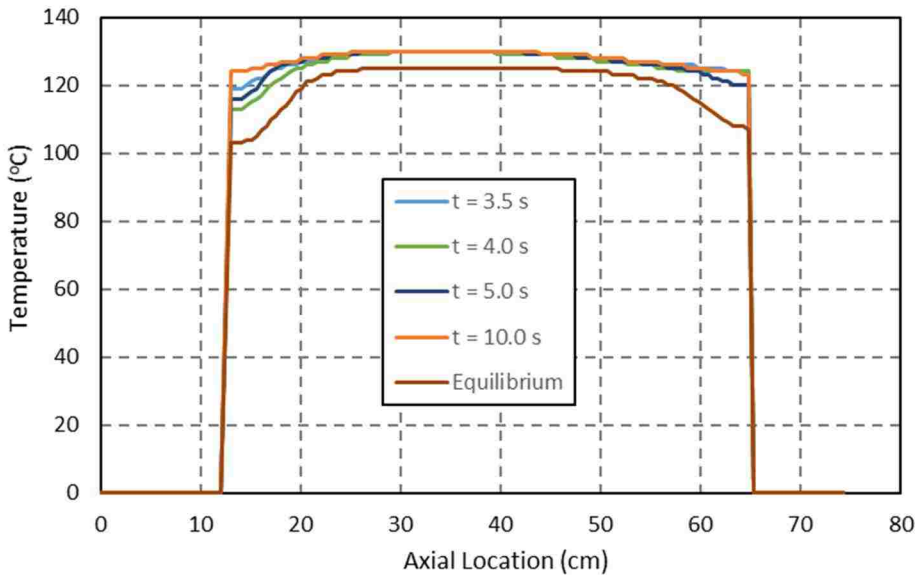

Figure 85. Long-term evolution of the cladding surface temperature.

6.3. Thermal-Hydraulic Response to Various Large Rapid Reactivity Additions

Having examined the various aspects of the thermal-hydraulic response of the ACRR to a $3.00 LRRA, we will now consider response trends for a range of LRRAs.

6.3.1. Fuel Response

As described earlier, except for relatively small prompt reactivity additions, there is an initial peak in the maximum fuel temperature due to the near-adiabatic heating of the reactor power pulse. Eventually, the maximum fuel temperature will peak again, as fuel heating continues and the coolant heat removal rate matches the heat transfer rate from the fuel. Figure 86 shows the peak fuel temperature as a function of the rapid reactivity addition.

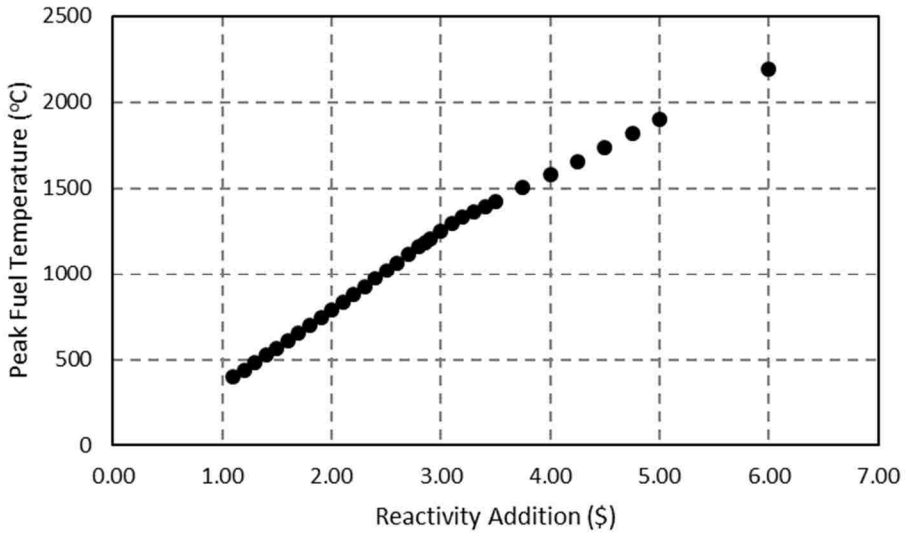

Figure 86. Variation of the peak maximum fuel temperature vs. reactivity addition.

Taking the peak maximum fuel temperature data plotted in Figure 86, we may develop an extrapolation. A linear fit of the data up to a $3 addition was obtained. This

resulting extrapolation is shown in Figure 87, and it represents the predicted peak maximum fuel temperature for what would effectively be a "step" reactivity addition.

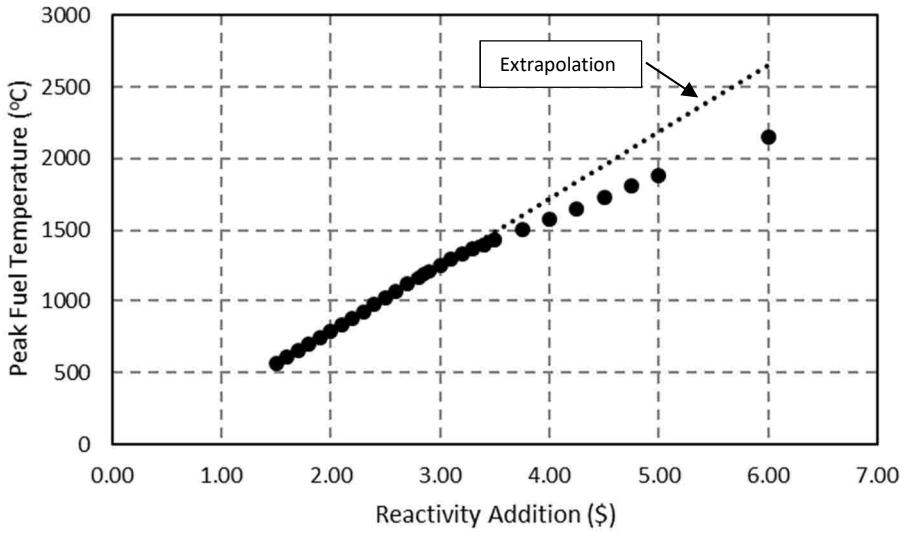

Figure 87. Extrapolation of the peak maximum fuel temperature illustrating the effect of the reactivity addition time.

The initial peak fuel temperature (due to the near-adiabatic heating of the initial reactor power pulse) may be subtracted from the ultimate peak fuel temperature described above to determine a post-pulse temperature rise. Figure 88 plots this post-pulse temperature rise as a function of reactivity addition. Below an addition of $1.90, there is no distinguishable initial fuel temperature peak, so only the post-pulse temperature rises for LRRAs ≥$1.90 are shown.

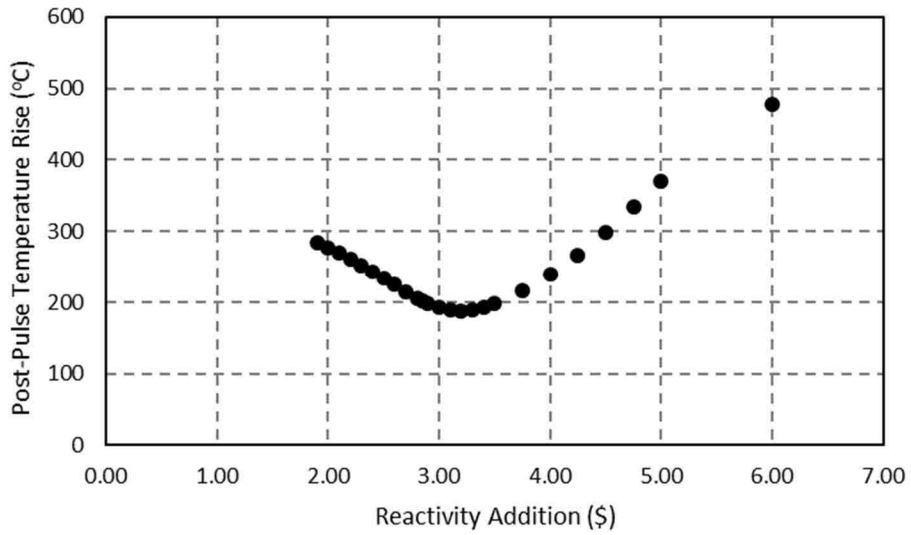

Figure 88. Post-pulse temperature rise following the initial pulse heating.

6.3.2. Coolant Response

Next, we will consider the trends in the response of the coolant to LRRAs. Several coolant parameters warrant consideration, such as the initial peak maximum coolant temperature, the peak pressure in the coolant channel, the peak maximum cladding temperature, and the peak maximum cladding surface heat flux. in the response of the coolant channel. In addition, it is important to determine the initiation of bulk boiling in the channel, and the extent and duration of the boiling. Lastly, we will consider the trends in the minimum critical heat flux ratio in the channel, because of its importance to determining the potential for cladding damage.

We begin with the peak maximum initial coolant temperature in the coolant channel resulting from the initial reactor power pulse, shown in Figure 89. The trend shows a discontinuity in the slope at a reactivity addition of ~$3.10. The trend, including the slope

discontinuity, is similar to that of the fuel temperature response. This is consistent with a dependence of the initial temperature rise upon the pulse energy yield.

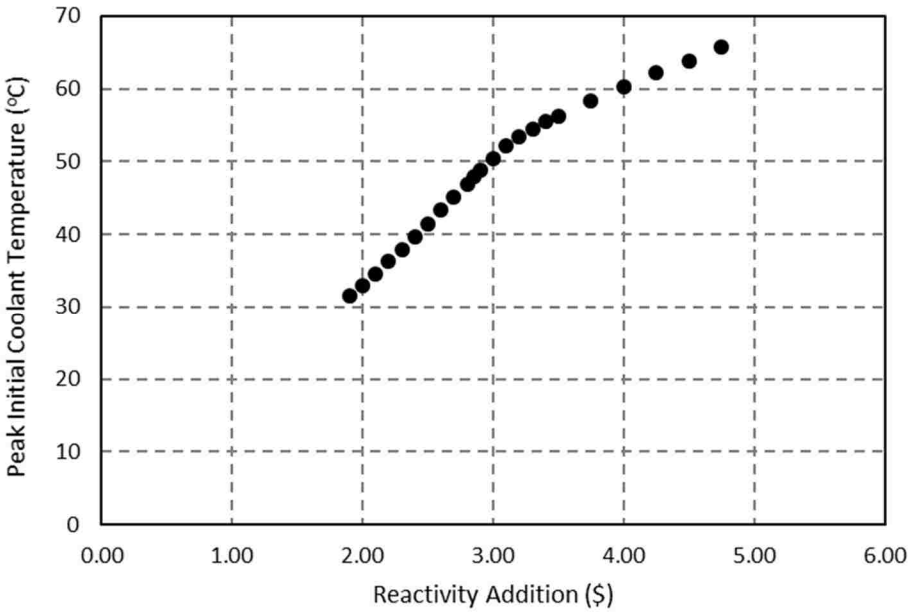

Figure 89. Variation of the initial peak maximum coolant temperature vs. reactivity addition.

Figure 90 shows the trend in the peak pressure as a function of reactivity addition. Up to an addition of ~$2.50, there is essentially no increase in the coolant pressure above the pressure at the channel inlet. After a reactivity addition of $2.50 the peak channel pressure begins to increase. At a reactivity addition of ~$2.80 a discontinuity in slope occurs, but the overall trend of increasing peak pressure continues. The peak pressure was observed to occur at the time of the reactor power peak, as opposed to the time of the initial peak in the fuel temperature.

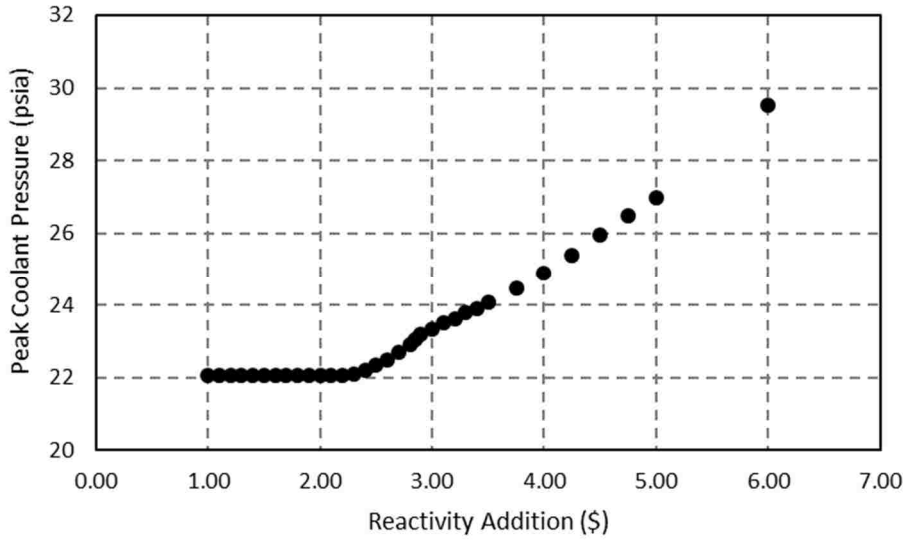

Figure 90. Variation of the peak maximum coolant channel pressure vs. reactivity addition.

The trend in the peak maximum cladding surface temperature is shown in Figure 91. There is a discontinuity in slope at $1.80. However, this is not a slope discontinuity related to the length of the reactivity addition time vs. a "step" reactivity addition. The discontinuity in slope here is due to the impact of the subcooled boiling heat transfer mechanism.

During the post-pulse transient, the maximum cladding surface heat flux will also reach a peak. Figure 92 shows the trend of this peak maximum cladding surface heat flux with the reactivity addition. The trend does exhibit a discontinuity in slope at ~$2.90.

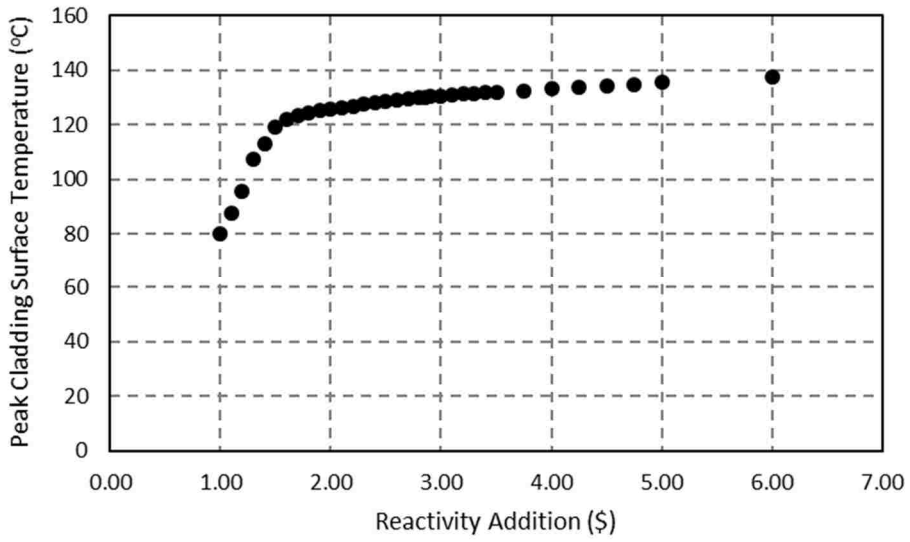

Figure 91. Variation of the peak maximum cladding surface temperature vs. reactivity addition.

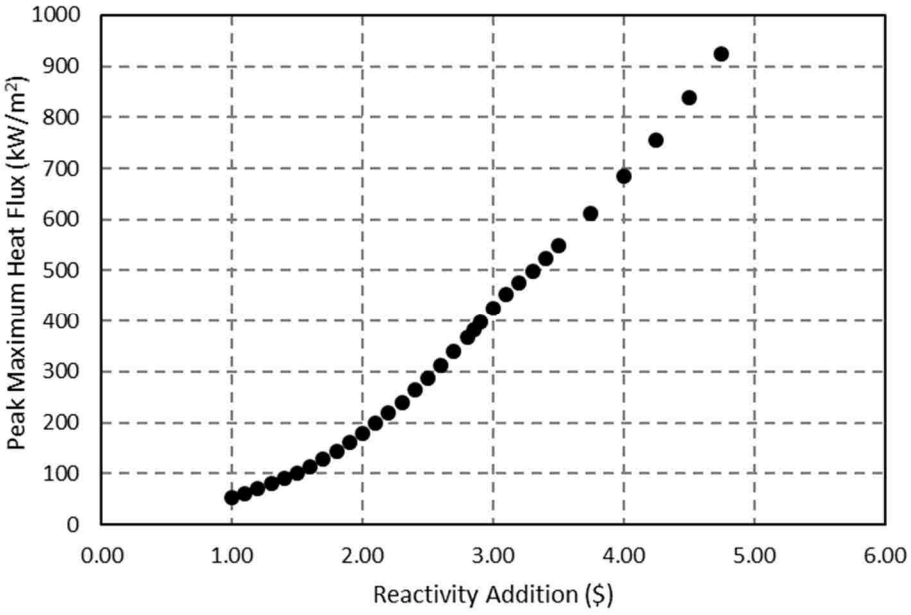

Figure 92. Variation of the peak maximum element heat flux vs. reactivity addition.

With the direct heating of the coolant, as well as the heat transfer from the cladding, the decrease in the coolant density initiates the development of natural circulation flow through the channel. Depending upon the rate at which significant natural circulation flow can be developed, as well as the heat transfer rate to the coolant, an instance of bulk boiling in the coolant channel may occur. Figure 93 shows the time at which bulk boiling develops in the channel. Bulk boiling does not occur for reactivity addition less than \$2.90. The time span before boiling begins trends rapidly downward as the reactivity addition increase, as the initial near-adiabatic direct heating of the coolant brings the coolant successively closer to the saturation temperature as the reactivity addition increases.

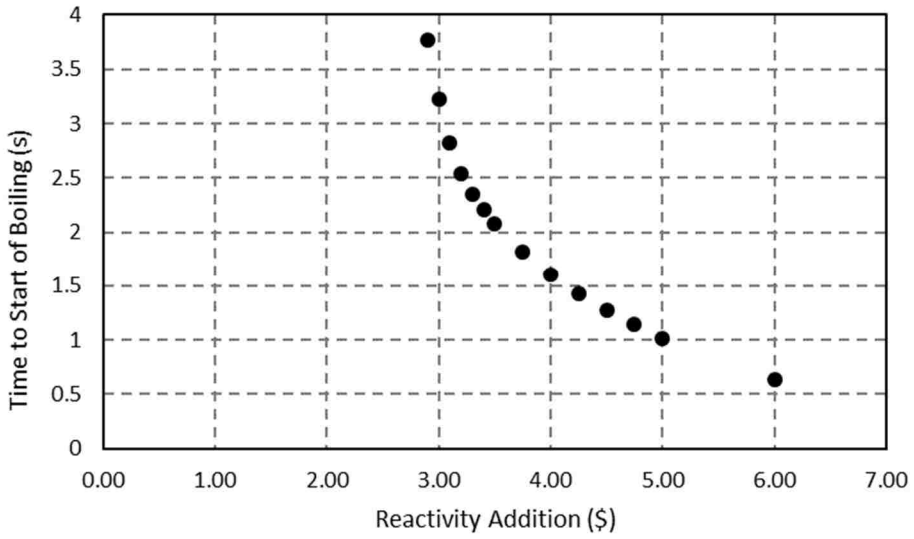

Figure 93. Variation of the time before bulk boiling occurs vs. reactivity addition.

Figure 94 shows the axial locations at which boiling begins for each reactivity addition. As seen earlier in Figure 89, as the reactivity addition increases, the coolant near the center of the channel will be closer to the saturation temperature. In addition, the heat transfer from the cladding increases with the reactivity addition, and is peaked near the

center of the channel. These facts support the trend showing that the starting point for boiling moves further down the coolant channel as the reactivity addition increases, and that the trend appears to be leveling off at higher reactivity additions.

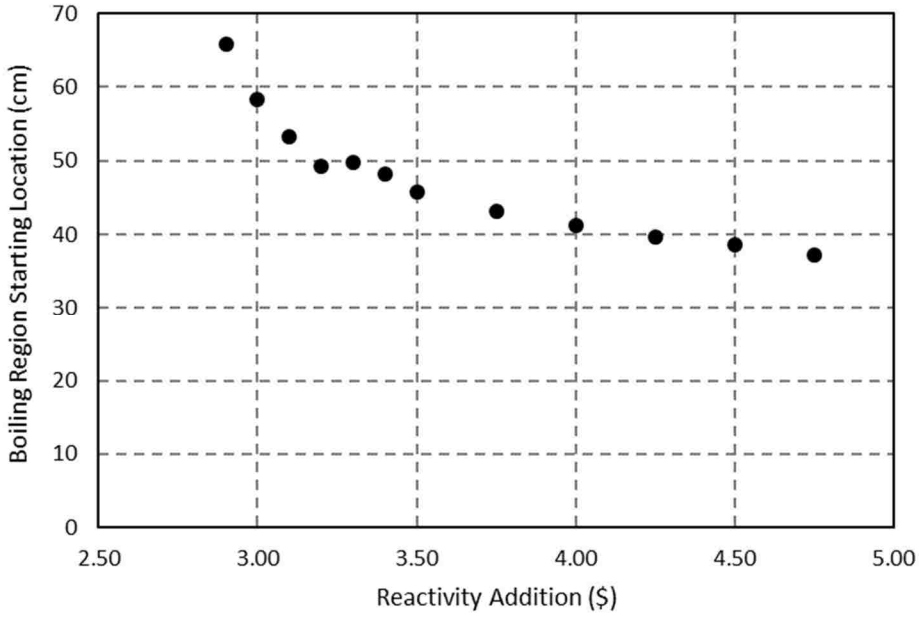

Figure 94. Variation of the axial location at which bulk boiling first occurs vs. reactivity addition.

Figure 95 shows the maximum axial extent of the bulk boiling region for each reactivity addition, and Figure 96 shows the time span during which the vapor region remains in the coolant channel. The boiling region length increases with reactivity addition, consistent with the increasing initial pulse energy deposition and the increasing post-pulse heating. The time span remains relatively constant at ~1 s for most of the range of reactivity additions, due to the increasing density driving for as the boiling region length increases. Eventually, the increased initial and post-pulse heating of larger reactivity additions increases the boiling region duration.

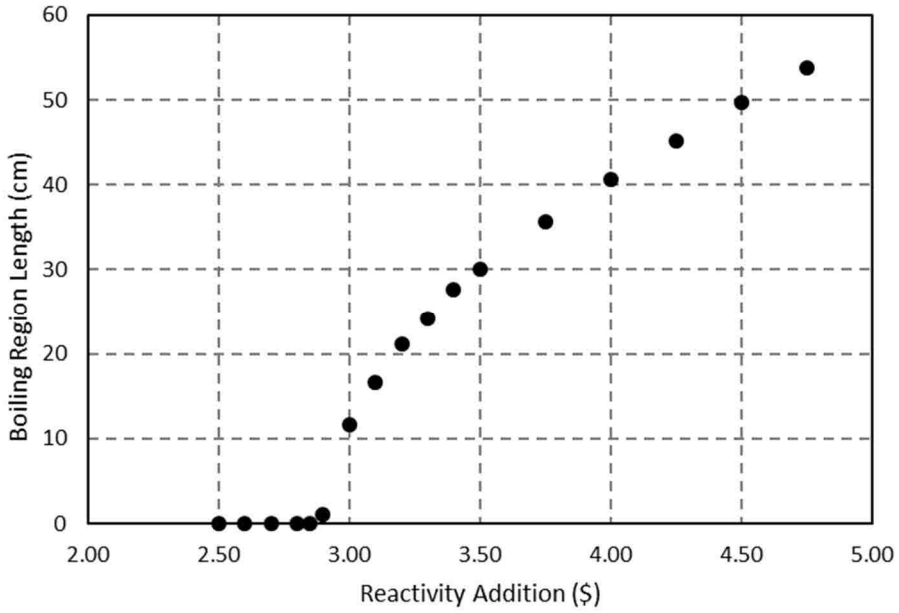

Figure 95. Variation of the axial extent of the bulk boiling region vs. reactivity addition.

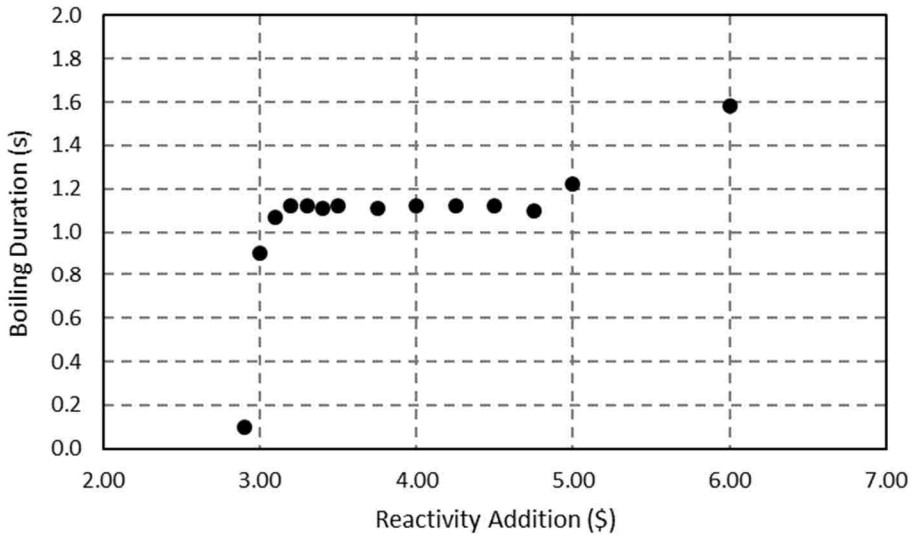

Figure 96. Variation of the time duration of a bulk boiling region vs. reactivity addition.

6.4. Impact of a Post-Pulse Rod Drop

The LRRA events which have been analyzed thus far have allowed for the reactor system to reach an equilibrium power level subsequent to the reactivity addition. This, however, is not typical of the operation of the ACRR. Typically, at a preset time after the initiation of the pulse operation, the reactivity control rods are released to fall into the core, and shut down the reactor. This post-pulse rod drop has a significant impact on the peak transient values of the fuel and coolant parameters. The preset time between the initiation of the pulse operation and the post-pulse rod drop is referred to as the rod holdup time, or RHU.

Cases were run using the "specified scram" feature of Razorback. This feature executes a specified negative reactivity addition over a specified time span, beginning at a specified time following a scram signal. The scram signal was set at 0.055 %FP so that the scram signal would happen at essentially $t \approx 0$ s, since the initial power level is 0.05 %FP. The scram action was set to begin 175 ms after the scram signal occurs. The scram reactivity addition was set to be \$2 more than the LRRA which initiated the run. The scram reactivity addition was set to occur over 2 s.

Figure 97 shows the impact upon the post-pulse temperature rise as a function of the reactivity addition. For reactivity additions between \$2.50 and \$4.75, a RHU time of 0.175 s essentially eliminates the post-pulse temperature rise. Thus, a post-pulse rod drop may be used to limit the temperature rise in the fuel to the magnitude of the initial fuel temperature rise due to the reactor power pulse.

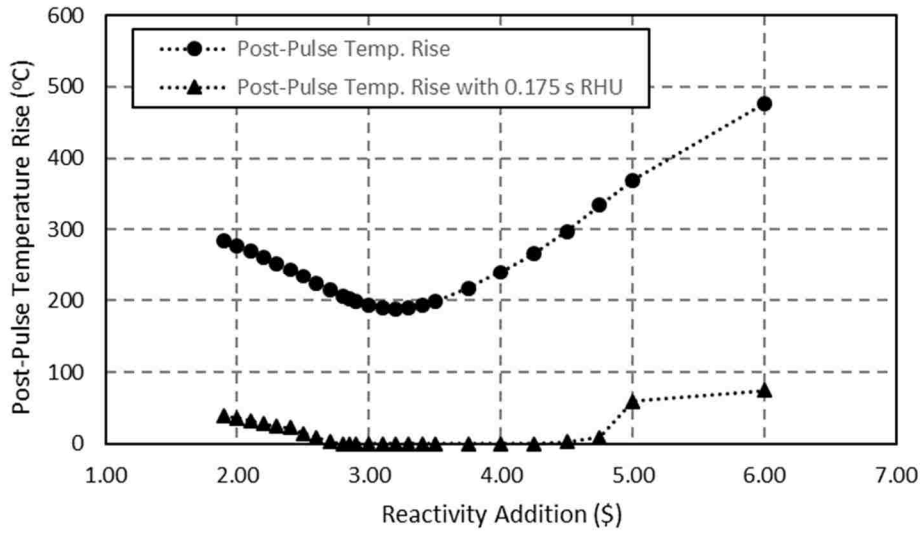

Figure 97. Impact of a post-pulse rod drop on post-pulse temperature rise.

Figure 98 shows the impact upon the peak cladding surface heat flux as a function of the reactivity addition. The post-pulse rod drop (0.175 s RHU) significantly reduces the peak cladding surface heat flux on the order of 40% for lower reactivity additions to ~10% for larger reactivity additions. This is not unexpected, given that the post-pulse rod drop significantly reduces the peak temperature attained in the fuel after the pulse.

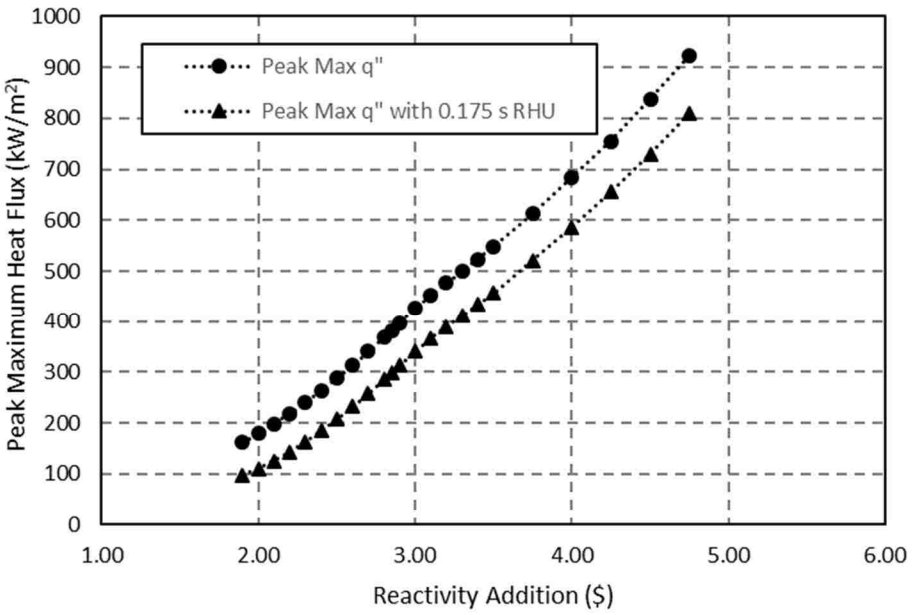

Figure 98. Impact of a post-pulse rod drop on the peak maximum heat flux.

Figure 99 shows the impact upon the maximum extent of the transient boiling region as a function of the reactivity addition. We note that the post-pulse rod drop (0.175 s RHU) increases the reactivity addition needed to induce bulk boiling in the flow channel by \$0.20 (from \$2.90 to \$3.10). Overall, there is an 8-10% reduction in the maximum boiling length.

The impact upon the duration of the transient boiling region is shown in Figure 100. Except for the difference in reactivity addition required to initiate a boiling region, the duration of the boiling region within the channel is largely unaffected by a post-pulse rod drop (at least for the 0.175 s RHU examined here).

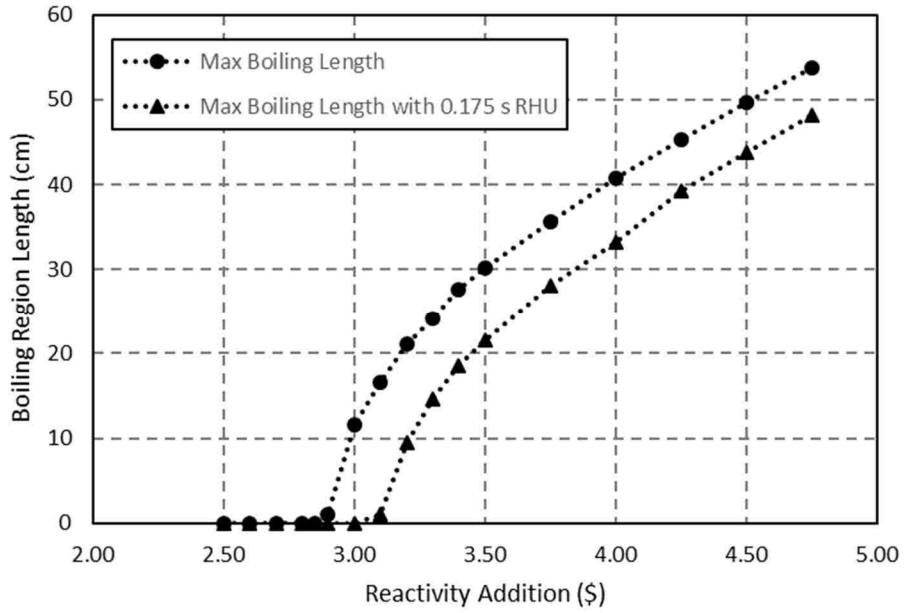

Figure 99. Impact of a post-pulse rod drop on maximum bulk boiling length.

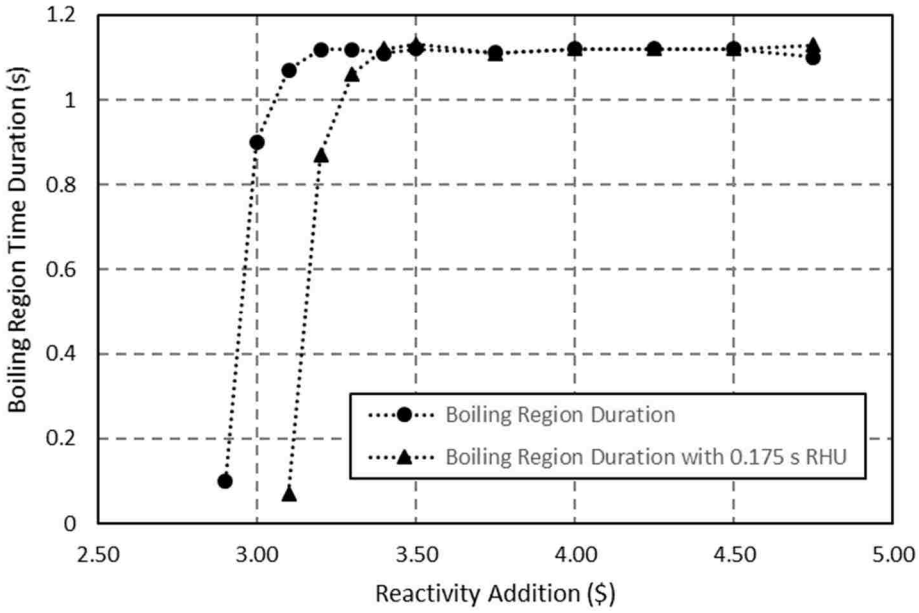

Figure 100. Impact of a post-pulse rod drop on the time duration of bulk boiling.

6.5. Discussion of Safety Analysis Implications

For the safety analysis of a research reactor, there are two primary goals related to the thermal-hydraulic response: (1) preventing an undesirable maximum fuel temperature, and (2) preventing an undesirable maximum cladding temperature. These components represent the primary barriers to the release of radioactive fission products from the fuel element. Two closely related underlying goals, which help prevent damage to these components, are (1) ensuring an adequate heat transfer capability from the fuel to the coolant, and (2) ensuring that an adequate coolant flowrate develops to effectively remove heat from the fuel element.

Following the initial near-adiabatic temperature rise of the fuel in response to the reactor power pulse, there is a subsequent fuel temperature rise that was referred to as the post-pulse temperature rise. This post-pulse temperature rise is driven by the magnitude of the delayed neutron fission power level shortly after the pulse. While a heat transfer rate from the element to the coolant is being established, due to the energy deposited in the fuel during the pulse, the delayed neutron fissions continue to deposit a significant amount of energy in the fuel. Thus, it is important that the effective heat transfer resistance characterizing the materials between the fuel and the cladding surface not overly restrict the efficient removal of heat from the fuel.

Meanwhile, the coolant, initially at a very low flowrate, will be accelerated due to the direct neutron/gamma interaction heating and increasing heat transfer from the element. However, the establishment of an adequate natural circulation flowrate will require time, due to the inertia of the coolant. As the heat transferred from the fuel element enters the coolant, the heat transfer rate may increase much more quickly than the coolant flowrate.

The result is a mismatch of heat transfer demand and heat removal capacity. If the mismatch is severe enough, it can potentially result in higher than desired cladding temperatures.

These two underlying goals will require tradeoffs. Maximizing the capability to transfer heat from the fuel to the coolant must be balanced with the capability of the natural circulation driving force to establish, over time, an adequate coolant flowrate. Otherwise, there is a risk of overheating the cladding. Conversely, ensuring adequate time to develop adequate coolant heat removal capability may require increasing the fuel-to-coolant heat flow resistance, and the risk of overheating the fuel. The ACRR fuel design is an example of this. The gap between the fuel and the niobium cup, and the gap between the niobium cup and the cladding introduce resistance to heat flow, but the high specific heat of the fuel material helps to avoid excessive fuel heating while the flow develops in the coolant channel.

Most likely, there will be little flexibility in the design of the fuel element or the coolant flow characteristics. In this case, the safety analysis process could determine and impose an operational reactivity addition limit. This will, of course, limit the peak power and energy release attained in LRRA operations. This will also necessarily limit the neutron flux and fluence levels attainable with the research reactor. These are important parameters for the researcher hoping to utilize the experiment irradiation locations of the research reactor.

In order to preserve higher allowable LRRAs, a specified post-pulse rod drop shutdown could be employed. This specified rod holdup (RHU) time allows one to reduce the delayed neutron fission energy deposition in the fuel after the pulse. This will

significantly reduce the post-pulse temperature rise. The RHU time will also result in a decrease in the overall length of the region experiencing boiling. The RHU can eliminate the occurrence of boiling for pulses at the lower reactivity range for which boiling occurs. In order to eliminate boiling over the entire range of reactivity additions, the analyst would have to "sacrifice" the pulse by initiating a RHU shutdown before the peak of the pulse.

Of course, when implementing a RHU shutdown, there will be a practical limit to how small of a RHU time can be achieved. There will inevitably be delays introduced by the response/reaction time of the electronics which implement the RHU shutdown. There will also be some delay introduced by the mechanism which releases the reactivity rods to fall and the inertia of the rods themselves. In either case, too short of a RHU time could initiate a shutdown before the pulse can fully develop (e.g., before the peak power is reached).

A RHU shutdown could be implemented in at least two ways: (1) a simple timer circuit which initiates the RHU shutdown after a specified time has been reached, or (2) a reactor trip set at a level ensured to initiate a shutdown for any given LRRA. However, the analyst would need to choose the trip setpoint carefully. The reactivity addition time for the LRRA, if less than an ideal "step" addition, will result in a change in the slope of the peak power vs. reactivity addition curve. If a power level trip is to be used, the change in the trend of peak power level must be properly predicted, and accounted for, when selecting the trip setpoint. Alternatively, a very low power level trip could be employed to activate the scram process early in the progression of the LRRA. However, if the trip is set too low, the shutdown action will impact the peak power attained in lower reactivity addition pulses, because the peak power will take longer to develop.

6.6. Conclusions

An overview of the thermal-hydraulic response characteristics of a natural circulation research reactor to a large rapid reactivity addition (LRRA) has been presented. The maximum fuel temperature was seen to incur an initial peak increase due to the near-adiabatic heating induced by the reactor power pulse. This was seen to be followed by a post-pulse temperature rise that peaks when a natural circulation coolant flow is established at a level which allows a matching of the heat transfer rate from the fuel to the coolant.

Rapid increases of the pressure of the coolant in the channel, followed by rapid decreases, were seen to occur. These pressure changes were associated with the initial neutron/gamma interaction heating induced in the coolant by the LRRA, and were seen to quickly dissipate following the initial heating. Associated with the initial pressure spike, was an initial expansion of the coolant in the channel. The expansion of the coolant outward from the axial center of the channel occurred, in both the upward and downward direction. Following this initial rapid expansion, the natural circulation driven flow increased until an equilibrium was achieved.

For higher LRRA values, regions of saturated boiling developed within the channel. The formation of "voids" (i.e., vapor regions) caused significant transient increases in the coolant flow until the vapor region was pushed from the channel. The flow would then decrease and reestablish its trend toward an equilibrium level.

Variation of magnitude of the LRRA were examined to identify overall trends of the characteristics of the thermal-hydraulic response. The impact of executing a post-pulse rod drop was also examined. The post-pulse rod drop was determined to have a significant impact on the post-pulse temperature rise in the fuel (essentially eliminating it for a range

of LRRAs). The post-pulse rod drop precluded the development of a saturated boiling region until slightly higher reactivity additions. However, it was not able to eliminate the occurrence of boiling over a wide range of LRRAs, as it did for the post-pulse temperature rise. This indicates that an energy buildup sufficient to initiate boiling was occurring during the pulse heating itself.

7. Large Rapid Reactivity Addition Events: Thermomechanical Response

7.1. Introduction

During a large rapid reactivity addition (LRRA), such as a pulse operation (or accident) in a research reactor, the reactor power will increase rapidly, resulting in a rapid temperature rise within the fuel. Since there is little time for significant heat transfer to occur during the pulse, the energy deposition during this time is essentially adiabatic. Thus, the resulting fuel temperature profile is approximately the same shape as the energy deposition profile. Typically, the radial energy deposition distribution within the fuel is strongly peaked at the outer edge of the fuel. The energy deposition profile within a fuel element of the ACRR is shown in Figure 101.

A fuel temperature gradient with the shape shown in Figure 101 can lead to significant thermal stresses within the fuel. During the preliminary fuel design selection testing for the ACRR [37] thermal stress fractures were found when the fuel test samples were subjected to high reactivity addition pulse operations. The final fuel design for the ACRR, in which each of the fuel pellet rings were changed to be two 180° half-circles (see Figure 2), was selected to reduce the thermal stresses which occur during high reactivity addition pulse operations.

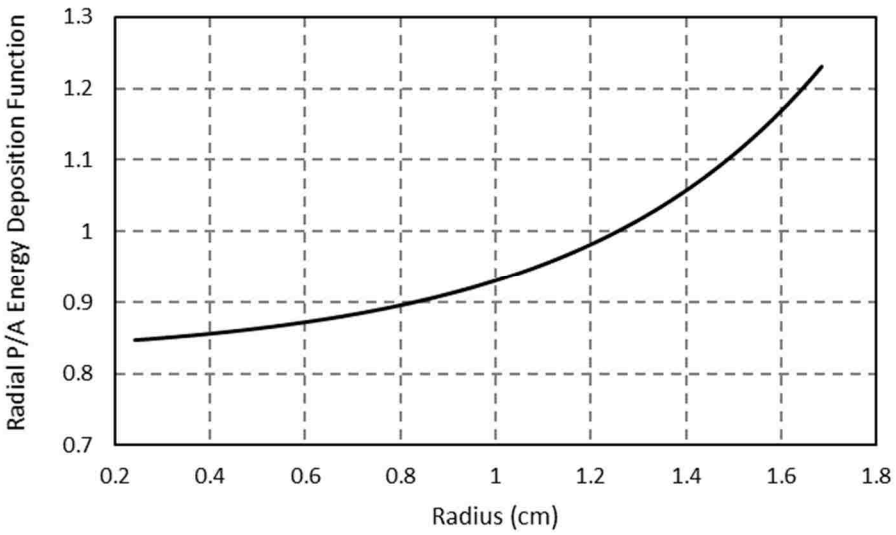

Figure 101. Radial fission energy deposition profile (peak-to-average) within the ACRR fuel pellets.

7.2. Overview of the Thermomechanical Response for the ACRR

For the purpose of evaluating the response of a research reactor to a large rapid reactivity addition (LRRA), we will consider a $3.00 reactivity addition to the ACRR. The reactivity will be introduced as a ramp over a time of 80 ms, i.e., a $37.5 per second ramp addition terminated after 80 ms. Figure 102 shows the reactor power resulting from the reactivity addition, peaking at 29.7 GW at a time of 81 ms, with a pulse width (at half-maximum power) of 7.4 ms. Subsequent to the power pulse, the reactor power decays over time from an elevated power level (~70 MW) due to the presence of delayed neutron emitting fission products produced during the power pulse.

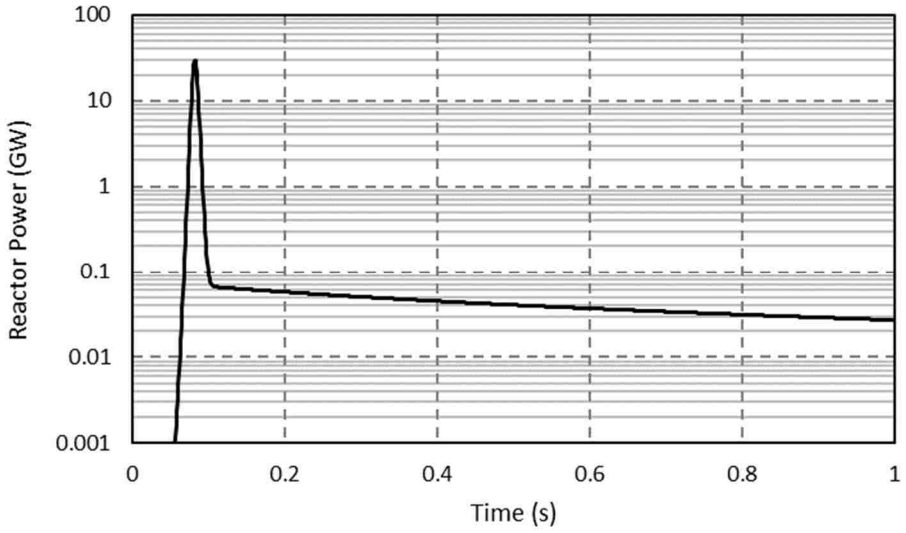

Figure 102. Initial reactor power history for a $3.00 LRRA.

Figure 103 shows the reactor power as it decays following the pulse, but eventually rises again to an equilibrium power level of 1.3 MW. This behavior occurs because after

the reactivity has been added, no further reactivity control system is modelled. Thus, as the power decays, the fuel will begin to cool off. As the fuel cools, the parasitic neutron absorption due to high fuel temperatures (known as the Doppler reactivity feedback effect) decreases, so that reactor power increases. Ultimately an equilibrium power level, commensurate with the added reactivity, is attained.

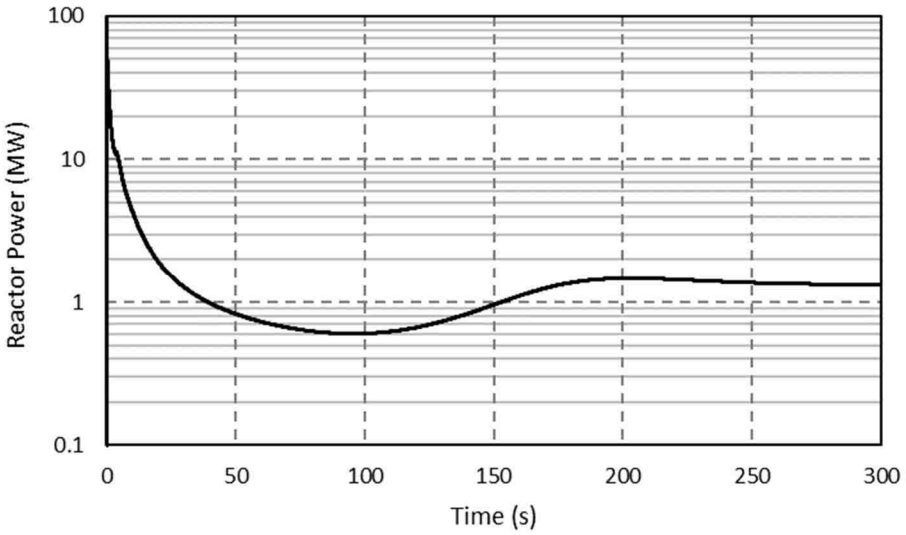

Figure 103. Reactor power history for a $3.00 LRRA.

Figure 104 shows the initial maximum fuel temperature response to the large rapid reactivity addition. The maximum fuel temperature increases rapidly to an initial peak value of 1060°C at a time of 97 ms (16 ms after the time of the peak power). The reactor power, even after the power pulse, is still at relatively high values. In addition, time is required for heat to be transferred to the coolant, and for the coolant flow (which is driven by natural circulation only) to develop sufficiently to carry away this heat. Thus, fuel temperature continues to rise over time.

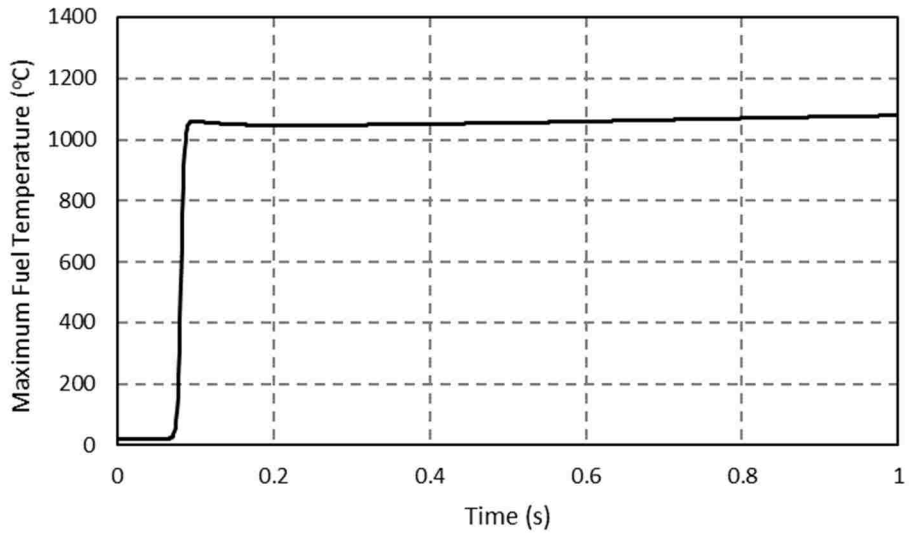

Figure 104. Initial maximum fuel temperature history for a $3.00 LRRA.

As shown in Figure 105, the maximum fuel temperature continues to increase until a peak is reached. The maximum fuel temperature then begins to decrease, until an equilibrium value of ~800°C is reached.

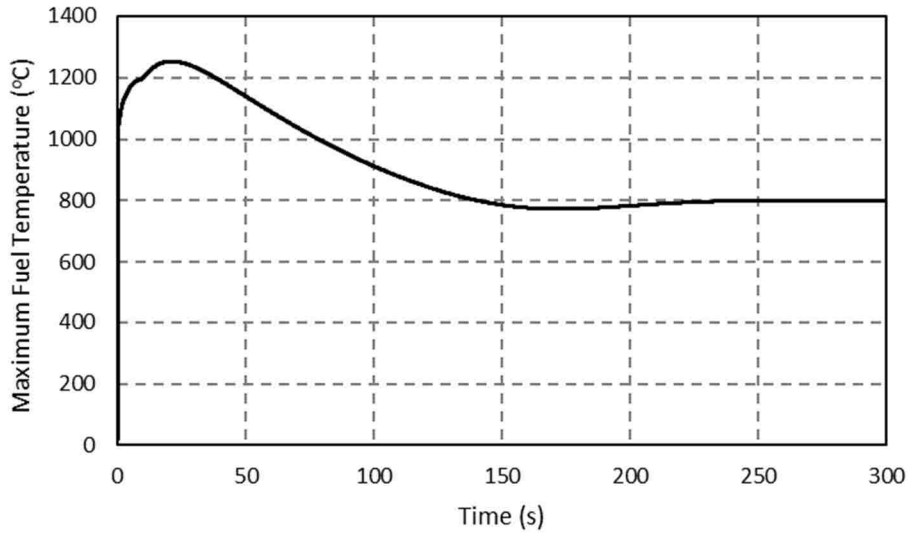

Figure 105. Maximum fuel temperature history for a $3.00 LRRA.

When evaluating the thermal expansion and stress response to the large rapid reactivity addition, we will be interested in the temperature distribution across the fuel element components. Figure 106 shows the temperature distribution within the inner and outer fuel pellets (left and right portions of the curve, respectively) at the time that the maximum tensile stress is at its peak value (t = 93 ms). Up to this point in time, the energy deposition within the fuel due to fission has been essentially adiabatic (i.e., little heat transfer out of or within the fuel material has taken place). As expected, the temperature distribution is strongly peaked toward the outer surface of the outer pellet, following the energy deposition profile described earlier (see Figure 101). Note, however, that some amount of heat transfer is occurring from the outer surface to the niobium can, as evidenced by the downturn of the temperature near the surface. The temperature distribution across the inner fuel pellet is much flatter in comparison.

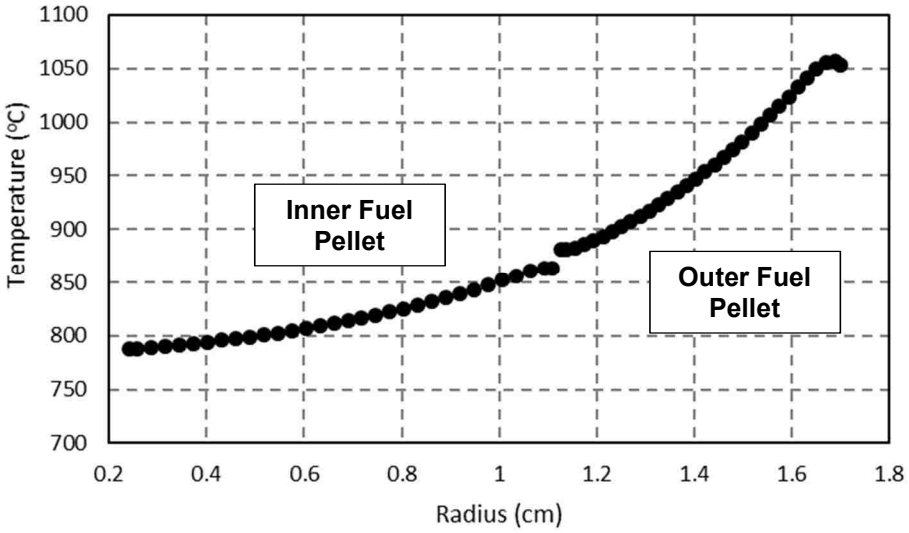

Figure 106. Initial inner and outer fuel pellet temperature profiles for a $3.00 LRRA.

After the reactor power and fuel temperature reach equilibrium values, the temperature distribution within the fuel pellets will have shifted so that the maximum temperature is at the inner surface of the inner pellet. The shape of the temperature distribution will be dictated by the thermal conductivity of the fuel and the dimensions of the fuel. Figure 107 shows the temperature distribution within the inner and outer fuel pellets after the reactor has reached equilibrium. The temperature discontinuity between the two pellets is due to the small helium-filled gap between the two fuel pellets.

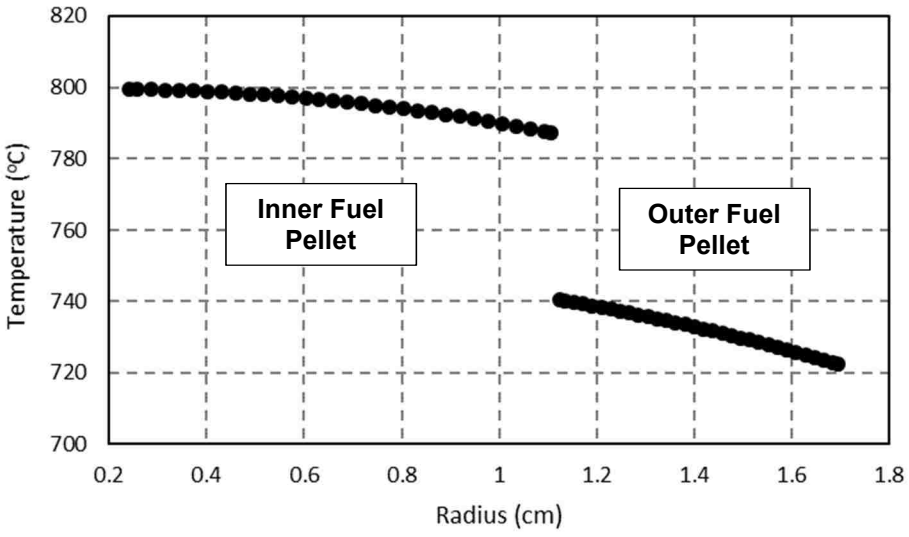

Figure 107. Equilibrium inner and outer fuel pellet temperature profiles for a $3.00 LRRA.

Before continuing, we note that in the analyses to follow, the ACRR fuel was treated as consisting of inner and outer annular rings. The Razorback thermomechanical analysis model addresses intact annular rings, and cannot directly evaluate the slotted annuli of the actual ACRR fuel.

7.2.1. Thermal Expansion Response

The $3.00 large rapid reactivity addition (LRRA) event was analyzed to determine the thermal expansion of the fuel element components. As seen earlier, the temperature of the fuel pellets increases rapidly at first, with little heat transfer to the niobium cup or within the fuel itself. In response to the temperature rise, the various components of the fuel element begin to expand. There is also a small amount of energy deposition directly into the niobium can and the stainless steel (SS) cladding due to neutron and gamma ray scattering. However, this only amounts to 0.40% and 0.46%, respectively, of the total energy deposition (compared to 97.85% in the fuel, and the remaining 1.29% in the coolant). The initial radial displacements of the outer radii of the outer fuel pellet, Nb can, and SS cladding early in the LRRA event are shown in Figure 108.

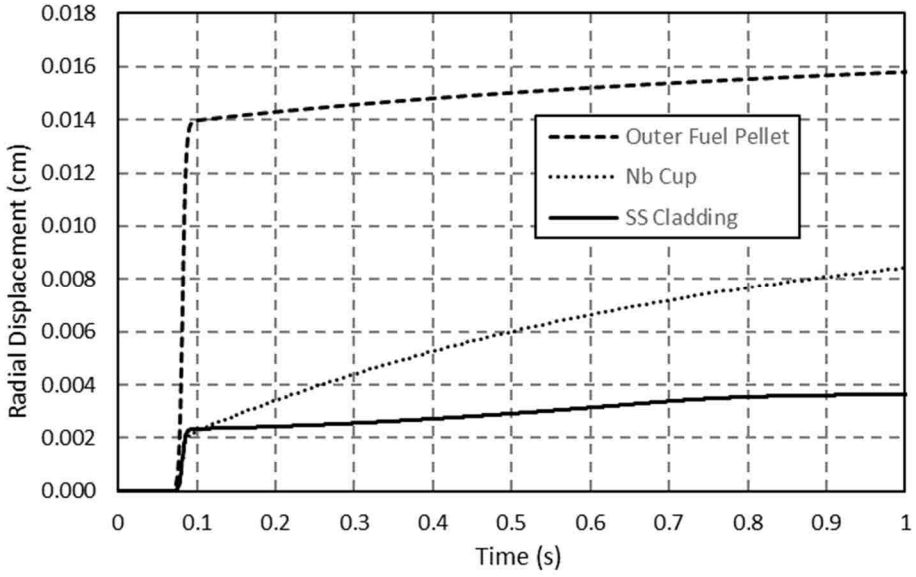

Figure 108. Initial radial displacement time histories for a $3.00 LRRA.

As shown in Figure 108, the expansion of the outer fuel pellet is significantly greater than that of the niobium, and thus, the gap space between the outer fuel pellet and

the niobium can is reduced. With the decrease in this gap space comes an increase in heat transfer from the fuel to the Nb, which causes an increase in the thermal expansion of the Nb cup. This expansion of the Nb is greater than that of the SS cladding. Thus, the gap space between the Nb and the SS cladding is reduced. This in turn increases the heat transfer to the cladding, causing it to expand. Figure 109 shows the initial evolution of the gap size between the outer fuel pellet and the Nb, and between the Nb and the SS cladding early in the LRRA event.

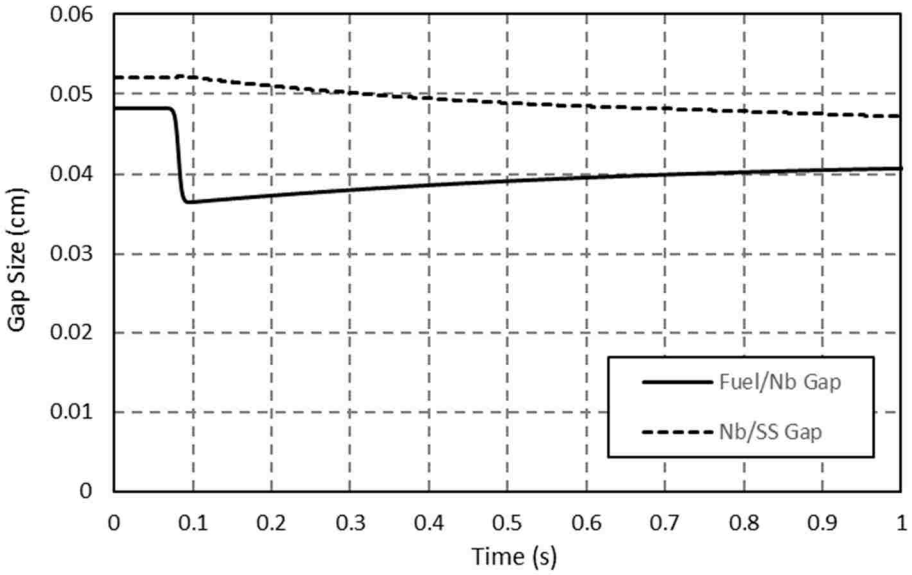

Figure 109. Initial gaps size time histories for a $3.00 LRRA.

Returning again to the radial displacements, as shown in Figure 110, each component will continue to expand, until a peak is reached where the fuel element component temperatures begins to decrease. Eventually, the radial displacements reach an equilibrium, and the thermal expansion ceases.

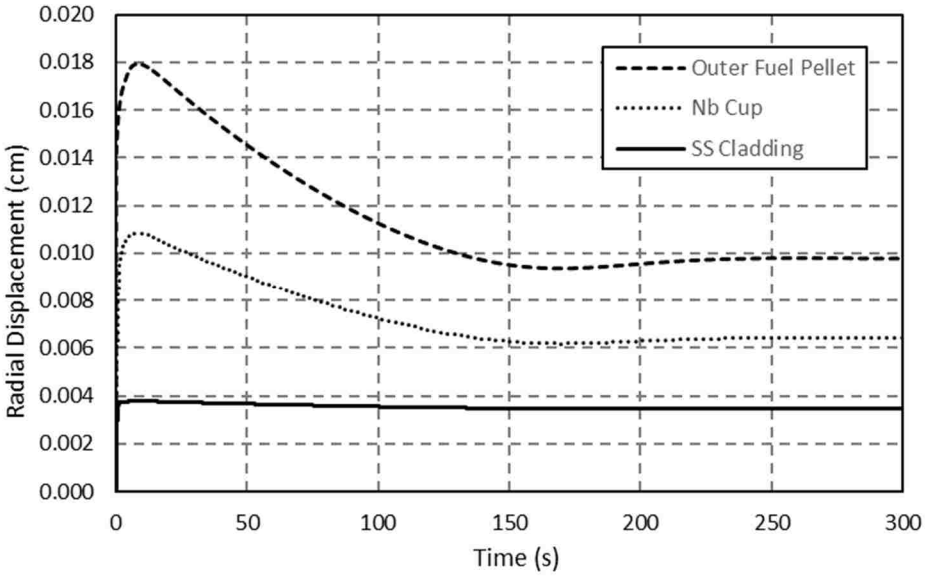

Figure 110. Radial displacement time histories for a $3.00 LRRA.

7.2.2. Thermal Expansion Stress Response

The $3.00 large rapid reactivity addition (LRRA) event was analyzed to determine the thermal expansion-induced mechanical stresses developed in the fuel element components. As seen earlier, the temperature of the fuel pellets increases rapidly at first, with little heat transfer to the niobium cup or within the fuel itself. In response to the temperature rise, the various components of the fuel element begin to expand, and stresses are induced.

The stress response of the outer fuel pellet will be examined first. Razorback logs the maximum tensile stress (radial or circumferential) in each material, at user-specified time intervals. As will be seen later, the maximum values are due to the circumferential stress (σ_θ). Figure 111 shows the maximum tensile stress within the outer fuel pellets of the fuel element early in the LRRA event. There is a rapid rise in the maximum tensile stress to a peak at ~93 ms, which is shortly after the pulse power peak at ~81 ms. The

maximum tensile stress then decreases as heat is transferred away from the outer pellet toward the niobium can and stainless steel cladding, and inward toward the inner fuel pellet.

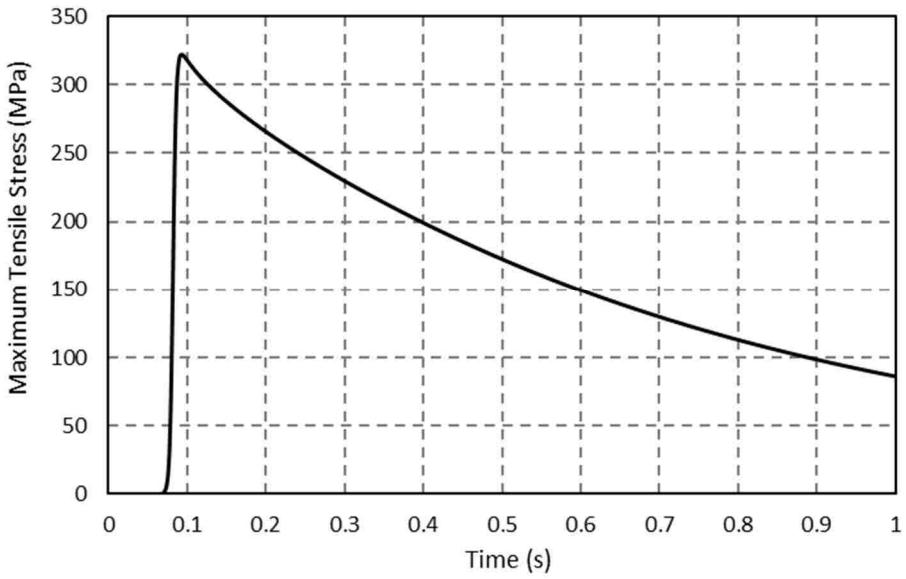

Figure 111. Initial maximum tensile stress time history in the outer fuel pellet for a $3.00 LRRA.

Figure 112 shows the time evolution of the maximum tensile stress in the outer fuel pellet. After the initial peak at ~325 MPa, the stress decreases as the heat transfer within and away from the fuel occurs. A second, lower peak maximum tensile stress of ~150 MPa occurs at about 16 s, as the fuel temperature distribution assumes an inner-peaked profile characteristic of a near steady-state distribution. The maximum tensile stress then decreases as the fuel element cools to an equilibrium state.

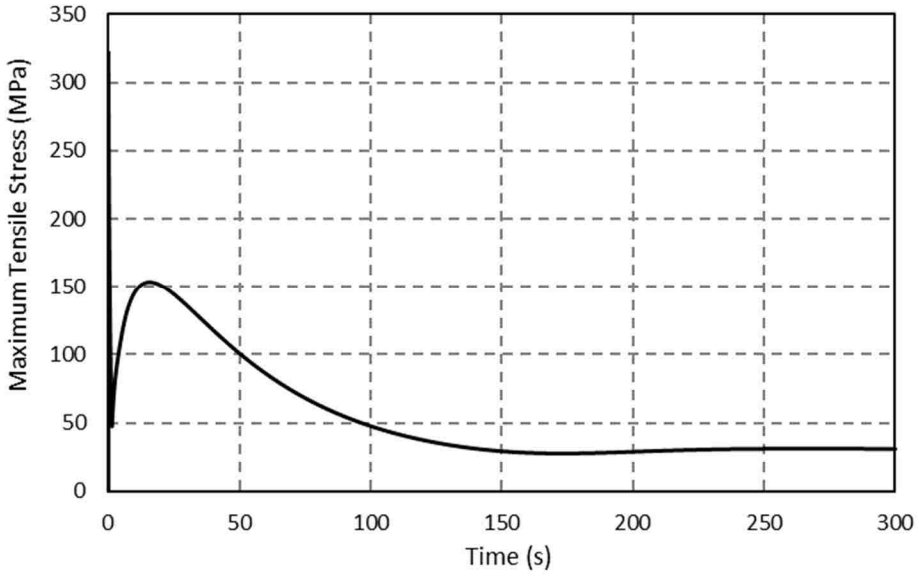

Figure 112. Maximum tensile stress time history in the outer fuel pellet for a $3.00 LRRA.

The maximum compressive stress within the outer fuel pellets follow very similar time histories. The initial peak maximum compressive stress is ~370 MPa, slightly higher in magnitude than the initial peak maximum tensile stress. The second peak of the maximum compressive stress, at ~140 MPa, is also slightly lower than that of the maximum tensile stress.

Next, we examine the stress distribution within the inner and outer fuel pellets at the time of the peak maximum tensile stress (t=93 ms). Razorback provides stress distribution results for each axial node, since the fission energy deposition may vary along the axial length of the fuel element. The results presented here are for the axial node at which the stress is highest.

Figure 113 presents the radial stress distribution for the inner and outer fuel pellet at the time of the peak maximum tensile stress (t=93 ms). The maximum radial stresses of the two pellets is relatively comparable in magnitude, with the inner pellet's being slightly

larger. The impact of the heat transfer occurring at the outer surface of the outer pellet (see Figure 106) is to induce a region of compressive stress which would not occur had a truly adiabatic heating have occurred. While the radial stress magnitudes are not negligible, the more significant stress is induced in the circumferential direction. Figure 114 shows the circumferential stress (or hoop stress) developed in the inner and outer pellets at the time of the initial peak of the maximum tensile stress.

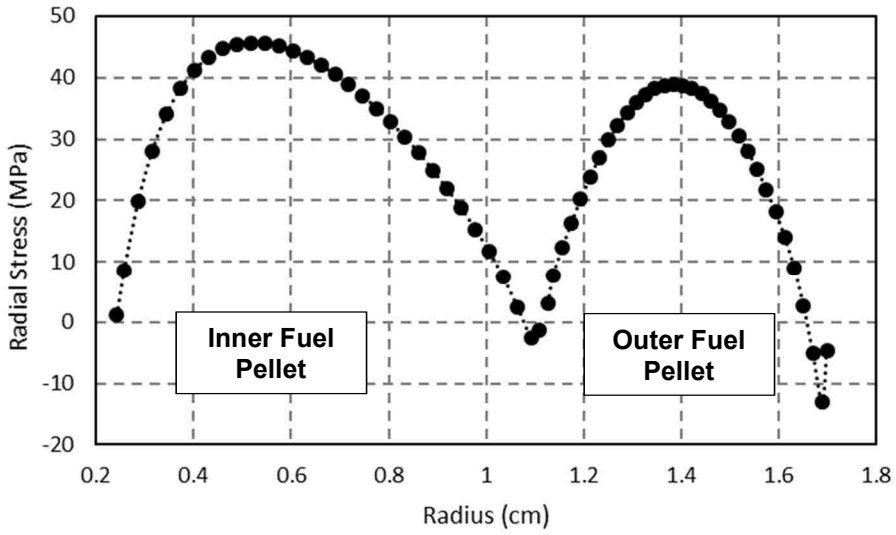

Figure 113. Radial stress profiles in the inner and outer fuel pellets at the time of the peak tensile stress for a $3.00 LRRA.

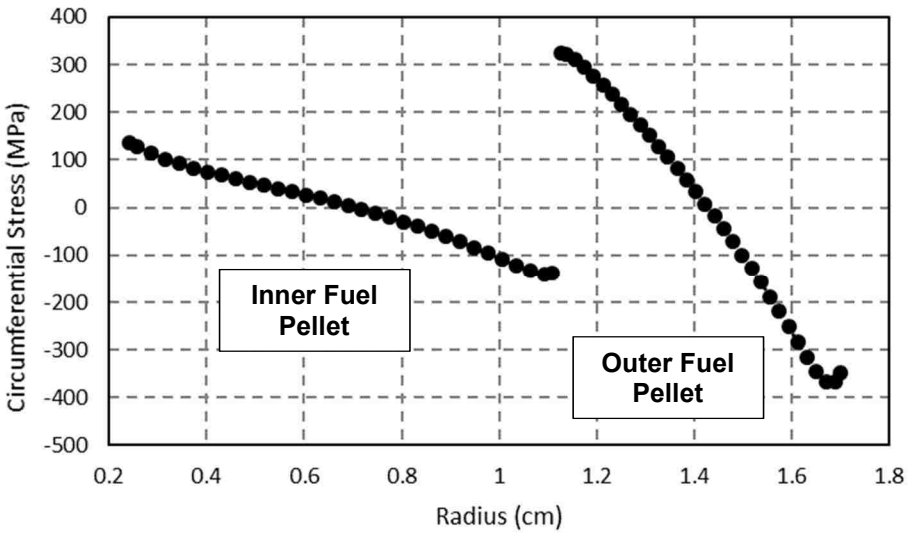

Figure 114. Circumferential stress profiles in the inner and outer fuel pellets at the time of the peak tensile stress for a $3.00 LRRA.

Finally, the system achieves equilibrium, and the temperature profile within the fuel becomes that shown in Figure 107 earlier. These profiles are peaked at the inner radii of the inner and outer pellets, and much flatter than the profiles resulting from the early adiabatic heating stage. Figure 115 and Figure 116 present the radial stress and circumferential stress distributions for the inner and outer fuel pellet after the system has reached equilibrium. The equilibrium stresses are significantly reduced from the stresses after the adiabatic heating stage (Figure 113 and Figure 114). Note that the radial stresses are now all compressive, and the circumferential stresses have shifted from a negatively sloped profile to a positively sloped profile.

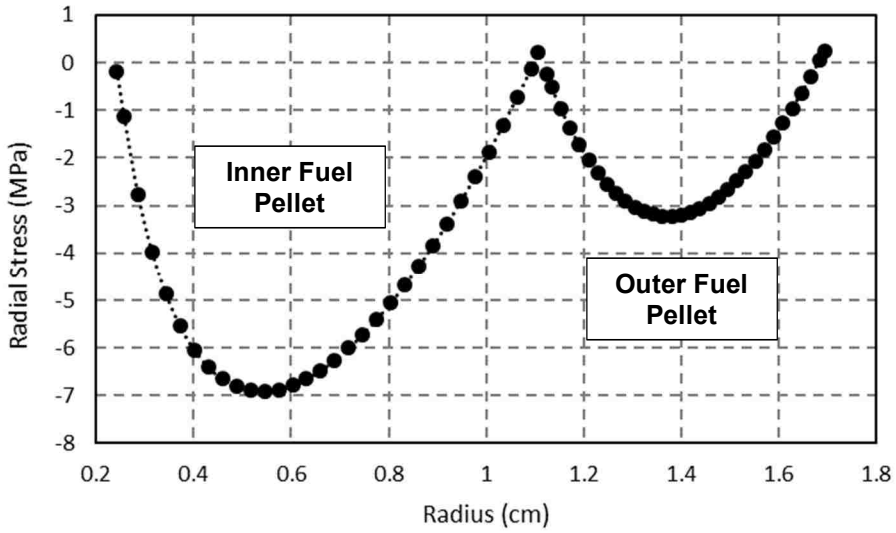

Figure 115. Equilibrium radial stress profiles in the inner and outer fuel pellets for a $3.00 LRRA.

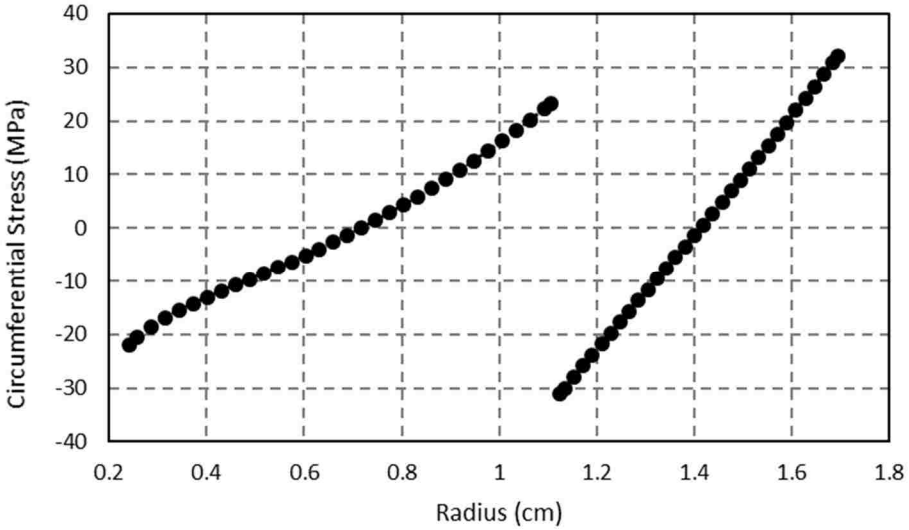

Figure 116. Equilibrium circumferential stress profiles in the inner and outer fuel pellets for a $3.00 LRRA.

The maximum tensile stress developed within the SS cladding is also of interest. Figure 117 shows the time history of the SS cladding maximum tensile stress, along with

that of the Nb cup. The stress within the Nb is much less than that of the SS cladding, since it is a thin-walled structure with a thermal conductivity much higher than SS. Although the SS cladding is also a thin-walled structure, its lower thermal conductivity leads to a greater temperature gradient across its thickness than in the Nb.

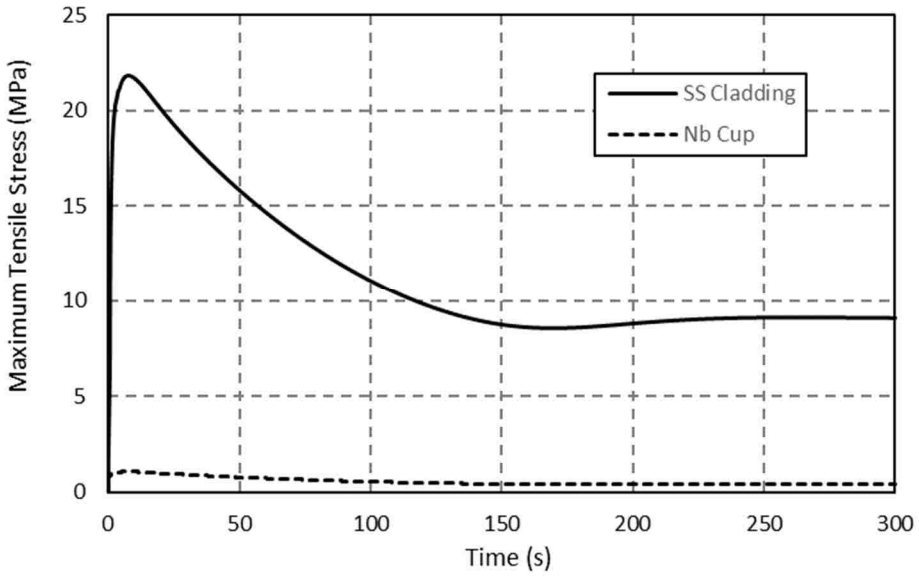

Figure 117. Maximum tensile stress time history in the cladding for a $3.00 LRRA.

7.3. Thermomechanical Response to Various Large Rapid Reactivity Additions

The potential for closure of a gap (particularly the fuel/Nb gap) increases as the reactivity addition increases. Figure 118 shows the trend of the minimum gap sizes (fuel/Nb and Nb/SS cladding) with the reactivity addition. Based upon the results, it appears that the outer fuel pellet's outer surface would not contact the inner surface of the niobium cup until a reactivity addition greater than \$12. This is a significant amount of reactivity for a pulsing reactor, and likely beyond the design of any "typical" pulse reactivity addition system.

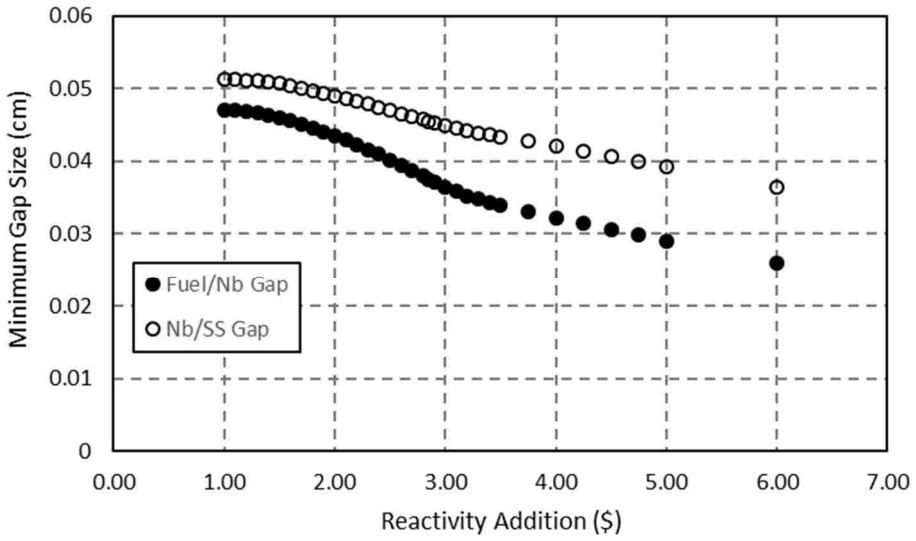

Figure 118. Minimum gap sizes in the fuel element for various reactivity additions.

Figure 119 shows the variation in the peak fuel tensile stress as a function of the reactivity addition. There is a discontinuity of the slope after a reactivity addition of ~\$3.

The shape of the trend in the peak fuel tensile stress is similar to that seen with the trend of the peak reactor power (see Figure 46).

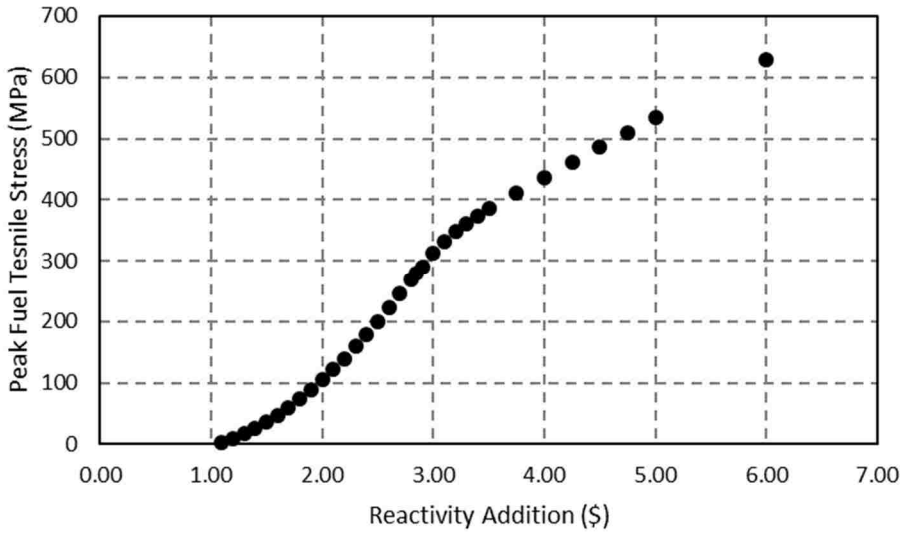

Figure 119. Peak tensile stress in the fuel for various reactivity additions.

Figure 120 shows another interesting result, considering the similarity of the trend in the peak fuel tensile stress with that of the peak reactor power. The figure shows the time at which the peak fuel tensile stress occurs as a function of the reactivity addition. In addition, the figure shows the time of the peak reactor power as a function of the reactivity addition. As can be seen, the time of occurrence of the peak fuel tensile stress is very close (a few ms after) the time of the occurrence of the peak power. One important consequence of this fact is that a post-pulse rod drop (i.e., a large negative reactivity addition executed at a specified time after the pulse) would be ineffective in reducing the peak tensile stress in the fuel.

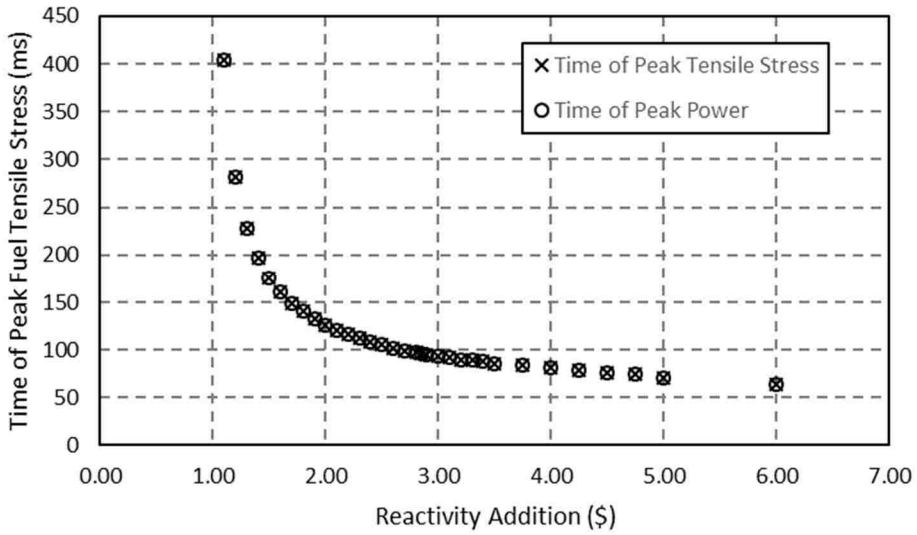

Figure 120. Time of the peak tensile stress in the fuel for various reactivity additions.

7.4. Impact of Reactivity Addition Time

The time over which the LRRA is imposed is referred to as the reactivity addition time. The shorter the reactivity addition time, the more closely the LRRA approaches a "step" change in reactivity. For the $3 LRRA under consideration so far, the reactivity addition time was 80 ms. A 50 ms reactivity addition time provides an effective "step" reactivity addition. Thus, we will examine a reactivity addition time of 50 ms and 100 ms, to see the impact of reactivity addition time has on the stress history.

Figure 121 shows the effect of reactivity addition times of 50 ms, 80 ms, and 100 ms, on the evolution of the gap size between the outer fuel pellet and the niobium cup for a $3 LRRA event. For the 50 ms addition time (compared to the 80 ms), the full reactivity addition of $3 occurs before appreciable fuel temperature reactivity feedback can reduce its impact. The result is that an additional 4.7 MJ of total reactor energy is released. This causes a small increase in the fuel temperature for the 50 ms addition time with respect to the 80 ms addition time. Based on the traces shown in Figure 121, this results in little additional thermal expansion, as the minimum fuel/Nb gap size for the two reactivity addition times (50 ms and 80 ms) is essentially the same. However, for the 100 ms reactivity addition time, even less of the total reactivity is added before the fuel temperature reactivity feedback impacts the transient. The overall result is that the gap size does not decrease as much as in the 80 ms reactivity addition time case.

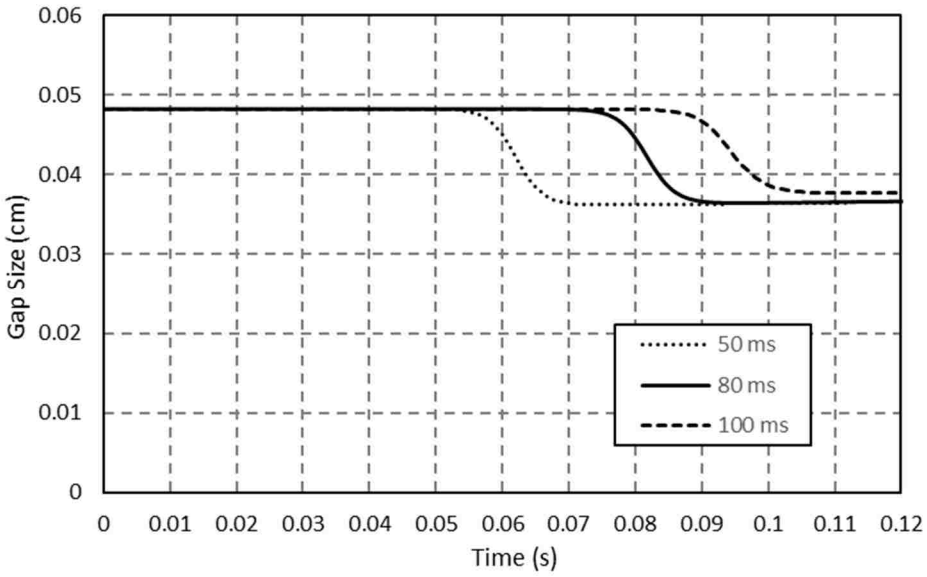

Figure 121. Impact of reactivity addition time on the evolution of the gap size for a $3.00 LRRA.

For the fuel/Nb gap size evolution shown in Figure 121, perhaps the most significant impact of reducing or increasing the reactivity addition time is the timing of the gap size change. Note that because the full reactivity addition is attained in the 50 ms case before significant fuel temperature reactivity feedback, any further decrease in the reactivity addition time below 50 ms will not result in a change in either the timing of the gap size change or the magnitude of the gap size change.

Figure 122 shows the effect of reactivity addition times of 50 ms, 80 ms, and 100 ms, on the maximum transient tensile stress in the fuel (i.e., the outer fuel pellet, where the worst-case tensile stress occurs). Reducing the reactivity addition time from 80 ms to 50 ms increases the peak maximum tensile stress by ~2.5%. For 100 ms, the peak maximum tensile stress is reduced by ~12%. Note also that the stress history curves are shifted in time, and that the slopes of the rise of the curves are impacted as well.

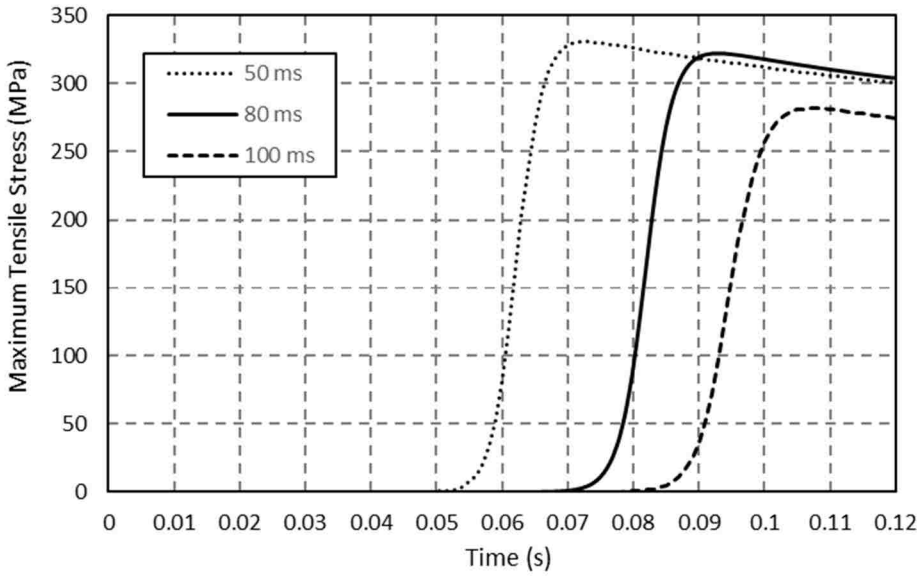

Figure 122. Maximum tensile stress in the fuel as a function of reactivity addition time for a $3.00 LRRA.

The impact on the radial and circumferential stress profiles is shown in Figure 123 and Figure 124 below. The reactivity addition time does have some effect, but it is relatively small. The is very little impact for decreasing the reactivity addition time from 80 ms to 50 ms. There is, however, some stress reduction achieved by increasing the reactivity addition time from 80 ms to 100 ms.

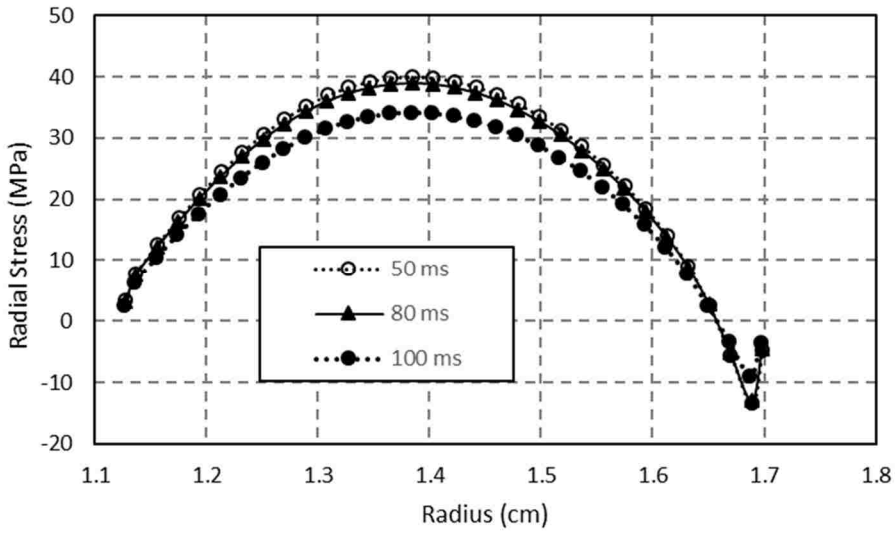

Figure 123. Outer fuel pellet radial stress as a function of reactivity addition time for a $3.00 LRRA.

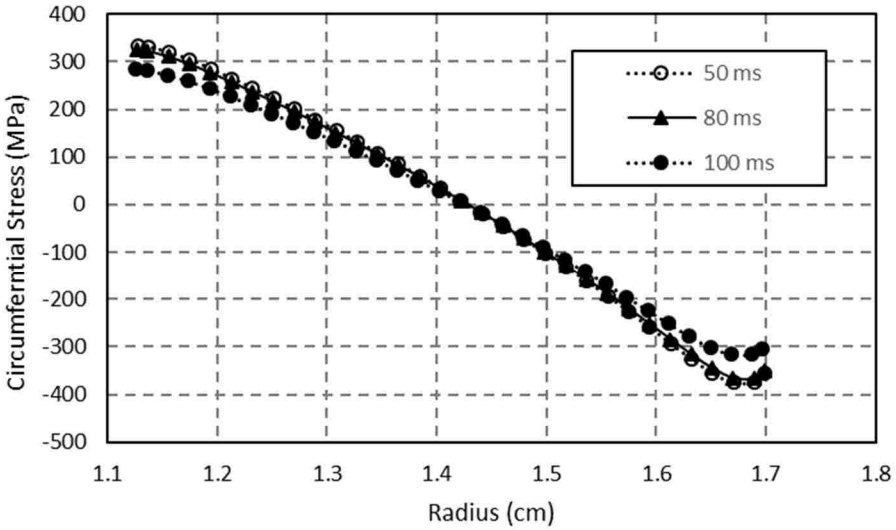

Figure 124. Outer fuel pellet circumferential stress as a function of reactivity addition time for a $3.00 LRRA.

7.5. Impact of Fission Energy Deposition Profile in Fuel

The stress profile within the fuel resulting from a LRRA also depends upon the temperature gradient produced by the reactor power pulse. The shape of the temperature profile follows the fission energy deposition profile during the adiabatic heating stage of the pulse, and these profiles can be highly peaked toward the outer surface of the fuel. If the energy deposition profile within the fuel were to be "flatter," then the stresses developed by the pulse would be decreased. Thus, we will examine a flat deposition profile, and one which is intermediate with respect to the ACRR's nominal profile, and the flat profile. Figure 125 shows the energy deposition profiles (i.e., the radial fuel peaking factor $F_r(r)$ profiles) which were examined.

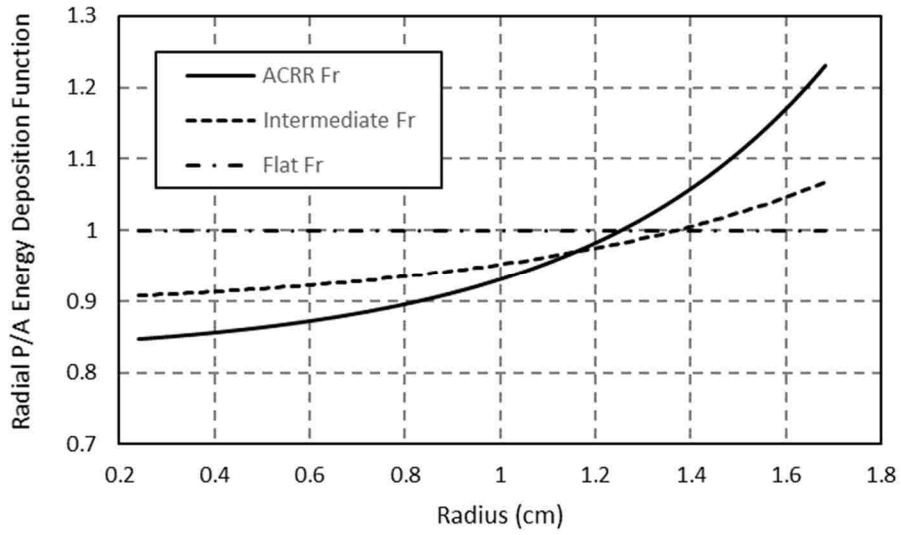

Figure 125. Fuel radial energy deposition profiles used in impact study.

Figure 126 shows the effect of the different fission energy deposition profile on the maximum transient tensile stress in the fuel (i.e., the outer fuel pellet, where the worst-case

tensile stress occurs). The "Intermediate Fr" reduces the peak maximum tensile stress by ~60%. This demonstrates that a significant reduction in the peak tensile stress can be achieved by "flattening" the energy deposition profile. Note particularly that the flat energy deposition profile essentially eliminates the initial peak in the maximum transient stress, and the stress at t = 0.12 s is ~10 times lower than that for the ACRR peaking profile at the same time.

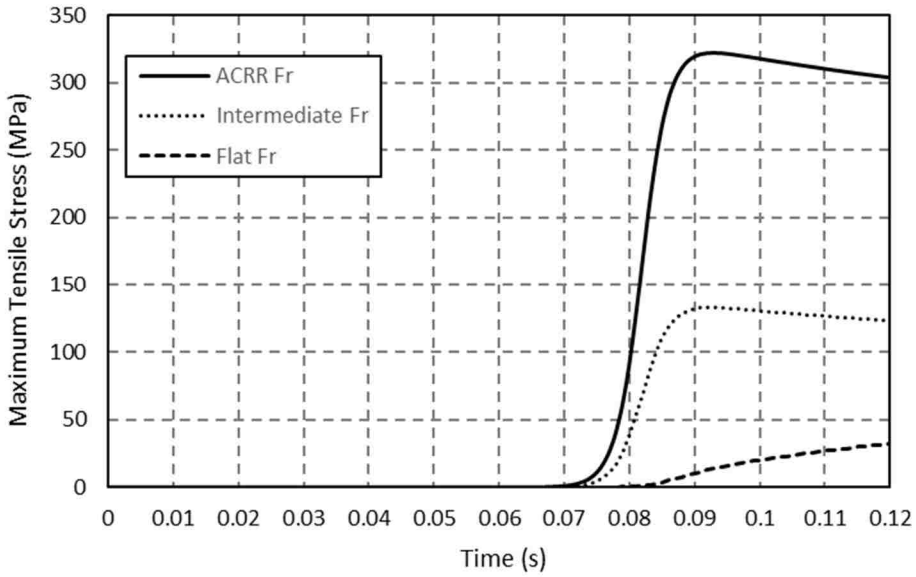

Figure 126. Maximum tensile stress in the fuel as a function of radial energy deposition profile for a $3.00 LRRA.

The impact on the radial and circumferential stress profiles is shown in Figure 127 and Figure 128 below. The shape of the energy deposition profile has a significant effect on the stresses developed.

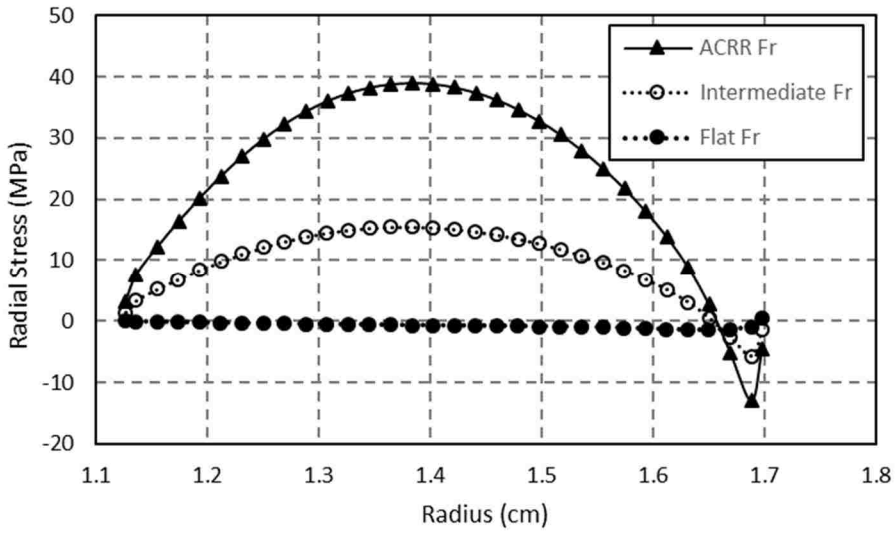

Figure 127. Outer fuel pellet radial stress as a function of radial energy deposition profile for a $3.00 LRRA.

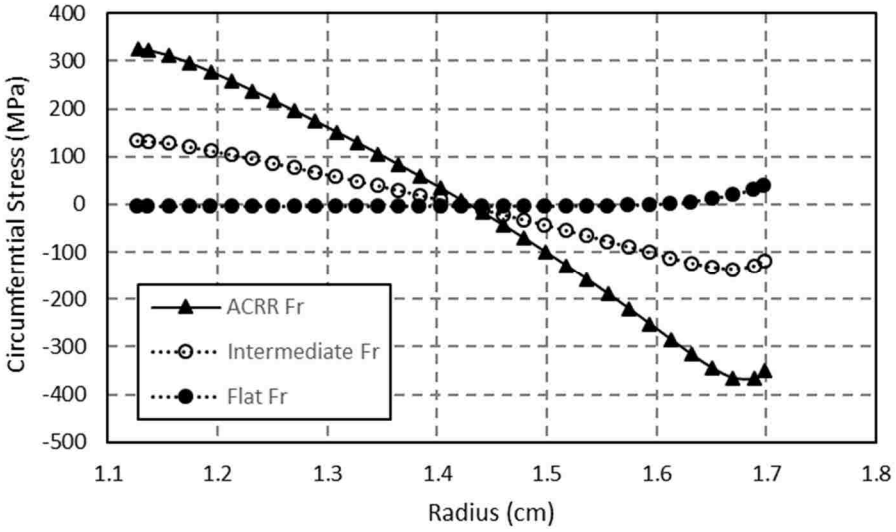

Figure 128. Outer fuel pellet circumferential stress as a function of radial energy deposition profile for a $3.00 LRRA.

7.6. Discussion of Safety Analysis Implications

The initial response of a research reactor to a large rapid reactivity addition (LRRA) is a near-adiabatic heating of the fuel. The energy deposition profile during this initial heating will be peaked toward the outer edge of the fuel. Thus, significant temperature changes will result in thermal expansion, and the significant temperature gradients will induce stresses. Thus, a primary concern associated with these thermal expansion induced stresses is the integrity of the fuel pellets.

If the integrity of the fuel is compromised (e.g., cracking occurs), then fission products normally retained within the fuel may become available for release from the new surfaces created by the cracking. Significant cracking or powdering would lead to a significant release of fission products into the free volume space within the fuel element cladding. The orientation of the cracking (e.g., radial, circumferential, or axial) can potentially decrease the effective thermal conductivity by introducing gaps into the conduction path. Lastly, a significant loss of fuel integrity would compromise the as-designed fuel pellet geometry, which is an important assumption for analyzing and predicting fuel element performance.

Based on the fuel stress results discussed above, one means of reducing the peak transient pressure during a LRRA would be to increase the reactivity addition time, although the impact was relatively small. However, to reduce the reactivity addition rate is in one sense simply a reduction in the overall reactivity addition, as this would reduce the peak system reactivity attained in the pulse. Thus, to reduce the reactivity addition rate would be to sacrifice the performance of the reactor.

A second possible stress reduction method would be to flatten the radial energy deposition profile. To do so, it would likely be necessary to resort to a graded ^{235}U enrichment (an enrichment which decreases with the fuel pellet radial location), or the introduction of a "filler" in the outer fuel pellet to decrease its effective fuel density compared to the inner fuel pellet. Such approaches would likely have disadvantages such as complications for fuel fabrication and associated increases in cost. An indirect approach would be to used reduced enrichment fuel pellets about the axial center of the fuel element to flatten the axial energy deposition profile.

Perhaps the most straightforward and effective means of stress reduction in the fuel would be to segment the fuel pellet rings into half-rings (i.e., two 180° semi-circular segments). This was the approach taken with what would eventually become the ACRR fuel design. According to one of the quarterly design reports [37] for the development of the ACRR, observed failures in fuel pellet tests led to the conclusion that a slotted annulus fuel pellet would significantly reduce the stresses produced during a pulse operation.

The current version of Razorback assumes the fuel to be annular rings, and is not capable of modeling the actual slotted annulus fuel pellet design of the ACRR fuel (see Figure 129 below). Boley and Weiner [38] present an analytical solution for a slotted annulus half-ring, although it is only valid away from the ends of the half-ring. In order to scope the stress reduction potential, the Boley and Weiner solution was programmed into Razorback, and used to produce a quasi-static solution for the fuel stress during a transient.

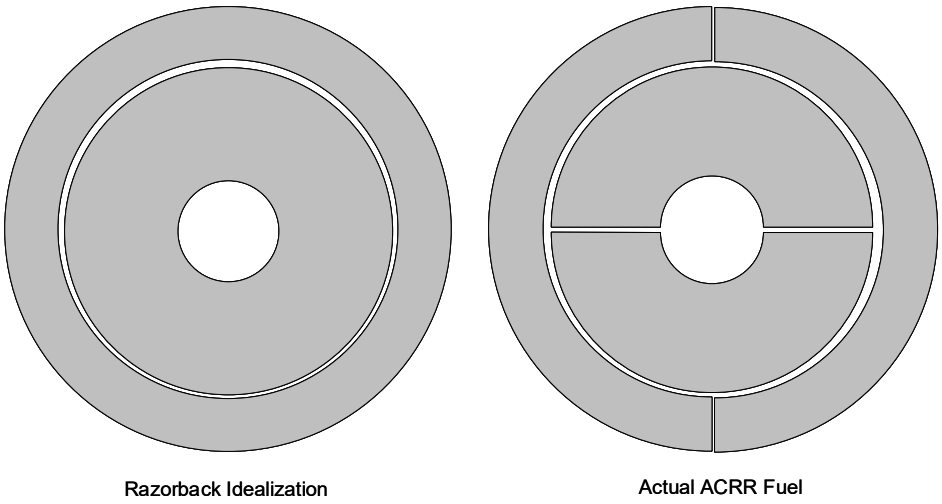

Figure 129. Razorback fuel pellet geometry vs. the actual ACRR fuel pellet design.

Figure 130 shows the maximum tensile stress history of the outer pellet of the fuel during the adiabatic heating phase of the LRRA. As may be seen the peak maximum tensile stress could be reduced from ~330 MPa to ~45 MPa. This is a significant stress reduction with no change to the reactivity addition time or the energy deposition profile.

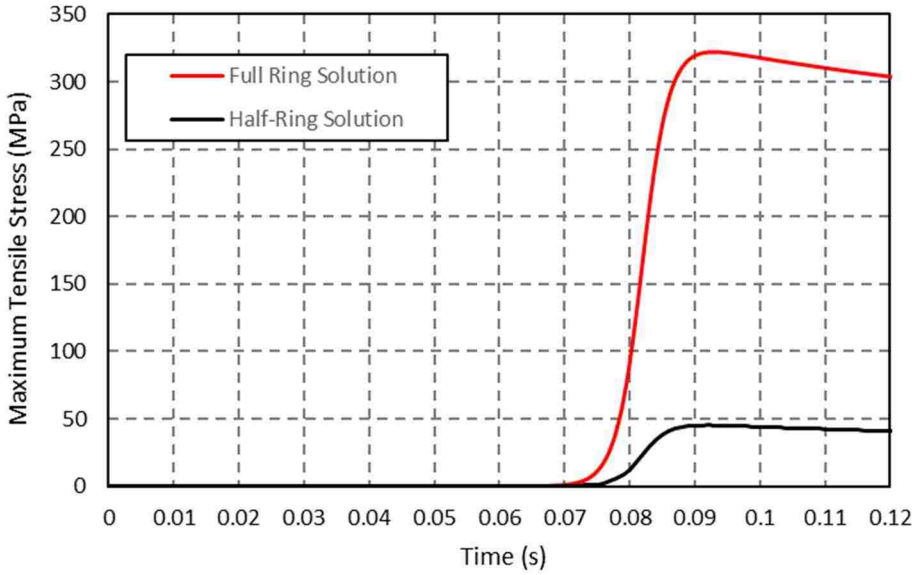

Figure 130. LRRA maximum tensile stress history for different fuel ring geometries.

Next, we examine the radial and circumferential stresses at the time of the peak (t=0.092 s). Figure 131 shows the radial stress comparison, and Figure 132 shows the circumferential stress comparison. There is a significant reduction of both the radial and circumferential stresses achieved by the slotted annulus design.

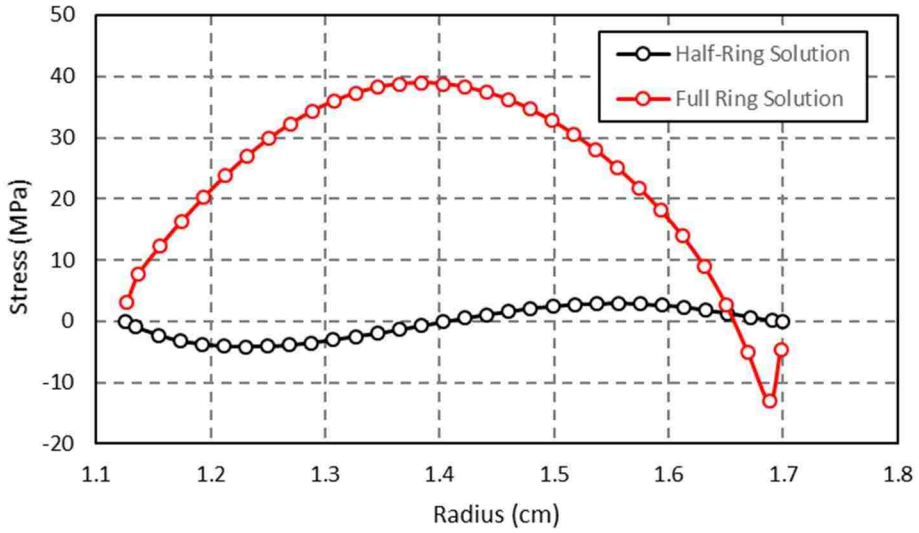

Figure 131. LRRA radial stress results for different fuel ring geometries.

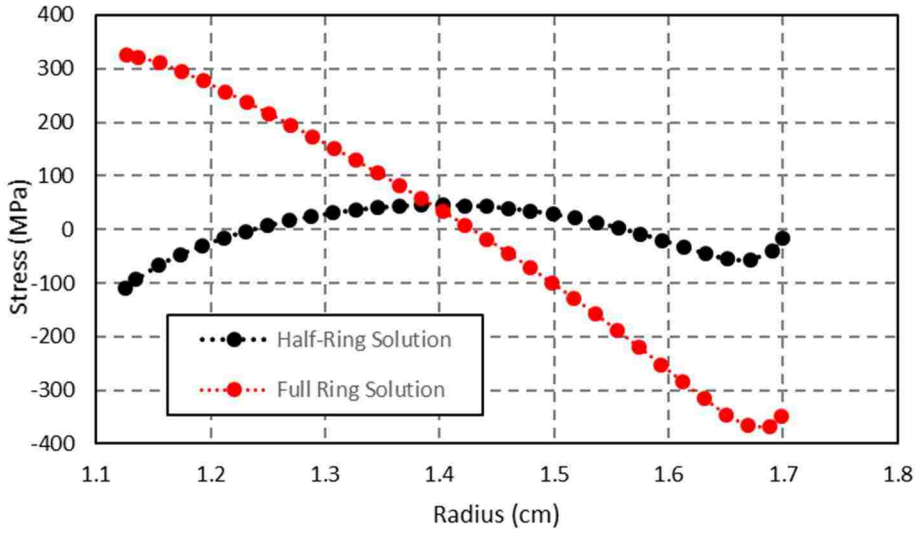

Figure 132. LRRA circumferential stress results for different fuel ring geometries.

Finally, we examine the radial and circumferential stresses after the reactor has reached equilibrium (t=300 s). Figure 133 shows the radial stress comparison. At equilibrium, the radial stress within the fuel is compressive under the full ring solution. For the half-ring solution, the radial stress is tensile near the inner radii, and becomes

compressive toward the outer radii (but zero at each inner and outer face). There is also a reduction in the magnitude of the peak compressive stress realized by the slotted annulus design.

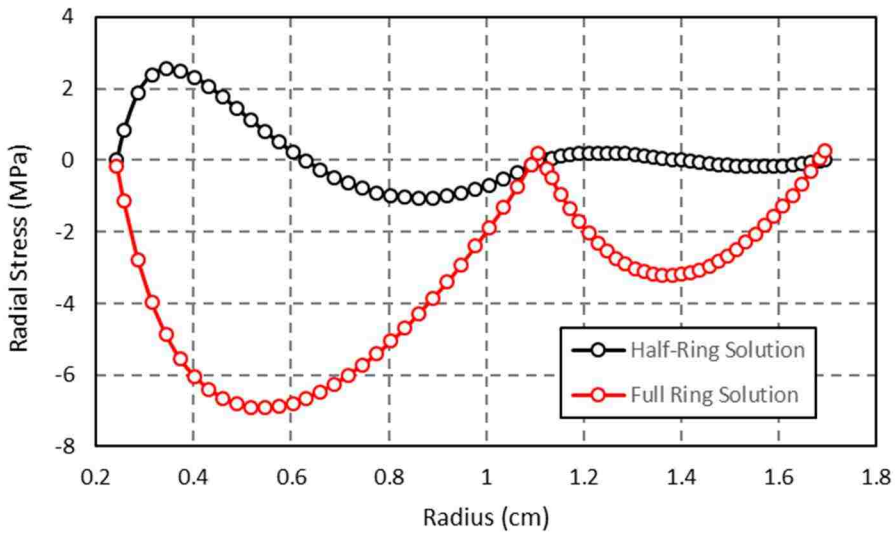

Figure 133. Post-LRRA equilibrium radial stress results for different fuel ring geometries.

Figure 134 shows the circumferential stress comparison at equilibrium. There is a reduction in the peak tensile stress for the inner fuel pellet, and a more significant reduction in the peak tensile stress for the outer fuel pellet that is achieved by the slotted annulus design.

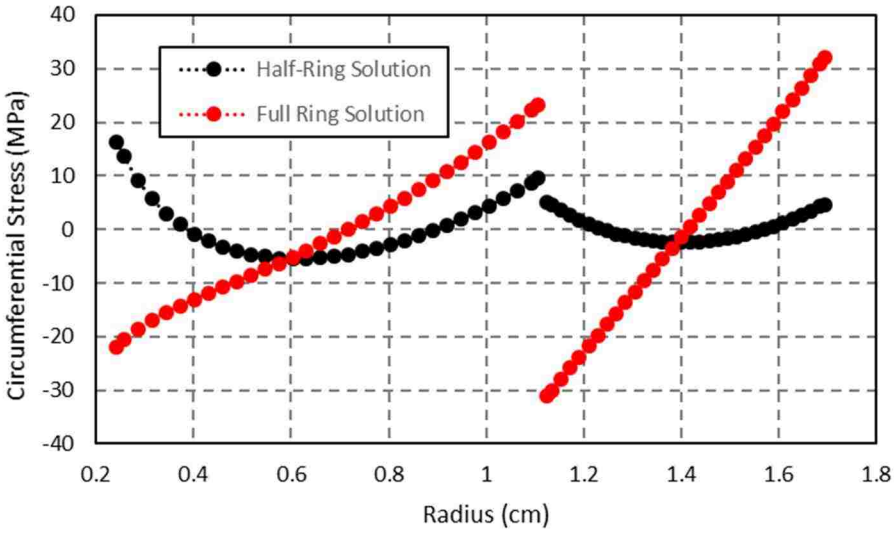

Figure 134. Post-LRRA equilibrium circumferential stress results for different fuel ring geometries.

7.7. Conclusions

An overview of the thermomechanical response characteristics of a natural circulation research reactor to a large rapid reactivity addition (LRRA) has been presented. The initial heating of the fuel due to the reactor power pulse was seen to be nearly adiabatic, and the resulting radial temperature profile in the fuel followed the shape of the fission energy deposition profile. The maximum fuel tensile stress was seen to rise rapidly to an initial peak very shortly after the peak power of the reactor power pulse. The tensile stress would then decrease significantly before rising again to a second peak, as heat transfer within and away from the fuel shifted the radial temperature profile. Eventually, an equilibrium stress profile was achieved.

Variation of magnitude of the LRRA were examined to identify overall trends of the characteristics of the thermomechanical response. The peak tensile stress in the fuel was seen to increase with the magnitude of the reactivity addition. Although thermal expansion caused the gap between the fuel and the niobium cup to decrease with the reactivity addition, the potential for closure of this gap was seen to be unlikely (except for very large reactivity additions).

An increase in the reactivity addition time of the LRRA (i.e., a slower reactivity addition ramp) was seen to be somewhat effective in reducing the peak tensile stress in the fuel. A "flattening" of the fission energy deposition profile, however, was seen to significantly reduce the peak tensile stress. The most effective means of reducing the peak tensile stress was seen to be changing the form of the fuel from annular rings to semicircular annular half-rings. The impact of a post-pulse rod drop was not examined, since the peak tensile stress was nearly coincident with the peak power of the pulse.

8. Conclusions

The evaluation of reactivity initiated accidents (RIAs) has been seen to be an important consideration in research reactor safety analysis. Many recent works from the international research reactor community have addressed these transients. However, these did not appear to have addressed large rapid reactivity additions (LRRAs), particularly those for which a reactor scram is not credited to limit the severity of the events being analyzed. This work has been an investigation of the response of a natural circulation cooled research reactor to such LRRAs.

A code designed to couple the kinetics response of the reactor, the thermal-hydraulic response of the fuel-coolant system, and the thermomechanical response of the fuel element materials was designed and developed. This code, named Razorback, was validated against measured data from the Annular Core Research Reactor (ACRR) at Sandia National Laboratories (SNL), for which LRRAs are a part of the ACRR's normal operation, and then utilized to investigate the response of the ACRR to a wide range of LRRAs.

The reactor power, pulse timing characteristics, and the initial temperature rise response characteristics of a natural circulation research reactor (i.e., the ACRR) to LRRAs have been presented. The peak power, energy yield, pulse width, and initial temperature rise were seen to follow a Nordheim-Fuchs model trend for reactivity additions up to ~$3. After which, the Nordheim-Fuchs model ceases to be effective due to the impact of a finite reactivity addition time (80 ms here for the ACRR), versus a step reactivity addition assumed for Nordheim-Fuchs. Peak power, energy yield, and initial temperature rise are

significantly overpredicted by Nordheim-Fuchs. Thus, the use of a Nordheim-Fuchs model for safety analysis purposes was seen to be acceptable, given that the predictions will be either reasonable or conservative. However, establishing reactivity controls based on Nordheim-Fuchs safety analyses could unnecessarily limit reactor performance capabilities. Also, any plans to utilize peak power, energy yield, or reactor period as trip setpoints should consider the impact of a finite reactivity addition time to avoid unnecessarily limiting reactor performance capabilities.

The thermal-hydraulic response characteristics of a natural circulation research reactor to a LRRA have been presented. The maximum fuel temperature was seen to incur an initial peak increase due to the near-adiabatic heating induced by the reactor power pulse, followed by a post-pulse temperature rise that peaks when a natural circulation coolant flow is established at a level which allows a matching of the heat transfer rate from the fuel to the coolant. Rapid increases in the pressure of the coolant in the channel were seen, along with an initial rapid expansion of the coolant outward from the axial center of the channel occurred, in both the upward and downward direction. For higher LRRA values, regions of saturated boiling developed within the channel.

A post-pulse rod drop was determined to have a significant impact on the post-pulse temperature rise in the fuel (essentially eliminating it for a wide range of LRRAs). However, it was not able to eliminate the occurrence of boiling over a wide range of LRRAs, as it did for the post-pulse temperature rise. An energy buildup sufficient to initiate boiling can thus occur during the pulse heating itself, for larger LRRAs.

The thermomechanical response characteristics of a natural circulation research reactor to LRRAs have been presented. The maximum fuel tensile stress was seen to rise

rapidly to an initial peak very shortly after the peak power of the reactor power pulse, due to initial fission heating radial profiles steeply peaked toward the outer surface of the fuel. Peak tensile stress in the fuel was seen to increase with the magnitude of the reactivity addition. Closure of the gaps between the fuel and its niobium cup was seen to be unlikely (except perhaps for very large reactivity additions).

An increase in the reactivity addition time of the LRRA was somewhat effective in reducing the peak tensile stress in the fuel. A "flattening" of the fission energy deposition profile was seen to significantly reduce the peak tensile stress. However, the most effective means of reducing the peak tensile stress was seen to be changing the form of the fuel from annular rings to semicircular annular half-rings. The impact of a post-pulse rod drop was not examined, since the peak tensile stress was nearly coincident with the peak power of the pulse.

The development and validation of the Razorback code has provided a valuable tool for the safety analysis of the ACRR, and potentially other research reactors. The code allowed for the examination of the response of a research reactor to various LRRAs, yielding valuable insight into the response phenomena and the implications in the realm of safety analysis. In addition, this code should provide a valuable tool for engineers (both experienced and aspiring) to investigate reactor behavior where actual reactor experiments may not be feasible.

9. Future Work

The significant overprediction of the steady-state temperature of the ACRR versus the reactor power level should be pursued. Work is underway to address the geometrically complicated features of an ACRR fuel element and instrumented fuel element using a finite element model code. An experimental approach has been identified to determine if the indicated power level of the ACRR is conservatively high.

More thermal-hydraulic data (e.g., flowrates and temperature profiles) is needed to provided further validation of the code. There is a particular need for data in the two-phase flow regime, which would be beneficial to further develop the code's two-phase flow model. Recent critical heat flux tests performed at the University of Wisconsin at Madison may be able to provide useful validation data.

Since in-situ measurement of thermal expansion and thermal stresses in the fuel element are not feasible, additional non-experimental validation will be pursued. A comparison of the thermal expansion and stress results against the results of a detailed finite element model should be possible in the near future from the work of a colleague.

Lastly, the application of the code to other research reactors (e.g., TRIGAs and plate fueled Material Test Reactors will be pursued. As part of this effort, there is a need to further implement and verify and validate, the Cartesian geometry capabilities of Razorback. The application of the code to the IAEA research reactor benchmark would allow for code-to-code comparisons with RELAP5 and PARET.

References

[1] International Atomic Energy Agency, "Applications of Research Reactors, IAEA Nuclear Energy Series No. NP-T-5.3," IAEA, Vienna, 2014.

[2] 10 CFR Part 50, *Domestic Licensing of Production and Utilization Facilities,* Code of Federal Regulations.

[3] "Guidelines for Preparing and Reviewing Applications for the Licensing of Non-Power Reactors, Format and Content, NUREG-1537 Part I," United States Nuclear Regulatory Commission, February 1996.

[4] T. Hamidouche, et al., "Overview of accident analysis in research reactors," *Progress in Nuclear Energy,* vol. 50, pp. 7-14, 2008.

[5] T. Hamidouche and A. Bousbia-Salah, "Assessment of RELAP5 point kinetic model against reactivity insertion transient in the IAEA 10 MW MTR research reactor," *Nuclear Engineering and Design,* vol. 240, pp. 672-677, 2010.

[6] I. H. Bokhari, "Analysis of reactivity induced accidents at Pakistan Research Reactor-1," *Annals of Nuclear Energy,* vol. 29, pp. 2225-2234, 2002.

[7] H. Kazeminejad, "Thermal-Hydraulic modeling of reactivity insertion in a research reactor," *Annals of Nuclear Energy,* vol. 45, pp. 59-67, 2012.

[8] Khater, et al., "Thermal-hydraulic modeling of reactivity accident in MTR reactors," *Annals of Nuclear Energy,* vol. 34, pp. 732-742, 2007.

[9] J. J. Duderstadt and L. J. Hamilton, Nuclear Reactor Analysis, New York: John Wiley & Sons, 1976.

[10] G. I. Bell and S. Glasstone, Nuclear Reactor Theory, New York: Van Nostrand Reinhold Co., 1970.

[11] G. B. West, et. al., "Kinetic Behavior of TRIGA Reactors, Report GA-7882," General Atomics Corporation, 1967.

[12] "Kansas State University SAR (redacted version)," December 2004. [Online]. Available: https://www.nrc.gov/docs/ML0525/ML052580517.pdf. [Accessed November 2018].

[13] "University of Texas at Austin SAR (redacted version)," December 2011. [Online]. Available: https://www.nrc.gov/docs/ML1215/ML12156A097.pdf. [Accessed November 2018].

[14] G. L. Mesina, "A history of RELAP computer codes," *Nuclear Science and Engineering,* vol. 182, pp. v-ix, 2016.

[15] A. P. Olson, et al., "A User Guide to PARET/ANL Version 7.6, ANL/RERTR/TM-11-38, Rev. 1," Argonne National Laboratory, Argonne, IL, May 2015.

[16] W. L. Woodruff, "A kinetic and thermal hydraulics capability for the analysis of research reactors," *Nuclear Technology,* vol. 64, pp. 196-05, 1984.

[17] B. Dionne, et al., "Summary of RELAP5 Assessments Performed in Relation to Conversion Analysis of Research Reactors, ANL/GTRI/TM-14-3," Argonne National Laboratory, Argonne, IL, April 2014.

[18] A. Bousbia-Salah and T. Hamidouche, "Analysis of the IAEA research reactor benchmark problem by the RETRAC-PC code," *Nuclear Engineering and Design,* vol. 235, pp. 661-674, 2005.

[19] T. Hamidouche, "Dynamic calculations of the IAEA safety MTR research reactor benchmark problem using RELAP5/3.2," *Annals of Nuclear Energy,* vol. 31, pp. 1385-1402, 2004.

[20] H. Kazeminejad, "Reactivity insertion limits in a typical pool-type research reactor cooled by natural circulation," *Annals of Nuclear Energy,* vol. 33, pp. 252-261, 2006.

[21] K. A. Jordan, et al., "Modern design and safety analysis of the University of Florida Training Reactor," *Nuclear Engineering and Design,* vol. 286, pp. 89-93, 2015.

[22] Y. Ronen, CRC Handbook of Nuclear Reactor Calculations, Vol. II, Boca Raton, FL: CRC Press, Inc., 1986.

[23] "MCNP - A General Monte Carlo N-Particle Transport Code Version 5, LA-UR-03-1987," Los Alamos National Laboratory, Los Alamos, NM, 2008.

[24] F. P. Incropera and D. P. DeWitt, Fundamentals of Heat and Mass Transfer, 2nd Edition, New York, NY: John Wiley & Sons, 1985.

[25] A. E. Bergles and W. M. Rohsenow, "The Determination of Forced-Convection Surface-Boiling Heat Transfer," *Journal of Heat Transfer,* vol. 86, no. 3, pp. 365-372, 1964.

[26] W. H. Jens and P. A. Lottes, "Analysis of Heat Transfer, Burnout, Pressure Drop and Density Data for High-Pressure Water, ANL-4627," Argonne National Laboratory, Argonne, IL, May 1951.

[27] F. W. Sears, An Introduction to Thermodynamics, the Kinetic Theory of Gases, and Statistical Mechanics, 2nd Edition, Reading, MA: Addison-Wesley Publishing Company, Inc., 1953.

[28] N. Zuber and J. A. Findley, "Average volumetric concentration in two-phase flow systems," *Journal of Heat Transfer,* vol. 87.4, pp. 453-468, 1965.

[29] R. T. Lahey and F. J. Moody, The Thermal-Hydraulics of a Boiling Water Nuclear Reactor, American Nuclear Society, 1984.

[30] T. Habiki and M. Ishii, "One-dimensional drift-flux model and constitutive equations for relative motion between phases in various two-phase flow regimes," *International Journal of Heat and Mass Transfer,* vol. 46, pp. 4935-4948, 2003.

[31] D. G. Talley, "RAZORBACK - A Research Reactor Transient Analysis Code, Version 1.0 - Volume 1: User's Manual, SAND2017-10561," Sandia National Laboratories, Albuquerque, NM, September 2017.

[32] D. G. Talley, "RAZORBACK - A Research Reactor Transient Analysis Code, Version 1.0 - Volume 2: Software Design and Development Report, SAND2018-4507," Sandia National Laboratories, Albuquerque, NM, April 2018.

[33] S. Talebi, et al., "A numerical technique for analysis of transient two-phase flow in a vertical tube using the Drift Flux Model," *Nuclear Engineering and Design,* vol. 242, pp. 316-322, 2012.

[34] D. G. Talley, "RAZORZBACK - A Research Reactor Transient Analysis Code, Version 1.0 - Volume 3: Verification and Validation Report, SAND2017-3372," Sandia National Laboratories, Albuquerque, NM, April 2017.

[35] B. D. Ganapol, "A highly accurate algorithm for the solution of the point kinetics equations," *Annals of Nuclear Energy,* vol. 62, pp. 564-571, 2013.

[36] S. P. Timoshenko and J. N. Goodier, Theory of Elasticity, New York: McGraw-Hill Book Company, 1970.

[37] Reactor Research and Development Department, "Annular Core Pulse Reactor Upgrade Quarterly Report - July-September 1975, SAND75-0630," Sandia National Laboratories, Albuquerque, NM, January 1976.

[38] B. A. Boley and J. H. Weiner, Theory of Thermal Stresses, Mineola, NY: Dover Publications, Inc., 1997.